Continuous crystallization of ultra-fine energetic particles by the Flash-Evaporation Process

Benedikt Risse

To cite this version:

Benedikt Risse. Continuous crystallization of ultra-fine energetic particles by the Flash-Evaporation Process. Food and Nutrition. Université de Lorraine, 2012. English. NNT : 2012LORR0144 . tel-01749359

HAL Id: tel-01749359

https://hal.univ-lorraine.fr/tel-01749359

Submitted on 29 Mar 2018

Université de Lorraine – École doctorale RP2E
École Nationale Supérieure des Industries Chimiques
Laboratoire : Réactions et Génie des Procédés

Thèse de doctorat

Spécialité : Génie des Procédés et des Produits

Présentée par :
Benedikt RISSE

Titre de la thèse :

Continuous crystallization of ultra-fine energetic particles by the Flash-Evaporation Process

Soutenue publiquement le 04 octobre 2012 à l'ISL, Saint – Louis, devant la commission d'examen :

Président :	E. PLASARI, Professeur (INPL, Nancy, France)
Rapporteurs :	T. KLAPÖTKE, Professeur (LMU München, Allemagne) U. TRÄGNER, Professeur (HS, Mannheim, Allemagne)
Examinateurs :	H. MUHR, HDR (INPL, Nancy, France) D. SPITZER, HDR (ISL, Saint - Louis, France) E. KOCH, Docteur (MSIAC, Bruxelles, Belgique)

Université de Lorraine – École doctorale RP2E
École Nationale Supérieure des Industries Chimiques
Laboratoire : Réactions et Génie des Procédés

Thèse de doctorat

Spécialité : Génie des Procédés et des Produits

Présentée par :
Benedikt RISSE

Titre de la thèse :

Continuous crystallization of ultra-fine energetic particles by the Flash-Evaporation Process

Soutenue publiquement le 04 octobre 2012 à l'ISL, Saint – Louis, devant la commission d'examen :

Président :	E. PLASARI, Professeur (INPL, Nancy, France)
Rapporteurs :	T. KLAPÖTKE, Professeur (LMU München, Allemagne) U. TRÄGNER, Professeur (HS, Mannheim, Allemagne)
Examinateurs :	H. MUHR, HDR (INPL, Nancy, France) D. SPITZER, HDR (ISL, Saint - Louis, France) E. KOCH, Docteur (MSIAC, Bruxelles, Belgique)

It was my personal goal to end this work with the ultimate formula:

$$X = a + b \times c \;,$$

With which the particle size, shape, color and taste, could be calculated only by inserting three variables.

As a rule of thumb, with every new result that was obtained, one question could be answered. However, following the same rule, with every new result two further questions came up.

Acknowledgement

First of all I want to thank the tutor and co-tutor of my doctoral thesis ***Hervé MUHR*** and ***Denis SPITZER*** for their thrust and support they gave to me.

I want to thank my colleagues I usually worked with and that have contributed to the success of this work. In particular, ***Marc COMET*** for proofreading and a lot of fun in the laboratory and bureau, ***Vincent PICHOT*** for the nice cooperation in terms of the nano-Hexolite and for giving me 3 g of nanodiamonds that I will try to reassemble in my free-time, ***Fabien SCHNELL*** for the numerous SEM analyses he made for me (once my 3 g diamond is finished you may apply a 3 g layer of platinum onto it), ***Dominique HASSLER*** for building the first cyclone and other things for me and for being the living example that adults are still allowed to play with toys, ***Christelle NICOLLET*** for the continuous explosive support and the nice cooperation, ***Jean URBAN*** for transferring my sketch of the atomization chamber and the cyclone system into a comprehensive drawing of lines and numbers, ***Michael SCHÄFER*** for his troubleshooting talent, ***Claude STEINBACH*** for the vacuum pump he gave to me and without it I would not have made such a progress and ***Philippe EBERHARDT*** for the numerous interesting discussions.

I also want to thank my colleagues ***Karine BONNOT, Pierre GIBOT, Kyang-Tae HAN, Silke BRAUN, Bernd WANDERS, Fabrice CISZEK*** and ***Barbara BASCHUNG*** for their help and the nice time at work. I also want to thank the other doctoral and former doctoral students ***Loic, Nelly, Benny, Arnaud*** and ***David*** for knowing that other PhD students have the same problems.

I would like to express my deep respect for the workers at the ***atelier central*** for the excellent work they have done.

The same applies to ***my parents.***

Very special thanks are dedicated to, my former professor at ENSIC ***Eduard PLASARI*** for teaching me the secrets of crystallization and being the president in my examination commission, ***Thomas KLAPÖTKE*** professor at the *LMU München* in the fields of energetic materials and ***Ulrich TRÄGNER,*** my former professor in mechanical engineering at the *Hochschule Mannheim,* in their function as rapporteurs and to ***Dr. Ernst-Christian KOCH*** from the MSIAC in Brussels, in his role as examiner of my work.

Résumé étendu

Introduction

La désensibilisation des explosifs vis-à-vis d'une initiation accidentelle, joue un rôle important depuis la découverte de la nitroglycérine. La nitroglycérine, synthétisée en 1847 par Ascanio Sobrero, est un liquide explosif ultrasensible, qui détone au moindre choc. La désensibilisation de la nitroglycérine par absorption dans du kieselguhr n'a été réalisée qu'en 1867 par Alfred Nobel [1].

Le terme « explosif » décrit des substances et des mélanges de substances, capables de libérer rapidement de grandes quantités d'énergie sous forme de pression et de chaleur. Lorsque la propagation du front de réaction se produit à une vitesse inférieure à celle du son dans l'explosif, on parle d'une déflagration. Une détonation apparaît quand la vitesse de la propagation est égale ou supérieure à la vitesse du son dans le matériau.

Du fait que le domaine militaire est le consommateur majeur des matériaux énergétiques, les exigences relatives aux systèmes contenant l'explosif sont très élevées.

Ainsi, on attend d'un système pyrotechnique qu'il soit insensible vis-à-vis d'une grande chaleur, comme cela peut arriver lors d'un incendie, ou encore vis-à-vis d'une forte sollicitation mécanique comme le tir direct, l'impact de shrapnels ou encore une détonation adjacente.

La méthode de désensibilisation d'un explosif la plus commune, consiste à le mélanger avec une cire ou un matériau énergétique moins sensible. L'addition d'une cire à un explosif pulvérulent présente l'avantage de sécuriser sa manipulation en réduisant sa sensibilité. Cependant, la perte de performance est un inconvénient de cette méthode. L'utilisation d'un liant énergétique permet de diminuer la perte de performance, par contre l'explosif devient en général à nouveau plus sensible.

Au fur et à mesure de la progression de la connaissance des explosifs et de leurs mécanismes d'initiation, la nécessité de développer des techniques de désensibilisation plus performantes s'est également imposée.

L'initiation accidentelle d'un explosif, par la chaleur, par l'électricité ou par une sollicitation mécanique, décrit un mécanisme involontaire, déclenchant une réaction de l'explosif.

La formation de *points chauds* joue un rôle important dans ce mécanisme. Le terme « point chaud », désigne toutes formes d'irrégularités comme des bulles de gaz, des pores, des impuretés ou encore des défauts cristallins, servant à convertir de l'énergie externe en chaleur [2, 3]. En outre, on distingue les points chauds internes, c'est-à-dire se situant à l'intérieur des grains de l'explosif, des points chauds externes, qui eux se situent à la surface des particules de l'explosif [4]. La compression adiabatique d'une bulle de gaz à la suite d'une impulsion mécanique représente le meilleur exemple d'un mécanisme de génération de chaleur.

La chaleur provenant de ce point chaud doit être, en fonction de la taille du point chaud, supérieure à une température critique pendant une durée de l'ordre de 10^{-5} à 10^{-3} s [5] pour déclencher une réaction de l'explosif. Le déroulement d'une détonation suit la chaîne séquentielle suivante :

Initiation → Point Chaud → Déflagration → Détonation.

Initiation: C'est l'événement accidentel premier qui apporte de l'énergie dans l'explosif par exemple par l'impact d'un projectile ou par la chaleur dégagée par un incendie.

Point Chaud: C'est la conversion de l'énergie apportée de l'extérieur en chaleur au niveau de points caractéristiques au sein de l'explosif.

Déflagration: Il s'agit d'un mécanisme de décomposition dont la vitesse du front de réaction est inférieure à la vitesse du son dans l'explosif. La vitesse de propagation, dépendant de la dissipation de la chaleur dans l'explosif, la déflagration peut également sous certaines conditions transiter en détonation.

Détonation: Il s'agit d'un mécanisme de décomposition, déclenché par une onde de choc traversant l'explosif, qui se propage à une vitesse supérieure à la vitesse du son dans l'explosif.

Dans des systèmes militaires, l'initiation est effectuée par un explosif primaire et un relais, permettant le passage de l'initiation directement à la détonation de la charge explosive:

Initiation → Détonation

Le passage par le point chaud représente le mécanisme d'initiation nécessitant l'énergie la plus basse pour déclencher une réaction de décomposition de l'explosif.

Du fait que le point chaud joue un rôle essentiel, son élimination permet de désensibiliser l'explosif par rapport aux influences externes.

Tarver *et al*.[5] ont découvert que la taille d'un point chaud doit être comprise entre 0,1 – 10 µm et que la température doit être d'au moins 700 K, pour déclencher une réaction. En outre, il existe une cohérence entre la taille d'un point chaud et sa température critique. Lorsque la taille du point chaud diminue, sa température critique augmente [5]. Ainsi, la réduction de la taille des particules permet de réduire la taille des points chauds, ce qui permet la désensibilisation de l'explosif du fait que des points chauds plus petits, requièrent des températures d'amorçage bien plus élevées [6].

Outre leur sensibilité réduite, les explosifs de granulométrie nanométrique possèdent une distance plus courte entre la déflagration et la détonation [5]. Du fait d'une taille de particule plus petite, les points chauds potentiels se trouvent plus régulièrement distribués dans la matière de l'explosif. Après l'initiation, qui exige une température plus élevée, la chaleur libérée peut plus rapidement diffuser vers les particules voisines, pour créer des points chauds supplémentaires.

Etat de l'art

Au cours des quinze dernières années, les procédés suivants ont été développés pour la préparation des explosifs nanostructurés :

- Le broyage humide
- Le procédé Sol-Gel
- La condensation sous vide
- L'électronébulisation
- La nanocristallisation assistée par ultrasons
- L'expansion rapide des solutions supercritiques

Dans le **broyage humide** [7], le cyclotriméthylènetrinitramine (RDX) est dispersé dans de l'eau avec quelques additifs et ensuite broyé pendant 1 h. Par la suite, le produit broyé est séparé sur un filtre de 100 nm et séché sous vide. Ce procédé est le seul procédé « top-down », qui a permis la préparation de 16 g de RDX par charge. Du fait de la présence de grandes quantités d'eau, le produit final humide est très sensible au mûrissement d'Ostwald.

Dans le **procédé Sol-Gel** [8, 9], le RDX, le tétraméthoxysilane et un catalyseur sont d'abord dissous dans un solvant commun, à la suite de quoi la solution est gélifiée. A l'aide d'un solvant dans lequel le RDX ne se dissout pas, tel que l'eau, on extrait le solvant d'origine, ce qui induit la cristallisation du RDX. L'eau restant dans les pores est ensuite extraite à l'aide de CO_2 supercritique. L'inconvénient de ce procédé est qu'il requiert un équipement important et qu'il ne permet pas de récupérer un produit pur étant donné la « contamination » du produit par la silice formée.

Dans la **condensation sous vide** [10, 11], le RDX est évaporé entre 145 et 202 °C sous pression réduite et ensuite déposé sur un support en quartz refroidi. Les plus petites particules ont une taille de 50 nm. L'inconvénient majeur de ce procédé est sa faible capacité de production et le mode opératoire discontinu. Etant donné la température de travail, qui dans certaines conditions peut être proche de la température de décomposition de l'explosif, ce procédé peut aussi représenter un risque non négligeable.

L'électronébulisation [12] est un procédé de séchage par atomisation, où une solution RDX-acétone est pompée lentement (2,8 mL/h) au travers d'un capillaire métallique ouvert. L'ouverture du capillaire est dirigée vers une plaque métallique positionnée à une distance de quelques centimètres du capillaire. Par l'application d'une haute tension entre le capillaire et la plaque métallique, un *cône de Taylor* se forme, qui est composé de gouttelettes très fines, attirées par la charge opposée de la plaque métallique. Pendant le vol des gouttelettes, le solvant s'évapore et l'explosif cristallise. Du fait du faible débit volumique, seules de petites quantités de RDX ont pu être préparées grâce à ce procédé. De plus, l'utilisation d'une haute tension en présence de vapeurs d'acétone, présente un risque important.

La **nanocristallisation assistée par ultrason** [13, 14] est aussi un procédé de séchage par atomisation. A l'aide de transducteurs ultrasoniques, une solution RDX-acétone est brumisée. Au moyen d'un flux gazeux inerte, l'aérosol est guidé dans un four électrique où le solvant s'évapore. L'explosif cristallisé est ensuite séparé du solvant gazeux dans un précipitateur électrostatique. Le flux gazeux passant le précipitateur électrostatique est condensé dans deux refroidisseurs situés en aval du précipitateur. Les travaux réalisés précédemment au laboratoire sur ce procédé ont montré que, pendant le fonctionnement de l'installation, la concentration de RDX dans le récipient augmentait, ce qui ne permettait pas une maîtrise totale de la brumisation. Dans une première étape d'optimisation, les transducteurs ultrasoniques ont été remplacés par une buse. Ceci a constitué, le premier pas vers la cristallisation-flash, qui fait l'objet du présent travail de thèse. Un schéma de fonctionnement de ce premier procédé est illustré ci-dessous (fig. 1).

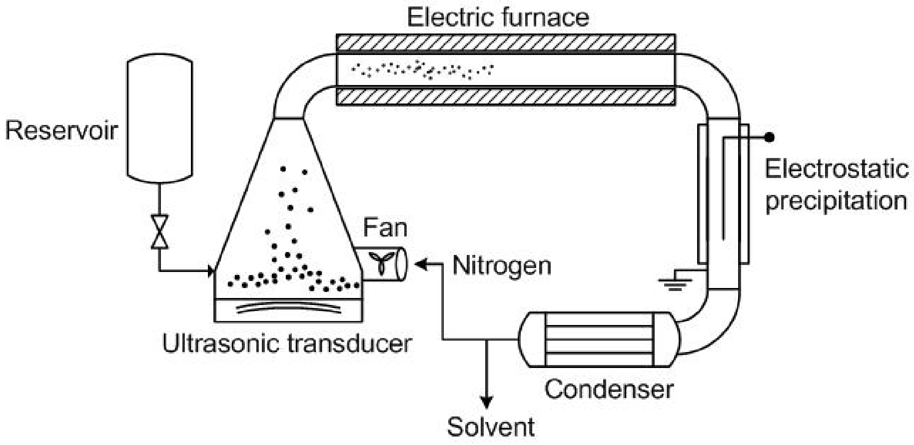

Fig.: 1 – Schéma de fonctionnement de la nanocristallisation assistée par ultrason.

La préparation de nanoparticules par détente rapide de solutions supercritiques [15, 16] est mieux connue sous le nom de RESS (pour **Rapid Expansion of Supercritical Solutions**). Dans le procédé RESS, le RDX est dissous dans du CO_2 supercritique à des températures comprises entre 70 et 75 °C et sous des pressions se situant entre 150 et 295 bar. La solution supercritique est ensuite détendue à une pression inférieure à la pression critique. Suite à la forte chute de la pression et de la température, la solubilité du RDX baisse rapidement ce qui déclenche sa cristallisation. Du fait de la forte chute de la température, le CO_2 condense à la surface du RDX ce qui est essentiel pour sa précipitation. En raison de la faible solubilité du RDX dans le CO_2 supercritique (0,25 mg RDX / 1 g CO_2 à 480 bar et 80 °C) et de la faible capacité de production qui en découle, ce procédé ne convient pas pour une application à grande échelle. Une image du procédé RESS, optimisé pour une production élevé, est illustrée dans la figure 2.

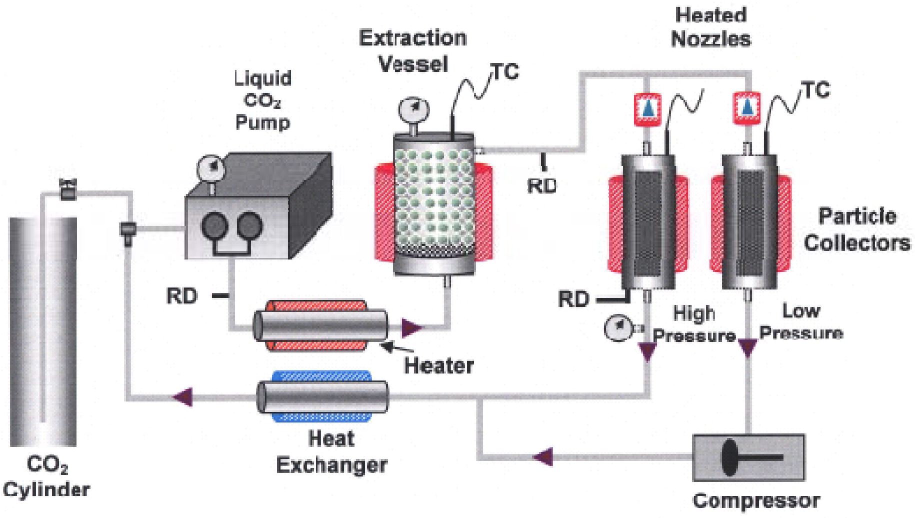

Fig.: 2 – Procédé RESS optimisé pour une capacité de production élevée [16].

Malgré la recherche intense dans ce domaine, la préparation en quantités importantes des explosifs nanostructurés n'a jamais été réalisée. En raison des faibles capacités de production obtenues par les différents procédés décrits ci-dessus, il était jusqu'à présent difficile d'obtenir des résultats significatifs sur le RDX nanométrique. L'ensemble des publications des dernières années se rapporte à des résultats obtenus avec des quantités réduites de matériau (< 1 g). L'objectif principal de la présente thèse de doctorat, a été le développement de la cristallisation-flash en vue de permettre l'usage dans des applications industrielles du nano RDX ainsi que d'autres explosifs nanométriques.

La cristallisation-flash

La cristallisation-flash est fondée sur le principe de l'évaporation flash, où une forte diminution de pression est appliquée à une solution chaude sous pression. Par la réduction de la pression ambiante, le point d'ébullition décroît de la même manière. Le liquide surchauffé est dans un état métastable, qui est caractérisé par le fait que la température du liquide est supérieure à la température d'ébullition. Du fait du déséquilibre thermodynamique de la solution, l'excès d'énergie thermique est converti en chaleur latente dans un processus d'évaporation adiabatique. La vitesse d'évaporation dépend considérablement du degré de surchauffe. Plus le liquide est surchauffé, plus l'énergie emmagasinée dans le liquide est importante et plus grande sera la partie de liquide évaporé.

Pendant l'évaporation-flash, une forte diminution de pression est appliquée à un fluide chaud et sous pression. A cause de cette rapide perte de pression, la température d'ébullition du fluide se réduit et le fluide entre dans un état d'instabilité thermodynamique. L'état métastable est marqué par le fait que la température du fluide est supérieure de la température d'ébullition. Cet état est décrit comme « fluide surchauffé ». Le degré de surchauffe est représenté par ΔT_S :

$$\Delta T_S = T_0 - T_S \qquad \text{Eq.: 1}$$

avec T_0,la température initiale du fluide et T_S, la température du fluide à l'état saturant après la perte de pression.

Dans l'état métastable, le fluide surchauffé tente de retrouver sa stabilité thermodynamique en perdant de l'énergie. Cette perte d'énergie est obtenue par la conversion d'énergie sensible en énergie latente. La force motrice dans ce processus est le degré de surchauffe. Pour des ΔT_S faibles le processus d'évaporation est lent, par contre il peut avoir un caractère « explosif » quand le degré de surchauffe monte. En fonction du degré de surchauffe on distingue : l'évaporation à la surface, ébullition faible, ébullition moyenne, ébullition rapide et l'évaporation-flash [17] (fig. 3).

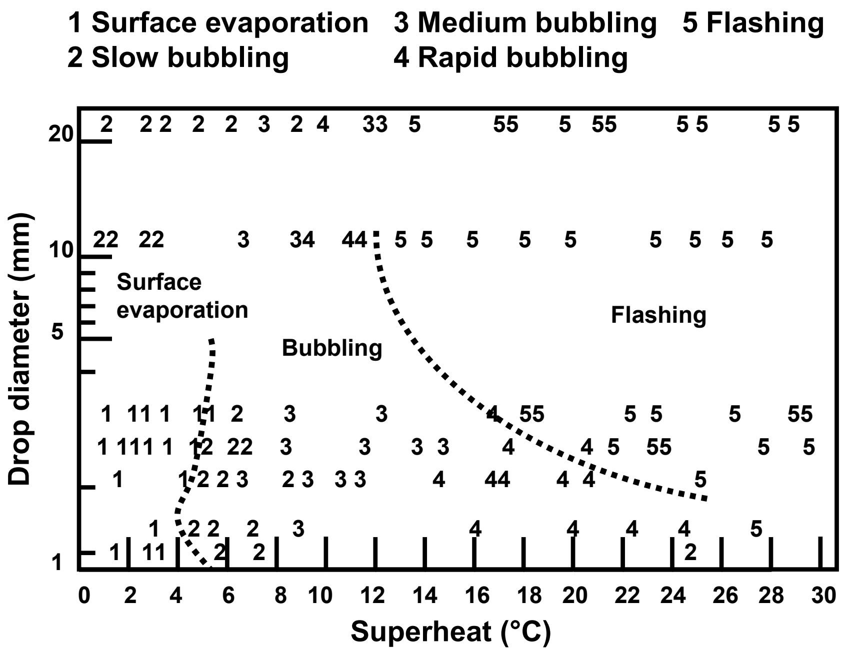

Fig.: 3 – Le caractère d'évaporation en fonction du dégrée de surchauffe [17].

Le degré de surchauffe dépend aussi, de façon importante, de la taille des gouttelettes. Une gouttelette de petite taille peut plus rapidement conduire la chaleur de l'intérieur vers la surface, par contre les gouttelettes plus grandes sont plus sujettes à l'évaporation-flash, même à faible degré de surchauffe. Le caractère violent de l'évaporation-flash est favorisé par la génération de sprays très fins.

La formation des bulles dépend aussi des propriétés physiques du fluide. D'après Owen et Jalil [17] un diamètre critique d_c doit être atteint pour que le germe de bulle pousse et induise l'évaporation. En connaissant le diamètre critique, le degré de surchauffe ΔT_S peut être calculé de la façon suivante :

$$\Delta T_S = \frac{4 \cdot \sigma \cdot \upsilon_G \cdot T_S}{h_{FG} \cdot d_c} \qquad \text{Eq.: 2}$$

avec T_S la température du fluide à l'état saturant, σ la tension superficielle, υ_G le volume spécifique, h_{FG} la chaleur d'évaporation et d_c le diamètre critique de la bulle. La formation des bulles est aussi fonction du terme de nucléation homogène ou hétérogène.

L'évaporation-flash n'a pas lieu simultanément avec la perte de pression. Le processus d'évaporation démarre une fraction de second plus tard après la perte de pression, après une suffisamment forte dégrée de surchauffe est atteinte. Le temps de retard t_D se réduit proportionnellement avec le dégrée de surchauffe ΔT_S croissant [18]:

$$t_D \propto \Delta T_S^{-\frac{2}{7}}$$

Pour un système, ne contenant que d'une seule composante, la quantité de liquide qui vaporise sous l'effet de l'évaporation-flash Δm_{flash}, peut être calculé avec la formule suivante :

$$\Delta m_{flash} = m_0 \cdot (T_0 - T_S) \frac{c_{p,l}(T_0)}{\Delta_{vap} H(T_S, p_S)} \qquad \text{Eq.: 3}$$

avec m_0, la masse initiale du liquide, $c_{p,l}(T_0)$ la chaleur spécifique du liquide à la température de surchauffe T_0 et $\Delta_{vap} H(T_S, p_S)$ l'enthalpie d'évaporation aux conditions saturantes. Cet équation est suffisamment précise pour ΔT_S jusqu'à 50 °C mais peut perdre en précision à températures plus élèves.

L'enthalpie d'évaporation aux conditions saturantes peut être à l'aide de l'équation de Clausius-Clapeyron:

$$\frac{dp}{dT} = \frac{\Delta_{vap} H}{T \cdot \Delta V_m} \qquad \text{Eq.: 4}$$

avec T la température en [K] et ΔV_m le change de volume molaire calculé à partir de :

$$\Delta V_m = V_{m,(g)} - V_{m,(l)} \qquad \text{Eq.: 5}$$

avec $V_{m,(g)}$, le volume molaire du gaz et $V_{m,(l)}$, le volume molaire du liquide. Du fait que le volume du gaz est plus important que le volume du liquide, le change de volume molaire peut être simplifie selon :

$$\Delta V_m \approx V_{m,(g)}$$

Considérant que le gaz est un gaz parfait, ΔV_m peut être exprimé comme :

$$\Delta V_m = \frac{R \cdot T}{p} \qquad \text{Eq. : 6}$$

avec R, la constante des gaz parfaits et p la pression. En supposant que $\Delta_{vap}H$ est indépendant de la température, la forme intégrée de l'équation 4 peut être reformulée :

$$\Delta_{Vap}H = \ln\frac{p_2}{p_1} \cdot \frac{R}{\left(\frac{T_2 - T_1}{T_2 \cdot T_1}\right)} \qquad \text{Eq.: 7}$$

pour T_1 et p_1, on peut prendre, de manière aléatoire, n'importe quelle température et sa pression de vapeur correspondante. Les valeurs de T_2 et p_2 sont définies par les conditions de processus.

Avec T_2 ou p_2 donnée, on calcule l'autre paramètre à l'aide l'équation d'Antoine :

$$\log p = A - \frac{B}{C + T} \qquad \text{Eq.: 8}$$

avec, A, B et C les constantes spécifiques d'Antoine. En fonction des paramètres utilisés, la température T et la pression p peuvent être exprimées en [°C] ou [K] et [bar], [Torr] ou [Pa].

Si la fonction de la température n'est pas connue ou que les tableaux ne sont pas disponibles, la valeur de $c_{p,l}(T_0)$ doit être déterminée par extrapolation. La figure 8 montre bien que la dépendance de $c_{p,l}$ à la température est presque linéaire pour plusieurs solvants, ce qui permet une précision suffisamment élevée.

L'usage d'un logiciel de simulation est fortement recommandé pour les processus à haute température et contenant plusieurs composants. Dans le cadre de cette thèse le logiciel SimSci Pro/II 8.1 a été utilisé pour les simulations numériques. En complément de la simulation numérique, SimSci Pro/II 8.1 est capable de calculer les propriétés physiques et thermodynamiques de plusieurs solvants sur une gamme importante de températures et de pressions.

L'importante quantité de solvant vaporisée en une seule étape d'évaporation est caractéristique de l'évaporation-flash. Le ratio d'évaporation X_{vap} est calculé comme suit :

$$X_{vap} = \frac{\Delta m_{flash}}{m_0} \qquad \text{Eq.: 9}$$

Le ratio d'évaporation idéal est $X_{vap} = 1$, indiquant l'entière évaporation du fluide. Dans ce cas, le solvant, le soluté et l'installation doivent fréquemment subir des charges thermiques très fortes. En pratique, de bons résultats ont déjà été obtenus avec $X_{vap} > 0,7$.

Le ratio d'évaporation peut également être décrit par l'insertion de l'équation 9 dans l'équation 3 :

$$X_{vap} = (T_0 - T_S)\frac{c_{p,l}(T_0)}{\Delta_{vap}H(T_S, p_S)} \qquad \text{Eq.: 10}$$

Les cas où $X_{vap} > 1$ sont intéressants car le soluté est légèrement chauffé après sa cristallisation, laissant envisager une plus faible humidité résiduelle.

En diminuant la pression dans la chambre d'atomisation, la température à l'état saturant T_S diminue aussi. Suivant le type de solvant utilisé et la pression finale, la température peut tomber en-dessous de -30 °C. Cette chute de température, ayant un effet protecteur pour le soluté, est avantageuse pour la nanocristallisation. Elle permet à la solubilité du soluté dans le liquide de décroitre de la même manière.

La solubilité du soluté dans le liquide joue un rôle important dans la nanocristallisation. En fonction de la supersaturation S la morphologie, la taille et la quantité des cristaux peuvent être contrôlées. La sursaturation S est définie de la façon suivante :

$$S = \frac{c}{c_\infty} \qquad \text{Eq.: 11}$$

avec c la concentration du soluté actuel et c_∞ la solubilité du soluté dans le liquide. En règle générale, plus la supersaturation du soluté est importante, plus nombreux sont les cristaux qui appariassent et plus leur croissance est rapide. Au contraire, une faible supersaturation, favorise la formation d'un seul grand cristal, poussant lentement.

Les deux types de cristallisation sont décrits comme « growth » mécanisme et « nucleation » mécanisme. On trouve le principe du mécanisme *growth* dans les procédés du type "séchage d'atomisation". Une solution est atomisée en gouttelettes régulières et très fines. En supposant que chaque gouttelette forme exactement un seul cristal, la taille finale du cristal dépend uniquement de la concentration et de la taille initiale de la gouttelette (fig. 4).

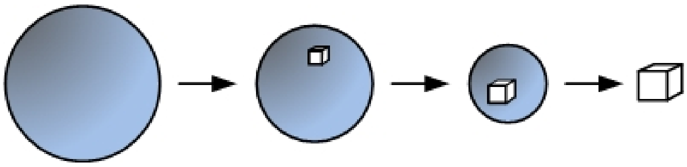

Fig.: 4 – Principe du mécanisme « *growth* ».

La préparation de nanoparticules d'après ce mécanisme nécessite la génération d'un spray extrêmement fin ayant aussi une très faible concentration de soluté. Le respect de ces conditions implique une capacité de production de nanoparticules très faible.

Contrairement au mécanisme *growth* la cristallisation d'après le mécanisme *nucleation* permet la préparation de nanoparticules en plus grande quantité. Le facteur limitant ayant l'influence la plus grande sur la taille des particules est le degré de supersaturation. Plus le degré de supersaturation est élevé, plus les cristaux qu'on peut obtenir seront nombreux et petits. Dans le cas de l'évaporation-flash, l'évaporation rapide du solvant permet d'obtenir un fort degré de supersaturation (fig. 5).

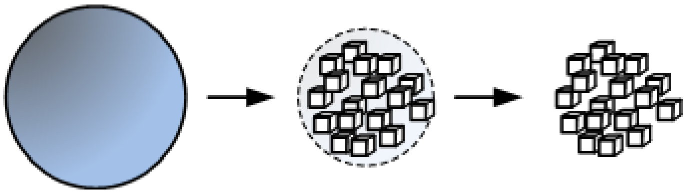

Fig.: 5 – Principe du mécanisme « *nucleation* ».

En pratique, on trouve plutôt une combinaison des deux mécanismes, où le mécanisme *nucleation* est souvent le mécanisme dominant [19]. La figure 6 présente un schéma, montrant la combinaison de *growth* et *nucleation*.

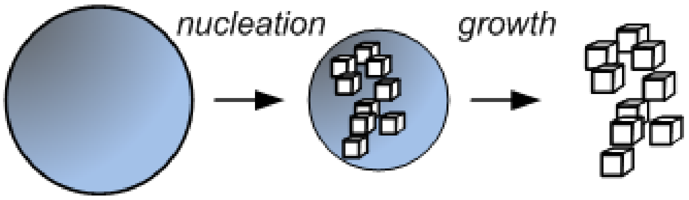

Fig.: 6 – Combinaison des mécanisms « growth » et « nucleation ».

Puisque la préparation des nanoparticules à grande échelle est un des objectifs majeurs de ce travail, le mécanisme *nucleation* revêt un rôle particulièrement important.

D'après l'équation 12, la taille critique d'un germe de cristal d_c dépend directement du degré de supersaturation S :

$$d_c = \frac{4 \cdot \sigma \cdot v}{R \cdot T \cdot \ln S} \qquad \text{Eq.: 12}$$

avec σ, l'énergie de la surface et v, le volume molaire. A cause de la complexité du processus de nanocristallisation, la détermination de la température exacte à partir de laquelle la cristallisation commence n'est pas possible.

La performance de l'évaporation-flash dépend fortement des propriétés du solvant. Pour l'évaporation-flash, un solvant approprié doit combiner une bonne solubilité avec des propriétés thermodynamiques spécifiques. Des matériaux énergétiques étant utilisés en tant que soluté, la température maximale admissible est prédéterminée par la nature de l'explosif. Comme l'étude paramétrique a été exécutée pour le RDX, les solvants étaient choisis en conséquence.

Sur la base des critères suivants, un solvant approprie était choisi. Pour obtenir la charge thermique sur l'explosif la plus faible possible, le point d'ébullition du solvant devait être compris entre 30 et 70 °C. Un point d'ébullition encore plus bas n'est pas recommandé pour des raisons de manipulation. En outre, la chaleur spécifique du solvant devrait être la plus importante possible. Par contre l'enthalpie d'évaporation devrait, en même temps, être très faible. Pour des raisons de sécurité, il est recommandé d'utiliser un solvant thermiquement stable jusqu'à, au moins, 300 °C. La table suivante montre un listage des solvants choisis pour le procédé (tab. 1).

Solvant	T_b **[°C]**	$c_{p,l}$ (at 25°C) **[J mol^{-1} K^{-1}]**	$\Delta_{vap}H$ (at 25°C) **[kJ mol^{-1}]**	φ **[kg m^{-3}]**	η **[10^{-3} Pa s]**
Acétone	56,2	119,95	29,1 [20]	787,5	0,3
Méthyl t-butyl éther (MTBE)	55,2	170,38	27,94	735,6	0,33
Ethyle acétate	77,0	163,91	31,94	894,3	0,43
Méthyle acétate	56,9	132,62	30,32	928,6	0,36
Diéthyl éther	34,4	161,98	26,52	708,1	0,22
Formiate de méthyle	31,7	107,93	27,92	967,5	0,33
Propanal	48,0	122,04	28,31	792,0	0,31

Tab.: 1 – Solvants appropriés pour l'évaporation-flash.

Avec l'exception de $\Delta_{vap}H$, toutes les valeurs de la table ci-dessous ont été calculées à l'aide du logiciel SimSci Pro/II. La température de fonctionnement de l'évaporation-flash étant relativement élevée, le modèle Peng-Robinson [21] a été choisi car il permet d'obtenir une haute précision près du point critique.

La solubilité du RDX aux différentes températures était connue uniquement pour l'acétone, le diéthyl éther et le méthyle acétate [22]. Pour l'acétone et le méthyle acétate, la solubilité en fonction de la température est montrée dans la figure 5. A cause de la faible solubilité du RDX dans le diéthyl éther (elle est inferieure à 100 mg par 100 g de solution), ces valeurs ne sont pas listées dans la figure suivante (fig. 7).

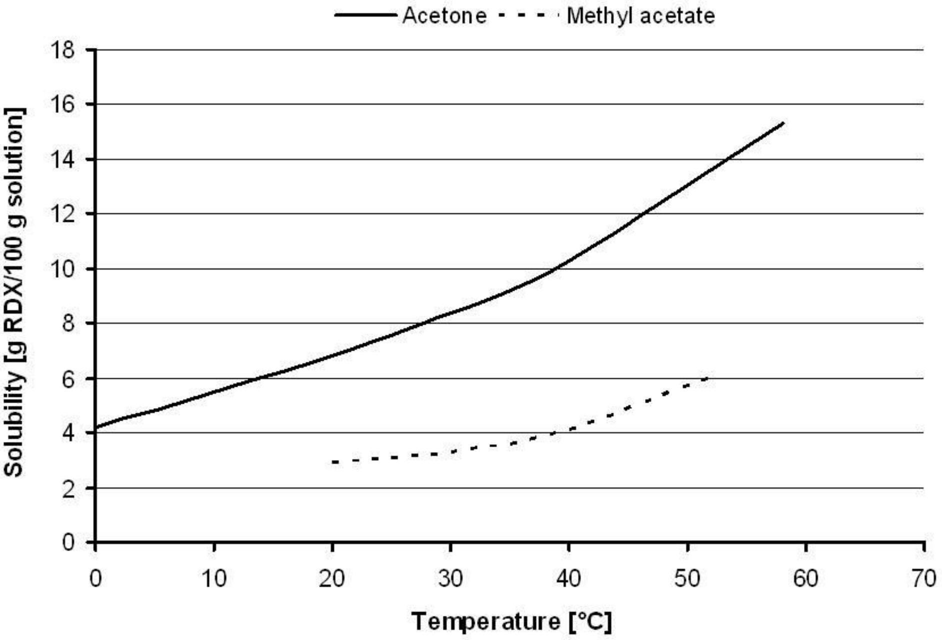

Fig.: 7 – Solubilité du RDX dans l'acétone et le méthyle acétate en fonction de la température [22].

Dans la plupart des solvants le RDX n'est que faiblement soluble. Grâce à la bonne solubilité de RDX dans l'acétone, ce dernier sera défini comme solvant standard dans cette thèse. En outre l'acétone possède une forte stabilité thermique et sa toxicité est bien documentée.

Les figures 8 et 9 montrent le déroulement de $c_{p,l}$ et $\Delta_{vap}H$ en fonction de la température entre -47 et 158 °C à 50 bar.

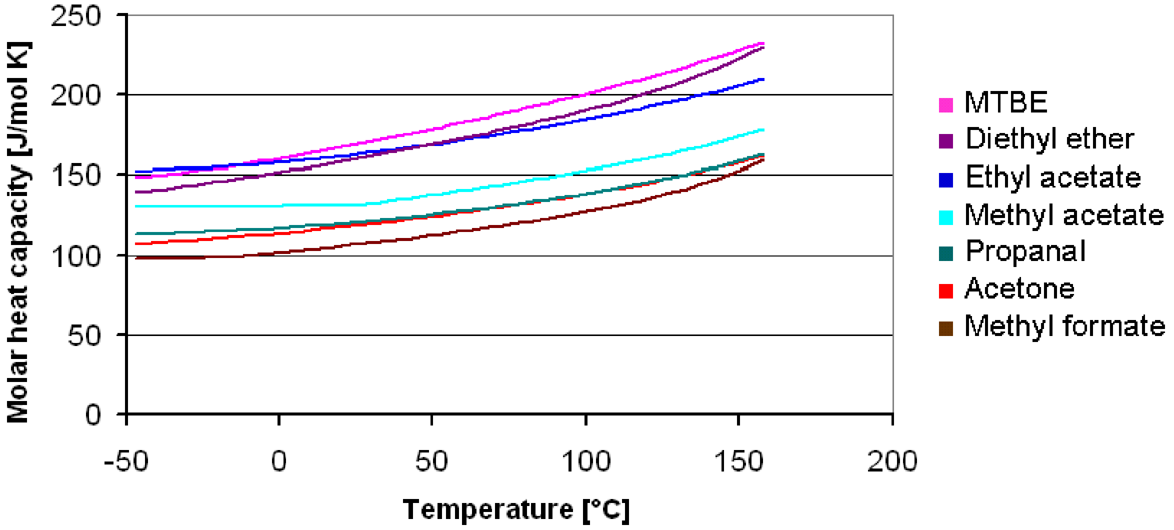

Fig.: 8 – Evolution de la chaleur spécifique $c_{p,l}$ en fonction de la température à 50 bar.

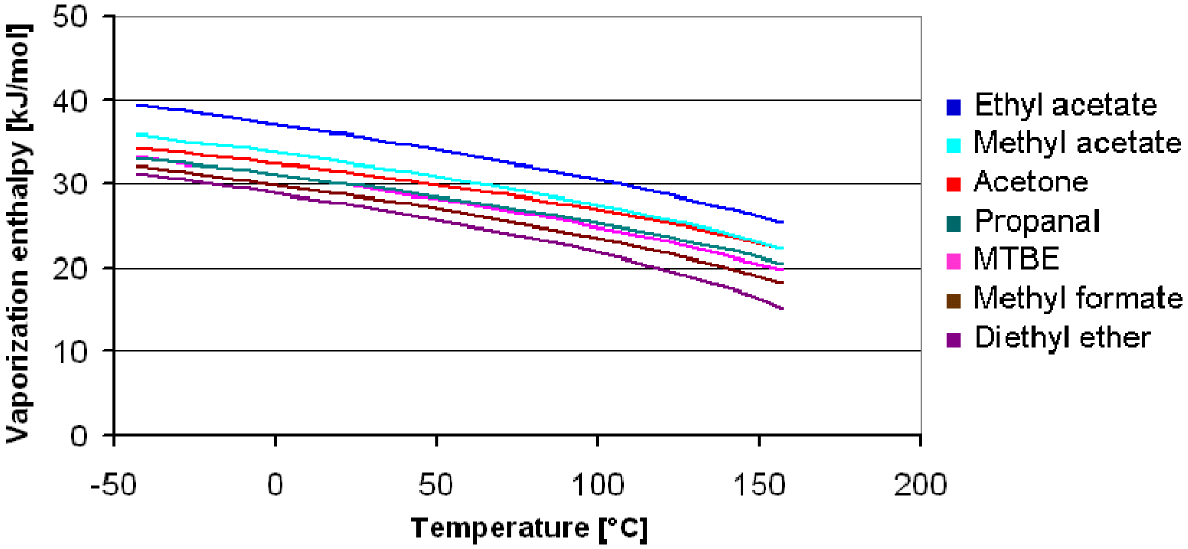

Fig.: 9 – Evolution de l'enthalpie d'évaporation $\Delta_{vap}H$ en fonction de la température à 50 bar.

Sur une plage de 200 °C la valeur de l'enthalpie d'évaporation diminue presque de 50 %, par contre la valeur de la chaleur spécifique monte environ de 50 %.

D'après le diagramme ODTX (One-Dimensional-Time-to-Explosion) du RDX (fig. 10), cet explosif se décompose à 160 °C après 10^4 seconds.

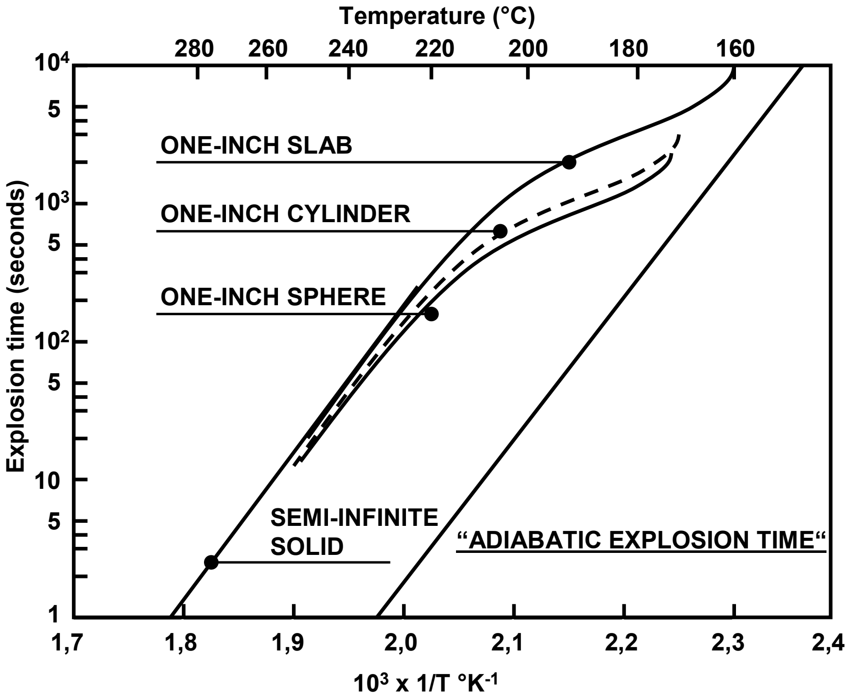

Fig.: 10 – Diagramme ODTX de RDX [23].

On peut constater que la température de surchauffe T_0 pour le RDX est limitée à 160 °C, ce qui représente la température limite supérieure du processus. La température limite inferieure est définie par la température et la pression à l'état saturant dans la chambre d'atomisation. Dans cette thèse, la pompe à vide utilisée ayant un débit volumique maximal de 35 m³/h, elle représente un facteur limitant.

En connaissant les conditions de fonctionnement du processus, les températures maximale et minimale, la température à l'état saturant T_S, le degré de surchauffe ΔT_S et le ratio d'évaporation X_{vap} on été calculés à l'aide du logiciel SimSci Pro/II (tab. 2).

Solvant	T_0 **[°C]**	T_S (5 mbar) **[°C]**	ΔT_S **[°C]**	X_{vap}	T_{crit} **[°C]**	P_{crit} **[bar]**
Acétone	160	-45,3	205,3	0,801	235,05	47,01
Méthyl t-butyl éther (MTBE)	160 **127**	11,2 -48,0	171,2 175,0	1,000 0,999	223,95	34,3
Ethyle acétate	160	-27,2	187,2	0,893	250,15	38,8
Méthyle acétate	160	-42,1	202,1	0,843	233,4	47,5
Diéthyl éther	160 **121**	15,9 -60,4	175,9 181,4	1,000 0,999	193,55	36,4
Formiate de méthyle	160	-60,3	220,3	0,828	214,05	60,0
Propanal	160	-50,7	210,7	0,875	231,25	49,2

Tab.: 2 – Calcul des conditions de fonctionnement.

On voit bien que le ratio d'évaporation de la plupart des solvants est principalement situé entre 0,8 et 0,9, exigeant un dégrée de surchauffe de plus de 200 °C. Par contre, l'utilisation de diéthyl éther ou de méthyl t-buthyl éther permet d'atteindre un ratio d'évaporation à des températures considérablement plus basses.

Par référence aux figures 8 et 9, le diéthyl éther et le méthyl t-buthyl éther ont les chaleurs spécifiques les plus élevées et, en même temps, les enthalpies d'évaporation les plus basses. Grâce à cette particularité thermodynamique les éthers conviennent mieux pour l'évaporation-flash

L'installation de l'évaporation-flash

L'installation développée dans ce travail, est divisée en une partie haute pression et une partie basse pression (fig. 11). La partie haute pression comprend les réservoirs B1, B2 et la buse D1. La haute pression dans les réservoirs est générée à l'aide d'azote comprimé. La partie basse pression comprend la chambre d'atomisation R1, les cyclones C1, C2 et la pompe à vide P1. La transition de la partie haute pression à la partie basse pression est réalisée par la buse à cône creux D1. Normalement, la pression en amont de la buse est au moins de 40 bar et en aval de la buse de 5 mbar absolu. La buse et les cyclones sont chauffés avec des éléments chauffants électriques de 150 W. Tous les circuits de chauffage sont contrôlés par des régulateurs Proportionnel-Intégral-Dérivé (PID).

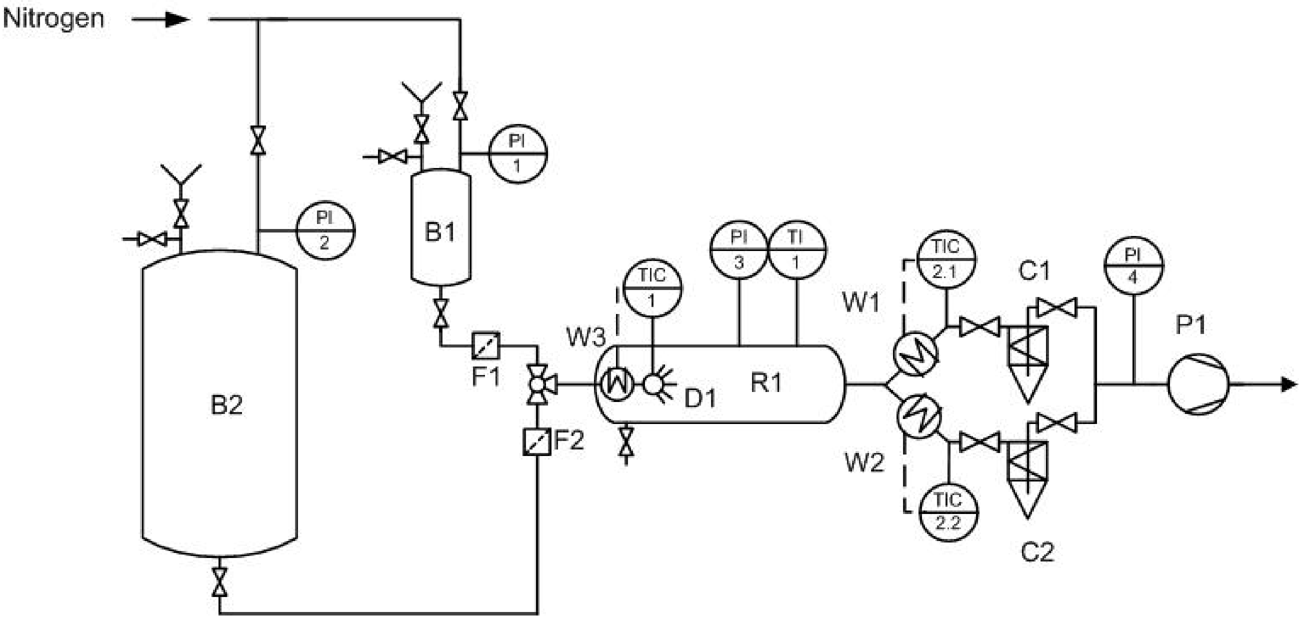

Fig.: 11 – Schéma fonctionnel de la cristallisation flash.

En table 3 sont listées les spécifications et descriptions des pièces individuelles.

Pièce	**Description**
B1	Réservoir haute-pression, 1 L, pression maximale 100 bar
B2	Réservoir haute-pression, 5 L, pression maximale 40 bar
C1/C2	Cyclones axiaux
D1	Buse à cône creux, diamètre 60; 80 et 100 µm
F1/F2	Filtre 10 µm
P1	Pompe à vide, débit volumique 35 m³/h
R1	Chambre d’atomisation, diamètre = 100 mm, longueur = 400 mm
W1/W2	Elément chauffant, 150 W
W3	Elément chauffant buse, 150 W
PI	Manomètre
TI	Indication de température
TIC	Indication et réglage de température

Tab.: 3 – Composants de l’installation.

Pendant le fonctionnement de l’installation, l’un des réservoirs sert comme réserve de solvant tandis que le second est rempli avec la solution d’explosif. Il y a toujours un cyclone en opération, le deuxième cyclone restant en attente.

La buse à cône creux appartient à la catégorie des buses à pulvérisation, récupérant l’énergie nécessaire pour l’atomisation directement du liquide sous pression. Au sein de la catégorie des buses à pulvérisation, la buse à cône creux créé le spray le plus fin. En forçant le liquide dans un mouvement axial à l'intérieure de la buse, il forme un cône caractéristique au moment de l'atomisation. Généralement, le mouvement de rotation du liquide est réalisé à l'aide des structures de déflection ou par une alimentation tangentiel du liquide (fig. 12).

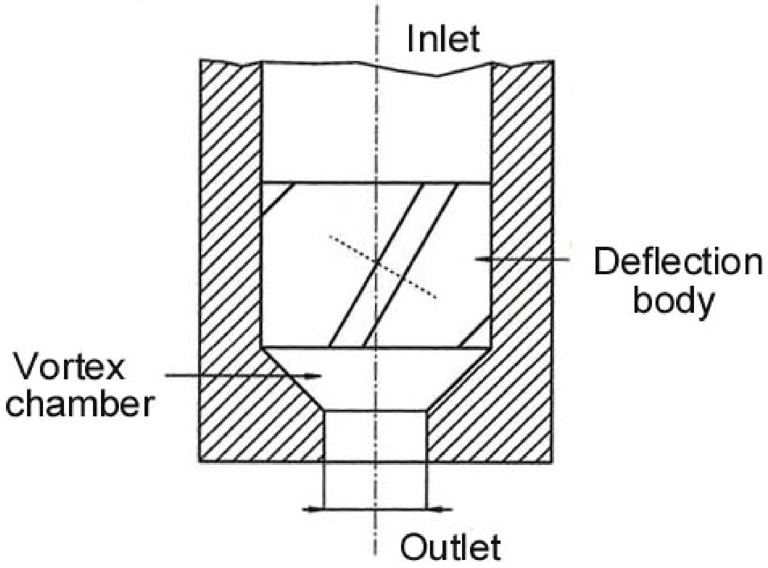

Fig.: 12 – Buse à cône creux avec une structure de déflection [24].

En traversant la buse, un moment de rotation radial agit sur le liquide. Le liquide est refoulé contre la paroi de la buse par effet de rotation, permettant la formation d'un cône de gaz au centre de l'orifice [25]. Une fois que le liquide a passé la buse, il diverge sous l'effet du moment radial, créant un cône creux qui peut avoir des formes différentes (fig. 13).

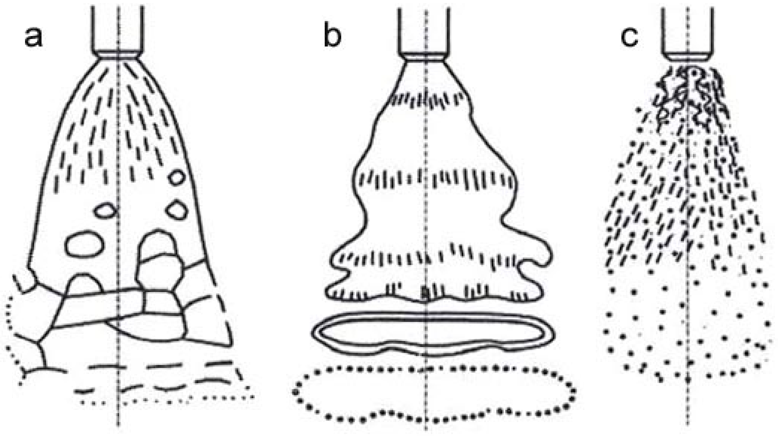

Fig.: 13 – Structures des cônes creux [24]: (a) contraction de boudin, (b) désintégration aérodynamique et (c) désintégration turbulente des lamelles.

Suivant les conditions de fonctionnement, le mécanisme de formation des gouttelettes peut varier entre la contraction de boudin, la désintégration aérodynamique et la désintégration turbulente des lamelles.

La désintégration turbulente des lamelles est caractérisée par un nombre de Weber We important. Le nombre de Weber donne des informations sur l'inertie du liquide par rapport à sa tension superficielle. Un nombre de Weber important implique une forte altération des gouttelettes par rapport à la forme sphérique idéale. Le nombre de Weber non dimensionné est calculé de la façon suivante :

$$We = \frac{\rho \cdot v^2 \cdot l}{\sigma} \qquad \text{Eq.: 13}$$

avec ρ la densité du liquide, v la vitesse, l la longueur caractéristique, dans ce cas le diamètre de la gouttelette, et σ la tension superficielle. La désintégration rapide de la lamelle en gouttelettes très fines, proche de l'orifice de la buse est caractéristique de la désintégration turbulente.

Indépendamment du mécanisme de formation des gouttelettes, le débit volumique maximal $\dot{V}$ qu'on peut obtenir est calculé d'après :

$$\dot{V}_{\max} = \frac{\pi \times d^2}{4} \times \sqrt{\frac{2 \times \Delta p}{\rho}} \qquad \text{Eq.: 14}$$

avec d le diamètre, ρ la densité du liquide et Δp la différence de pression avant et après la buse.

Des forces de frottement, apparaissant entre le liquide et la paroi de la buse, lorsque les nombres de Reynolds sont importants, peuvent réduire le débit volumique maximal. A l'aide de l'index de débit μ, décrivant le ratio entre le débit volumique réel et théorétique, des buses différentes peuvent être comparées entre elles.

$$\mu = \frac{\dot{\mathrm{V}}_{\mathrm{Re}\,al}}{\dot{\mathrm{V}}_{theo}} = \frac{4 \times \dot{\mathrm{V}}_{\mathrm{Re}\,al}}{\pi \times D^2 \times \sqrt{\frac{2 \times \Delta p}{\rho}}} \qquad \text{Eq.: 15}$$

Dans le cadre de cette thèse des buses à cône creux de la société Autriche *Plantfog* ont été utilisées (fig. 14). Des buses pourvues d'orifices de D = 60, 80 et 100 µm étaient disponibles. D’après le producteur la longueur L du conduit est de 300 µm.

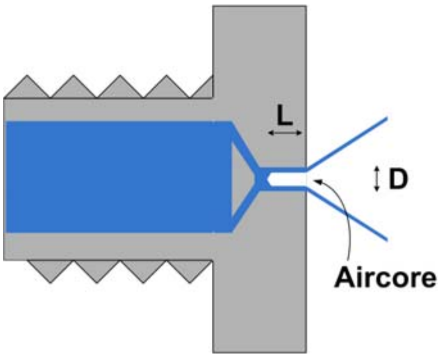

Fig.: 14 – Buse à cône creux.

Dans ce type de buse, le moment de rotation du liquide est obtenu grâce à une arrivée tangentielle par deux petits canaux.

Le ratio L/D joue un rôle important du fait qu’un canal trop long peut produire une chute de pression trop élevée, causant l’évaporation du liquide déjà à l’intérieure de la buse. Ce phénomène peut apparaitre en cas de L/D entre 3 et 12 (fig. 15) [26].

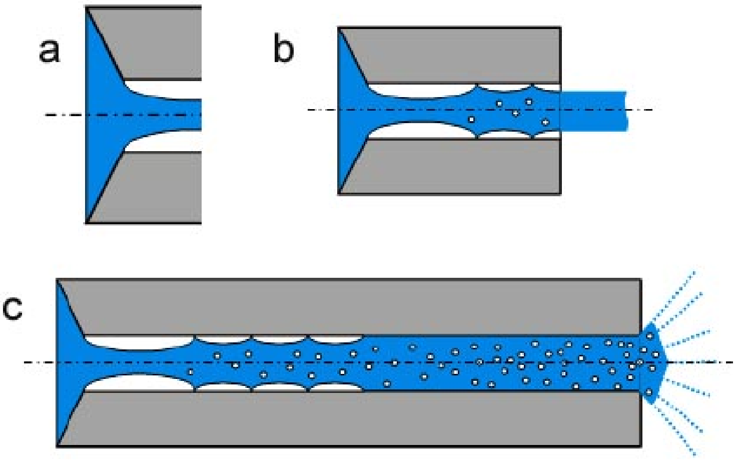

Fig.: 15 – Ecoulement en fonction du ratio L/D:
a) L/D ≈ 3, **b)** L/D jusqu’à 12 et **c)** L/D > 12 [26].

Le cas a) L/D ≈ 3 représente le cas idéal où le liquide part de la buse sans s'évaporer. Dans les cas b) et c) une évaporation partielle ont déjà lieu à l’intérieure de la buse. En vue de la cristallisation-flash une évaporation prématurée est indésirable car le produit cristallisé peut bloquer la buse. D’après Richter [24], le ratio L/D donne aussi des informations sur l’index de débit µ. Pour les buses, ayant un orifice de forme angulaire (à 90°), une relation entre l'index de débit μ et le ratio de L/D existe (tab. 4).

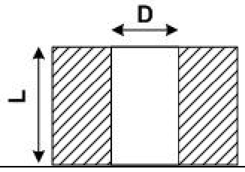	0,6 ≤ μ ≤ 0,65	0,75 ≤ μ ≤ 0,85	μ ≈ 0,62
	$0{,}5 \le L/D \le 1$	$2 \le L/D \le 5$	$L/D = 5$

Tab.: 4 – L'index de débit μ en fonction du ratio L/D [24].

Jusqu'à maintenant aucune méthode numérique permettant de déterminer la taille de gouttelettes d'une buse à cône creux n'existait.

Avec la création des particules, la séparation était un des problèmes majeur. Pour assurer une production en continu, deux cyclones identiques ont été installés en parallèle. Les cyclones étaient du type « cyclone axial », ayant l'entrée et la sortie sur un axe avec un corps de déflection fuselé, dirigeant le flux gazeux dans un mouvement rotatif (fig. 16).

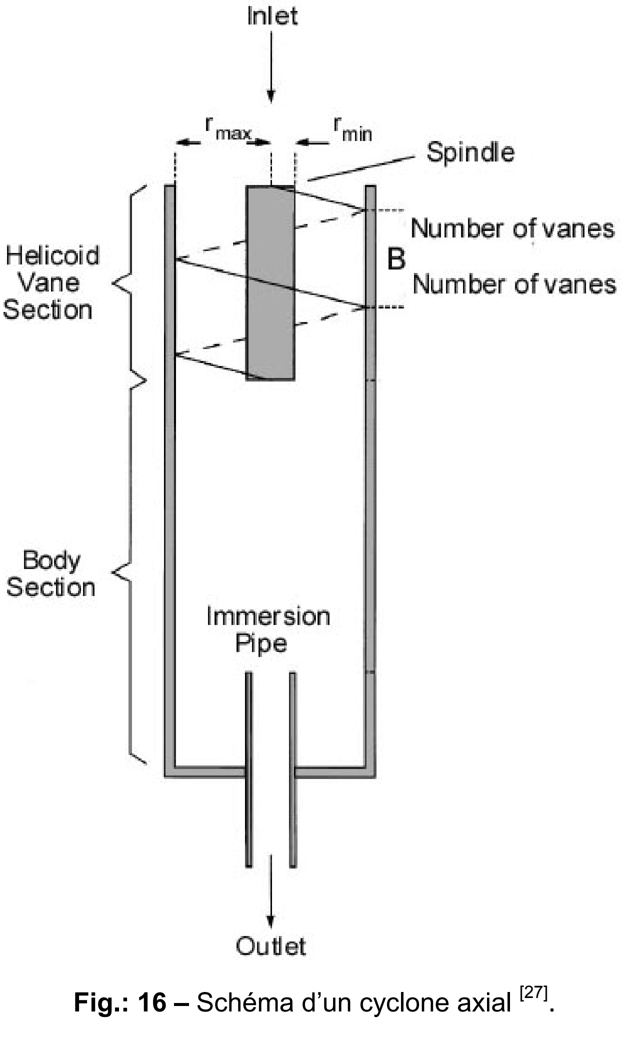

Fig.: 16 – Schéma d'un cyclone axial [27].

Le flux gazeux, chargé en particules ultrafines, entre le cyclone par le haut. En passant par le corps de déflection, les particules solides sont accélérées et dirigées vers la paroi du cyclone. Grâce au mouvement rotatif, une force centrifuge F_c agit sur le débit gazeux et les particules :

$$F_c = m \cdot \omega^2 \cdot r \qquad \text{Eq.: 16}$$

avec m la masse, ω la vitesse angulaire et r le rayon. Comme la force centrifuge dépend proportionnellement de la masse, la force centrifuge agissant sur les particules solides est considérablement plus forte.

En réduisant la pression de fonctionnement du cyclone, le diamètre « cut-off » diminue [28, 29, 30, 31]. Avec la pression décroissante, le nombre de molécules de gaz dans le cyclone diminue et les interactions entre les molécules de gaz et les particules solides décroissent. Sans les interactions inter-particulaires entre les molécules de gaz et les particules solides ultrafines, les particules solides sont déviées sous l'effet de la force centrifuge. Connu sous le nom de "loi de Stoke", la force de résistance F_{drag} agit sur les petites particules bougeant dans un liquide continu à faible nombres de Reynold :

$$F_{drag} = 3 \cdot \pi \cdot \eta_L \cdot d \cdot v_{rel} \qquad \text{Eq.: 17}$$

avec η_L, la viscosité dynamique du fluide et v_{rel}, la vitesse relative entre les particules et l'environnement.

A cause de la faible pression de fonctionnement et de la petite taille des particules, on s'approche à la limite des mécaniques de continuum. Ceci est le cas quand le libre parcours moyen est dans le même ordre de grandeur que la taille de particules. Dans ce cas, la loi de Stokes doit être adaptée par le facteur de correction de Cunningham Cu :

$$F_{drag} = \frac{3 \cdot \pi \cdot \eta_L \cdot d \cdot v_{rel}}{Cu} \qquad \text{Eq.: 18}$$

Sous conditions normales, le mouvement d'une particule est dominé par les collisions entre particules avoisinantes. Dans un environnement à basse pression, les particules ont moins de collisions avec d'autres molécules. Il en résulte un mouvement plus rapide. Cet effet est pris en considération par le facteur de correction de Cunningham :

$$Cu = 1 + \frac{2\lambda}{d}\left(1{,}257 + 0{,}4e^{\frac{-0{,}55d}{\lambda}}\right) \qquad \text{Eq.: 19}$$

avec λ le libre parcours moyen et d le diamètre de particule. Le libre parcours moyen est calculé comme suit :

$$\lambda = \frac{k \cdot T}{\pi \cdot d \cdot p \cdot \sqrt{2}} \qquad \text{Eq.: 20}$$

avec k la constant de Boltzmann.

Le nombre de Knudsen indique si le processus doit être traité comme un flux continu ou un flux moléculaire :

$$Kn = \frac{2\lambda}{d} \qquad \text{Eq.: 21}$$

Pour les nombres de Knudsen < 0,01 les lois des mécaniques de continuum peuvent être appliquées. Ceci est souvent le cas quand la pression de fonctionnement est comprise entre 10^3 à 10^0 mbar.

Un nombre de Knudesn de 0,01 < Kn < 0,5 signale la région transitoire entre les mécaniques de continuum et le régime moléculaire. Cette région est également appelée : régime Kndusen. Le régime Knudsen existe principalement dans une plage allant de 10^0 - 10^{-3} mbar.

Le régime moléculaire est indiqué par un nombre de Knudsen Kn > 0,5, apparaissant surtout à une pression inférieure à 10^{-3} mbar.

Un cyclone axial, développé par Chien *et al.*[32], est capable de séparer les nanoparticules dans le vide (fig. 17).

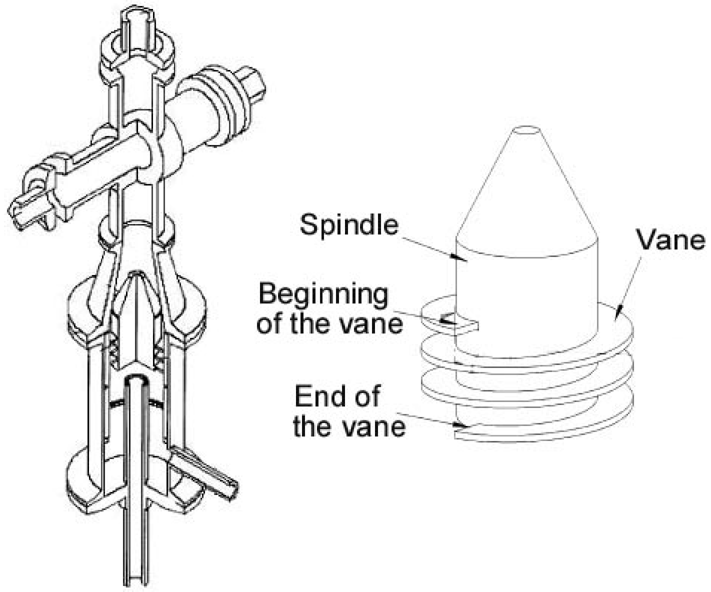

Fig.: 17 – Cyclone axial assemblé. [28, 32].

D’après les auteurs [32], le diamètre aérodynamique de séparation d_{pa50} peut être calculé pour le cyclone axial selon :

$$d_{pa50} = 0{,}106\left(\frac{P_{cyc}}{P_{760}}\right)^2 \frac{\mu\left(r_{\max}{}^2 - r_{\min}{}^2\right)^2 \cdot \left(B - N\omega\right)}{\rho_{po} \cdot n \cdot \xi \cdot Q_0 \cdot r_{\min}{}^2 \cdot N^2 \cdot \lambda_0} \qquad \text{Eq.: 22}$$

avec P_{cyc} la pression moyenne dans le cyclone [Torr], P_{760} est égale à 760 Torr, μ la viscosité dynamique [Ns/m²], $r_{\max}$ le rayon à l’intérieur du cyclone, $r_{\min}$ le rayon du fuseau, B la pente de l’ailette [m], N le nombre des ailettes, ω l’épaisseur de l’ailette [m], ρ_{Po} l’unité de densité [1000 kg/m³], $n\xi$ le nombre de tours effectués par une particule le cyclone d’où la valeur de 1,5 choisie pour ξ, Q_0 le débit volumique standard [m³/s] et λ_0 le libre parcours moyen sous conditions standard [m].

D’après Hsu *et al.*[33], deux mécanismes de séparation existent pour le cyclone illustré ci-dessus. On distingue la séparation par diffusion de la séparation par centrifugation. En supposant qu’un flux laminaire est présent, la séparation des particules au-dessous de 40 nm est contrôlée par la diffusion. Le diamètre « cut-off » dans un système contrôlé par la diffusion peut être calculé de la façon suivante :

$$d_{pa50,diff} = \frac{4 \cdot n \cdot \xi \cdot k \cdot T \cdot Cu}{3 \cdot Q_0 \cdot \mu \cdot \ln 2} \qquad \text{Eq.: 23}$$

Si le flux reste laminaire et la taille de particules supérieure à 40 nm, on calcule le diamètre « cut-off » de la manière suivante :

$$d_{pa50} = \sqrt{\frac{9 \cdot \mu \left(r_{\max}{}^{2} - r_{\min}{}^{2}\right)^{2} (B - N\omega)^{2} \ln 2}{8\pi \cdot n \cdot \xi \cdot Q_{0} \cdot r_{\min}{}^{2} \cdot N^{2} \cdot B \cdot C}} \qquad \text{Eq.: 24}$$

Pour éviter le blocage du cyclone, le dépôt des particules doit être effectué après leur passage par le cyclone. Dans ce but un tube plongeur, illustré dans les figures 16 et 17, a été installé, créant ainsi une zone de repos où les particules peuvent se déposer. Le design du cyclone proposé par Chien et Maynard [27, 32] ne convient pas pour une opération en continu. Pour faciliter l'enlèvement du produit, le tube faisant office de sortie, a été déplacé de 180° (fig. 18). Le corps de déflection peut être déplacé verticalement pour faire varier le nombre d'ailettes.

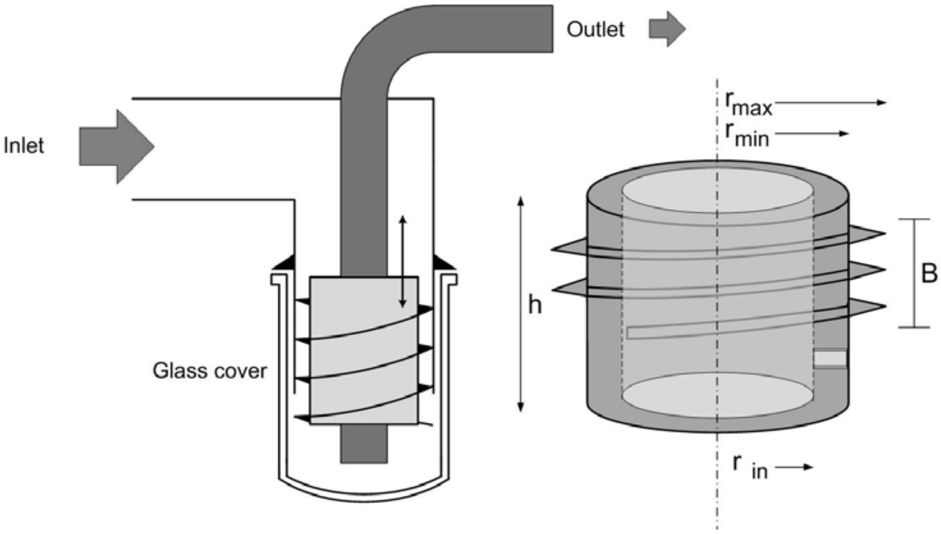

Fig.: 18 – Design du cyclone utilisé dans cette thèse.

Les dimensions du cyclone sont listées dans le tableau suivant (tab. 5) :

Index	**Dimensions**
r_{in}	14 mm
r_{max}	28,5 mm
r_{min}	17 mm
B	21 mm
N	3
h	50 mm
ω	2 mm

Tab.: 5 – Dimensions du cyclone.

Etant donné que la pression dans la chambre d'atomisation ne tombe pas au-dessous de 10^0 mbar, le procédé peut être traité par les lois des mécaniques de continuum.

Pendant l'opération, la période pendant laquelle l'explosif est chauffé doit être la plus petite possible. Cette durée est décrite comme étant le temps d'exposition t_m. L'élévation de température pouvant induire la décomposition de l'explosif dissout, la solution ne devra pas être chauffée trop longtemps. Le temps d'exposition est calculé à l'aide du volume de la buse et du débit volumique :

$$t_m = \frac{V}{\dot{V}} \qquad \text{Eq.: 25}$$

avec V, le volume de la buse chauffée et $\dot{V}$, le débit volumique. Pour assurer un traitement thermique modéré, le volume chauffé doit être le plus petit que possible. En mettant l'élément chauffant directement à l'extérieur de la buse, on arrive à réduire considérablement le volume et le temps d'exposition (fig. 19).

Fig.: 19 – Assemblage de la buse 60 µm avec l'élément chauffant.

En utilisant une buse de 60 µm avec un volume de 1,7 mL, le temps d'exposition peut varier entre 9,7 et 10,7 s. Avec un temps d'exposition si court, la décomposition de l'explosif pendant l'opération est peu probable.

Le nombre de Reynolds non dimensionné sert d'indicateur à un écoulement laminaire ou turbulent. Le type découlement est particulièrement important puisque les processus de transmission du matériau et de la chaleur en dépendent fortement. Le nombre de Reynolds Re se calcule comme suit :

$$\mathrm{Re} = \frac{v \cdot l_c}{\upsilon} \qquad \text{Eq.: 26}$$

Avec la vitesse v, la longueur caractéristique l_c et la viscosité cinétique υ. Pour l'écoulement tubulaire, la longueur caractéristique est égale au diamètre intérieur du tube. Un nombre de Reynolds au-dessous de 2200 ou 2300 indique un écoulement laminaire, un nombre de Reynolds au-dessus de 2300 représente un écoulement turbulent.

Pour déterminer le type d'écoulement dans la chambre d'atomisation et le cyclone, il faut d'abord calculer le volume de gaz qui se forme au moment de l'évaporation-flash. En supposant la présence d'un gaz parfait et que la température du gaz monte immédiatement à 0 °C après l'atomisation, le volume de gaz peut être calcule d'après :

$$p \cdot V_g = n \cdot R \cdot T \qquad \text{Eq.: 27}$$

En replaçant $n = \frac{m}{M}$ et $m = \rho_l \cdot V_l$, l'équation se transforme en :

$$V_g = \frac{V_l \cdot \rho_l \cdot R \cdot T}{M \cdot p} \qquad \text{Eq.: 28}$$

En connaissant la coupe transversale du tube, la vitesse découlement v peut être calculée facilement :

$$v = \frac{\dot{V}}{A} \qquad \text{Eq.: 29}$$

La viscosité exacte du gaz doit être calculée ou extraite de la littérature. Avec le nomogramme de Perry [34], la viscosité du gaz de plusieurs solvants en fonction de la température peut être déterminée facilement (fig. 20).

Les coordonnées X/Y pour l'acétone sont: X = 8,4 ; Y = 13,2. La variation de la viscosité en fonction de la pression ne doit pas être prise en considération, car la viscosité du gaz entre 0,01 et 20 bar reste à peu près constante.

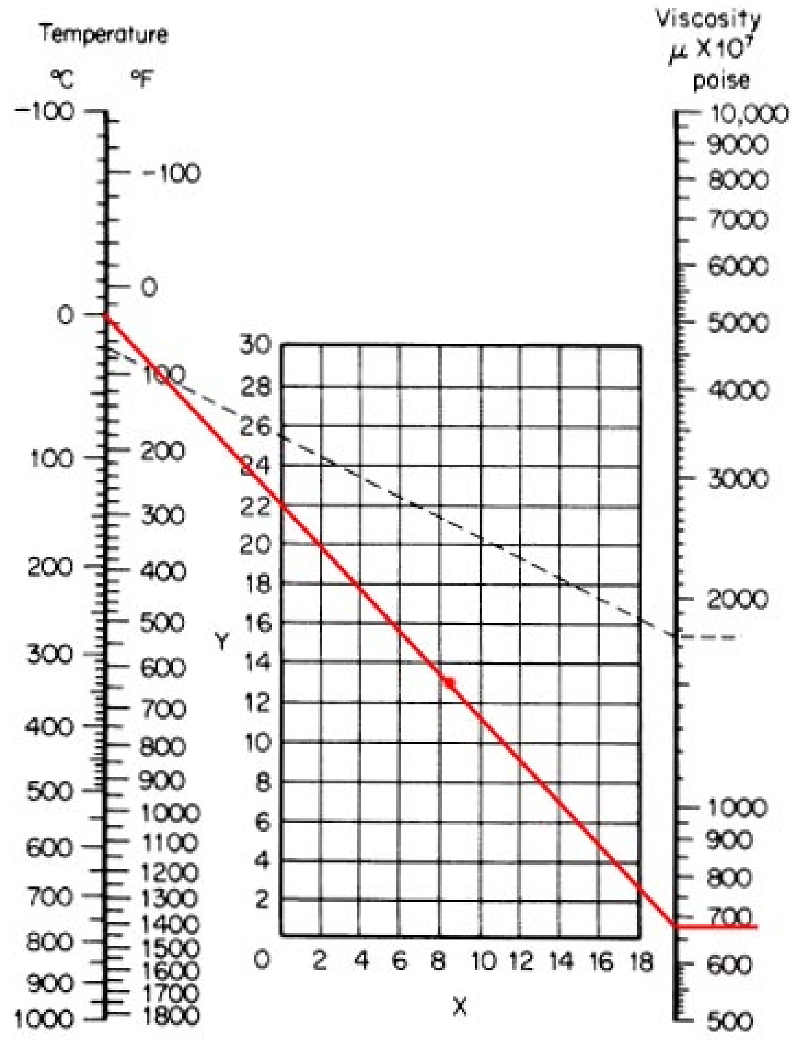

Fig.: 20 – Nomogramme de Perry: Détermination de la viscosité dynamique des gaz en fonction de la température [34]. La ligne rouge correspond à l'acétone.

En ce qui concerne les différents solvants envisagés, l'acétone et le méthyl tertio-butyl éther (MTBE) ont été choisis pour ce travail. Parmi les solvants étudiés, l'acétone dispose des plus mauvaises propriétés thermodynamiques, mais est néanmoins un très bon solvant. Le MTBE a été utilisé en raison de ses propriétés thermodynamiques extraordinaires, permettant de travailler à des températures plus basses. Comme l'acétone et le MTBE sont miscibles en toutes proportions, et que leurs points d'ébullition ne diffèrent que d'un degré Celsius, la préparation de solvants binaires a également été possible.

L'étude paramétrique

Concernant l'optimisation des conditions opératoires, une étude paramétrique a été menée. Ses objectifs étaient la réduction de la taille et de la distribution de taille des particules de RDX nanostructuré, en considération également des aspects économiques et de sécurité. Le RDX a été choisi pour l'étude paramétrique parce qu'il n'existe que sous deux formes allotropiques, dont l'une est tellement peu stable qu'elle se transforme spontanément en la forme la plus stable [35, 36].

Avant d'engager l'étude paramétrique, un essai standard a été réalisé, afin d'identifier les différents paramètres influençant le procédé. L'essai standard a aussi servi comme référence pour les différents essais. Globalement, les cinq paramètres suivants ont été étudiés :

- La température de la buse,
- La pression de la buse,
- Le type de solvant,
- Le diamètre de la buse,
- La concentration de RDX.

Les conditions de l'essai standard sont indiquées dans le tableau ci-dessous (tab. 6).

Buse [µm]	**Température**		**Solvant v/v [Acétone/MTBE]**	**Pression [bar]**	**Conc.-RDX [%-wt]**
	Buse [°C]	**Cyclone [°C]**			
60	160	80	100/0	40	1,0

Tab.: 6 – Paramètres du procédé de l'essai standard.

Dans l'étude paramétrique, nous avons toujours étudié la variation d'un seul paramètre à la fois, les autres paramètres restant constants. Chaque expérience de l'étude paramétrique a été répétée plusieurs fois pour des raisons de reproductibilité. Une quantité d'environ 1 g de produit a été préparée à chaque fois et aussitôt analysée par DSC, par BET et par diffraction des rayons X. De plus, certains échantillons ont également été caractérisés par spectroscopie Raman et par microscopie électronique à balayage (MEB).

Le produit obtenu grâce à l'essai standard, examiné par MEB et illustré dans la figure suivante, montre une taille moyenne de 599 nm avec un écart de 238 nm (fig. 21).

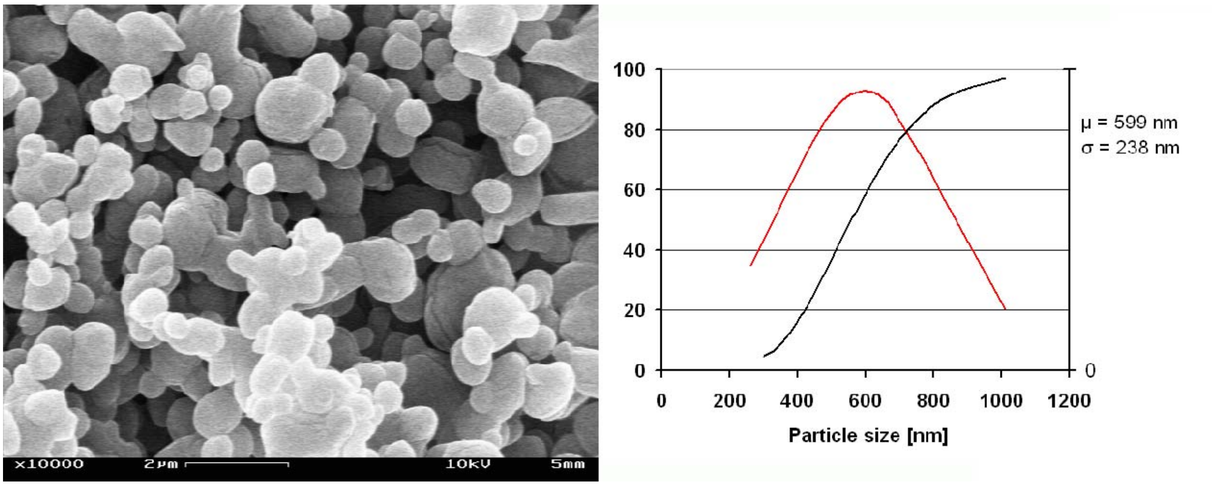

Fig.: 21 – Image MEB du RDX obtenu grâce à l'essai standard et sa distribution de taille.

La température de la buse correspond à la température de surchauffe T_0. Plus le solvant est surchauffé, plus fort est le procédé d'évaporation et plus la quantité de solvant évaporée est importante. L'essai standard a eu lieu à 160 °C. Pour l'étude paramétrique, des expériences supplémentaires ont été réalisées à 150, 170 et 180 °C. Du fait de la forte charge thermique et du faible rendement, seulement un essai a été effectué à 180 °C. L'augmentation de la température de la buse conduit à une réduction de la taille et de la distribution de taille des particules. L'exploitation des images MEB montre que la taille moyenne des particules obtenues lors de l'essai standard est de 599 nm avec un écart de 238 nm. Lorsque la buse est chauffée à 170 °C, la taille moyenne diminue à 499 nm avec un écart de 186 nm (fig. 22). La même tendance a été observée à l'aide des mesures BET, où on note une corrélation entre l'augmentation de la surface spécifique et l'augmentation de la température de la buse.

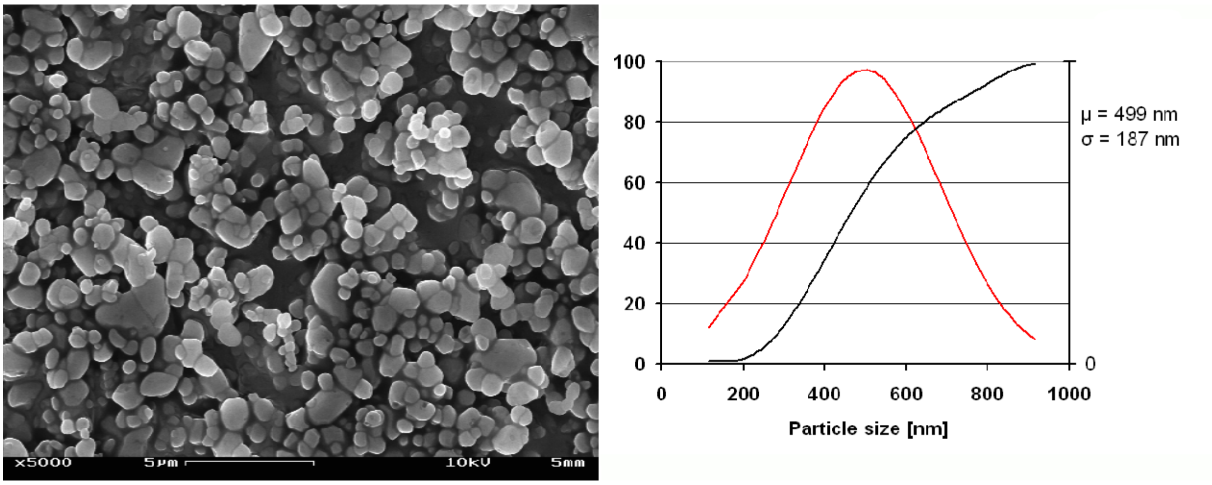

Fig.: 22 – Image MEB de RDX préparé à 170 °C et sa distribution de taille.

D'après Richter [24] l'augmentation de la pression conduit à une réduction de la taille des gouttelettes. La buse qui a été utilisée est une buse à cône creux de la société Plantfog [37]. Elle a un orifice de 60 µm de diamètre. Bien que le fabricant recommande une pression d'utilisation de 100 bar, l'essai standard a été conduit à une pression de 40 bar. Dans le cadre de l'étude paramétrique, d'autres expériences ont été menées à des pressions de 50, 60 et 70 bar. Des expériences à des pressions inférieures à 40 bar n'ont pas été menées du fait que la formation de la structure de cône creux n'était pas complète. L'exploitation des mesures BET a montré que l'augmentation de la pression conduit à des particules de plus petites taille. L'analyse des clichés MEB du RDX préparé à 70 bar, met en évidence une faible réduction de la taille moyenne mais un élargissement de la distribution de taille des particules formées (fig. 23).

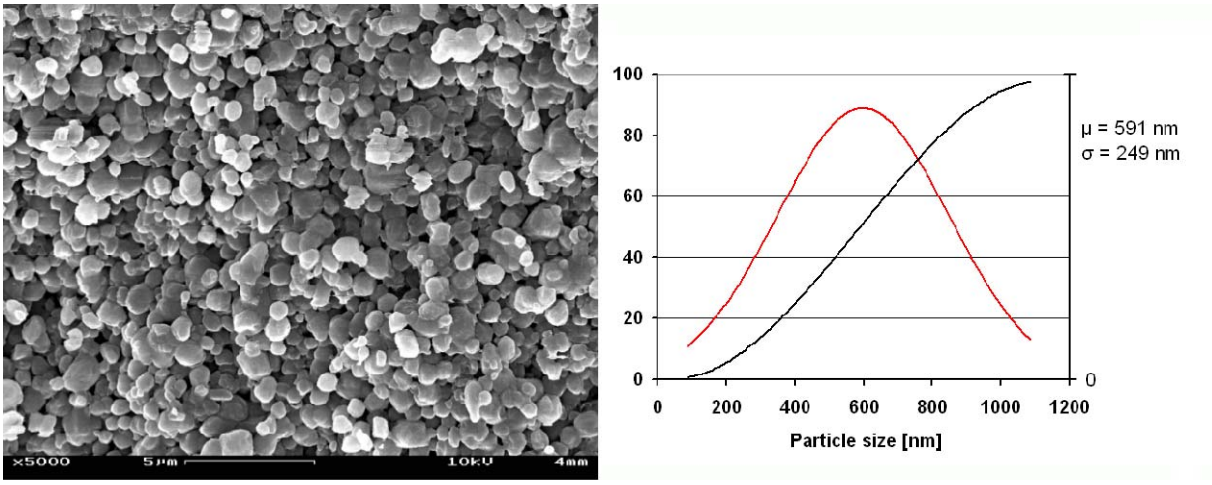

Fig.: 23 – Image MEB de RDX préparé à une pression de 70 bar et sa distribution en taille.

Du fait de l'utilisation de RDX, le choix des solvants appropriés était relativement limité. Parmi le groupe des solvants à point d'ébullition bas [38], l'acétone possède la solubilité la plus élevée pour le RDX. Du fait que le RDX est pratiquement insoluble dans le MTBE, des mélanges binaires d'acétone/MTBE ont été utilisés pour l'étude paramétrique. L'essai standard a été conduit avec de l'acétone pur. Les autres essais de l'étude paramétrique ont été réalisés avec des mélanges d'acétone/MTBE v/v de 90/10, de 80/20, de 70/30 et de 60/40. Grâce aux propriétés thermiques favorables du MTBE, le ratio d'évaporation X_{vap} augmente avec la teneur croissante en MTBE. En même temps, la solubilité en RDX diminue. Les résultats de cette étude ont montré que, comme pour l'augmentation de la température, l'ajout de MTBE accélère le processus d'évaporation. De plus, la solubilité plus faible permet d'atteindre une sursaturation plus élevée, conduisant à la formation de germes cristallins bien plus nombreux. Le RDX préparé à partir de la solution acétone/MTBE 60/40 possède ainsi des tailles de particules plus petites et une distribution plus étroite. La taille moyenne est de 434 nm avec un écart de 132 nm (fig. 24).

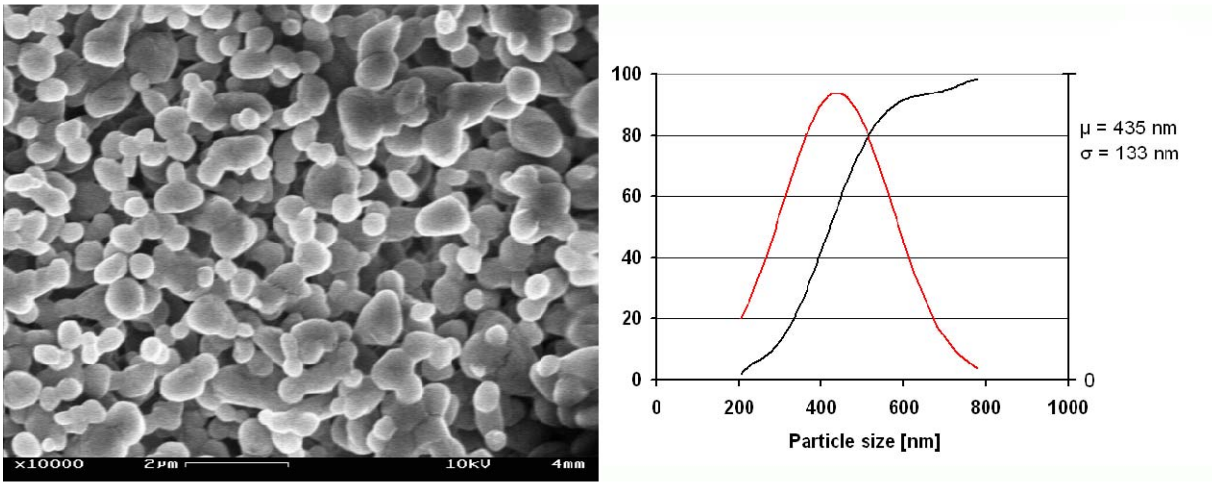

Fig.: 24 – Image MEB de RDX préparé à partir d'un solvant binaire d'acétone/MTBE 60/40 et sa distribution en taille.

D'après Richter [24], l'utilisation d'une petite buse doit favoriser la formation d'un spray plus fin. Les diamètres des buses disponibles sont de 60, de 80 et de 100 µm. Les expériences ont été conduites exceptionnellement avec une solution à 0,7% de RDX pour éviter le colmatage des cyclones. La comparaison des résultats obtenus avec les buses de 60 et de 80 µm de diamètre a montré une augmentation de la taille des particules accompagnée d'un élargissement de la distribution de taille avec l'augmentation de la taille de l'orifice de la buse. Avec la buse de 60 µm, on a ainsi obtenu une taille moyenne de 650 nm avec un écart de 252 nm. Dans les mêmes conditions expérimentales, mais avec la buse de 80 µm, la taille moyenne est montée à 887 nm avec un écart de 322 nm (fig. 25).

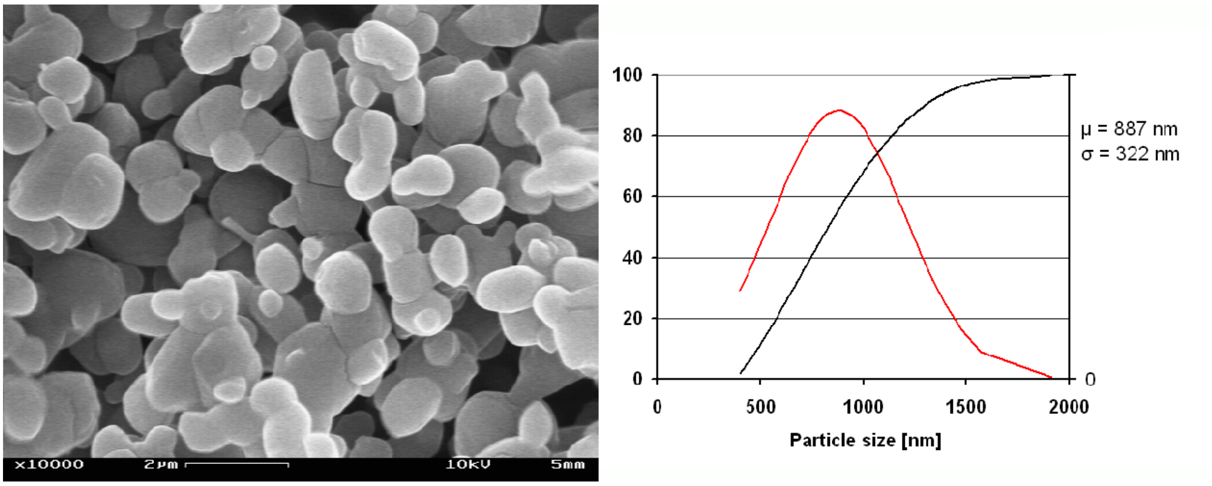

Fig.: 25 – Image MEB de RDX préparé à l'aide d'une buse à cône creux de 80 µm et une solution contenant 0,7 % de RDX et sa distribution en taille.

Dans les expériences menées avec la buse de 100 µm, le débit volumique a augmenté à un tel point, qu'on pouvait observer la formation des gouttelettes dans la chambre d'atomisation. La condensation de l'acétone provoque le redissolution du RDX, ce qui abaisse fortement le rendement. Le rendement obtenu avec la buse de

100 µm est ainsi plus de trois fois inférieur à celui qui est atteint avec la buse de 60 µm.

La concentration d'explosif dans le solvant surchauffé joue un rôle important sur la taille des particules et sur la capacité de production. L'essai standard a ici été réalisé avec une solution de 1 % de RDX. En ce qui concerne l'étude paramétrique, les autres concentrations en RDX testées ont été : 0,5; 0,7; 1,5 et 2,0 %. Les mesures de BET ainsi que les images MEB ont montré une réduction de la taille moyenne et de la distribution de taille des particules, avec l'augmentation de la concentration en RDX. La taille moyenne du RDX préparé à partir de la solution à 0,5 % de RDX est de 673 nm. Avec une concentration en RDX de 2 %, la taille moyenne se situe à 408 nm avec un écart de seulement 174 nm (fig. 26).

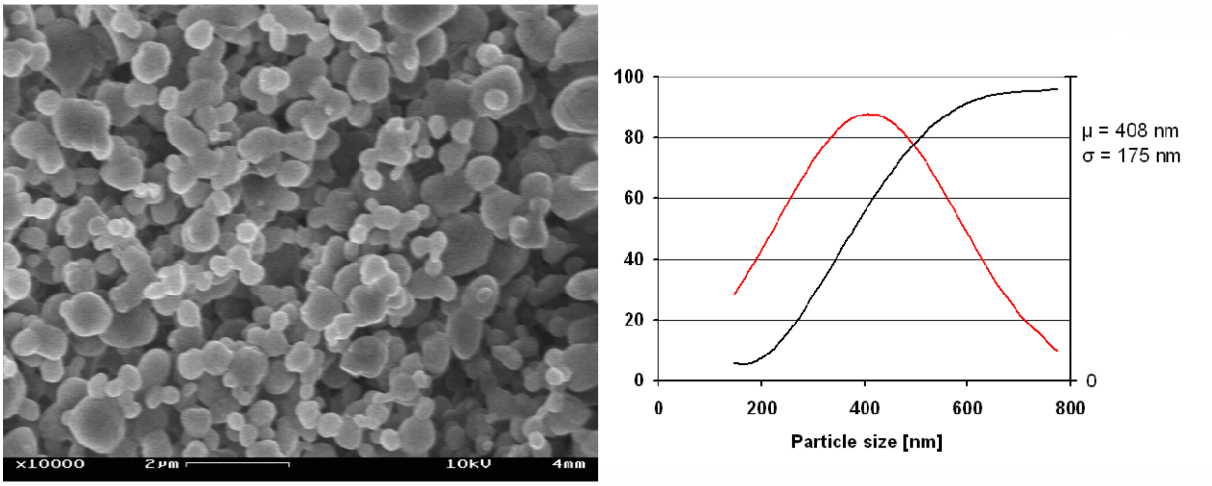

Fig.: 26 – Image MEB de RDX préparé à partir d'une solution contenant 2,0 % de RDX et sa distribution en taille.

Ce résultat provient du fait qu'une sursaturation plus importante est produite plus rapidement. Cela implique une augmentation du nombre de germes cristallins, ce qui a pour conséquence la diminution de la taille des particules. Un autre effet, qui semble jouer un rôle important, est l'initiation de l'évaporation par les germes cristallins. Du fait que le liquide surchauffé, au moment de la diminution de pression, se trouve dans un état métastable, les cristaux dans le liquide peuvent servir comme germes, provoquant l'évaporation du liquide plus rapidement et plus tôt.

On notera ici un résultat remarquable : l'augmentation de la capacité de production induite par l'augmentation de la concentration en RDX du solvant. La capacité de production la plus élevée (4,2 g/h) a ainsi été réalisée avec une solution contenant 2 % en masse de RDX.

A l'issue de l'étude paramétrique, une expérience a été réalisée avec des paramètres optimisés (tab. 7).

Buse [µm]	Température		Solvant v/v [Acétone/MTBE]	Pression [bar]	Conc.-RDX [%-wt]
	Buse [°C]	Cyclone [°C]			
60	170	100	75/25	50	1,5

Tab.: 7 – Paramètres optimisés.

Par rapport à l'essai standard, la température de la buse, la pression de la buse et la concentration en RDX, ont donc été augmentées. Un mélange d'acétone/MTBE 75/25 a été utilisé comme solvant.

Cette expérience a conduit à une diminution de la taille moyenne des particules, cependant moins forte que celle qui était attendue. D'après les images MEB, la taille moyenne des particules est de 482 nm avec un écart de 195 nm (fig. 27).

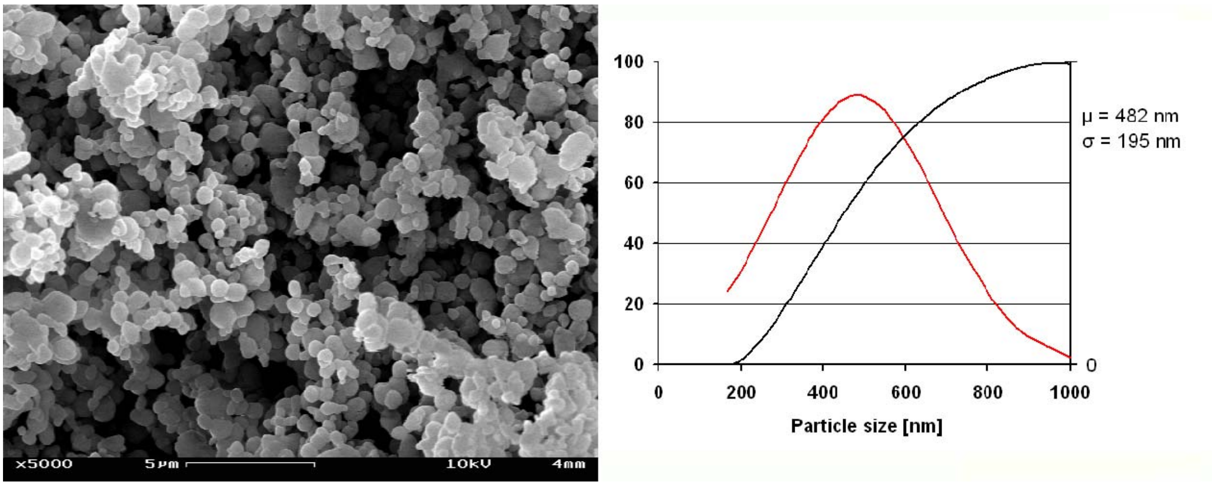

Fig.: 27 – Image MEB de RDX préparé sous conditions optimisés et sa distribution en taille n.

Tout au long de l'étude paramétrique, il a été constaté que la taille des cristallites variait toujours entre 600 et 700 Å. Ceci laisse supposer, que les mécanismes de la nucléation et de croissance du cristal sont reproductibles. Ce résultat montre aussi, étant donné que la taille des particules varie, qu'un autre mécanisme régissant l'agrégation des particules primaires entre-elles, doit entrer en ligne de compte.

Autres matériaux nanocristallisés

La polyvalence du procédé de nano cristallisation flash a également été illustrée par la cristallisation de deux autres matériaux énergétiques, une hexolite et le CL-20.

Des compositions nanostructurées de RDX et de TNT (hexolite) avec un rapport massique de 60/40 ont ainsi été élaborées par la cristallisation flash en une seule étape. Le ratio des deux explosifs dans le produit final correspond exactement au ratio dans la solution initiale. La taille des particules dans le composite obtenu est comprise entre 100 et 300 nm. A partir des observations MEB (fig. 28 et 29) on suppose une distribution submicronique des deux explosifs.

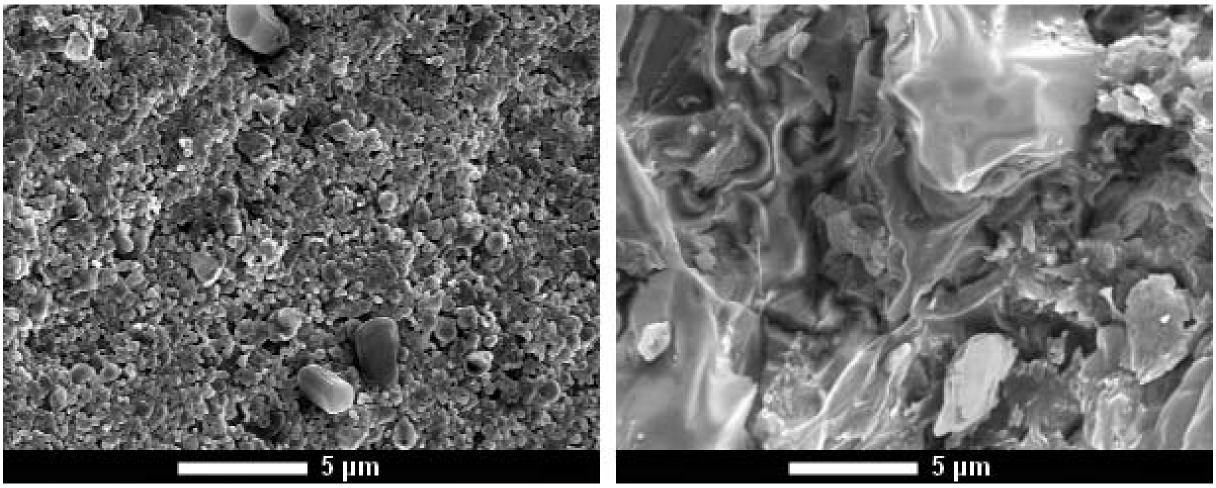

Fig.: 28 – Image MEB d'une hexolite RDX/TNT 60/40 ; grandissement 5.000x, hexolite nanocristallisée (gauche) et hexolite microstructurée (droite).

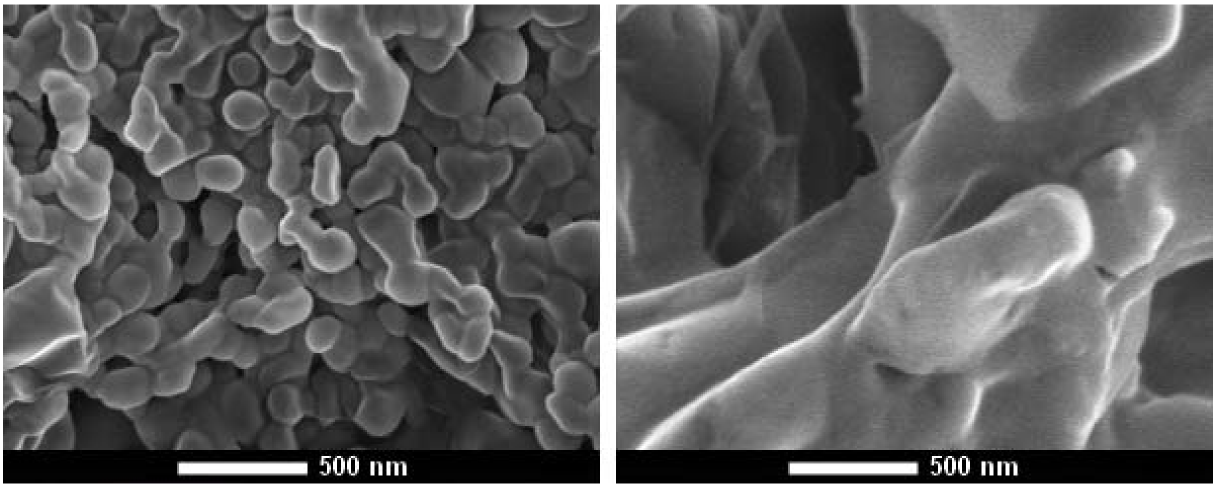

Fig.: 29 – Image MEB d'une hexolite RDX/TNT 60/40 ; grandissement 50.000x, hexolite nanocristallisée (gauche) et hexolite microstructurée (droite).

La morphologie de cette hexolite, structure « core-shell » ou particules isolées, reste encore à déterminer. A l'aide de la spectroscopie de Raman, la distribution de RDX et de TNT ont été déterminée dans un comprimé sur une surface de 50 x 50 µm (fig. 30).

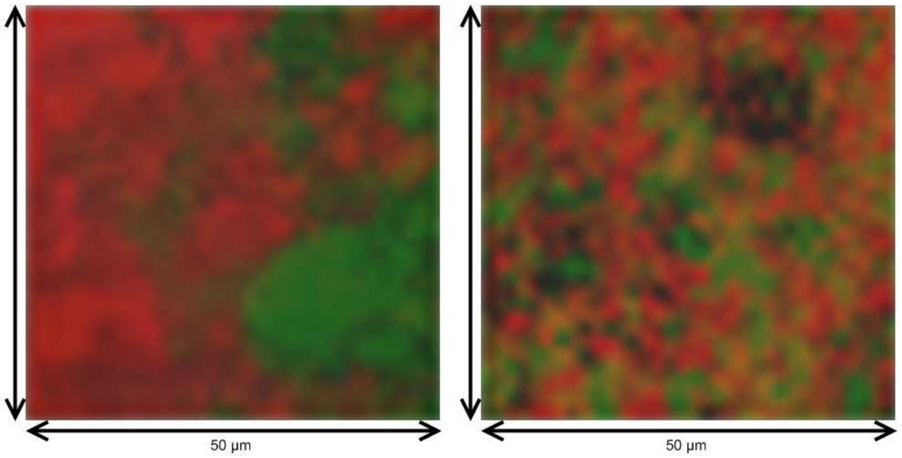

Fig.: 30 – Distribution de RDX et TNT dans une hexolite microstructurée (gauche) et nanocristallisée (droite).

Les pics caractéristiques choisis pour l'identification de RDX et de TNT étaient :

Vert: TNT – Pic à 1620 cm^{-1}, mesuré entre 1610 - 1630 cm^{-1}
Rouge : RDX – Pic à 1272 cm^{-1}, mesuré entre 1260 - 1280 cm^{-1}.

La formation des cristaux co-cristallisés de RDX et de TNT peut être exclue étant données des mesures de diffraction de rayons-X. Le diagramme de diffraction de l'hexolite nanocristallisée n'est qu'une superposition des signaux de RDX et de TNT (fig. 31).

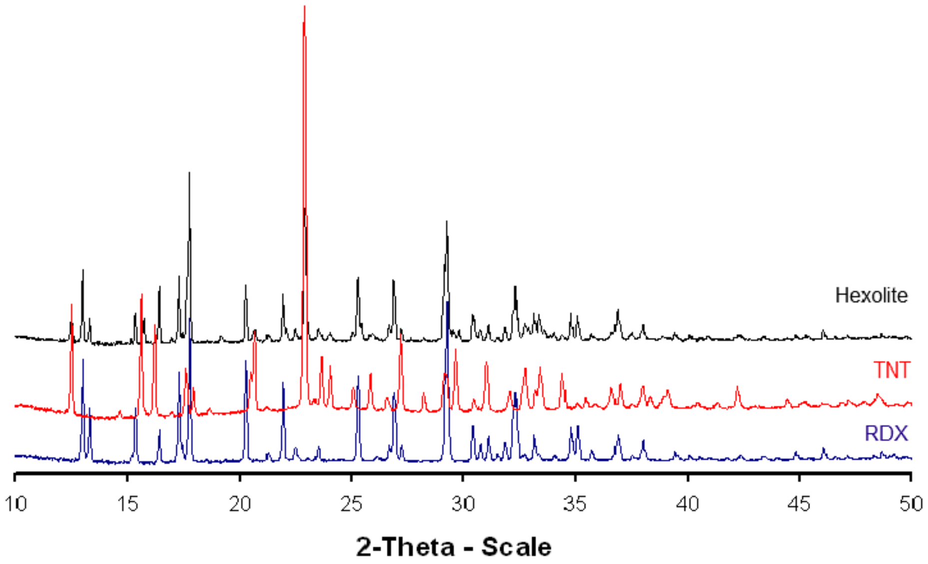

Fig.: 31 – Diagrammes de diffraction d'hexolite nanocristallisée (noire), de TNT (rouge) et de RDX (bleue).

Une distribution aussi homogène de RDX et de TNT nanostructurés est particulièrement importante pour la synthèse de nanodiamants par détonation. **La préparation de plus de 150 g de ce matériau énergétique a permis la fabrication des premières charges nanostructurées au monde.**

La cristallisation sélective des allotropes de CL-20 est un autre domaine d'application de la cristallisation flash. A la température ambiante, le CL-20 peut exister sous forme de quatre structures différentes : α, β, ε et γ (fig. 32).

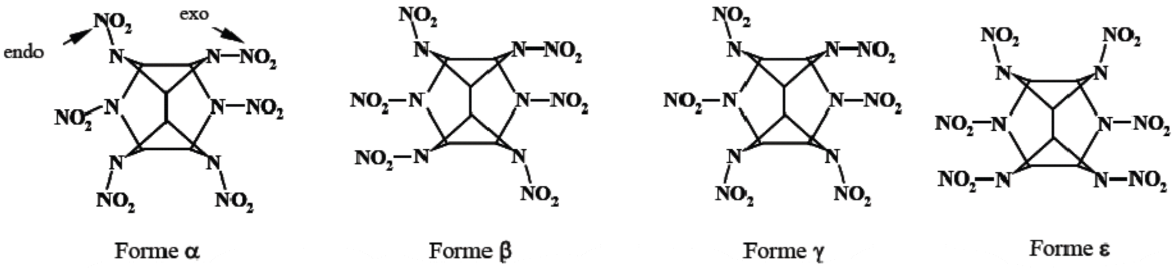

Fig.: 32 – Phases allotropiques de CL-20 stable à la température ambiante [39].

La structure de ε-CL-20 est favorisée grâce à ses propriétés thermodynamiques et énergétiques (tab. 8).

Forme	ρ **[g cm^{-3}]**	D **[m s^{-1}]**	T_m **[°C]**
ε monoclinique	2,044	9660	167
β orthorhombique	1,985	9380	163
α orthorhombique	1,971	-	170
γ monoclinique	1,923	-	260

Tab.: 8 – Propriétés des phases allotropiques de CL-20 [39].

La stabilité thermodynamique des structures individuelles décline dans l'ordre ε > γ > α-hydrat > β [40], correspondant en même temps à une augmentation de la sensibilité à l'initiation. La formation de la structure-β est favorisée par les procédés de cristallisation rapides. Ainsi, l'optimisation des paramètres du procédé a permis la préparation sélective de β-CL-20 et de α-CL-20. La taille moyenne du β-CL-20 était de 293 nm avec un écart de 80 nm (fig. 32).

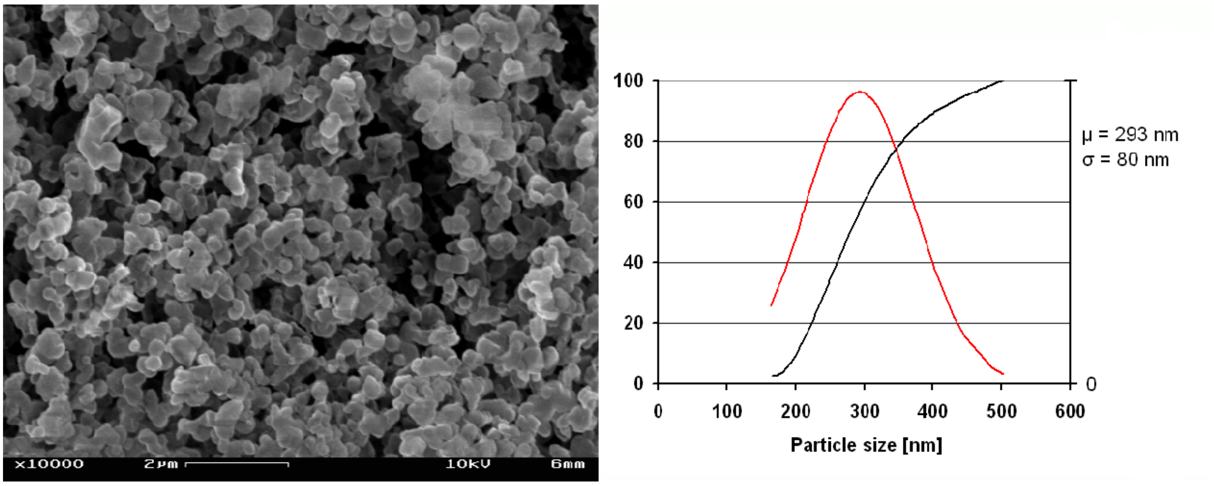

Fig.: 32 – Image MEB de β-CL-20 et sa distribution en taille.

L'identification de la phase de CL-20 était effectuée à l'aide de son spectre de Raman. La zone entre 700 à 950 cm^{-1} montre des signaux caractéristique pour chaque phase (fig. 33).

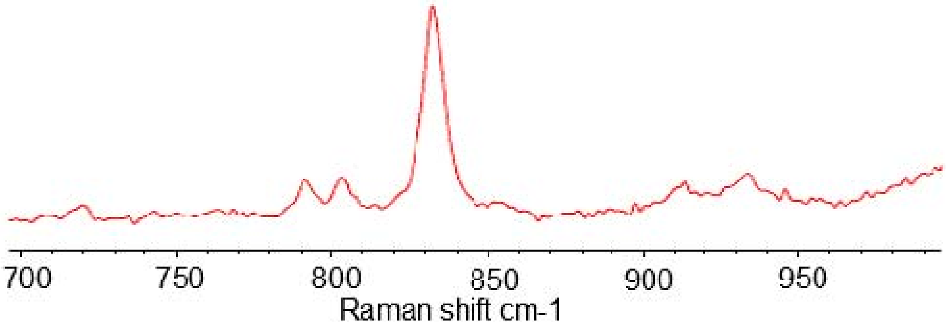

Fig.: 33 – Spectre de Raman de β-CL-20 entre 700 à 950 cm^{-1}.

Du fait que l'allotrope-α est stabilisé en présence d'eau, quelques pourcents d'eau ont été ajoutés au solvant. En raison de l'évaporation incomplète, la concentration d'eau augmente dans l'atmosphère de la chambre d'atomisation pendant une courte période. Le α-CL-20 préparé de cette manière présente une taille moyenne de 401 nm avec un écart de 106 nm (fig. 34).

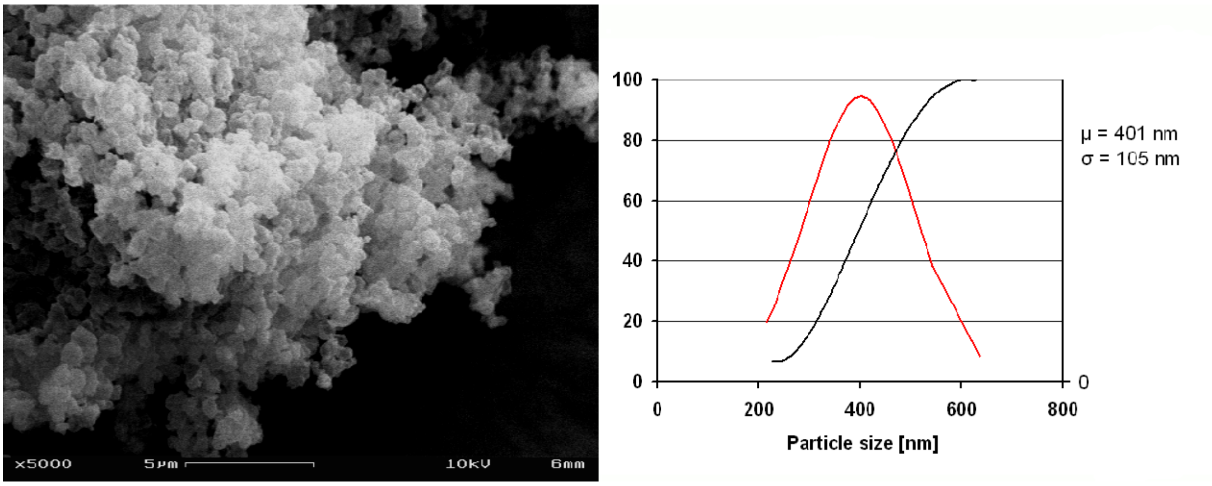

Fig. : 34 – Image MEB de α-CL-20 et sa distribution en taille.

Le signal caractéristique de α-CL-20 est montré dans la figure suivante (fig. 35).

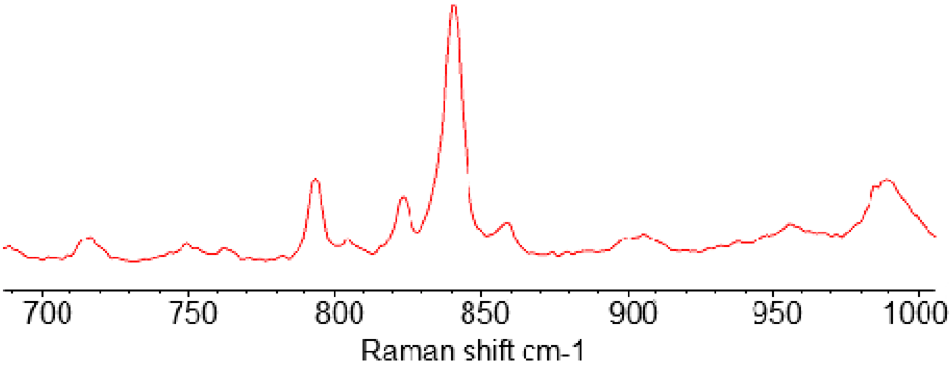

Fig.: 35 – Spectre de Raman de α-CL-20 entre 700 à 1000 cm^{-1}.

La cristallisation-flash, pour laquelle nous avons déposé une demande de brevet, mise au point et décrite dans ce travail, représente un procédé très prometteur pour la production industrielle de particules nano, submicroniques et ainsi que pour des compositions énergétiques, inertes ou hybrides inertes/énergétiques.

En nanocristallisant différents explosifs, nous avons démontré que le procédé développé intéresse de nombreux autres domaines d'applications. L'utilisation des solvants classiques permet l'application de la cristallisation-flash à nombreuses substances différentes.

Les possibilités d'application qu'offrent ce procédé sont quasiment infinies. Par le choix d'un solvant ou d'un mélange de solvants adéquat, la cristallisation-flash peut être utilisée pour un grand nombre de substances organiques et inorganiques, pour lesquelles les procédés plasma ou autres procédés à haute température ne conviennent pas.

Un autre domaine important auquel le procédé développé donne accès, est la production des nano-composites. Ces compositions, contenant 2, 3 ou plusieurs composés, peuvent être élaborées par ce procédé en une seule étape. De plus, ce procédé pourra aussi être mis en œuvre pour l'enrobage d'épaisseur nanométrique ou micrométrique de nanoparticules et/ou de microparticules dispersées.

En utilisant deux ou plusieurs buses isolées, la réalisation de produits composés de deux ou de plusieurs distributions de taille différentes, est également réalisable. Avec l'automatisation de l'extraction des particules, le procédé d'élaboration pourra être connecté directement aux autres procédés de transformation, permettant ainsi de réduire l'exposition de l'opérateur aux nanoparticules.

Un complément intéressant pour la cristallisation-flash serait l'installation d'un granulomètre de mesure de mobilité des particules permettant la mesure in-situ et en temps réel de la distribution de taille des particules à partir de la phase gazeuse, pouvant ainsi assurer un pilotage et une régulation en temps réel des différents paramètres du procédé dans le but de produire en continu un produit de qualité donnée.

Références

[1] Nobel, A.; Patent No. 78,317, May 26, **1868.**

[2] Field, J.; *Acc. Chem. Res*., **1992**, 25, pp. 489-496.

[3] Czerski, H.; Thesis, Ignition of HMX and RDX. Cambridge, England, **2006**.

[4] Zygmunt, B.; *Prop. Expl. Pyr.*, 7, **1982**, pp. 107-109.

[5] Tarver, C.; Chidester, S.; Nichols, A.; *J. Phys. Chem.,* 100, **1996**, pp. 5794-5799.

[6] Stepanov, V.; Anglade, V.; Bezmelnitsyn, A.; Krasnoperov, L.; *AIChE Annual Meeting*, **2006**, San Francisco.

[7] Redner, P.; Kapoor, D.; Patel, R.; Chung, M.; Martin, D.; Production and characterization of nano-RDX, Report, U.S. Army, RDECOM-ARDEC Picatinny, NJ 07806-5000, **2006**.

[8] Tillotson, T.; Hrubesh, L.; Fox, G.; Simpson, R.; Lee, R.; Swansiger, R.; Simpson, L.; Sol-Gel processing of energetic materials, 5th international symposium on aerogels, France, **1997**.

[9] Simpson, R.; Lee, R.; Tillotson, T.; Hrubesh, L.; Swansiger,R.; Fox, G.; US 2005/0092405.

[10] Frolov, Y.; Pivkina, A.; Ul'yanova, P.; Zav'yalov, S.; *Comb. Expl. and Shock Waves*, 38 (6), **2002**, pp. 709-713.

[11] Pivkina, A.; Ul'yanova, P.; Frolov, Y.; Zav'yalov, S.; Schoonman, J.; *Prop. Expl. Pyr*., 29 (1), **2004**, pp. 39-48.

[12] Radacsi, N.; Stankiewicz, A.; Creyghton, Y.; van der Heijden, A.; ter Horst, J.; *Chem. Eng. Technol*. **2011,** 34 (4), pp. 624-630.

[13] Spitzer, D.; Baras, C.; DE 10 2007 003 396 A1, 23.01.2007.

[14] Spitzer, D.; Baras, C.; Schäfer, M.; Ciszek, F.; Siegert, B.; *Prop. Expl. Pyr*., 36, **2011**, pp. 65-74.

[15] Krasnoperov, L.; Elkina, I.; Zhang, X.; *Prop. Expl. Pyr.*, 30 (3), **2005**, pp. 178-183.

[16] Stepanov, V.; Dissertation: PRODUCTION OF NANOCRYSTALLINE RDX BY RESS: PROCESS DEVELOPMENT AND MATERIAL CHARACTERIZATION, **2008,** New Jersey Institute of Technology, USA.

[17] Owen, I.; Jalil, J.; *Int. J. Multiphase Flow*, 17 (5), **1991**, pp. 653-660.

[18] Lienhard, J.; Day, J.; *ASME Jl. Bas. Engng,* **1970**, pp. 515-522.

[19] Paul, E.; Tung, H.; Midler, M.; *Powder Technol.,* 150, **2005**, pp. 133-143.

[20] Majer, V.; Svoboda, V., Enthalpies of Vaporization of Organic Compounds: A Critical Review and Data Compilation, Blackwell Scientific Publications, Oxford, **1985**, 300.

[21] Peng, D.; Robinson, D.; *Ind. Eng. Chem. Fundam.*, 15 (1), **1976**, pp. 59-64.

[22] Fedoroff, B.; Sheffield, O.; *Encyclopedia of explosives and related items*, **1966**, Vol. 3, Picatinny Arsenal, New Jersey, USA.

[23] Zinn, J.; Mader, C.; *J. App. Phys.,* 31(2), **1960**, pp. 323-328.

[24] Richter, T.; Zerstäuben von Flüssigkeiten, 2. Auflage, **2008**, Expert Verlag.

[25] Piesche, M.; Nonnenmacher, S.; *Chem. Ing. Tech.*, 71 (7), **1999**, pp. 688-692.

[26] Günther, A.; Rossmeissl, M.; Wirth, K.; *ILASS-Europe 2010, 23rd Annual Conference on Liquid Atomization and Spray Systems*, Brno, Czech Republic, September **2010.**

[27] Maynard, A.; *J. Aerosol Sci.,* 31 (2), **2000**, pp. 151-167.

[28] Tsai, C.; Chen, S.; Przekop, R.; Moskal, A.; *Environ. Sci. Technol.,* 41, **2007**, pp. 1689-1695.

[29] Chen, S.; Tsai, C.; *J. Nanopart. Res*., 9, **2007**, pp. 71-83.

[30] Paglianti, A.; Brunazzi, E.; Talamelli, A.; *AIChE J.*, 49 (1), **2003**, pp. 41-51.

[31] Ober, F.; Mayer, M.; Büttner, H.; *Chem. Ing. Tech.*, 75 (5), **2003**, pp. 568-572.

[32] Chien, H.; Hsu, Y.; Tsai, C.; US 6,969,420 B2, Nov. 29, **2005**.

[33] Hsu, Y.; Chein, H.; Chen, T.; Tsai, C.; *Environ. Sci. Technol.*, 39, **2005**, pp. 1299-1308.

[34] Perry, R.; Perry's Chemical engineers' handbook, 7th edition, **1997**, McGraw-Hill.

[35] McCrone, Walter; *Anal. Chem.*, 22 (7), **1950**, pp. 954-955.

[36] Karpowicz, R.; Sergio, S.; Brill, T.; *Ind. Eng. Chem. Prod. Res. Dev.,* 22, **1983**, pp. 363-365.

[37] http://www.plantfog.at/HD_D/Preisliste_HD-Duesen_D.htm , Hollow cone nozzles from the Plantfog company, 20.06.2012.

[38] Fedoroff, B.; Sheffield, O.; *Encyclopedia of explosives and related items*, **1966**, Vol. 3, Picatinny Arsenal, New Jersey, USA.

[39] Dumas, S,; These, Dosage du polymorphisme : spectrométrie IRTF et chimiométrie, Application aux formes polymorphes du CL-20.Université Claude-Bernard, Lyon, **2003.**

[40] Foltz, M.; Coon, C.; Garcia, F.; Nichols III, A.; *Prop. Expl. Pyr.*, 19, **1994**, pp. 19-25.

Contents

Introduction

The desensitization of explosives towards accidental initiation already plays an important role since the development of the nitroglycerin. Nitroglycerin, developed in 1847 by Ascanio Sobrero, is a liquid, highly sensitive explosive that might already explode by a slight shock. First in 1867, Alfred Nobel [1] succeeded, by absorbing the explosive in kieselguhr, in desensitizing nitroglycerin so far that it could be handled safely. However, today one expects more from a desensitized explosive.

As the military is the largest consumer of energetic materials, their demands on the explosive containing systems, are accordingly high. One expects that todays explosive devices are resistant towards: great heat, as it might occur in the case of a fire, or the influence of a strong mechanical load e.g. direct fire, impact of shrapnel or an adjacent detonation.

The most common way to desensitize an explosive is mixing it with a wax or a less sensitive energetic material. The addition of wax to a powdery explosive has the advantage of improving handling capabilities and reducing the sensitivity. The loss of performance is the biggest drawback of this method. With the use of energetic binders, the loss of performance can be reduced, however the sensitivity increases again.

The more profound the knowledge about explosives and their initiation mechanism became, the better ways of their desensitization were developed. From the hot-spot theory one learns, that the first step in the decomposition mechanism happens in a few micron-sized area, called hot-spot, within the explosive. Consequently, one focused on preventing the formation of potential hot-spots, by reducing the particle size of the explosive down into the nanometre range. With decreasing hot-spot size, the critical temperature to ignite the explosive considerably rises, making the ignition of the explosive more difficult [2].

In the past fifteen years, different processes for the preparation of nano-explosives were developed since then. Despite the intensive research on this topic, a large scale production of nano-explosives was not possible so far. However, the current knowledge confirms the desensitization, occurring with decreasing particle size.

Within the framework of this doctoral thesis, a continuous operating flash-crystallization process was developed, with which a large number of ultra-fine explosives can be prepared. A continuous operating pilot-plant, developed at the same time, is already capable of preparing various explosives and explosive-compositions in large amounts. In this work, the process will be discussed in detail and a parametric study with an explosive will be performed. Furthermore, the scope of application of this process will be demonstrated on two further energetic materials.
In total a large number of energetic and inert materials and compositions were already successfully nanocrystallized by this process, however for confidential reasons and reason of space they all can not be mentioned in this work.

References

[1] Nobel, A.; Patent No. 78,317, May 26, **1868.**
[2] Tarver, C.; Chidester, S.; Nichols, A.; *J. Phys. Chem.,* 100, **1996**, pp. 5794-5799.

1 Explosives

Explosive is a common designation for substances or mixtures of substances, able of releasing large amounts of energy in form of pressure and heat in a very short time. This vaguely formulated definition does not take all explosive relevant properties into consideration, that is why a more detailed description of this term is desirable.

Due to the sheer endless number of explosive materials and compositions, a better understanding of this subject is achieved by explaining the three dominating decomposition regimes *combustion, deflagration* and *detonation* at first*.*

The **combustion** describes the slowest decomposition mechanism an explosive or propellant can undergo. Characteristic for the combustion regime is the entire oxidation of all intermediate products, forming the most stable combustion products. The combustion requires large amounts of oxygen. Because the oxygen balance for many explosives is negative, meaning that not enough oxygen is bound in the explosive molecule itself, the missing oxygen for a complete combustion must be taken from the environment. Combustion usually takes place when the explosive is spread over a large area and is locally ignited. The large surface is well suited for the oxygen transfer and the heat dissipation with the environment. A combustion may turn over into a deflagration and detonation if heat dissipation is hindered.

The **deflagration** of an explosive takes place, when the reaction front goes through the material slower than the material speed of sound. The heat of reaction, released from the reaction front, heats up the surrounding un-reacted material and nourishes the propagation of the deflagration (fig. 1.1). The reaction front propagates in the same direction as the heat flow in the explosive. The combustion products formed in the deflagration reaction differ from the products formed in the combustion regime. As the deflagration products depend on the oxygen balance of the explosive, characteristic products such as C or CO, being low in oxygen, are formed [1].

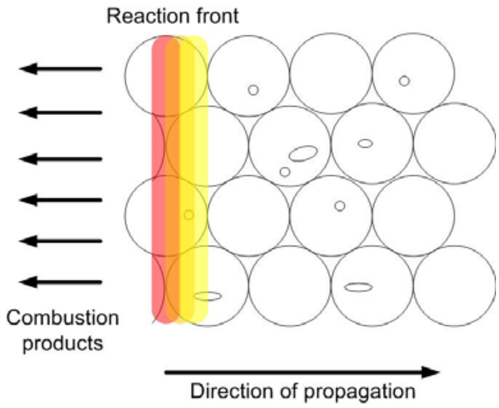

Fig.: 1.1 – Deflagration mechanism.

The propagation speed of the reaction front of black powder and nitrocellulose, two typical deflagrating substances, are shown below (tab. 1.1).

Substance	D **[m s^{-1}]**
Black powder	max. 500
Nitrocellulose	< 2000

Tab.: 1.1 – Deflagration speed of black powder and nitrocellulose [2].

A **detonation** occurs when, after initiation, the reaction front passes through the explosive faster than the speed of sound. A shock wave, traversing the material at such a high speed, generates a dynamic compression zone [2, 3] behind the shock wave front. The compaction effect causes a strong adiabatic heating of the explosive around specific areas, containing pores or gaseous inclusions, leading to its detonation and, in turn, the emission of further shock waves (fig. 1.2).

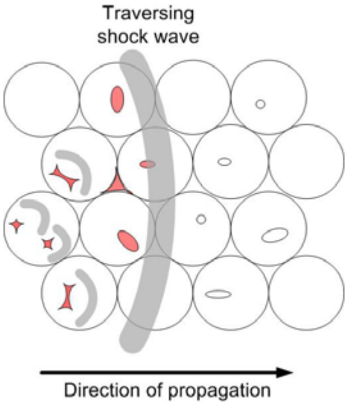

Fig.: 1.2 – Detonation mechanism.

In table 1.2, the detonation velocity with the corresponding density of various explosives are listed.

Substance	D **[m s^{-1}]**
RDX	8750 at 1,82 g cm^{-1}
TNT	6900 at 1,60 g cm^{-1}
β-HMX	9100 at 1,89 g cm^{-1}
Nitroglycerine	7600 at 1,59 g cm^{-1}
Picric acid	7350 at 1,71 g cm^{-1}

Tab.: 1.2 – Detonation speed of various explosives [2].

If the external conditions are appropriate, a combusting or deflagrating explosive may pass over into a detonation. In a confined space where heat dissipation of a deflagrating explosive is hindered, local overheating can accelerate the speed of reaction, turning the deflagration into a detonation. The inertia effect of a loose pile of a powdery explosive may already be a sufficient confinement, hindering heat dissipation. The smallest diameter where the transition into a stable detonation is still possible is known as the **critical diameter** [2, 4].

By knowing their primary decomposition behaviour, the large group of energetic materials can be divided into **propellants** and **explosives**, the latter further subdivided into **primary** and **secondary explosives**.

1.1 Propellants

Propellants are used in applications where the controlled propulsion of a certain object is wanted. They basically consist of a fuel and an oxygen source, combined in a single molecule or as an intimate mixture of oxidiser and fuel. Probably the most prominent representatives are black powder and nitrocellulose.

The largest consumption of propellants is located in the fields of: gunpowder, solid-fuel rockets and the mining industry. For these applications the deflagrating behaviour of the particular energetic material is highly desired due to its gradually decomposition, resulting in a *pushing-effect*. A deviation from the deflagrating behaviour towards a detonation can have disastrous consequences and must be avoided by all means.

1.2 Primary explosives

Primary explosives are substances or compositions that may detonate rapidly through the influence of a moderate external stimulus like shock, friction, heat or electrostatic discharge. They are mainly used for detonators and primers to *translate* an electrical, optical or mechanical signal into a detonation, strong enough to initiate a secondary explosive. The high detonating behaviour of primary explosives is also reflected by their noticeably smaller critical diameter. For a safe initiation of a secondary explosive, only a small amount of an adequate primary explosive is needed, making the handling of those materials safer.

A list with a series of primary explosives and their pyrotechnic properties is shown below (tab. 1.3).

Primary explosive	D **[m s^{-1}]**
Mercury fulminate **ONC-Hg-CNO**	5000 at 4,0 g cm^{-1}
Lead azide **$Pb(N_3)_2$**	4630 at 3,0 g cm^{-1} 5180 at 4,0 g cm^{-1}
Silver azide **AgN_3**	1500 – 1700 in unconfined state
Lead styphnate 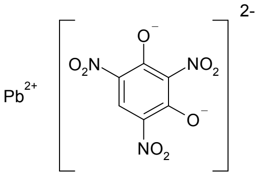	5200 at 2,9 g cm^{-1}

Tab.: 1.3 – Primary explosives and their detonation speed [2, 5].

The classification of explosives according to their specific sensitivity towards impact, friction and electrostatic discharge (ESD) is described later. A predefined threshold value decides if an explosive is classified as a primary or secondary explosive. For a better comparison, all explosives having a higher sensitivity than pentaerythritol tetranitrate (PETN) can be considered as primary explosives and all explosives less sensitive are considered as secondary explosives. The sensitivity to impact and friction of PETN are 5 J and 20 N, respectively.

1.3 Secondary explosives

Secondary explosives are used as filling for most types of military warheads, shaped charges in all sizes and as additives in propellants. In contrast to the pushing effect of deflagrating propellants, detonating explosives have a strong *shattering-effect* on the surrounding area. They are less sensitive to external stimuli than primary explosives. The detonation of a secondary explosive must be initiated by a strong primary explosive, generating a strong shock wave. In certain cases, the primary explosive must be coupled with an additional booster-charge, otherwise no reaction or a deflagration may occur.

Most secondary explosives in military applications are chemical uniform substances blended with a few percent of a binder or wax to improve handling capabilities. In the following, a short overview about the secondary explosives, that were used in this work, is given.

1.3.1 RDX

Cyclotrimethylenetrinitramine (fig. 1.3), also called Cyclonite or RDX was first synthesized by Henning [6] in 1899 for medical use. He found out that rapidly heated RDX explodes without leaving residues.

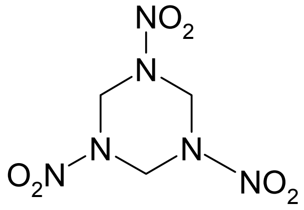

Fig.: 1.3 – Structural formula of RDX.

Physical and pyrotechnical properties: RDX forms colorless orthorhombic crystals with a maximum density of 1,82 g/cm³ [2]. It has a molar weight of 222,1 g. The melting point is in-between 204 and 206 °C, just followed by the decomposition. Its solubility [7] in selected solvents at 20 °C is shown in table 1.4.

Solvent	c_∞ **[g RDX / 100 g of solution]**
Acetic anhydride	4,0
Acetone	6,8
Benzene	0,05
Carbon tetrachloride	0,0013
Chloroform	0,015
Dimethylformamide	25,5
Methyl acetate	2,95
Water	0,005
TNT (molten)	4,4 (at 80°C)

Tab.: 1.4 - Solubility of RDX in different solvents at 20 °C [7].

At room temperature, RDX can exist in two polymorphic forms [8, 9], referred to as α- and β-RDX. It was found that RDX, crystallized from high boiling solvents such as nitrobenzene or molten TNT, forms the β-polymorph, recognizable by its dentric structure, whereas the more stable α-polymorph of RDX forms plates. McCrone [8] stated that β-RDX is only stable for a few seconds. Later, the group of Karpowicz *et al.*[9] succeeded to prove that β-RDX may exist for longer periods up to an hour. They also found that β-RDX easily converts to α-RDX by shaking or by contact with α-RDX. Due to the instable character of the β-polymorph, its formation can be neglected.

At its maximum density the detonation velocity of RDX reaches 8750 m/s. RDX has a negative oxygen balance of –21,6 %, meaning that for a complete oxidation an excess of oxygen is required. The impact and friction sensitivities, according to the French norm [10, 11], are 7,4 Nm and 120 N, respectively.

Explosives, exposed for a prolonged time to elevated temperatures, can explode after a while. This behaviour is known as one-dimensional-time-to-explosion (ODTX). The graph depicted in figure 1.4 shows the ODTX-curve of RDX at different temperatures.

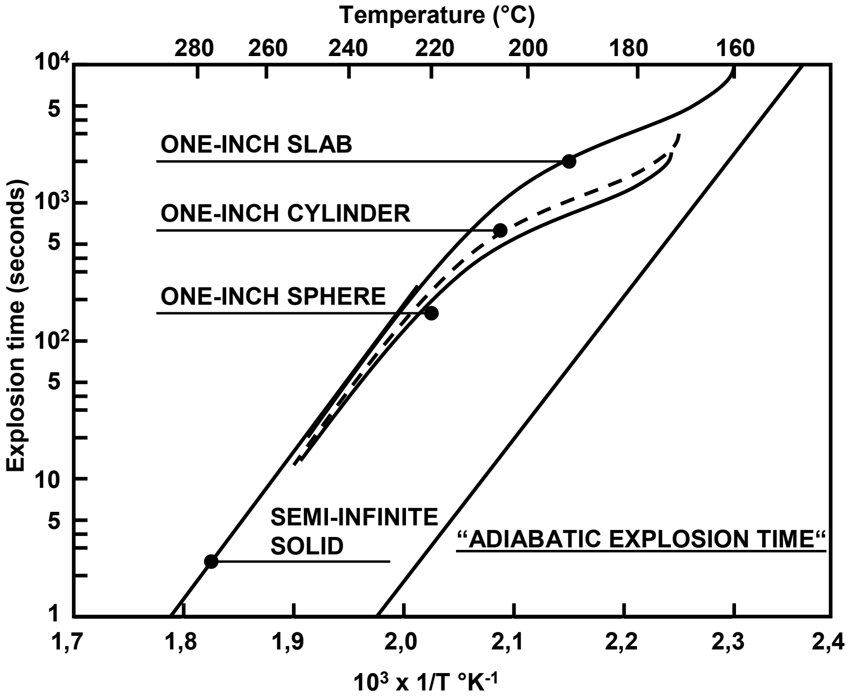

Fig.: 1.4 – ODTX-diagram of RDX [12].

RDX is mainly used for military and civil applications. Due to its unfavourable melting point, that is only about 3 °C lower than the decomposition onset, it is often used in combination with plasticizers or mixed with molten TNT.

1.3.2 TNT

2,4,6-Trinitrotoluene, better known as TNT, was first synthesized by Wilbrand [13] in 1863 by the direct nitration of toluene and cooking the solution for several days. Its molecular structure is depicted below (fig. 1.5):

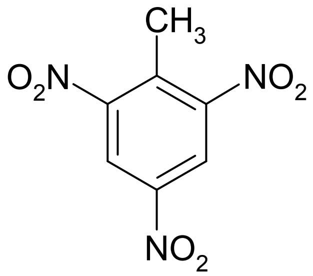

Fig.: 1.5 – Structural formula of TNT.

Physical and pyrotechnical properties: TNT may exist in an orthorhombic and a monoclinic form [14]. The monoclinic bright yellow form melts at 81 °C, whereas the less stable orthorhombic form initially undergoes a phase-transition at 70 °C followed by its melting at 81 °C. The solid-solid phase transition may also happen independently after prolonged storage, as Gallagher and Sherwood [14] have observed. Under the microscope, TNT forms needle like shaped crystals. Its molar weight is 227,1 g and the maximum density is 1,64 g/cm³. The solubility of TNT in selected solvents is shown in the table below [15] (tab. 1.5).

Solvent	c_∞ **[g TNT / 100 g of solution]**
Acetone	109
Benzene	67
Chlorobenzene	33,9
Chloroform	19
Diethyl ether	3,29
Methyl acetate	72,1
Toluene	55
Water	0,012

Tab.: 1.5 - Solubility [15] of TNT in different solvents at 20 °C.

Pressed TNT with a density of 1,60 g/cm³ reaches detonation velocities of 6900 m/s [2]. The oxygen balance is –73,9 %. The sensitivity to impact and friction in accordance with the French norm [10, 11] are 15 Nm and 353 N [2], respectively. The thermal behaviour of TNT, being exposed to elevated temperatures, is figured in the corresponding ODTX-diagram (fig. 1.6).

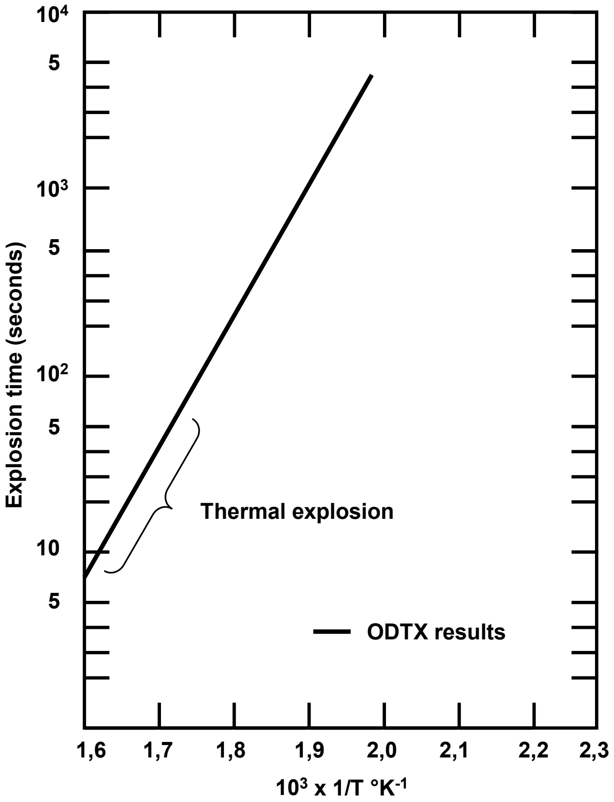

Fig.: 1.6 – ODTX-diagram of TNT [16].

Due to its low vulnerability to impact and friction and to its low production costs, TNT is widely used for military and civil applications. Its low melting point is advantageous for casting processes. Molten TNT undergoes a noticeably shrinking during its solidification [15], resulting in the formation of cracks and voids. In addition, pure TNT has the tendency to form large crystals. To attain a certain granulometry, pure TNT is often blended with less than 2 percents of hexanitrostilbene, avoiding the formation of large crystals.

1.3.3 CL-20

Its correct designation is 2,4,6,8,10,12-hexanitro-2,4,6,8,10,12-hexaazaisowurtzitane, also called HNIW, but it is best known as CL-20. “CL”, which stands for China Lake, is a relatively young explosive that has been first synthesized by Nielsen [17] in 1987 in the laboratories of the Naval Air Warfare Center Weapons Division in China Lake. Like RDX, CL-20 belongs to the group of nitramines but, contrary to classical nitramine explosives, it has a polycaged structure instead (fig. 1.7).

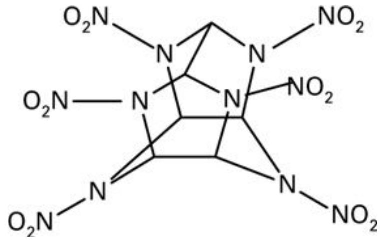

Fig.: 1.7 – Structural formula of CL-20.

Physical and pyrotechnical properties: The physical properties of CL-20 are extraordinary. At room temperature CL-20 can exist in 4 different allotropic phases, designated as α-, β-, γ-, and ε-CL-20. In figure 1.8, the characteristic positions of the functional groups of each of the four polymorphs are pictured. Besides the already mentioned four polymorphs, two further polymorphs exist, called δ- and ξ-CL-20. These two additional polymorphs are only stable under elevated pressure, which is why these polymorphs are not further discussed in this work.

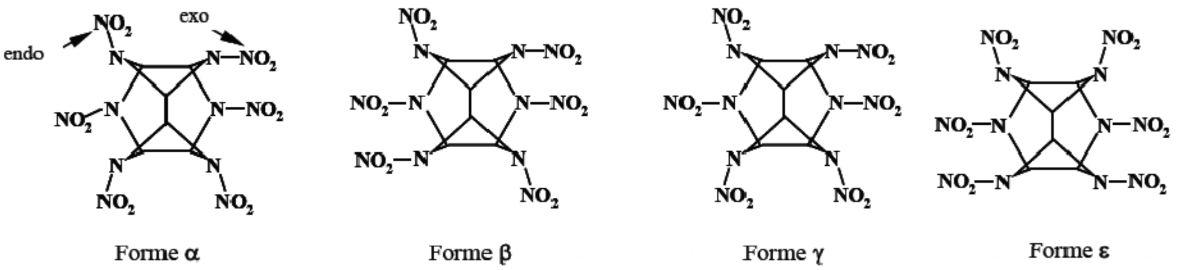

Fig.: 1.8 – Structure of the four at room temperature and ambient pressure stable polymorphs [18].

From the existing four polymorphs, the ε-phase is the most wanted form due to its elevated thermodynamic stability, high density and detonation velocity [18] (tab. 1.6).

Form	ρ [g cm^{-3}]	D [m s^{-1}]	T_m [°C]
ε monoclinic	2,044	9660	167
β orthorhombic	1,985	9380	163
α orthorhombic	1,971	-	170
γ monoclinic	1,923	-	260

Tab.: 1.6 – Properties of the different phases of CL-20 [18].

According to Foltz *et al.*[19], the thermodynamic stability of the different CL-20 phases decreases in the following order: ε > γ > α-hydrate > β. The solubility of ε-CL-20 in selected solvents [20] is shown in table 1.7.

Solvent	c_∞ **[g ε-CL-20 / 100 g of solution]**
Acetone	94,6 - 109
Ethanol	0,63 – 0,87
Ethyl acetate	42,97 – 45,0
Methylene chloride	0 – 0,03
Water	<0,005 – 0,0095

Tab.: 1.7 - Solubility [20] of ε-CL-20 in different solvents at 25 °C.

The molar weight of CL-20 is 438,2 g. The oxygen balance is – 10,95 %, resulting in a considerably better fuel-oxygen ratio than RDX or TNT.

CL-20 is the strongest, manageable, non-nuclear, existing explosive. Detonation velocities above 9300 m/s and the high densities of its polymorphs are unique so far. The sensitivity [2] to impact and friction of the ε-polymorph are 4 Nm and 48 N, respectively. Thus, from its sensitivity, CL-20 can be ranged between primary and secondary explosives. The decomposition behaviour of CL-20 towards prolonged heating (fig. 1.9) [21] is similar to this of RDX.

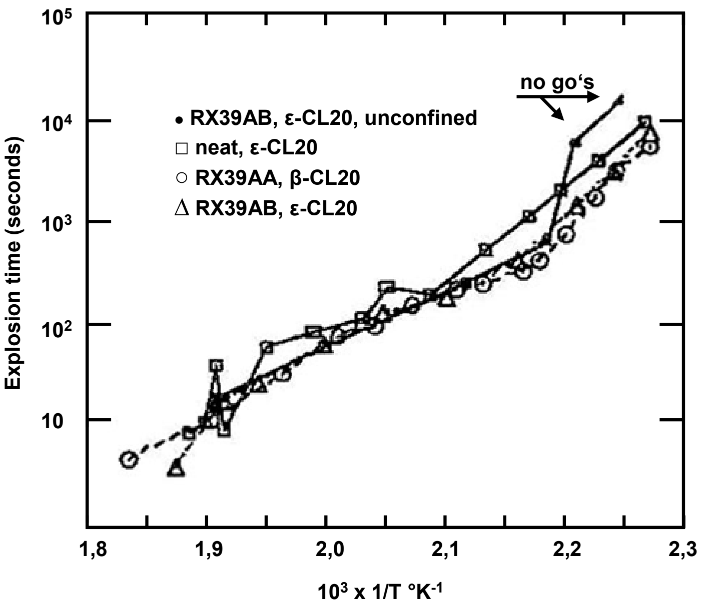

Fig.: 1.9 – ODTX diagram of CL-20 [21].

Despite its high sensitivity towards impact and friction, CL-20 is one of the most promising explosives for future military applications. The high detonation speed and the elevated density of CL-20 enable the miniaturization of existing warheads.

1.4 Explosive test methods

As mentioned earlier, explosives and propellants are classified by their sensitivity towards initiation. The explosives in this work were characterized by means of their sensitivity to friction, impact and electrostatic discharge. The following figure shows the equipment used for the sensitivity measurements (fig. 1.10).

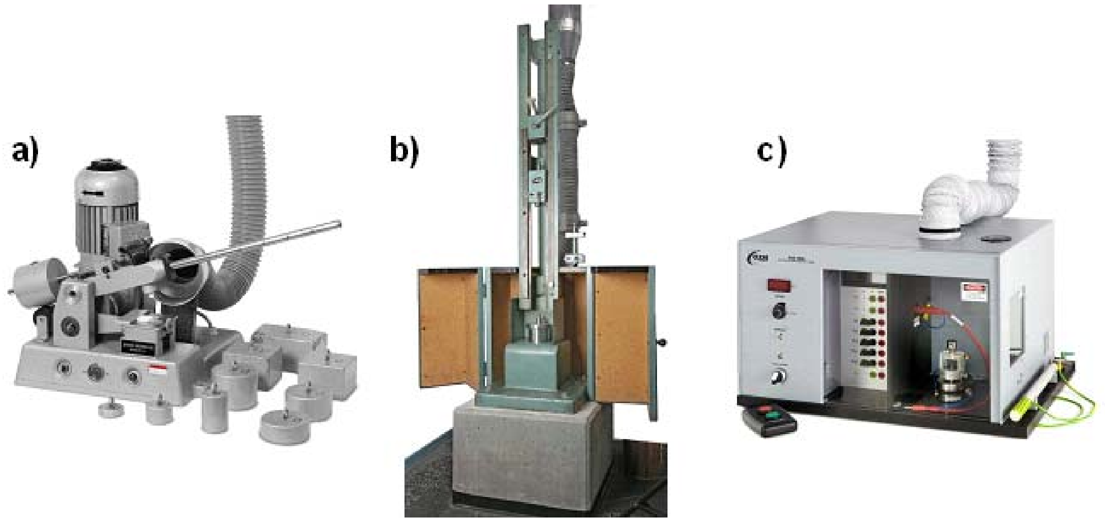

Fig.: 1.10 – a) *Julius-Peters Reibeapparat* for friction sensitivity measurements, b) fall-hammer apparatus for measurement of the impact sensitivity, c) *OZM Research ESD 2008* for measurement of the sensitivity to electrostatic discharge.

Impact sensitivity:

According to the French norm NFT 70-500, 40 mm³ of the testing material are placed between two steel pistons with defined length, diameter, surface condition and hardness. The upright standing pistons are held in position by a steel collar of also defined size and hardness. A free movable weight of 1 or 5 kg is positioned above the piston-collar assembly. The falling height of the weight can be adjusted from 0 up to 100 cm. Guide rails on both sides of the weight ensure a vertical impact of the falling weight on the piston-collar assembly. The impact sensitivity threshold value is indicated by six negative results at a specific height. The measuring range of the apparatus ranges from 1,56 to 50 J.

Friction sensitivity:

The measurement of the friction sensitivity is described in the French norm NF T70-503 [10]. A small sample of about 10 mm³ of the explosive is spread on a 25 x 25 mm porcelain plate with defined roughness. From above, a porcelain cylinder with defined curvature and roughness is placed on the explosive sample. The contact pressure of the porcelain cylinder on the explosive apparatus is set by different weights that can be mounted at different positions on a level. With a total of nine different weights and six different mounting positions on the lever, a measuring range from 5 to 360 N can be covered. A positive reaction of the explosive can already be a sort of *crackling, sparks or a change in color*; therefore the type of reaction should be specified. Six negative reactions indicate the friction sensitivity threshold value.

Electrostatic discharge sensitivity:

The electrostatic discharge sensitivity, called ESD, is measured by filling a short silicon tube with a small sample of the powdery explosive and placing it between two electrodes arranged in a defined distance between them. By discharging a capacitor with defined capacity and voltage, an electric spark between the electrodes is formed, capable of initiating the explosive. Six negative reactions indicate the electrostatic discharge sensitivity threshold value.

1.5 Ignition of explosives

The understanding of the ignition and the propagation process of explosives represents an essential part in their desensitization. As a basic rule, the ignition of an explosive, whether in form of a deflagration or a detonation, is an interplay of released and dissipated energy [22]. This rule can be applied to a single explosive crystal as well as to the whole charge.

Field [22] assumes that the initiation of an explosive is triggered by heat. Similar to a sequence cascade, the course of a detonation starts with its initiation (fig. 1.11).

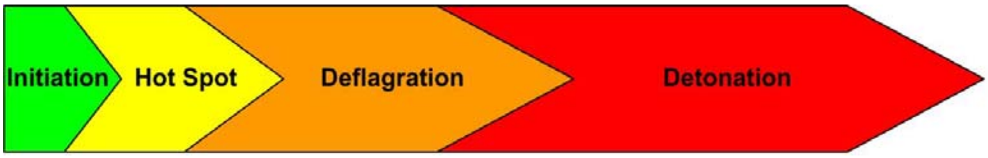

Fig.: 1.11 – Scheme: Evolution of a detonation.

First of all, the **initiation** of an explosive can be considered as the supply of external energy in the form of impact, friction, electrostatic discharge, heat or a radiation source. An explosive in a thermodynamic stable state does not explode without warning. Even the highly sensitive nitrogen tri-iodide is stable, until the supplied energy from the slightest touch sets it off.

Specific regions inside of the explosive are prone for initiation. Heterogeneities in the material such as cavities, inter-crystalline voids, gaseous inclusions, crystal cracks or impurities represent weak points where the supplied mechanical energy is converted into thermal energy. Some of the basic initiation processes for explosives are [22, 23]:

(a) adiabatic compression of gaseous inclusions, cavities and voids;
(b) viscous and plastic deformation;
(c) frictional heating;
(d) inter-crystalline shearing;
(e) spark discharge.

a) Adiabatic compression takes place when a sufficient high shock wave, traversing the explosive, encounters small gas bubbles, cavities or pores. The shock wave compresses these hollow spaces whereupon the temperature in the cavity and the surrounding material rapidly rises. The adiabatic compression is not only limited to cavities inside of the explosive. The presence of gas bubbles in liquid explosives can also have a sensitizing effect [22]. In loosely packed dry granulated explosives, the gaps between the individual particles, also affected by adiabatic compression, may also create spots of local heating

b) In the case of open pores, channels and interstices, heat may be generated by viscous and plastic deformation. Under the influence of impact or friction, solid material that is pushed into those open cavities undergoes a strong plastic deformation and heats up.

c) Frictional heating, where the explosive particles are rubbed against each other, is limited by the melting point of the material. Because, the temperature can not exceed the explosive melting temperature, the energy release by frictional heating is relatively low.

d) Inter-crystalline shearing is well described in the work of Copp *et al.*[24]. According to the authors, breaking of the crystals by shear happens only when the applied force exceeds the binding energy of an existing crystal defect. By partially destroying the crystal structure, the lattice energy in the affected area will be liberated, capable to create hot spots in this area. The lattice energy, and therefore the maximum releasable energy, strongly depends on the type of molecular bond being present in the explosive. Explosives with energy-rich ionic bonds are sensitive to shear and friction, whereas explosives with low lattice energy are insensitive to friction.

e) An electrical spark, traversing the explosive, has the ability to break chemical bonds [23] and cause strong local heating.

All those initiation processes from a) to e) have in common that the temperature may rise to several hundred Kelvin in a micron-sized small area and have to last for at least a few milliseconds [25]. This phenomenon, better known as **hot-spot,** is considered as the origin of every deflagration and detonation, respectively. Zygmunt [26] even subdivides hot-spots into internal and external hot-spots, depending on whether they are formed inside of an explosive particle or not. To sum up, inhomogeneities such as gaseous inclusions, pores, impurities, crystal cracks and crystal defects represent weak points prone for accidental initiation. According to

Tarver [25], the size of a hot-spot must be in-between 0,1 – 10 µm, and keep a temperature of at least 700 K for about 10^{-5} – 10^{-3} seconds, to ignite an explosive.

Outgoing from the formation of one or more hot-spots, the **deflagration** of the explosive sets in, capable to pass over into a **detonation**.

All steps from initiation, over hot-spot formation, to deflagration and detonation strongly depend on heat releasing and heat dissipation processes. Where heat dissipation predominates, the decomposition of the explosive may stagnate or come to a standstill, however if the heat releasing processes dominate, the reaction may accelerate until turning into a detonation. Numerous factors such as explosive type, granulometry, dimensions of the charge, density etc. are relevant for the heat dissipation processes.

The described detonation scheme: *initiation → hot-spot → deflagration → detonation*, rather represents the *accidental initiation* of explosives by means of localized hot-spots. A direct transition from initiation to detonation can be achieved by a strong shock wave [22, 27], created by a primary explosive.

By this knowledge, the sensitivity of an explosive can be varied in a wide range by the specific alteration of one or more parameters. Because, the conversion of mechanical energy into heat only happens in areas containing inhomogeneities, the elimination of those regions, prone for the creation of hot spots, is of highest importance. It is assumed that, decreasing the particle size of the explosive hinders the formation of internal hot-spots [28], furthermore the higher surface to mass ratio benefits heat dissipation processes. With decreasing particle size, the probability of inclusions or impurities in the particle itself diminishes and a higher overall homogeneity can be attained.

Summary of the chapter

The term explosive describes substances and mixtures of substances capable of releasing large amounts of energy, in form of pressure and heat, within a very short time. If propagation of the reaction front happens slower than the speed of sound in the explosive, a deflagration occurs. A detonation appears if the speed of the reaction front is equal or higher than the inner material speed of sound. The initiation of an explosive requires an external energy source. Mechanical or electrical energy, acting on the explosive, are converted into heat at characteristic points, forming hot-spots. Gaseous and liquid inclusions, open pores, crystal defects or impurities may act as hot-spots. To initiate an explosive, the size of a hot-spot must be of several micrometers. By elimination of potential hot-spots, a desensitization of explosives against unwanted initiation can be attained. With decreasing particle size, the probability diminishes that crystal defects, inclusions and suchlike are formed, impeding the formation of hot-spots.

References

[1] Agrawal, J.; *High Energy Materials,* **2010**, Weinheim, Germany, WILEY-VCH.
[2] Köhler, Josef; Meyer, Rudolf: *Explosivstoffe,* 9 Auflage, **1998**, Weinheim, Germany, WILEY-VCH.
[3] Suceska, M.; *Test methods for explosives*, **1995**, New York, USA, Springer.
[4] Eyring, H.; Powell, R.; Duffey, G.; Parlin, R.; *Chem. Rev.,* 45 (1), **1949**, pp. 69-181.
[5] Fedoroff, B.; Aaronson, H.; Reese, E.; Sheffield, O.; Clift, G.; *Encyclopedia of explosives and related items*, Vol. 1, **1960**, Picatinny Arsenal, New Jersey, USA.
[6] Henning, German Patent 104,280
[7] Fedoroff, B.; Sheffield, O.; *Encyclopedia of explosives and related items*, Vol. 3, **1966**, Picatinny Arsenal, New Jersey, USA.
[8] McCrone, W.; *Anal. Chem.*, 22 (7), **1950**, pp. 954-955.
[9] Karpowicz, R.; Sergio, S.; Brill, T.; *Ind. Eng. Chem. Prod. Res. Dev.,* 22, **1983**, pp. 363-365.
[10] norme française NF T70-503
[11] norme française NF T70-500
[12] Zinn, J.; Mader, C.; *J. App. Phys.,* 31(2), **1960**, pp. 323-328.
[13] Wilbrand, J.; *Annalen der Chemie und Pharmacie*, 128, **1863**, pp. 178-179.
[14] Gallagher, H.; Sherwood, J.; *J. Chem. Soc., Faraday Trans*., 92 (12), **1996**, pp. 2107-2116.
[15] Kaye, S.; *Encyclopedia of explosives and related items*, Vol. 9, **1980**, Picatinny Arsenal, New Jersey, USA.
[16] Tarver, C.; McGuire, R.; Lee, E.; Wrenn, E.; Brein, K.; *Symposium (International) on Combustion*, 17 (1), **1979**, pp. 1407-1413.
[17] Nielsen, A.; US Patent 5,693,794; Dec. 2, **1997**.
[18] Dumas, S,; These, Dosage du polymorphisme : spectrométrie IRTF et chimiométrie, Application aux formes polymorphes du CL-20.Université Claude-Bernard, Lyon, **2003.**
[19] Foltz, M.; Coon, C.; Garcia, F.; Nichols III, A.; *Prop. Expl. Pyr.*, 19, **1994**, pp. 19-25.
[20] von Holtz, E.; Ornellas, D.; Foltz, M.; Clarkson, J.; *Propellants Expl. Pyr.,* 19, **1994**, pp. 206-212
[21] Simpson *et al.*, *Prop. Expl. Pyr.*, 22, **1997**, pp. 249-255.
[22] Field, J.; *Acc. Chem. Res*., 25, **1992**, pp. 489-496.
[23] Czerski, H.; Thesis, Ignition of HMX and RDX. Cambridge, England, **2006**.
[24] Copp *et al., Phil. Trans., A,* 241, **1948,** pp. 197-296.
[25] Tarver, C.; Chidester, S.; Nichols, A.; *J. Phys. Chem.,* 100, **1996**, pp. 5794-5799.
[26] Zygmunt, B.; *Prop. Expl. Pyr.*, 7, **1982**, pp. 107-109.
[27] Spitzer, D.; Thèse de doctorat, Etude de rôle des defauts de taille microscopique dans la transition choc → détonation du monocristal de pentrite, Strasbourg, France, **1993.**
[28] Stepanov, V.; Anglade, V.; Bezmelnitsyn, A.; Krasnoperov, L.; *AIChE Annual Meeting*, **2006**, San Francisco.

2 Nano-explosives

In the past years a clear trend to nano energetic materials could be observed worldwide. The outstanding properties of nanomaterials led to the development of various new energetic compositions. In the case of classical explosives, their nanostructuration shall enhance their detonation properties and safety.

2.1 Properties

By the changed surface to mass ratio of nanoparticles, several properties may emerge, being previously not important in micron-size systems. The relatively low Van-der-Waals forces as well as the low electric surface charge for micron-size systems or compounds become important as the particle size decreases. These effects, for example, are important for the stability of carbon nanotubes.

An early discovered effect is the increasing solubility occurring with decreasing particle size, first described by Ostwald [1] studying the solubility of red and yellow mercury oxide. According to its discoverer, *Ostwald-ripening* designates the particle growth of polydisperse samples in saturated solutions. If a polydisperse sample is given into a saturated solution of the same solute, at first, the smallest particles dissolve in the solution due to their higher solubility, but then crystallize on the surface of the undissolved larger crystals. In this way, the larger particles grow at the expense of the smaller particles. This effect is not limited to solid particles, finely dispersed droplets in emulsions also underlie the same effect. From a modified Kelvin equation, describing the dependence of the vapour pressure with decreasing droplet size, the increasing solubility of the dispersed phase in the surrounding medium can be calculated as follows (eq. 2.1):

$$c(r) = c_\infty \exp\left(\frac{2\gamma V_m}{RTr}\right) \qquad \text{Eq.: 2.1}$$

with $c(r)$ the solubility in dependence of the radius, γ the surface tension [N m^{-1}], V_m the molar volume [m^3 mol^{-1}], R the ideal gas constant [J K^{-1} mol^{-1}], T the temperature [K], r the radius [m] and c_∞ the solubility of the bulk material [mol L^{-1}]. Monodisperse samples are immune towards Ostwald-ripening as the dissolution and recrystallization phenomenon are everywhere the same.

Also important becomes the formation of small liquid films enclosing a solid core, described as the *deliquescence problem* [2]. This appears when a droplet condenses out of the vapour phase and then partially dissolves the outer shell of the nanoparticle. In cases of high solubility, the liquid film may even exist in an unsaturated environment. Under adverse conditions, the presence of the liquid film may provoke the recrystallization of the nanoparticles.

The dependency of the melting point from the surface energy was early described by Pawlow [3]. Pawlow claimed that a substance can only be considered as homogenous when it is infinite large. In micrometric and larger dimensions, one takes advantage of this effect in the preparation of sintered metals [4, 5]. While in micrometric dimensions the surface melting effect is limited to the surface of the particle, sufficient small nanoparticles can melt completely because of their high surface to mass ratio.

With regard to explosives, the detonation properties of nano-explosives may differ noticeably from their micron-size counterparts. As mentioned in chapter 1, hot-spots represent a key role in the ignition process of explosives. Tarver [6] calculated for cyclotetramethylene-tetranitramine (HMX), a homologon of RDX, the critical temperature of different sized hot-spots. For a 2 µm sized hot-spot he calculated a critical temperature of 985 K, whereas the critical temperature for a 0,2 µm sized hot-spot already rises to 1162 K. Therefore, decreasing the particle size of the explosive will consequently limit the maximum attainable hot-spot size and increases its critical temperature. In addition, assuming that the total number of potential hot-spots remains constant, they will be more homogeneously distributed than in a micrometric explosive.

Due to the higher critical temperature and the evenly distributed potential hot-spots, it is assumed that nano-explosives may have a shorter run-up to detonation distance than micron-sized explosives [6], because the released heat in a nano-explosive can diffuse faster to the surrounding particles where further hot-spots may occur.

In regard to the further processing, nano-explosives are better to process than micron-sized particles. Except for TNT, most military explosives are not suited for cast processing because of their high melting points. Usually, powdery explosives like RDX or HMX are mixed with molten TNT in order to facilitate the further processing. These compositions, pressed or casted, are less powerful than pure RDX or HMX. In contrast to that, nanostructured explosives have a good compression behaviour, allowing the formation of pressed charges, but also have a self-lubricating effect when exposed to friction.

2.2 Specific health and safety hazards

Besides extraordinary physical properties, nanoparticles may have a high toxic potential. Due to their small size, nanoparticles are ought to enter the human body easily by the lungs, the gastro-intestinal tract or by the skin [7]. Once inside of the body the particles may even pass the blood-brain barrier, usually serving as a natural defence mechanism of the human body. The toxic potential also depends on the nature of the material. Metals or metal oxides such as silver, zinc, titanium oxide or silicon oxide are harmless in the micrometric state, but can become highly toxic in the nanometre scale [8]. Substances that are usually insoluble in water also hold the risk of accumulating inside of the human body. The effects of nanomaterials on the human body can not be predicted. As most commercially available nanomaterials are inorganic (metals, metal oxides, salts), not much is known about organic nanomaterials. Due to the lack of a uniform regulation, most nanoparticles are treated as their micrometric counterparts. However, nanomaterial specific safety guidelines shall reduce the risk of working with them [7]. If possible, powdery compositions should be replaced by pastes or dispersions. Closed apparatus are to give priority, otherwise a fume hood should be installed directly at the source of formation or a slight negative pressure should be applied to the installation to avoid any emission. The number of persons exposed to the nanomaterials and the time of exposition must be limited. The persons working with the nanomaterials must wear appropriate protective clothing, such as breathing mask with P3 particle filter, rubber gloves, closed eye goggles and protective clothing with a hood.

In the context of this work, the inherent risk outgoing from explosives must also be taken into consideration. Usually the work and the storage of energetic materials is subject to strict safety directives. The production hall must be equipped with blow-out walls, and dangerous processes, e.g. including primary explosives, are remote-controlled. Because only small amounts of secondary explosives in a non-confined state will be handled in this work, the risk outgoing from the explosive in contrast to the potential toxic risk of the nanoparticles is very low. Nevertheless, from every new nanocrystallized explosive, the sensibility to impact, to friction and to electrostatic discharge must be determined.

2.3 Production processes described in the literature

The properties of nanoparticles may differ strongly from their micrometric counterparts. Because every system strives for a low-energy state, the formation of a small total surface, the crystallization process must be interrupted in an early state. Due to the inherent risk, the classic crushing processes for the large scale production of nanoparticles can not be applied to explosives. Over the last years, the following preparation techniques, capable of producing small amounts of submicron energetic particles, were described in the literature. Besides the wet-milling process, all described techniques are bottom-up processes:

- Wet-milling
- Sol-Gel processes
- Vacuum-condensation
- Electrospray
- Ultrasound assisted nanocrystallization
- Rapid expansion of supercritical solutions

2.3.1 Wet-milling process

The work of Redner *et al.*[9] describes the batch-wise production of submicron RDX by a wet-milling process. In his work, 20 g of Class 5 RDX, with a mean particle size of 30 µm, were dispersed in a solution consisting of water, isobutanol and a dispersant, improving the wetting behaviour. The suspension with a solid content of 10 % was filled into a not further specified mill, and the particles were grounded at agitation rates from 2000 RPM to 3500 RPM. The particles, filtered through a Stericup Millipore filter with 100 nm pore size were dried in a vacuum oven. The product yield was about 80 % from the initial amount. The particle size strongly depended on the milling time. According to the author, after 60 minutes of milling at 3000 RPM a mean particle size of 310 nm, with a crystallite size between 65 and 70 nm was obtained. The particles had a smooth surface and a uniform particle size distribution (PSD). Redner [9] reported that product, which was left on the wet filter for two days, drastically "changed its properties". This particular sample, examined with a field emission scanning electron microscope (FESEM), exhibited large micron structures in the order of 5 to 10 µm. It is assumed that storing the milled particles on a wet filter for a prolonged period, the particles recrystallized as a result of Ostwald-ripening.

2.3.2 Sol-Gel process

By developing new detonators with a fast energy release that are also insensitive to unintended initiation, the group of Tillotson [10] was the first that embedded energetic materials into a silica matrix. They prepared a gel by dissolving the explosive and the reaction mixture, consisting of tetramethoxysilane and a catalyst, in a mutual solvent and allowing the composition to solidify (gelification). Then the pore liquid, the solvent, was displaced by a solvent in which the energetic material was insoluble, causing the dissolved explosive to precipitate in the pores of the silica matrix. The finished xerogel is obtained by drying of the wet material. Improvements of this process can be obtained by extracting the pore liquid with supercritical CO_2, in which RDX has a very low solubility. This method allows the formation of light aerogels. According to the patent US 2005/0092405 [11], the pore size from those aerogels and xerogels ranges from 2 – 50 nm. RDX based aerogels and xerogels with compositions up to 80 %-wt of RDX and 20 %-wt of SiO_2 were prepared. With increasing RDX content a non-uniform growth of orthorhombic crystals occurred. RDX imbedded in the silica matrix was less sensitive towards shock than the pure substance. Ignition tests showed that pellets of RDX-xerogels with 80 %-wt RDX and 20 %-wt SiO_2 were able to be ignited, whereas compositions with only 33 %-wt RDX failed to be ignited.

2.3.3 Vacuum-condensation

For the first time, Frolov *et al.*[12] describe the preparation of ammonium nitrate, and RDX nanoparticles by means of the vacuum condensation technique. The explosives, placed onto a heatable plate, where continuously sublimed inside of an evacuated chamber. The explosive vapours deposited on a cooled quartz-glass plate on the top of the vacuum chamber. The sublimation of the RDX was performed at temperatures ranging from 145 and 202 °C, whereas the sublimation of the ammonium nitrate occurred between 105 to 139 °C. The glass plates to recover the particles were placed in-between 10 and 210 minutes in the vacuum chamber. Calculated after the Debye-Scherrer equation, a crystallite size of 31 nm for RDX and of 55 nm for ammonium nitrate was determined. In a more recent publication, nano-RDX was produced in the same manner by the group of Pivkina [13]. In vacuum, bulk RDX was evaporated at 158 °C and the condensing vapour was collected for 30 s. Transmission electron microscope (TEM) analysis of the deposited particles revealed a particle size of about 50 nm.

2.3.4 Electrospray method

The electrospray method, described by Radacsi *et al.*[14], is a process capable of preparing submicron RDX. A conductive solution of RDX and acetone is pumped through a metal capillary, serving as a nozzle. The volume flow rate amounts 2,8 mL/h. The opening of the capillary is directed towards a grounded plate, positioned about 10 - 70 mm away from the capillary opening. Between the capillary and the grounded plate, an electric potential between 3,8 and 4,9 kV is applied. At a sufficient high potential difference, when the electrostatic forces overcome the surface tension of the solution, a Taylor-cone arises from which a continuous flow of droplets is emitted, attracted by the grounded plat, the opposite pole. While the droplets flies through the air, the solvent evaporates and the electric charge accumulates at the surface. When the charge reaches a certain threshold value, the droplet disrupts as a consequence of the *Coulomb fission*. The distance of the grounded plate must be large enough to ensure a complete evaporation of the solvent. The crystallized RDX, that is still charged, deposits on the opposite charged plate. According to the author, the median particle diameter that was attained by this method was around 400 nm.

2.3.5 Ultrasound assisted spray crystallization

The process developed and patent by Spitzer *et al.*[15, 16], can be considered as a continuous operating spray drying process (fig. 2.1). By means of ultrasonic transducers, oscillating with a frequency of 1,7 MHz, a RDX-acetone solution was atomized. The atomized solution formed a fine mist hovering a few centimetres above the liquid surface. By means of a fan, an inert gas stream circulates in the installation, carrying the mist into the electric furnace. The furnace was operated in-between 90 – 130 °C. Inside the furnace, the acetone evaporated and the RDX crystallized. In an electrostatic precipitator, the crystallized RDX was separated from the gas stream. The precipitator was operated with a voltage of 8kV. The production capacity of this process is about 1-3 g/h and particles with a diameter from 30 to 100 nm were obtained.

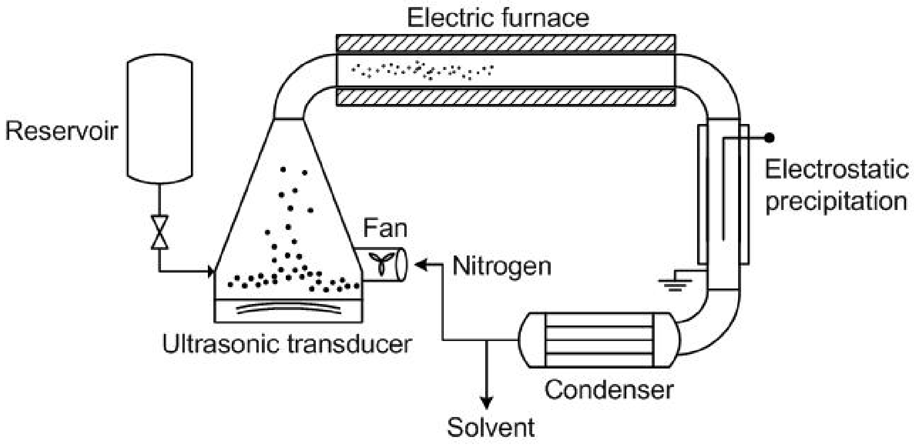

Fig.: 2.1 – Flow diagram of the continuous spray crystallization process.

2.3.6 Rapid expansion of supercritical solutions

The formation of crystalline explosives by rapid expansion of supercritical solutions, abbreviated RESS, was initially described by Teipel [17] in 1997, who prepared 10 µm large TNT particles from supercritical carbon dioxide. In 2005, the group of Krasnoperov [18] succeeded in the preparation of nano-RDX by this process. Supercritical CO_2 with a pressure from 15 - 29,5 MPa and a temperature in-between 343 and 348 K was allowed to flow through a bed of RDX coated glass beads. Then, the CO_2 saturated with RDX was expanded over a sapphire nozzle (diameter 100 and 150 µm, respectively) into a collection vessel, inducing the crystallization of the RDX. After the depressurization of the supercritical fluid, the CO_2 condensed on the RDX particles, serving as condensation seeds, and led to an increase of their mass. The mass of the RDX-dry ice composition had to be large enough to enable the precipitation at the bottom of the collection vessel. The formed RDX particles had a mean particle diameter ranging from 110 to 220 nm. Because of the low solubility of RDX (0,25 mg RDX / 1 g CO_2 at 480 bar and 353 K), the production capacity by this process is relatively low. Stepanov [19] performed an up-scaling of the RESS process in order to increase the production capacity. For a RDX production capacity of about 6 g/h, the CO_2 consumption rose to 35 kg/h [19]. The up-scaled version of the RESS process is depicted in figure 2.2.

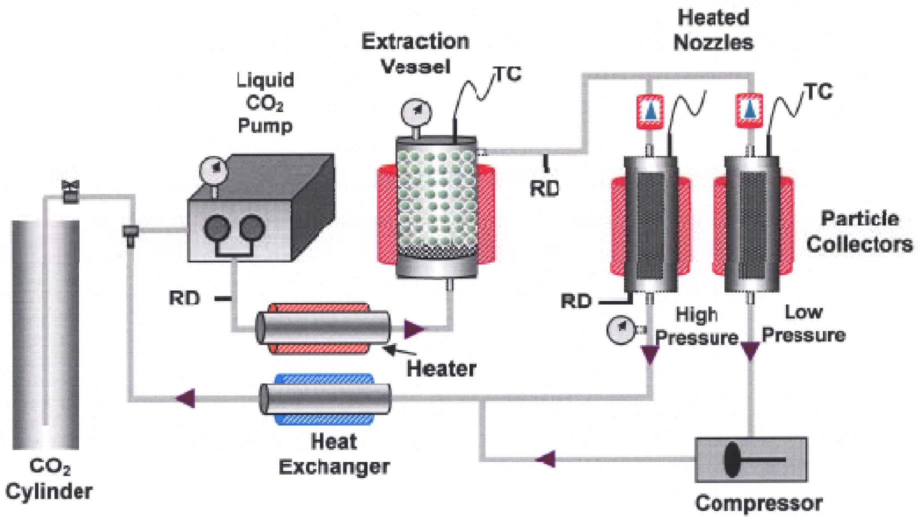

Fig.: 2.2 – For the production of nanocrystallized RDX up-scaled RESS process [19].

2.4 Analytical methods

In the fields of nanotechnology and material science special attention is given to the particle size, Particle Size Distribution (PSD) and their influence on the properties of explosives. As far as possible, and of interest, every product was characterized by Differential Scanning Calorimetry (DSC), X-Ray Diffraction (XRD), nitrogen adsorption (BET) to determine the specific surface area and Scanning Electron Microscopy (SEM). In addition, their sensitivity to impact, to friction and to electrostatic discharge was also determined by the methods described in chapter 1.

2.4.1 Differential scanning calorimetry

The differential scanning calorimetry, in the following referred as DSC, is a measuring technique suited for the measurement of the thermodynamic behaviour of a given substance in a definite temperature range. A small amount of the sample, about 1 – 3 mg, is filled into a crucible which is then hermetically sealed by a press. An empty crucible, also hermitically sealed, serves as reference. Both crucibles, placed into an oven on separate supports, are then slowly heated up to a predetermined final temperature. From both crucibles, the heat flow and temperature were continuously measured. The crucible where the sample has to pass through states of phase change or decomposition requires more or less energy than the reference sample to keep the same temperature. Depending on the scanned temperature range and the type of sample, mostly the following thermodynamic properties are measured by this method: specific heat capacity of the solid or liquid phase, the melting and boiling point, decomposition temperature, enthalpy of fusion, evaporation and decomposition. The model that was used for this work was a Q 1000 DSC, from TA instruments.

2.4.2 X-ray diffraction

X-ray diffraction, abbreviated XRD, is used in the identification and characterization of crystalline substances. If an energy rich X-ray beam hits an atom, the electrons surrounding the atom start to oscillate with the same frequency as the excitation beam. Because of the shell like distribution of the electrons, destructive interferences prevent a measurable signal leaving the sample. In a crystalline sample, these interferences may underlie a mutually reinforcing behaviour causing the emission of detectable X-ray beams in characteristic directions. In a powdery sample the crystals are randomly oriented; therefore, the direction of the diffracted X-ray beams depends on the position of the incoming X-ray beam. This error is compensated by setting the sample into rotation as well as varying the angle of the X-ray source and detector. The crystallite size LC of a crystalline sample is calculated by Scherrer's equation:

$$LC = \frac{180}{\pi} \cdot \frac{k \cdot \lambda}{\cos\theta \cdot \sqrt{FWHM^2 - s^2}} \qquad \text{Eq.: 2.2}$$

with λ the wavelength of the X-ray radiation expressed in [Å], k a shape factor that is known as Scherrer constant which is usually set at $k = 0.89$, s as a correction factor for the instrumental broading which is zero under ideal conditions and $FWHM$ as the full width at half maximum of a given peak expressed in degree. The diffractometer used in this work was a BRUKER D8 Advance (Cu Kα radiation λ = 1.54 Å).

2.4.3 Specific particle surface

The measurement of the specific particle surface by the gas adsorption technique was named by their inventors Brunauer, Emmett and Teller (BET). The measuring principle bases on the adsorbing behaviour of nitrogen molecules at extremely cold temperatures. A dry sample is evacuated and cooled down to -196 °C. At these low temperatures, the oscillating behaviour of the nitrogen gas molecules is assumed to be negligible. The evacuated sample, filled into a measuring cell, is placed in liquid nitrogen. Then, gradually small amounts of gaseous nitrogen are supplied to the sample. The nitrogen adsorbs at the sample surface and decreases the pressure in the measuring cell. The nitrogen forms a monolayer on the sample surface. By knowing the molecule diameter of nitrogen, the specific surface of the sample can be calculated, usually expressed in m² / g. The device used in this work was a Beckman Coulter SA 3100.

By knowing the prevailing particle shape: spheres, rods, tubes or platelets, the median particle size can be calculated from the samples specific surface. The BET-surface is indicated as:

$$\text{Surface}_{\text{BET}} = \text{Surface}_{\text{sample}} / \text{Mass}_{\text{sample}}$$

Assuming that the particle shape is spherical, the surface-term expressed as: $4*\pi*r^2$, and the mass-term expressed as: $\rho*4/3*\pi*r^3$ results in the following equation:

$$S_{BET} = \frac{4 \times \pi \times r^2}{\rho \times \frac{4}{3} \times \pi \times r^3} = \frac{3}{\rho \times r} \qquad \text{Eq.: 2.3}$$

With S_{BET} the specific particle surface, ρ the density and *r* the particle radius.

2.4.4 Scanning electron microscopy

Scanning electron microscopy (SEM) is a useful tool in material science for surface analysis. A bundled electron beam is accelerated and guided over the sample surface with a grid structure. The electrons hitting on the sample surface interact in different ways with the sample whose detection gives information about the surface. To avoid interactions with air molecules, the measuring chamber is evacuated. At high magnification, the electron beam may charge the particle surface and heat up the sample. For this purpose, the sample must be coated with a thin conductive layer of approximately 10 nm of platinum, gold or graphite. Because of the nearly stepless magnification, objects from several millimeters to just a few nanometers can be observed in detail. The SEM that was used in this work was a ZEISS-DSM 982 Gemini.

By means of SEM images, the PSD of the different samples was determined. By choosing a circular area with 5 or 10 µm diameter, all particles within this area were measured. The number of measured particles usually amounted 50 to 100 particles. The measurements were used to determine the median particle size and the particle size distribution of the sample.

2.5 Evaluation of the existing processes

A fabrication process, capable of producing large amounts of nanocrystallized explosives, must comply economic as well as safety relevant aspects. The processes mentioned above only partially fulfil these requirements (tab. 2.1):

Process	**Pros**	**Cons**
Wet-milling	+ High production capacity	- Batch process - Recrystallization due to residual moisture - After-treatment necessary - Top-down process - Large amounts of explosive present in the installation
Sol-Gel	+ Bottom-up process	- Pure nano-explosives can not be prepared - Laborious - Batch process - Expensive raw materials
Vacuum-condensation	+ Bottom-up process + Small particles	- Low production capacity - Not suited for a scale-up
Electrospray method	+ Bottom-up process	- Combination of evaporating solvents and high voltage - Low production capacity - Narrow parameter range
Ultrasound assisted spray crystallization	+ Bottom-up process + Continuous production	- Combination of evaporating solvents and high voltage - Residual moisture - Evaporation vs. atomization
RESS	+ Bottom-up process + Very small particles + Solvent free particles	- High pressure and temperature required - Low production capacity - Expensive - Only applicable to single substances - Condensing CO_2 on RDX particles necessary

Tab.: 2.1 – Advantages and drawbacks of the different production processes.

The RESS process is one of the few processes which is worth considering for a scale-up. By the use of supercritical CO_2 as solvent, the finished product is absolutely dry and does not recrystallize. The process and all of its components base on an already existing technique, decreasing time and development costs. Unfortunately, because of the low solubility of RDX in supercritical CO_2, the high consumption of CO_2 makes this process economically unattractive and the high working pressure of more than 300 bar represents a substantial hazard.

The nanocrystallization process developed by Spitzer and Baras [15] is the only process that has been designed for a continuous production already from the start. As part of my master thesis performed on this process before, it was found that this process is not suited for a long-term production. The piezo-electric material from which the ultrasonic transducers were made, tended to perish rapidly after several hours of use. Also, the aerosol generated by the transducers had a lower RDX concentration than the original solution, causing the accumulation of explosive in the atomization vessel. The resulting particle size, considerably depended on the furnace temperature, that was limited by the explosive decomposition temperature.

Recapitulatory, the analysis of the processes clearly showed the weak points of the different techniques and demonstrated where the focus must be concentrated. Especially of interest are the RESS process described by Krasnoperov [18] and Stepanov [19] and the continuous nanocrystallization process developed by Spitzer and Baras [15]. Outgoing from the knowledge of my master thesis, the flash-crystallization process emerged, combining the advantages of the two processes.

Summary of the chapter

By the nanostructuration of energetic materials, advantages over classical micron-sized materials are expected. The surface to mass ratio changes by the nanostructuration, what may change significantly the physical properties of the material. By the increased surface to mass ratio, the particle posses a larger percentage of surface molecules, that may have completely different properties due to their increased energy level, than molecules in the inside of the particle. For instance, one can observe that with decreasing particle size the melting temperature also decreases, whereas the solubility increases. In view of the detonation properties of nanostructured explosives, desensitization against accidental initiation, but higher decomposition velocities are expected at the same time.

Because of the high reactivity of nanoparticles and the sensitivity of explosives, the large-scale production of nanostructured explosives failed so far. The different processes described in literature are rather suited for the production of small amounts less than 1 g. Outgoing from the results of my master thesis, the flash-crystallization process emerged, combining the advantages of the RESS- and the continuous nanocrystallization process.

References

[1] Ostwald, W.; *Z. Phys. Chem.*, 34, **1900**, pp. 495-503.

[2] Shchekin, A.; Rusanov, A.; *J. Chem. Phys.,* 129, **2008**, pp. 154116.1-154116.5.

[3] Pawlow, P.; *Z. Phys. Chem.*, 65, **1908**, pp. 1-5.

[4] Lichtenecker, K.; *Ztschr. Elektrochem.*, 48 (11), **1942**, pp. 601-604.

[5] Wang, Z.; Petroski, J.; Green, T.; El-Sayed, M.; *J. Phys. Chem. B*, 102 (32), **1998**, pp. 6145-6151.

[6] Tarver, C.; Chidester, S.; Nichols, A.; *J. Phys. Chem.,* 100, **1996**, pp. 5794-5799.

[7] Meier, P.; *sicher ist sicher – Arbeitsschutz aktuell,* 2, **2008,** pp. 59-61.

[8] Kühling, W.; *Aus dem Labor auf den Teller, Die Nutzung der Nanotechnologie im Lebensmittelsektor, Bund für Umwelt und Naturschutz Deutschland*, **2008**.

[9] Redner, P.; Kapoor, D.; Patel, R.; Chung, M.; Martin, D.; Production and characterization of nano-RDX, Report, U.S. Army, RDECOM-ARDEC Picatinny, NJ 07806-5000, **2006**.

[10] Tillotson, T.; Hrubesh, L.; Fox, G.; Simpson, R.; Lee, R.; Swansiger, R.; Simpson, L.; Sol-Gel processing of energetic materials, 5th international symposium on aerogels, France, **1997**.

[11] Simpson, R.; Lee, R.; Tillotson, T.; Hrubesh, L.; Swansiger,R.; Fox, G.; US 2005/0092405

[12] Frolov, Y.; Pivkina, A.; Ul'yanova, P.; Zav'yalov, S.; *Comb. Expl. and Shock Waves*, 38 (6), **2002**, pp. 709-713.

[13] Pivkina, A.; Ul'yanova, P.; Frolov, Y.; Zav'yalov, S.; Schoonman, J.; *Prop. Expl. Pyr.*, 29 (1), **2004**, pp. 39-48.

[14] Radacsi, N.; Stankiewicz, A.; Creyghton, Y.; van der Heijden, A.; ter Horst, J.; *Chem. Eng. Technol.* **2011,** 34 (4), pp. 624-630.

[15] Spitzer, D.; Baras, C.; Schäfer, M.; Ciszek, F.; Siegert, B.; *Prop. Expl. Pyr.*, 36, **2011**, pp. 65-74.

[16] Spitzer, D.; Baras, C.; DE 10 2007 003 396 A1, 23.01.2007.

[17] Teipel, U.; Förter-Barth, U.; Gerber, P.; Krause, H.; *Prop. Expl. Pyr.*, 22, **1997**, pp. 165-169.

[18] Krasnoperov, L.; Elkina, I.; Zhang, X.; *Prop. Expl. Pyr.*, 30 (3), **2005**, pp. 178-183.

[19] Stepanov, V.; Dissertation: Production of nanocrystalline RDX by RESS: Process development and material characterization, **2008,** New Jersey Institute of Technology, USA.

3 Flash-crystallization process

The flash-crystallization process is a very rapid and efficient crystallization process that is hardly described in the literature. In its main features this process bases on the flash-evaporation technique, an evaporation process mainly used for the large-scale desalination of sea water [1].

3.1 The fundamentals of flash-evaporation

During flash-evaporation, a heated and pressurized liquid undergoes a sudden and strong pressure drop. Because of the rapid pressure drop, decreasing the liquids saturation pressure and with it the boiling temperature, the liquid is not anymore in a thermodynamic stable state with its environment. The liquid is now in a metastable state which is marked by the liquid’s temperature being higher than the actual boiling temperature, however, without any evaporation taking place. This state is described as superheated state, characterized by the degree of superheating ΔT_S:

$$\Delta T_S = T_0 - T_S \qquad \text{Eq.: 3.1}$$

with T_0, the initial temperature of the liquid and T_S, the saturation temperature of the liquid after the pressure drop.

In the metastable state, the superheated liquid strives to attain its thermodynamic stable state by the removal of energy. The energy removal happens by the conversion of sensible heat into latent heat. The driving force in this process is the degree of superheating. At small ΔT_S, the evaporation process occurs slowly, whereas at higher degrees of superheating the process may have an explosion-like character. In experiments with water droplets of different diameters, Owen and Jalil [2] found out that, with increasing degree of superheating, the conversion of sensible heat to latent heat became more and more violent. They differentiated between surface evaporation, slow bubbling, medium bubbling, rapid bubbling and flash-evaporation (fig. 3.1).

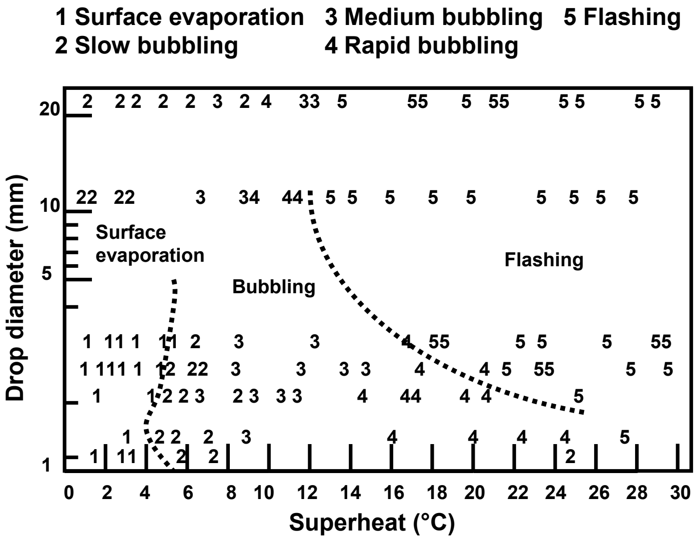

Fig.: 3.1 – Evaporation behaviour of superheated water droplets [2].

Besides the degree of superheating, the droplet diameter also played an important role. Small droplets may conduct the heat from the centre faster to the surface and are favoured for less violent evaporation types, whereas larger droplets are prone for flash-evaporation even at relatively low degrees of superheating. The violent evaporation behaviour occurring at flash-evaporation is of high interest for the generation of very fine sprays.

The formation of bubbles also depends on the liquids physical properties. According to Owen and Jalil [2], the bubble nucleus must reach the critical diameter d_c to ensure that the bubble grows and boiling occurs. By knowing the critical diameter, the required degree of superheating ΔT_S is calculated by:

$$\Delta T_S = \frac{4 \cdot \sigma \cdot \upsilon_G \cdot T_S}{h_{FG} \cdot d_c} \qquad \text{Eq.: 3.2}$$

with T_S the saturation temperature, σ the surface tension, υ_G the specific volume, h_{FG} the heat of vaporization and d_c the critical bubble diameter. The bubble formation is also distinguished by homogeneous and heterogeneous nucleation. Similar to the formation of hot-spots in explosives, the formation of bubbles in superheated liquids is promoted by the presence of foreign bodies, such as rough surfaces, sharp edges, dispersed particles or dissolved gases [3, 2]. Those aspects play an important role in systems where flash-evaporation is ought to happen already in the tubing or inside of the nozzle [4].

In various publications, [2, 5, 6] it is mentioned that flash-evaporation does not happen simultaneously with the pressure drop. The flash process sets in a fraction of a second after the pressure drop, when a sufficient high degree of superheating is attained. The delay time t_D, with which the evaporation sets in, decreases proportionally with increasing degree of superheating ΔT_S [7]:

$$t_D \propto \Delta T_S^{-\frac{2}{7}}$$

For a single-component system, the amount of vaporizing liquid Δm_{flash} can, with a good precision, be calculated by the following equation:

$$\Delta m_{flash} = m_0 \cdot (T_0 - T_S) \frac{c_{p,l}(T_0)}{\Delta_{vap} H(T_S, p_S)} \qquad \text{Eq.: 3.3}$$

with m_0 the initial amount of liquid, $c_{p,l}(T_0)$ the specific heat capacity of the liquid at the overheating temperature T_0 and $\Delta_{vap} H(T_S, p_S)$ the vaporization enthalpy at the saturation conditions. This equation is sufficiently precise for ΔT_S up to about 50°C, but at higher degrees of superheating the relative error increases.

The vaporization enthalpy at the saturation conditions can be calculated by the Clausius-Clapeyron equation:

$$\frac{dp}{dT} = \frac{\Delta_{vap} H}{T \cdot \Delta V_m} \qquad \text{Eq.: 3.4}$$

with T the temperature in [K] and ΔV_m the molar volume change, calculated by:

$$\Delta V_m = V_{m,(g)} - V_{m,(l)} \qquad \text{Eq.: 3.5}$$

with $V_{m,(g)}$, the molar volume of the gas and $V_{m,(l)}$, the molar volume of the liquid. As the gas volume is many times larger than the liquid volume, the molar volume change can be simplified to:

$$\Delta V_m \approx V_{m,(g)}$$

Furthermore, assuming that the gas can be considered as an ideal gas, ΔV_m can be expressed as:

$$\Delta V_m = \frac{R \cdot T}{p} \qquad \text{Eq.: 3.6}$$

with R, the ideal gas constant and the pressure p. If also assumed that $\Delta_{vap} H$ is temperature independent for small ranges, the integrated form of equation 3.4 reformulated to $\Delta_{vap} H$ is:

$$\Delta_{Vap} H = \ln \frac{p_2}{p_1} \cdot \frac{R}{\left(\frac{T_2 - T_1}{T_2 \cdot T_1} \right)} \qquad \text{Eq.: 3.7}$$

for T_1 and p_1, a random pair of temperature and corresponding vapour pressure must be chosen, whereas T_2 and p_2 are the saturation conditions of the flash-evaporation process.

The saturation conditions T_2 and p_2, are either fixed by the technical possibilities of the process itself or by external specifications, e.g. the saturation temperature T_S may not fall below a certain limit.

With either T_2 or p_2 given, the remaining parameter is calculated by means of the Antoine-equation:

$$\log p = A - \frac{B}{C + T} \qquad \text{Eq.: 3.8}$$

whereby, A, B and C are substance-specific dimensionless constants. Depending on the used parameter set, the temperature T and pressure p may be expressed in [°C] or [K] and [bar], [Torr] or [Pa], respectively.

The correct value for $c_{p,l}(T_0)$, if the corresponding temperature-function is not known or no charts are available, must be extrapolated from at least two known values of $c_{p,l}$. As one can see in figure 3.3, showing the temperature dependence of $c_{p,l}$ for different solvents, the increase has almost a linear behaviour, ensuring a sufficiently high accuracy.

For larger ΔT_S and especially multi-component systems, the use of an appropriate simulation software with a well equipped material database is highly recommended. In this work, the chemical engineering software SimSci Pro/II 8.1 was used for the numeric simulation of the flash-evaporation process. Besides the numeric simulation of the most common operation units of the chemical industry, SimSci Pro/II 8.1 is able to calculate the physical and thermodynamical date of numerous substances and mixtures over a large temperature and pressure range.

Today, flash-evaporation is mainly used in multi-step desalination processes of sea water [5] and for concentrating of aqueous solutions [8]. It has the advantage over conventional evapourators that its evaporation rate is independent of the heat exchange surface and significantly faster. It also has the advantage that, by knowing the thermodynamic behaviour of the used components, the process features an outstanding controllability and versatility.

3.2 Flash-crystallization process

The flash-crystallization process bases on the main principle of the flash-evaporation technique. A solution gets heated, then is exposed to a strong pressure drop and subsequently evaporates. However, the dissolved material completely crystallizes and then gets separated as a dry solid.

The large proportion of liquid that must be evaporated within a single evaporation stage is characteristic of the flash-crystallization process. The evaporation-ratio is abbreviated as X_{vap}:

$$X_{vap} = \frac{\Delta m_{flash}}{m_0} \qquad \text{Eq.: 3.9}$$

The ideal evaporation-ratio is $X_{vap} = 1$, indicating the total evaporation of the solvent. In such cases, the solvent, the solute and the installation must meet very high thermal demands. In practice, satisfying results were already attained with $X_{vap} > 0,7$.

The evaporation-ratio can also be described with thermodynamic units only by replacing Δm_{flash} from the above equation by the equation 3.3:

$$X_{vap} = (T_0 - T_S)\frac{c_{p,l}(T_0)}{\Delta_{vap}H(T_S, p_S)} \qquad \text{Eq.: 3.10}$$

As will be shown later, X_{vap}, calculated from the heat balance of the process, may also take values > 1, namely when large values for ΔT_S are chosen. In practice, such cases are relatively rare, as the used solvent must possess certain thermodynamic properties and must meet the thermal demands of the solute. Cases of $X_{vap} > 1$ are of interest as the solute gets slightly heated after crystallization, promising a lower residual moisture. To attain an almost complete evaporation, high ΔT_S in the order of about 200 °C can be necessary. As an example, using acetone as solvent that is intend to be evaporated completely at ambient pressure, the overheating temperature T_0 must be 237 °C and the pressure of at least 47 bar. At such high temperatures, the enormous thermal load may cause decomposition of the solute. This can be avoided by reducing the post-expansion pressure.

With decreasing pressure in the atomization chamber, the saturation temperature T_S decreases too. Depending on the solvent and the final pressure, temperatures below –30 °C can be easily achieved in the atomization chamber. The strong temperature drop in the order of about 200 °C has several advantages. At first, the initially strongly heated solute cools down within a fraction of a second, next, the solubility in the cool liquid decreases with the same speed.

The flash-crystallization process is well suited for the nanostructuration of organic substances being thermally stable to at least 180 °C. Because the solutions are going through extreme thermal conditions, from nearly 200 °C to –40 °C, they must comply several specific demands.

3.2.1 Particle size control

The control of the particle size plays in every crystallization process a major role. Depending on the desired properties of the final product, the corresponding crystallization process has to fulfill special requirements.

For example, the formation of highly pure single crystals without any inclusions requires a very slow crystallization process. Usually, a perfectly shaped small crystal is fixed on a support which is then placed in a saturated solution. In order that the dissolved material from the solution crystallizes on the surface of the *seed crystal*, a supersaturation of the solution is required. The supersaturation S is defined as:

$$S = \frac{c}{c_\infty} \qquad \text{Eq.: 3.11}$$

with c the actual concentration and c_∞ the solubility. As a rule of thumb, the higher the supersaturation, the faster the crystal growth, the more crystal defects are formed. Therefore, in order to form only a perfect single crystal, a low supersaturation is needed. In practice, this can be achieved by placing the saturated solution with the seed crystal in a quite place and allowing the solvent to evaporate slowly, or by slowly cooling a saturated heated solution. Both techniques can take from days to months, to obtain a single, perfectly shaped crystal.

The dominating mechanism in this example is known as *growth* mechanism. The final crystal size depends on the amount of dissolved material and the duration, the crystal is allowed to grow. In the case of spray drying, the *growth* mechanism can be considered as being droplet limited, meaning that every droplet forms exactly one particle (fig. 3.2). After the formation of a first nucleus, the remaining dissolved material crystallizes on the surface of this nucleus and the particle starts to grow. According to this simplified model, the final particle size solely depends on the volume of the droplet and the concentration of the solute.

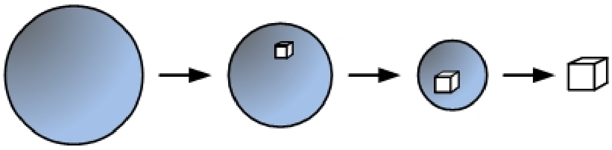

Fig.: 3.2 – Schematic of the *growth* mechanism.

To ensure that only one particle is formed per droplet, the evaporation process must happen slowly in order to create only one nucleus, on whose surface the remaining dissolved material will crystallize. Despite the simplicity of this model, the preparation of nanoparticles may be very complex and expensive, as the formation of an extremely fine spray and the use of very low concentrated solutions must be complied.

In contrast to the formation of a single perfectly shaped crystal, the formation of many, but smaller crystals is achieved by a high supersaturation. Similar to the principle of the flash-evaporation if a saturated solution suddenly becomes highly supersaturated, crystal nuclei will be formed throughout the solution. This mechanism is defined as the *nucleation* mechanism (fig. 3.3), as the final particle size in this model is significantly controlled by the degree of supersaturation and the speed with which the supersaturation is generated.

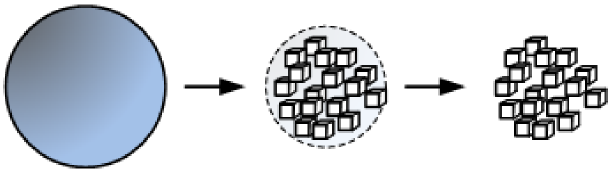

Fig.: 3.3 – Schematic of the *nucleation* mechanism.

In practice, both particle growth mechanisms co-exist whereby the nucleation mechanism is generally ought to be the predominating mechanism [9]. A schematic, combining both *nucleation* and *growth*, is depicted in figure 3.4.

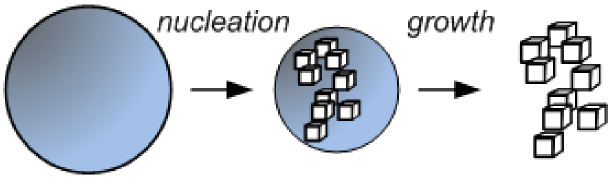

Fig.: 3.4 – Schematic of the combined *nucleation* and *growth* mechanisms.

In a system combining both particle growth mechanisms, the *nucleation* process determines the number or particles that will be formed and the subsequent *growth* mechanism defines the final particle size [9].

As the objective of this work is the large-scale production of an ultra-fine product, the *nucleation* process appears to play a key role in view of the increase of the production capacity and the decrease of the particle size.

In the following formula [10, 11], the direct relation of the critical nucleus size d_c to the degree of supersaturation S is shown:

$$d_c = \frac{4 \cdot \sigma \cdot v}{R \cdot T \cdot \ln S} \qquad \text{Eq.: 3.12}$$

with σ, the surface energy and v, the molecular volume. Due to the complexity of the nanocrystallization process, the correct determination of S is difficult, as the exact temperature, at which the formation of crystal nuclei sets in, is not known.

3.2.2 Requests to the solvent

For flash-crystallization, a potential solvent with a good solubility must also comply specific thermodynamic and physical requirements before it can be used. Because energetic materials will be used as solute, the maximum temperature is predefined by the admissible thermal load of the explosive. For this purpose, the ODTX-graphs of RDX, TNT and CL-20, shown in chapter 1, provide information about the thermal decomposition of explosives at elevated temperatures. As this work is primarily about the nanostructuration of RDX, the solvents were chosen accordingly.

On the basis of different criteria, suited solvents were selected. To keep the thermal load to the solute as low as possible, the standard boiling temperature should be between 30 and 70 °C. Lower boiling solvents are less suited as they become to laborious to handle. In addition, the solvents specific heat capacity should be as high as possible, whereas the heat of vaporization must be very low at the same time. Because of safety reasons, the solvent must be thermally stable to at least 300 °C. The properties of the solvent which were examined for being used in the flash-crystallization process are reported in table 3.1.

Solvent	T_b **[°C]**	$c_{p,l}$ (at 25°C) **[J mol^{-1} K^{-1}]**	$\Delta_{vap}H$ (at 25°C) **[kJ mol^{-1}]**	φ **[kg m^{-3}]**	η **[10^{-3} Pa s]**
Acetone	56,2	119,95	29,1 [12]	787,5	0,3
Methyl t-butyl ether (MTBE)	55,2	170,38	27,94	735,6	0,33
Ethyl acetate	77,0	163,91	31,94	894,3	0,43
Methyl acetate	56,9	132,62	30,32	928,6	0,36
Diethyl ether	34,4	161,98	26,52	708,1	0,22
Methyl formate	31,7	107,93	27,92	967,5	0,33
Propanal	48,0	122,04	28,31	792,0	0,31

Tab.: 3.1 – Selection of low-boiling solvents.

With the exception of $\Delta_{vap}H$, all values were calculated or taken from the SimSci Pro/II data base. From the variety of thermodynamic models that SimSci Pro/II offers, the Peng-Robinson model [13] was chosen for its accuracy near the critical point.

From the above listed solvents, the solubility of RDX at different temperatures is only known for acetone, diethyl ether and methyl acetate [14]. For acetone and methyl acetate, the dissolving behaviour in dependence of the temperature is shown in figure 3.5. Because of the low solubility in diethyl ether, below 100 mg per 100 g of solution, these values were not listed.

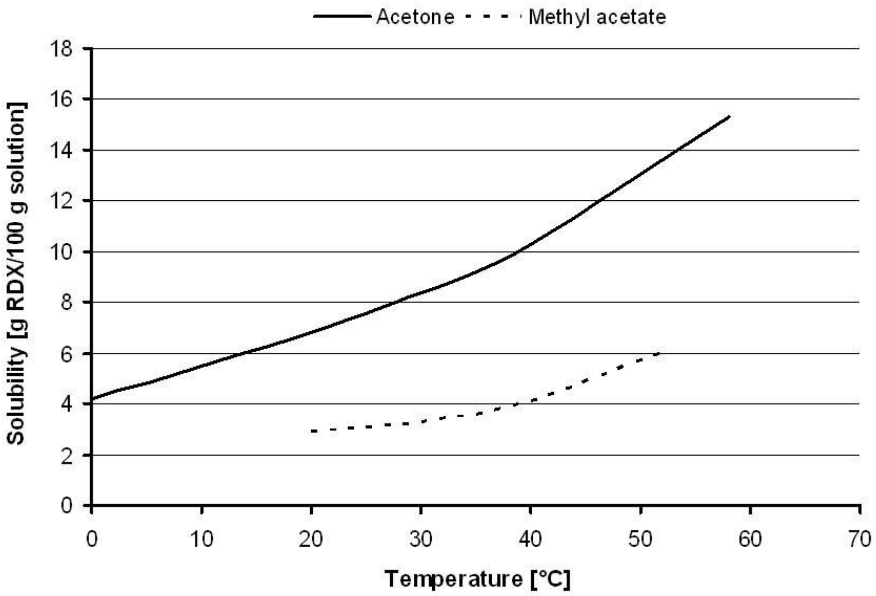

Fig.: 3.5 – Solubility of RDX in acetone and methyl acetate at different temperatures [14].

In most common solvents RDX is hardly soluble. Because of the higher solubility, acetone was chosen as the standard solvent in this work. From the above listed solvents, acetone has the highest solubility, it is inexpensive, it is thermally stable to a large extent and its low toxicity is well documented.

Figure 3.6 and 3.7 are showing the temperature dependence of $c_{p,l}$ and $\Delta_{vap}H$ in a range from -47 to 158 °C at 50 bar.

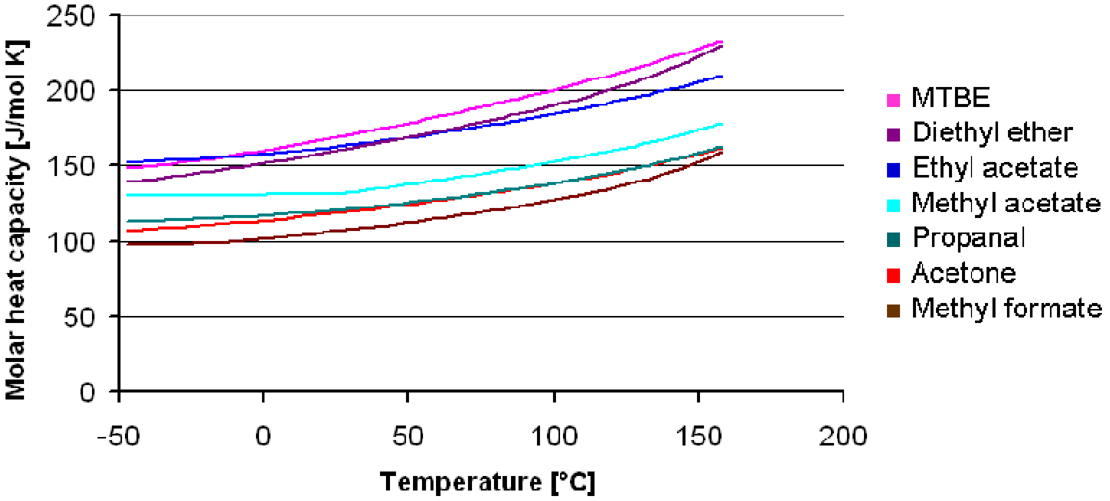

Fig.: 3.6 – Specific heat capacity $c_{p,l}$ in dependence of the temperature at 50 bar.

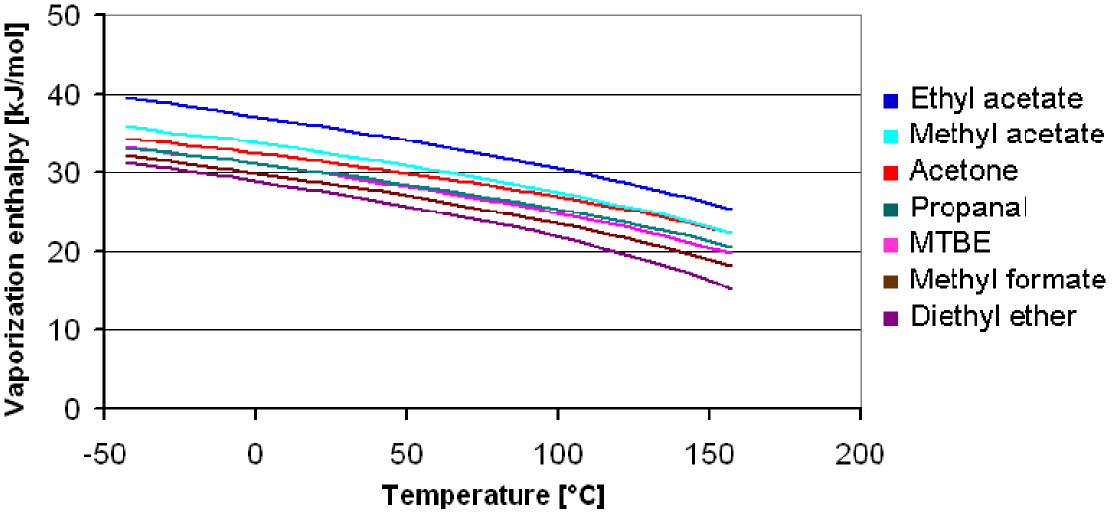

Fig.: 3.7 – Vaporization enthalpy $\Delta_{vap}H$ in dependence of the temperature at 50 bar.

The deployment of the curves in figure 3.6 and 3.7 makes clear why equation 3.3 is only sufficiently accurate for small ΔT_S. Over a temperature range of 200 °C, the vaporization enthalpy has almost halved while the specific heat capacity increased about 50 %.

According to the ODTX-diagram, RDX decomposes at 160 °C after 10^4 seconds. Therefore, the overheating temperature T_0 is set at 160 °C, representing the upper limit of the process. The lower limit of the process is defined by the post-expansion conditions, either the saturation temperature or the saturation pressure. In anticipation of chapter 3.3, the available vacuum pump represented the limiting factor in this work. Under full load, 5mbar absolute pressure was the lowest pressure that could be kept constant.

In the following table (tab. 3.2), using the afore mentioned upper and lower limits of the process, the saturation temperature T_S, the degree of superheating ΔT_S and the evaporation-ratio X_{vap} were calculated, using SimSci Pro/II.

Solvent	T_0 **[°C]**	T_S (5 mbar) **[°C]**	ΔT_S **[°C]**	X_{vap}	T_{crit} **[°C]**	P_{crit} **[bar]**
Acetone	160	-45,3	205,3	0,801	235,05	47,01
Methyl t-butyl ether	160 **127**	11,2 -48,0	171,2 175,0	1,000 0,999	223,95	34,3
Ethyl acetate	160	-27,2	187,2	0,893	250,15	38,8
Methyl acetate	160	-42,1	202,1	0,843	233,4	47,5
Diethyl ether	160 **121**	15,9 -60,4	175,9 181,4	1,000 0,999	193,55	36,4
Methyl formate	160	-60,3	220,3	0,828	214,05	60,0
Propanal	160	-50,7	210,7	0,875	231,25	49,2

Tab.: 3.2 – Calculation of the evaporation ratio.

It is striking that with most solvents evaporation-ratios in-between 80 and 90 % were attained, requiring degrees of superheating of more than 200 °C. However with both ethers a complete evaporation can already be reached at noticeably lower temperatures. Referring to the figures 3.6 and 3.7, both ethers have the highest specific heat capacity and the lowest vaporization enthalpy at the same time. This thermodynamic property predestines the ethers for use in the flash-crystallization process.

The annex of chapter 3 contains detailed tables with the temperature dependent properties of the studied solvents in-between -50 to 200 °C, being calculated with SimSci Pro/II.

3.3 Description of the installation

A process flow chart of the flash-crystallization process is shown in figure 3.8.

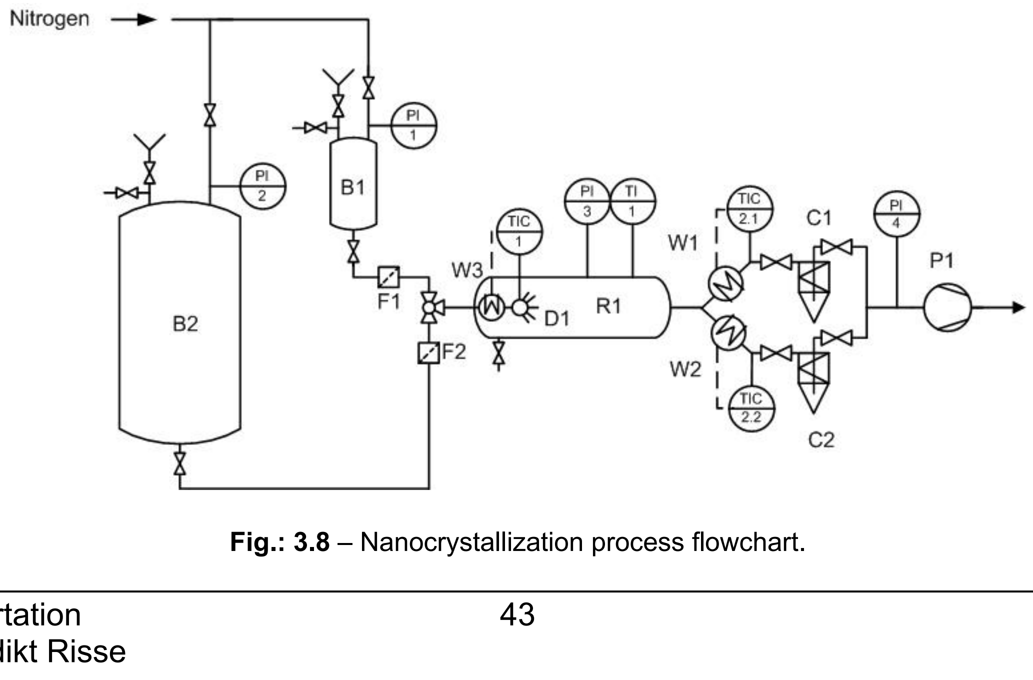

Fig.: 3.8 – Nanocrystallization process flowchart.

The installation is divided into two sections, called the high-pressure and the low-pressure section.

The high-pressure section comprises the containers B1 and B2, each equipped with an inline filter F1 and F2 that are connected via a three-way valve with the heated nozzle D1. The nozzle, which is installed in the atomization chamber, represents the transition from the high-pressure to the low-pressure section. The low-pressure section starts directly after the nozzle, comprising the atomization chamber R1, two heatable axial cyclones C1 and C2 and the vacuum pump P1. In table 3.3, the single components are described in detail:

Part	**Description**
B1	High-pressure container, 1 L, max. pressure 100 bar
B2	High-pressure container, 5 L, max. pressure 40 bar
C1/C2	Axial cyclone units
D1	Hollow cone nozzle, dia. 60; 80 and 100 µm
F1/F2	Filter 10 µm
P1	Vacuum pump, flow rate 35 m^3/h, 500 r.p.m
R1	Atomization chamber, d_i = 100 mm, length = 400 mm
W1/W2	External cyclone heating, 150 W
W3	Nozzle heating sleeve, 150 W
PI	Pressure reading
TI	Temperature display
TIC	Temperature regulation and display

Tab.: 3.3 – Components of the flash-crystallization installation.

During operation, one of the containers is filled with the explosive-solution while the other is filled with pure solvent. By means of compressed nitrogen, fed from a gas cylinder that is not shown in figure 3.8, both containers are set under pressure. Nozzles with orifices of 60, 80 and 100 µm can be used in this process. Because of the small orifice, the nozzles are prone to clogging. For this reason, the outlets of B1 and B2 are equipped with inline filters with 10 µm mesh size. By means of a three-way valve, both containers are connected with the nozzle, enabling a faster change between solvent and solution. During the warm-up phase, the cyclones and the nozzle are heated to their final temperature while the vacuum pump is running. As soon as the target temperatures are attained, the solvent feed to the nozzle is opened causing the nozzle temperature to drop about 20 to 30 °C. With the solvent feed, the pressure in the atomization chamber climbs to a few millibar. As soon as the nozzle has regained its target temperature, the solution feed to the nozzle is opened, initializing the crystallization process. The cyclones are operated in an alternating mode. While the gas flow passes one cyclone, the other cyclone is in a stand-by mode. During the crystallization process, switching between the cyclones and removal of the product enables a continuous production. The particle-free gas flow leaves the cyclones and passes the vacuum pump. The high operating temperature of the vacuum pump excludes the condensation of the solvent.

The operating conditions such as nozzle temperature T_0, saturation temperature T_S, pre-expansion pressure p_0 and the saturation pressure p_S are continuously monitored.

3.3.1 Hollow cone nozzle

The hollow cone nozzle belongs to the category of single component pressure nozzles, taking the energy that is needed for the atomization directly from the pressurized liquid. Within the group of pressure nozzles, the hollow cone nozzle creates the finest spray pattern. The characteristic spray cone of the hollow cone nozzle is generated by forcing the fluid into a rotary movement along its longitudinal axis. The rotary movement of the liquid can be generated by the tangential supply of the liquid or by means of interior constructions deflecting the stream (fig. 3.9).

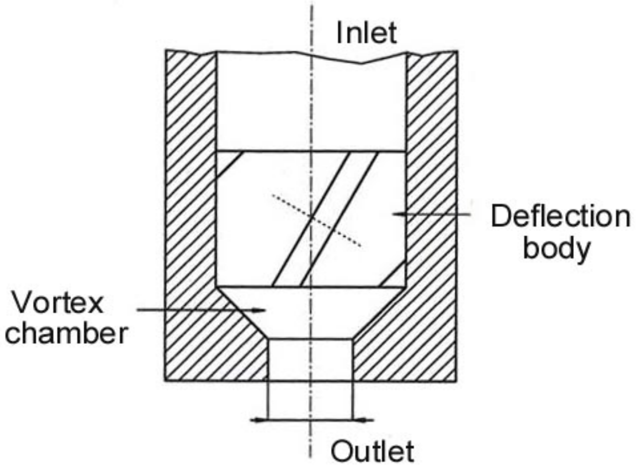

Fig.: 3.9 – Axial hollow cone nozzle with deflection body [15].

The liquid, passing the interior construction, gets deflected where a radial momentum acts on it. Due to the rotary movement of the fluid, the liquid is pressed against the inner nozzle wall prior its atomization, allowing the formation of an air core in the centre of the orifice [16]. After the liquid has left the nozzle, the radial momentum causes the liquid to diverge, forming a hollow cone which can have various forms (fig. 3.10).

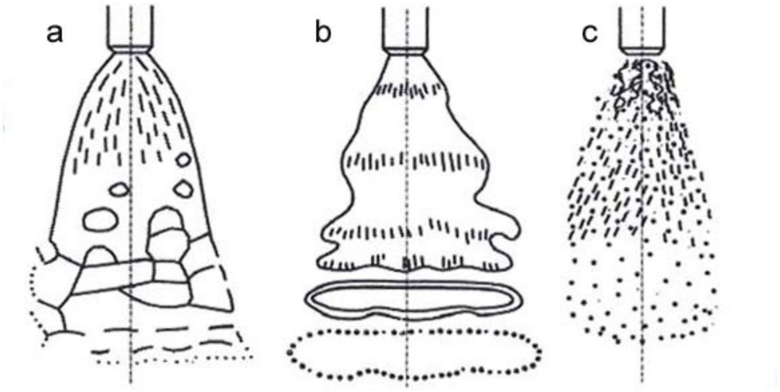

Fig.: 3.10 – Hollow cone forms [15]: (a) edge-bead contraction, (b) aerodynamic wave disintegration and (c) turbulent lamella disintegration.

Depending on the operating conditions, the droplet formation mechanism may vary between edge-bead contraction, aerodynamic wave disintegration or turbulent lamella disintegration.

Edge-bead contraction usually happens at low flow velocities where the liquid forms a stable lamella. With increasing distance from the nozzle, the surface of the lamella continuously increases while the film thickness diminishes. At a certain distance the lamella becomes unstable. Due to the liquid's surface tension, the lamella disintegrates, forming relatively large droplets.

Aerodynamic wave disintegration happens at higher flow velocities. A stable lamella is formed that interacts with the gaseous atmosphere. The lamella forms waves which, at a certain film thickness, disintegrate into rings first and then into droplets with defined size.

The turbulent lamella disintegration is characterized by high Weber numbers. The Weber number gives information about the fluid's inertia in relation to its surface tension. A high Weber number indicates a heavy deviation from the ideal spherical droplet shape. The dimensionless Weber number is calculated after:

$$We = \frac{\rho \cdot v^2 \cdot l}{\sigma} \qquad \text{Eq.: 3.13}$$

with ρ the liquid density, v the velocity, l the characteristic length, which is in this case the droplet diameter, and σ the surface tension. Also characteristic for the turbulent lamella disintegration is the rapid droplet formation, occurring very close to the nozzles orifice.

Independent from the droplet formation mechanism, the maximum attainable volume flow $\dot{V}$ is calculated as follows:

$$\dot{V}_{\max} = \frac{\pi \times d^2}{4} \times \sqrt{\frac{2 \times \Delta p}{\rho}} \qquad \text{Eq.: 3.14}$$

with d the diameter, ρ the liquid density and Δp the pressure difference in front of and behind the nozzle. Friction forces, occurring at high Reynolds numbers between the fluid and the wall, decrease the maximum attainable volume flow. By means of the dimensionless flow index μ, describing the ratio between the real and the theoretical volume flow whereby $\mu = 1$ indicates the ideal case of a frictionless flow, different nozzle types and operating conditions can be compared with each other:

$$\mu = \frac{\dot{\mathrm{V}}_{\mathrm{Re}\,al}}{\dot{\mathrm{V}}_{theo}} = \frac{4 \times \dot{\mathrm{V}}_{\mathrm{Re}\,al}}{\pi \times D^2 \times \sqrt{\frac{2 \times \Delta p}{\rho}}} \qquad \text{Eq.: 3.15}$$

In this work, hollow cone nozzles with different nozzle diameter from the Austrian company Plantfog were used (fig. 3.11). Nozzles with D = 60, 80 and 100 µm diameter were tested. According to the manufacturer, the channel length L is 300 µm for all nozzle types.

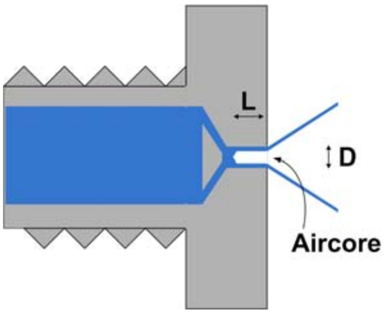

Fig.: 3.11 – Design of the hollow cone nozzle.

The rotary movement of the liquid around its longitudinal axis in the orifice is achieved by the tangential feed of the liquid, by means of two small channels.

The ratio L/D is of importance, as long nozzle channels may generate excessive pressure drops, causing the premature evaporation already inside of the nozzle.

According to Günther [17], this phenomenon may already appear at L/D ratios between 3 and 12 (fig. 3.12).

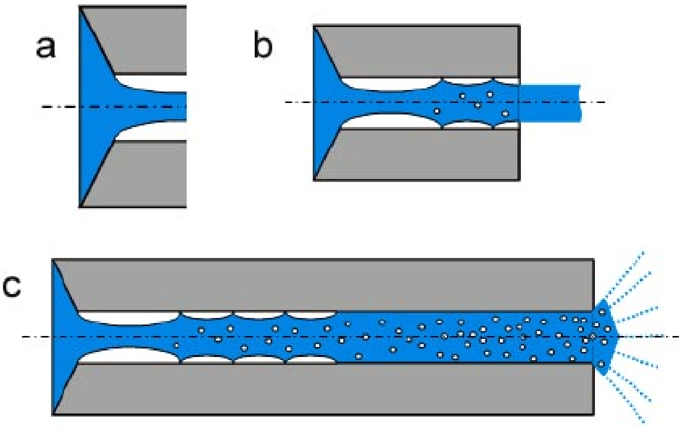

Fig.: 3.12 – Flow behaviour in dependence of the length to diameter ratio: **a)** L/D ≈ 3, **b)** L/D up to 12 and **c)** L/D > 12 [17].

The case a) L/D ≈ 3 represents the ideal case, where the liquid leaves the nozzle without evaporation happening. In the cases b) and c), partial evaporation already happens inside of the nozzle. With regard to the flash-crystallization process, the premature evaporation is unwanted as the crystallizing product could block the nozzle.

According to Richter [15], the L/D ratio also gives information about the flow index μ. For nozzles with sharp opening at large Reynolds numbers, the following relation exists (tab. 3.4):

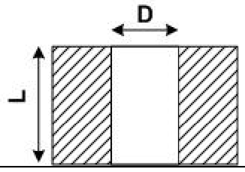	$0{,}6 \le \mu \le 0{,}65$	$0{,}75 \le \mu \le 0{,}85$	$\mu \approx 0{,}62$
	$0{,}5 \le L/D \le 1$	$2 \le L/D \le 5$	$L/D = 5$

Tab.: 3.4 – Prediction of the flow index μ in dependence of L/D [15].

In the following (tab. 3.5), the maximum volume flow $\dot{V}$ was calculated for the three available hollow cone nozzles using a Δp = 40 bar and ρ = 790 kg/m³.

	60 µm	80 µm	100 µm
Ratio: L/D	5	3,75	3
Max. volume flow [mL/min]	17,07	30,34	47,42

Tab.: 3.5 – Maximum volume flow, calculated for nozzles with 60, 80 and 100 µm opening.

Up to present, an exact numerical method to predict the droplet size of hollow cone nozzles does not exist. In the literature mostly empiric formulas for specific applications can be found. An overview of the different existing models and their drawbacks is given in the work of Lefebvre [18].

3.3.2 Cyclone system

The separation of ultra-fine particles, without destroying them, is one of the major challenges in this large scale production process. The cyclone system used in this work is composed of two identical axial cyclones that are arranged in parallel to each other. Characteristic for these types of cyclones, are the axial inlet and outlet and a turbine-like vane, directing the gas flow into a rotary movement (fig. 3.13).

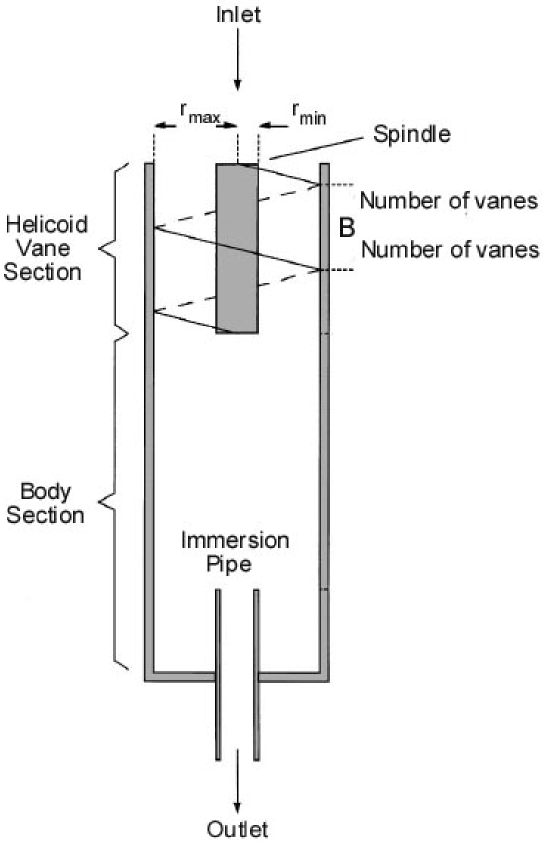

Fig.: 3.13 - Schematic of an axial cyclone [19].

The incoming dust-loaded gas flow hits the vane where it gets deflected and accelerated by following the winding. Due to the rotary movement, centrifugal forces F_c act on the gas flow and the particles:

$$F_c = m \cdot \omega^2 \cdot r \qquad \text{Eq.: 3.16}$$

with m the mass, ω the angular velocity and r the radius of the circular path. Because the centrifugal force is proportional to the mass, the centrifugal forces acting on the solid particles are significantly larger.

Various authors [20, 21, 22, 23] reported about the decreasing cut-off diameter in cyclones, occurring with decreasing operating pressure.

With decreasing operating pressure and with it the number of gas molecules in the cyclone, the interactions between the crystallized particles and the surrounding fluid diminish. With less interactions occurring between the ultra-fine particles and the gas molecules, the particles can move freely inside of the cyclone, where the centrifugal forces are acting on them. This relation is known as Stokes' law, describing the drag force F_{drag} acting on small spherical particles moving in a continuous fluid at low Reynolds-numbers:

$$F_{drag} = 3 \cdot \pi \cdot \eta_L \cdot d \cdot v_{rel} \qquad \text{Eq.: 3.17}$$

with η_L, the dynamic viscosity of the surrounding fluid and v_{rel}, the relative speed between the particles and the environment.

Because of the low operating pressure and the expected small particles, one may reach the limit of the continuum mechanics. This happens when the mean free path and the particle size are of the same order. In such cases, the Stokes' law must be extended by the dimensionless Cunningham correction factor Cu:

$$F_{drag} = \frac{3 \cdot \pi \cdot \eta_L \cdot d \cdot v_{rel}}{Cu} \qquad \text{Eq.: 3.18}$$

Under normal conditions, particle motion in a continuous fluid is dominated by collisions between adjacent particles. Small particles in a low pressure environment have fewer collisions with other molecules, resulting in a faster movement. This effect is respected by the Cunningham correction factor:

$$Cu = 1 + \frac{2\lambda}{d}\left(1{,}257 + 0{,}4e^{\frac{-0{,}55d}{\lambda}}\right) \qquad \text{Eq.: 3.19}$$

with λ the mean free path and d the particle diameter. The mean free path is calculated after:

$$\lambda = \frac{k \cdot T}{\pi \cdot d \cdot p \cdot \sqrt{2}} \qquad \text{Eq.: 3.20}$$

with k the Boltzmann constant.

The Knudsen number indicates if the process must be treated as a molecular or a continuous flow:

$$Kn = \frac{2\lambda}{d} \qquad \text{Eq.: 3.21}$$

For Knudsen numbers < 0,01, especially in rough vacuum between 10^3 and 10^0 mbar, the laws of continuum mechanics can be applied. The region between 0,01 < Kn < 0,5, representing the transition region from continuum mechanics to the molecular regime, is called Knudsen regime. The Knudsen regime mainly occurs in fine vacuum in a pressure range between 10^0 - 10^{-3} mbar. The molecular regime is indicated by Kn > 0,5, appearing in high vacuum at pressures below 10^{-3} mbar.

An axial cyclone, capable of separating nanoparticles in vacuum, was developed by Chien *et al.*[24] (fig. 3.14).

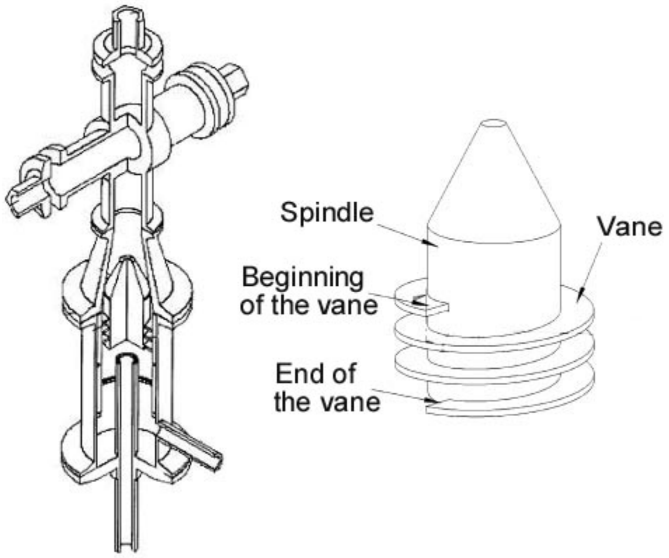

Fig.: 3. 14 – Axial cyclone in assembled state [24, 20].

According to the authors [24], the aerodynamic cut-off diameter d_{pa50} of the said axial cyclone can be calculated after:

$$d_{pa50} = 0{,}106\left(\frac{P_{cyc}}{P_{760}}\right)^2 \frac{\mu\left(r_{\max}{}^2 - r_{\min}{}^2\right)^2 \cdot \left(B - N\omega\right)}{\rho_{po}\cdot n\cdot\xi\cdot Q_0\cdot r_{\min}{}^2\cdot N^2\cdot\lambda_0} \qquad \text{Eq.: 3.22}$$

with P_{cyc} the average pressure in the cyclone [Torr], P_{760} equal 760 Torr, μ the dynamic viscosity [Ns/m²], $r_{\max}$ the inner radius of the cyclone, $r_{\min}$ the radius of the spindle, B the pitch of vanes [m], N the number of vanes, ω the vane thickness [m], ρ_{Po} the unit density [1000 kg/m³], $n\xi$ the number of turns a particle makes in the cyclone whereby the value 1,5 was chosen for ξ, Q_0 the standard volumetric flow rate [m³/s] and λ_0 the mean free path under standard conditions [m].

Hsu *et al.*[25] found out that, operating the axial cyclone from fig. 3.14 in vacuum, two separation mechanisms coexist: diffusion and centrifugal separation. Assuming that laminar flow is present, the diffusion controlled separation is the dominating mechanism for particles smaller than 40 nm. The cut-off diameter in a diffusion dominated separation can be calculated after:

$$d_{pa50,diff} = \frac{4\cdot n\cdot\xi\cdot k\cdot T\cdot Cu}{3\cdot Q_0\cdot\mu\cdot\ln 2} \qquad \text{Eq.: 3.23}$$

For particles bigger than 40 nm in diameter and with laminar flow assumed, the cut-off diameter is calculated after:

$$d_{pa50} = \sqrt{\frac{9 \cdot \mu \left(r_{\max}{}^{2} - r_{\min}{}^{2} \right)^{2} (B - N\omega)^{2} \ln 2}{8\pi \cdot n \cdot \xi \cdot Q_{0} \cdot r_{\min}{}^{2} \cdot N^{2} \cdot B \cdot C}} \qquad \text{Eq.: 3.24}$$

To avoid clogging of the cyclone body, deposition is ought to happen after the particles have passed the cyclone. For this purpose, an immersion pipe, as shown in figure 3.13 and 3.14, is serving as outlet, creating a rest area around the pipe where the particles can deposit.

The cyclone design proposed by Chien and Maynard [24, 19] is not suited for a continuous operation. To facilitate the product removal, the immersion pipe was relocated about 180° (fig. 3.15). The body section of the cyclone forms a glass cover, hold in place by a quick release fastener. The cyclone spindle can be moved vertically, allowing too vary the number of vanes.

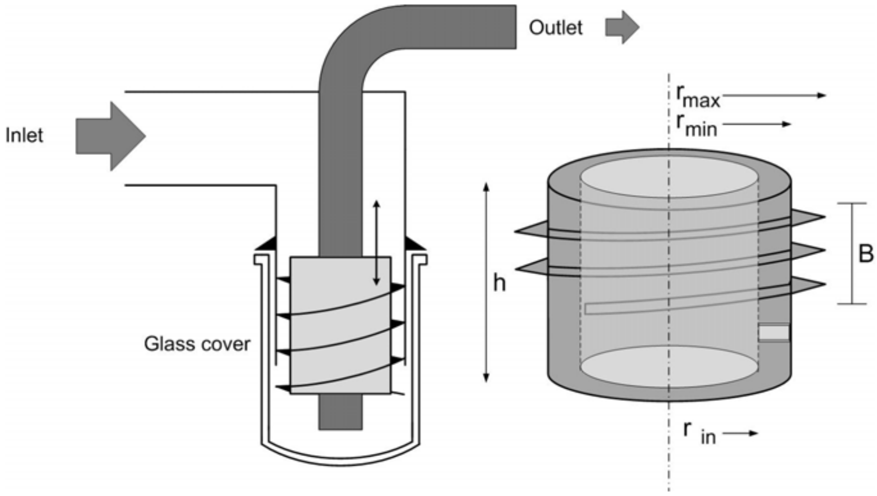

Fig.: 3.15 – For continuous production improved cyclone design.

The relevant dimensions of the improved cyclone are listed in table 3.6:

Index	Dimension
r_{in}	14 mm
r_{max}	28,5 mm
r_{min}	17 mm
B	21 mm
N	3
h	50 mm
ω	2 mm

Tab.: 3.6 – Cyclone dimensions.

3.3.3 Fluid mechanics

This chapter deals with the flow-related conditions in the high-pressure and the low-pressure section. As the pressure in the atomization chamber and the cyclone will not drop below 10^0 mbar, the process can be treated with the laws of continuum mechanics.

The median retention time t_m, describes the period during which the explosive-solution is superheated. As the high temperatures may decompose the dissolved explosive, the solution should not be heated for a too long time. The median retention time is calculated by the nozzle volume and the volume flow rate:

$$t_m = \frac{V}{\dot{V}} \qquad \text{Eq.: 3.25}$$

with V, the heated volume and $\dot{V}$, the volume flow rate. To ensure a gentle production, the heated volume should be as small as possible. This is attained by attaching the heating jacket directly to the nozzle as shown in figure 3.16.

Fig.: 3.16 – Nozzle assembly with 60 µm nozzle, thermocouple and heating jacket.

The total volume enclosed by this construction is only 1,7 mL. The lowest volume flow, using a 60 µm nozzle at 40 bar, varies between 9,5 and 10,5 mL/min, resulting in a median retention time between 9,7 and 10,7 s.

With such a short retention time in the heated nozzle, decomposition of the dissolved explosive is very unlikely even at higher temperatures.

The dimensionless Reynolds number, already mentioned in relation to the hollow cone nozzles, acts as an indicator for laminar or turbulent flow. Heat and material transmission processes differ greatly if laminar or turbulent flow is present. The Reynolds number Re is calculated after:

$$\mathrm{Re} = \frac{v \cdot l_c}{\upsilon} \qquad \text{Eq.: 3.26}$$

with the velocity v, the characteristic length l_c and the kinetic viscosity υ. For tube flow, the characteristic length l_c is equal to the inner diameter of the tube. Empirically determined for tube flow, a Reynolds number below 2200 or 2300 indicates a laminar flow and above a turbulent flow regime.

To determine the flow regime in the atomization chamber and the cyclone, the gas volume, created by the flash-evaporation, must be calculated at first. Assuming that the gas behaves as an ideal gas and that the gas temperature immediately rises to 0 °C after atomization, the gas volume can be calculated with the ideal gas equation:

$$p \cdot V_g = n \cdot R \cdot T \qquad \text{Eq.: 3.27}$$

by replacing $n = \frac{m}{M}$ and $m = \rho_l \cdot V_l$, the equation transforms to:

$$V_g = \frac{V_l \cdot \rho_l \cdot R \cdot T}{M \cdot p} \qquad \text{Eq.: 3.28}$$

Because the volume V_l will be replaced by the liquid flow rate, the resulting V_g is also a volume flow. By knowing the cross-sectional area of the tube, the corresponding flow velocity v can be easily calculated:

$$v = \frac{\dot{V}}{A} \qquad \text{Eq.: 3.29}$$

The correct gas viscosity of the evaporated solvent must be calculated or can be taken from the literature. In nomograms, such as the nomogram proposed by Perry [26], the gas viscosity in dependence of the temperature of numerous solvents can be read of (fig. 3.17). To use the nomogram, the substance specific X and Y coordinates of the gas in question must be located, then a straight line, originating from the searched temperature and crossing the X-Y coordinate, must be drawn to obtain the viscosity in the Poise unit.

The X/Y-coordinates for acetone are: X = 8,4 ; Y = 13,2. The pressure dependence of the viscosity must not taken into consideration as the viscosity over a pressure range from 0,01 to 20 bar is almost constant.

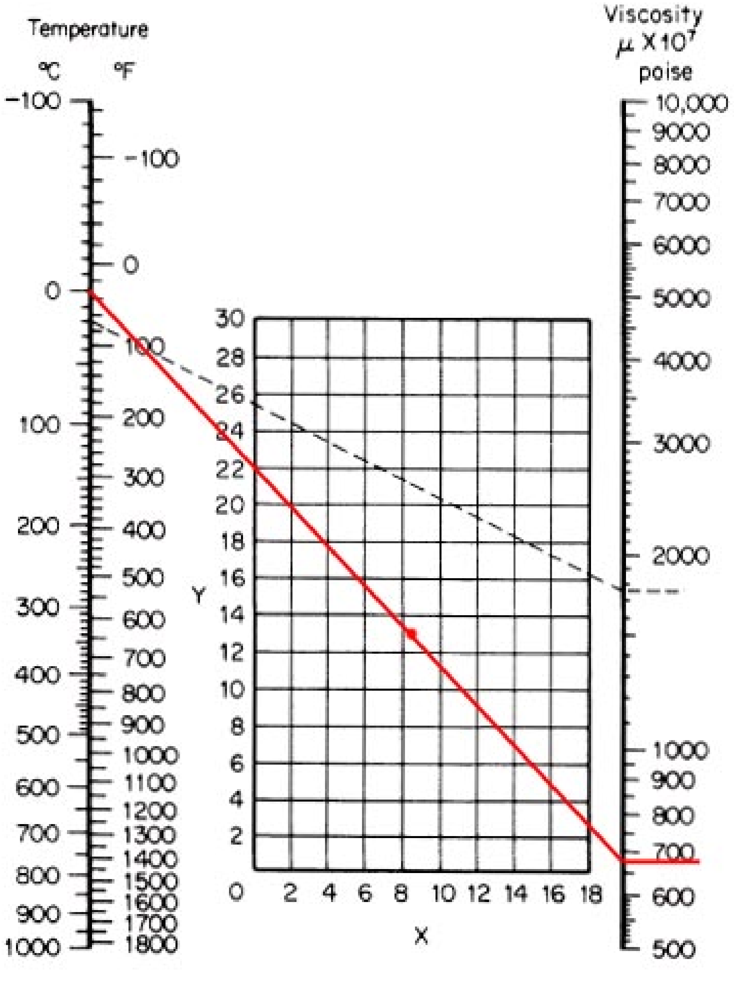

Fig.: 3.14 – Nomogram: Determination of the dynamic viscosity of gases in dependence of the temperature [26]. Red line corresponds to acetone.

As an example, the Reynolds numbers inside of the atomization chamber and the cyclone are calculated for an experiment which has been performed several times.

Conditions: Acetone, heated to 160 °C, is atomized by means of a 60 µm hollow cone nozzle with an overpressure of 40 bar. Under these conditions, the volume flow rate varied between 9,5 and 10,5 mL/min and the pressure on the suction side of the vacuum pump, measuring point PI-4, rose to 4 - 5 mbar. For simplification, a constant volume flow of 10 mL/min and a pressure of 5 mbar were used in the following calculation. Despite the temperature in the spray cone dropped to –30 °C, a gas temperature of 0 °C was used in the calculations instead. An explanation for this will follow in this chapter.

Calculation of the gas flow rate:

$$\dot{V} = V_g = \frac{V_l \cdot \rho_l \cdot R \cdot T}{M \cdot p} = \frac{10 \cdot 10^{-6} m^3 \cdot 790 kg \cdot 8{,}314 J \cdot 273 K \cdot mol}{m^3 \cdot \min \cdot mol \cdot K \cdot 58 \cdot 10^{-3} kg \cdot 500 Pa} = 0{,}618 \frac{m^3}{\min} \approx 37 \frac{m^3}{h}$$

Referring to table 3.3, the maximum flow rate of the vacuum pump is only 35 m³/h. The deviation of about 2 m³/h originates from the higher gas temperature and the higher pressure that were used for the calculation.

The velocity inside must be calculated for the atomization chamber and the cyclone separately. The calculation of the referring cross-section and flow velocity are shown below (tab. 3.7).

Atomization chamber	Axial cyclone
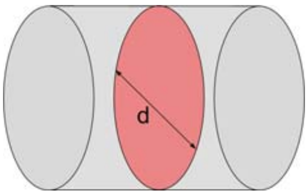	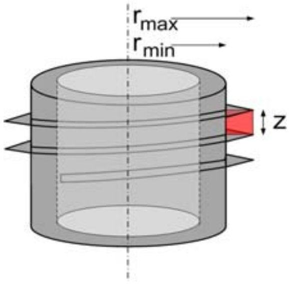
$A = \frac{d^2}{4} \cdot \pi$	with $z = \frac{B - N \cdot \omega}{N}$ $A = \left(r_{\max} - r_{\min}\right) \times z$
$A = 7{,}85 \cdot 10^{-3} m^2$	$A = 5{,}75 \cdot 10^{-5} m^2$
$v = \frac{\dot{V}}{A} = 4713{,}3 \frac{m}{h} = 1{,}3 \frac{m}{s}$	$v = \frac{\dot{V}}{A} = 643 \frac{km}{h} = 178 \frac{m}{s}$

Tab.: 3.7 – Calculation of the velocity in the atomization chamber and the axial cyclone.

The viscosity of the acetone vapour at 0 °C was red off from figure 3.14. The dynamic viscosity of the acetone vapour at 0 °C is approximately $675 \cdot 10^{-7} P$. The conversion factor from Poise P to SI-units is: $1\ P = 0{,}1\ Pa\ s$.

Because the kinetic viscosity ν is required, the dynamic viscosity η must be transformed accordingly:

$$\nu = \frac{\eta}{\rho} \qquad \text{Eq.: 3.30}$$

Assuming that the acetone vapour behaves as an ideal gas, its density can be calculated by transposing the ideal gas equation to:

$$\rho = \frac{m}{V} = \frac{M \cdot p}{R \cdot T} \qquad \text{Eq.: 3.31}$$

The kinetic viscosity of acetone vapour at 0 °C at 5 mbar is: $5{,}28 \cdot 10^{-4} \frac{m^2}{s}$.

To calculate the Reynolds number, the characteristic length l_c had to be determined. For circular pipes, such as the atomization chamber, the characteristic length is equal to the inner diameter. However, the inside of the cyclone has a rectangular flow cross-section (tab. 3.7). For all types of channels and pipes differing from the circular profile, the hydraulic diameter d_h must be used as characteristic length. The hydraulic diameter is defined by the ratio between the cross-section area A and the wetted perimeter U_b:

$$d_h = \frac{4A}{U_b} \qquad \text{Eq.: 3.32}$$

With the knowledge of the characteristic length for the atomization chamber and the cyclone, the Reynolds-number was calculated.

Atomization chamber, with $\dot{V} = 37\ m^3 h^{-1}$: $\mathrm{Re}_{Atom} = 246{,}2$

Axial cyclone, with $l_c = d_h = 9{,}96\ mm$ and $\dot{V} = 37\ m^3 h^{-1}$: $\mathrm{Re}_{Cyclone} = 2346{,}3$

The low Reynolds number for the atomization chamber indicates a laminar profile, whereas the high Reynolds number in the cyclone indicates a turbulent flow. Because the boundary between laminar and turbulent flow can not be clearly defined by a single Reynolds number, it is more likely that an intermediate flow profile prevails in the cyclone.

Because in vacuum technology the maximum attainable differential pressure can not exceed 1 bar, the pipe flow coefficient L_{Rl} must be taken into consideration during the planning stage. The pipe flow coefficient defines the maximum possible volume flow through a pipeline for a given operating pressure:

$$L_{Rl} = \frac{\pi \cdot d^4}{128 \cdot \eta \cdot l} \frac{(p_1 + p_2)}{2} = \frac{\pi \cdot d^4}{128 \cdot \eta \cdot l} \bar{p} \qquad \text{Eq.: 3.33}$$

As can be seen from this formula, the flow coefficient strongly depends on the tube diameter. Even a stronger vacuum pump could not increase the volume flow if the diameter is too small.

In this work, the cross-section of the cyclone represents the bottle-neck. Using the hydraulic diameter d_h, the median operating pressure $\bar{p} = p_S =$ 5 mbar, the gas viscosity at 0 °C and the following channel length l:

$$l = 2 \cdot \left(\frac{r_{\max} + r_{\min}}{2} \right) \cdot N \cdot \pi \qquad \text{Eq.: 3.34}$$

gives: $L_{Rl} = 9{,}96 \cdot 10^{-3} m^3 s^{-1} = 35{,}88\, m^3 h^{-1}$, showing us that the vacuum pump with its nominal volume flow rate of 35 m³/h, defines the saturation pressure in the installation. A higher volume flow rate at the same pressure is not possible, even with a stronger vacuum pump.

3.3.4 Heat supply by the environment

Assuming that the atomization chamber represents a closed system in a stationary state, one would assume that the mass and energy leaving the system is equal to the mass and energy entering the system. With regard to the mass, this statement is true but with regard to the energy, a deviation from the theory can be observed. Figure 3.18 shows a simplified version of the atomization chamber, with $\dot{Q}$ indicating the corresponding heat flows.

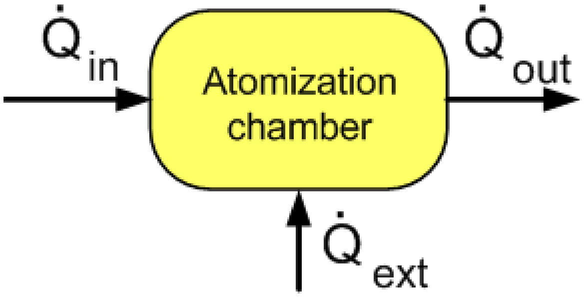

Fig.: 3.18 – Heat flows of the atomization chamber.

A heat balance of the atomization chamber looks as follows: $\dot{Q}_{out} = \dot{Q}_{in} + \dot{Q}_{ext}$.

$\dot{Q}_{in}$ represents the known heat flow accompanying the atomized solution, whereas $\dot{Q}_{ext}$ represents the heat flow originating from the environment.

Because of the strong temperature drop in the atomization chamber, the installation cools down and a temperature gradient between the atomization chamber and the environment arises. This heat flow may represent an energy source that can be important in an up-scaled version of the process. It also explains why earlier in this chapter a higher temperature was chosen for the calculation of the Reynolds number.

The heat flow $\dot{Q}$, traversing the atomization chamber, is calculated as follows:

$$\dot{Q} = \frac{\lambda_L \cdot 2\pi \cdot l \cdot (T_2 - T_1)}{\ln \frac{r_2}{r_1}} \qquad \text{Eq.: 3.35}$$

with the thermal conductivity λ, the inner and outer radius of the chamber r_1 and r_2 as well as the temperature inside and outside of the chamber wall T_1 and T_2. The value for the thermal conductivity must be taken from the literature. By attaching one thermocouple on the outside and the other one on the inside of the atomization chamber, the heat flow $\dot{Q}$ traversing the atomization chamber can be calculated. As the temperature of the aerosol in the atomization chamber is not throughout constant, the total heat flow must be integrated over the whole length of the atomization chamber, making numerous measurements necessary.

An easier method to determine the total heat flow, is to measure only the temperature difference ΔT between the centre of the spray cone and the end of the atomization chamber:

$$\dot{Q} = c_{p,gas} \cdot \dot{m}_{gas} \cdot \Delta T \qquad \text{Eq.: 3.36}$$

with $c_{p,gas}$ the specific heat capacity of the gas at constant pressure, $\dot{m}$ the mass flow rate and ΔT the temperature difference between.

The knowledge of $\dot{Q}_{ext}$ may be important in larger plants, as the additional energy could cause an overheating of the vacuum pump.

Summary of the chapter

The flash-evaporation process differs from other evaporation techniques by its high evaporation speed, which is independent of the size of the heat exchange surface. The flash-evaporation process uses a pressurized solvent that is heated above its normal boiling temperature. If the superheated solvent is exposed to a strong pressure drop an adiabatic evaporation process starts. The excess of thermal energy converts within the fraction of a second to latent heat. Even at low degrees of superheating, the evaporation speed is higher than with conventional processes.

In contrast to industrial flash-evaporation processes, solely used for increasing the concentration of solutions, the whole solvent gets removed in the flash-crystallization process. Within a single evaporation stage, the evaporation ratio must be > 70 %. Such high evaporation rates are only accessible by strong superheating. To reduce the thermal load acting on the solvent and the dissolved material, the thermodynamic properties of different solvents were examined. It was found that solvents with a low vaporization enthalpy but a high specific heat capacity at the same time are best suited for this process. Diethyl ether and methyl tert-butyl ether possess such high specific heat capacities, that they could serve as thermal storage in binary solvents. Due to its good solubility for RDX, its thermal stability and low toxicity, acetone will be used as the standard solvent in this work.

The flash-crystallization installation consists of a high-pressure and a low-pressure part. The high-pressure section is made of two storage tanks for storing the explosive-solution and a heated nozzle by which the solution gets superheated and atomized. The nozzle joins into the atomization chamber which is already a part of the low pressure-section. The low pressure-section also includes two axial cyclones and the vacuum pump.

With high pressure, the superheated solvent is atomized into the evacuated atomization chamber where the solvent instantaneously evaporates and cools down.

The removal of the solvent and the great temperature drop induce the crystallization of the dissolved explosive. The particle loaded gas flow is directed through the axial cyclone where the solid components are separated. Operating cyclones at reduced pressure is advantageous as it lowers the cut-off diameter. Using two cyclones in parallel, a continuous operation of the process is achieved.

References

[1] El-Fiqi, A.; Ali, N.; El-Dessouky, H.; Fath, H.; El-Hefni, M.; *Desalination*, 206, **2007**, pp. 311-321.
[2] Owen, I.; Jalil, J.; *Int. J. Multiphase Flow*, 17 (5), **1991**, pp. 653-660.
[3] Sher, E.; Bar-Kohany, T.; Rashkovan, A.; *Prog. Energy Combust. Sci.,* 34, **2008**, pp. 417-439.
[4] Simoes-Moreira, J.; Vieira, M.; Angelo, E.; *J. Thermophys. Heat Transfer*, 16 (3), **2002**, pp. 415-424.
[5] Mutair, S.; Ikegami, Y. ; *International Journal of Mathematical, Physical and Engineering Sciences,* 4, **2010**.
[6] Vieira, M.; Simoes-Moreira, J.; *J.Fluid Mech.,* 572, **2007**, pp. 121-144.
[7] Lienhard, J.; Day, J.; *ASME Jl. Bas. Engng,* **1970**, pp. 515-522.
[8] Kaiser, R.; Flash-Kristallisation; Ein neues Verfahren zur Produktgestaltung kristalliner Güter, **2009**, Universitätsverlag Karlsruhe.
[9] Paul, E.; Tung, H.; Midler, M.; *Powder Technol.,* 150, **2005**, pp. 133-143.
[10] Mullin, J.;Crystallization, 4th Ed, **2004,** Elsevier Butterworth- Heinemann.
[11] Larson, M.; Garside, J.; *Chem. Eng. Sci.,* 41 (5), **1986**, pp. 1285-1289.
[12] Majer, V.; Svoboda, V., Enthalpies of Vaporization of Organic Compounds: A Critical Review and Data Compilation, Blackwell Scientific Publications, Oxford, **1985**, 300.
[13] Peng, D.; Robinson, D.; *Ind. Eng. Chem. Fundam.*, 15 (1), **1976**, pp. 59-64.
[14] Fedoroff, B.; Sheffield, O.; *Encyclopedia of explosives and related items*, **1966**, Vol. 3, Picatinny Arsenal, New Jersey, USA.
[15] Richter, T.; Zerstäuben von Flüssigkeiten, 2. Auflage, **2008**, Expert Verlag.
[16] Piesche, M.; Nonnenmacher, S.; *Chem. Ing. Tech.*, 71 (7), **1999**, pp. 688-692.
[17] Günther, A.; Rossmeissl, M.; Wirth, K.; *ILASS-Europe 2010, 23rd Annual Conference on Liquid Atomization and Spray Systems*, Brno, Czech Republic, September **2010.**
[18] Lefebvre, A.; *Part. Part. Syst. Charact*., 6, **1989**, pp. 176-186.
[19] Maynard, A.; *J. Aerosol Sci.,* 31 (2), **2000**, pp. 151-167.
[20] Tsai, C.; Chen, S.; Przekop, R.; Moskal, A.; *Environ. Sci. Technol.,* 41, **2007**, pp. 1689-1695.
[21] Chen, S.; Tsai, C.; *J. Nanopart. Res*., 9, **2007**, pp. 71-83.
[22] Paglianti, A.; Brunazzi, E.; Talamelli, A.; *AlChE J.*, 49 (1), **2003**, pp. 41-51.
[23] Ober, F.; Mayer, M.; Büttner, H.; *Chem. Ing. Tech*., 75 (5), **2003**, pp. 568-572.
[24] Chien, H.; Hsu, Y.; Tsai, C.; US 6,969,420 B2, Nov. 29, **2005**.
[25] Hsu, Y.; Chein, H.; Chen, T.; Tsai, C.; *Environ. Sci. Technol*., 39, **2005**, pp. 1299-1308.
[26] Perry, R.; Perry's Chemical engineers' handbook, 7th edition, **1997**, McGraw-Hill.

4 Nanocrystallization of RDX

Even though the developed process is suited for numerous energetic materials, the parametric study in this chapter was solely performed on RDX. In contrast to CL-20, forming four stable crystalline modifications, RDX only forms two crystal modifications at room temperature, from which one is so unstable that it transforms into the stable allotrope after a short period [1, 2].

Serving as a reference, one experiment was defined as standard with which the experiments from the parametric study were compared. The experiments of this parametric study have been performed three times for reasons of reproducibility. In every of the three runs per experiment, the preparation of approximately one gram of nanocrystallized product was carried out.

Each product was characterized by DSC, BET and XRD. Furthermore, selected samples were characterized by SEM and Raman spectroscopy.

Standard experiment conditions:

The conditions of the standard experiment are listed in the table below (tab. 4.1).

Nozzle [µm]	**Temperature**		**Solvent v/v [Acetone/MTBE]**	**Pressure [bar]**	**RDX-Conc. [%-wt]**
	Nozzle [°C]	**Cyclone [°C]**			
60	160	80	100/0	40	1,0

Tab.: 4.1 – Experimental conditions of the standard experiment.

1 litre of a 1 %-wt RDX-acetone solution was filled in the small reservoir. The larger reservoir was filled with pure acetone. To both reservoirs an over-pressure of 40 bar was applied, using compressed nitrogen. For atomization, a 60 µm hollow cone nozzle was used. The nozzle temperature was set to 160 °C. The saturation pressure T_S in the installation was limited by the flow rate of the solution and the used vacuum pump. The cyclone intakes were both heated to 80 °C and the cyclones were used in an alternating mode.

Taking the process into operation in a safe and trouble-free manner requires a special procedure. During the heat-up phase, the pressure in the section, enclosed by the 3-way valve and the nozzle, is the same as in the atomization chamber. After reaching the target temperature, opening the valve with the RDX solution could

cause a premature crystallization of the explosive, risking clogging the nozzle. Therefore, the said section must be purged with pure solvent at first. Immediately after opening the valve, the temperature in the spray cone drops to approximately -30 °C and the pressure in the atomization chamber rises to 5 mbar absolute. The temperature inside of the nozzle also drops about 20 °C. After the nozzle has regained its target temperature, the intake flow is switched to the RDX-acetone solution. This point indicates the beginning of the nanocrystallization process.
First visible deposits in the glass cover of the cyclone can be observed a few seconds later. With the before mentioned operating conditions, the flow rate accounts approximately 10 mL/min. The atomization chamber is equipped with two sight glasses, allowing the permanent observation of the crystallization process. Quite distinctive is the broad spray cone, first occurring when the nozzle temperature is higher than the corresponding boiling temperature of the solvent. Due to the almost 180° wide spray cone, noticeable amounts of the crystallized explosive were thrown against the inner wall of the atomization chamber. Even though a similar but less intense behaviour was already observed in preliminary experiments, it turned out that the inner diameter was still too small.

The installation pressure was measured behind the cyclones near the suction side of the vacuum pump. Measuring the pressure directly at the atomization chamber had to be excluded, as the high particle loading can easily damage the sensing element. However, both cyclones and the atomization chamber were equipped with Bourdon-tube pressure gauges, only showing an approximate value, but resisting the rough conditions. The pressure measured near the suction side also served as indicator for a clogged cyclone.

With increasing amount of deposited material, the flow resistance of the cyclone increased and the pressure at the suction side dropped, indicating the moment to change the cyclone. Thereto, the second cyclone had to be taken into operation at first, and only then the active cyclone could be isolated by closing the inlet and outlet valve. After aerating the isolated cyclone, the glass cover could be removed and the product could be recovered. Subsequently the emptied cyclone was put together and evacuated again. After approximately one gram of product had been collected, the crystallization process was stopped by rinsing the nozzle with pure solvent and allowing it to cool down.

Before the process was started again for a second or third run, the nozzle had to be removed and cleaned before. It was found that after stopping the process, the nozzle was slightly clogged afterwards. To ensure constant conditions, the nozzle had to be removed and purged in counter current flow with a few millilitres of acetone and water.

Evaluation of the results:

The spray time and product mass from the three runs of the standard experiment are listed in table 4.2.

Standard experiment	Forerun time [min]	Spray time [min]	Mass [g]	Mass flow [mg min^{-1}]
Run # 1	0	30	1,0216	34,05
Run # 2	2	30	1,0859	36,19
Run # 3	1	29	1,1171	38,52

Tab.: 4.2 – Spray time and collected mass from standard experiment.

In this experiment a total amount of 3,22 g of nanocrystallized RDX was collected, corresponding to a mass yield of 40,75 %. The forerun time was necessary to ensure an unchanged quality. Product collected during the forerun time was discarded. The total spray time during the standard experiment amounted 92 minutes, resulting in a median flow rate of 10,86 mL/min.

Due to the intense spray cone broadening, large amounts of the nanocrystallized product deposited at the inside of the atomization chamber. After the experiment, the whole installation, except for the tube section between the cyclone outlet and the vacuum pump, was rinsed with acetone. The acetone with the dissolved RDX was collected and subsequently evaporated. The remaining RDX was weighed and examined for purity by means of nuclear magnetic resonance (NMR) analysis. It was found that less than 1 % of the initial amount of RDX had passed the cyclone without getting separated. Particles that have passed the cyclone may get caught by a baffle plate at the suction side of the vacuum pump; otherwise they are caught by the oil of the vacuum pump.

The collected RDX from all three runs was analysed using differential scanning calorimetry (DSC), X-ray diffraction (XRD) and measurement of the specific surface (BET). The product was also examined with a scanning electron microscope (SEM) in order to determine the particle size and PSD. For the DSC measurements, gold-plated crucibles were filled with about 1 – 3 mg of the nanocrystallized product and were then sealed with a gold-plated lid. The RDX sample was measured against an empty, also hermetically sealed, gold-plated crucible. Both crucibles were heated from 25 °C to 400 °C with a heating rate of 5 °C/min. During the measurement, a slight nitrogen flow of 10 mL/min was flowing over the crucibles. From run # 1 of the standard experiment, the corresponding DSC thermogram is shown in figure 4.1. The melting temperature and the subsequent decomposition of the nanocrystallized RDX are represented as endothermic and exothermic peaks in the thermogram.

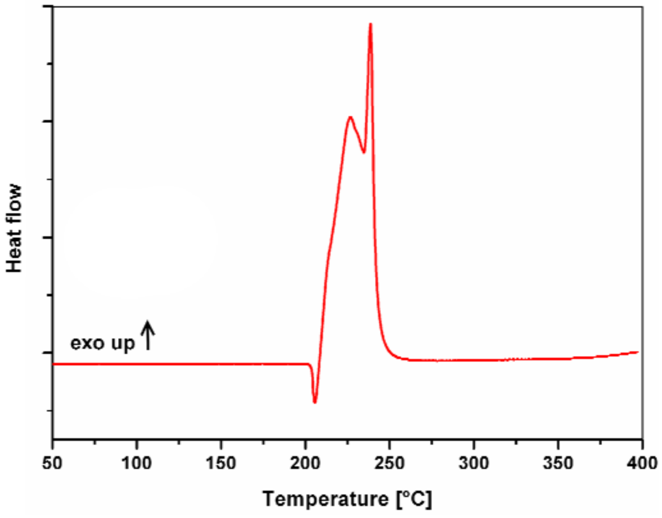

Fig.: 4.1 – DSC curve of nanocrystallized RDX from the standard experiment run # 1.

The thermograms of the other two runs look very similar which is why they will not be presented here. The melting temperatures of the individual RDX samples are: run # 1 205,04; run # 2 205,98 and run # 3 205,64 °C.

The product from run # 2 was examined with a SEM (fig. 4.2). The sample was prepared by spreading the tip of a spatula of the product onto adhesive tape, glued onto a sample carrier. Subsequently, the sample was sputtered with an approximately 5 nm thick layer of platinum. Within a 10 µm circular area, the size of each particle was measured and a Gaussian distribution was generated.

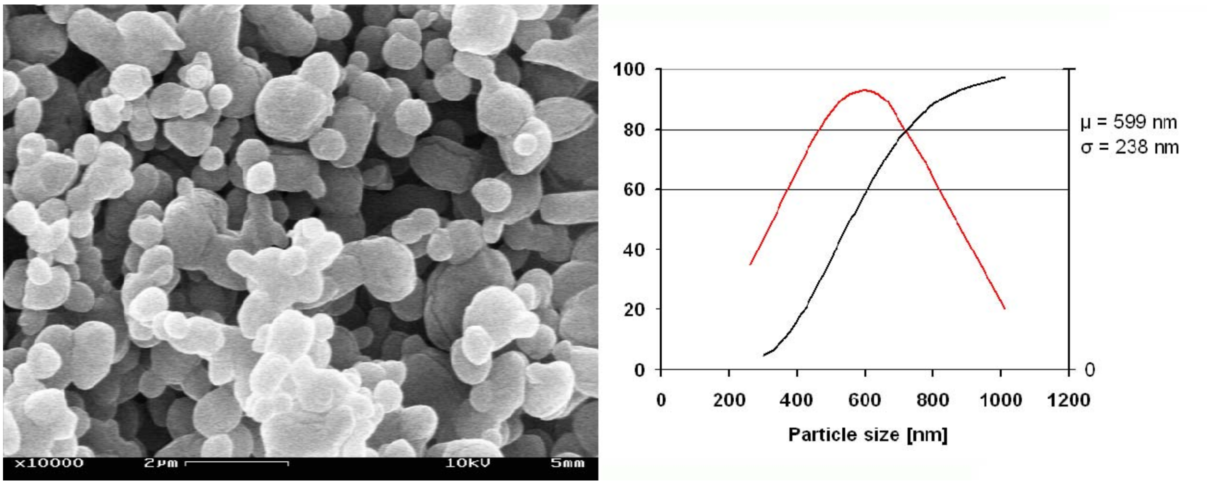

Fig.: 4.2 – SEM image and PSD of nanocrystallized RDX from the standard experiment.

As can be seen from figure 4.2, the prevailing shape of the particles is spherical, allowing the use of equation 2.3 to calculate the median particle diameter from its specific surface. The median particle size, indicated as μ, is 599 nm with a variance σ of 238 nm. From every sample the specific surface was measured by the BET method, after the samples were degassed for 1 hour at 80 °C under vacuum. The results are listed below (tab. 4.).

Standard experiment	**Sample weight [g]**	**Mass loss [%-wt]**	S_{BET} **[m^2 g^{-1}]**	LC **[Å]**
Run # 1	1,007	1,06	3,33	620,1
Run # 2	1,059	0,97	3,76	599,8
Run # 3	1,097	0,92	3,32	638,5

Tab.: 4.3 - Specific surface and median particle diameter of nanocrystallized RDX from the standard experiment.

Crystallinity of the product was verified by XRD. From the diffraction pattern (fig. 4.3), the crystallite size LC was calculated after the Scherrer equation.

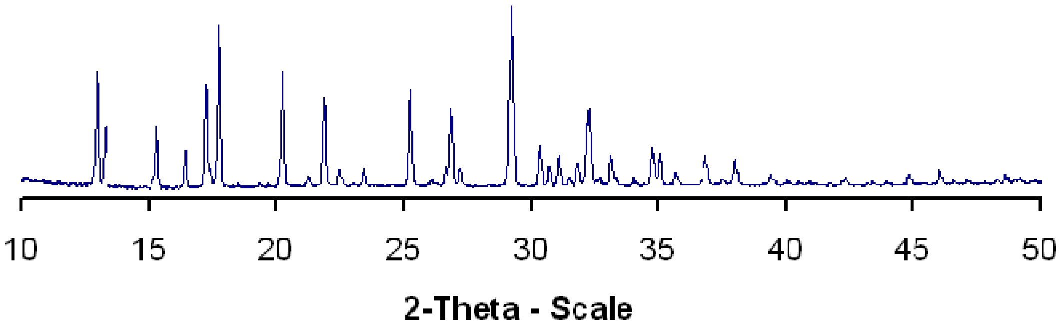

Fig.: 4.3 – Diffraction pattern of nanocrystallized RDX.

The results of the standard experiment have shown that submicron particles in the order of 600 nm can already be formed by this process, but individual microparticles were still present. In view of decreasing the particle size and obtaining a narrower particle size distribution, the optimal process conditions will be searched as part of a parameter study. The studied parameters will also be evaluated by process relevant criteria.

4.1 Optimization of the crystallization parameters

Particle properties, such as particle size, structure or PSD can be controlled, in a broad range, by only a few process parameters. In order to evaluate the influence and the importance of the individual parameters, a parametric study on the following five process parameters was performed:

- Nozzle temperature
- Nozzle pressure
- Type of solvent
- Nozzle diameter
- RDX-concentration

For reasons of reproducibility, each experiment was performed three times, indicated as run # 1, run # 2 and run # 3. Per run, about 1 g of material was prepared, being sufficient for the envisaged analyses.

4.1.1 Variation of the nozzle temperature

As known from equation 3.3, the overheating temperature T_0 is of great importance for the flash-crystallization process, as it directly controls the amount of evaporating solvent Δm_{flash}. With increasing overheating temperature, the evaporation ratio X_{vap} rises and the flash-evaporation happens more violently. It is assumed that the large particle size distribution from the standard experiment was caused by a partial evaporation of the solvent. While the major part of the solvent in the standard experiment, $X_{vap} = 0{,}8$, was instantaneously evaporated as a consequence of the flash-evaporation effect, the remaining droplets may have promoted the formation of the larger particles. Because of the high thermal load, acting on the solvent, the solute and the installation, the maximum overheating temperature was limited in this parametric study to 180 °C. According to the ODTX-diagram of RDX, the explosive first decomposes after 700 s at 180 °C. Therefore, the decomposition of the explosive during normal operation does not occur.

The process parameters of the first part of the parametric study are listed below (tab. 4.4).

Nozzle [µm]	**Temperature**		**Solvent v/v [Acetone/MTBE]**	**Pressure [bar]**	**RDX-Conc. [%-wt]**
	Nozzle [°C]	**Cyclone [°C]**			
60	150/ 160/ 170/ 180	80	100/0	40	1,0

Tab.: 4.4 – Process parameters: Variation of the nozzle temperature.

In order to study the influence of the temperature on the particle properties four experiments at different nozzle temperatures were performed. The nozzle temperature in these experiments was set to 150, 160, 170 and 180 °C, respectively.

4.1.2 Variation of the nozzle pressure

From practice it is known that the droplet size of a pressure nozzle decreases with increasing pressure. Unfortunately, this effect fades at higher pressures [3], so that after exceeding a certain threshold pressure, the droplet size only marginally decreases. However, increasing the nozzle pressure increases the flow rate, which is why hollow cone nozzles can be operated at various flow rates, while the spray quality remains constant.

According to the manufacturer [4], the 60 µm nozzles should be operated at 100 bar. As the standard experiment was performed at 40 bar, working at lower pressures does not seem reasonable. For this reason, only experiments with increasing nozzle pressure were performed. The different nozzle pressures that were studied in this parametric study were 40, 50, 60 and 70 bar. As the volume flow rate rises simultaneously with the pressure, the cyclones were heated up to 100 °C in the experiments performed at 60 and 70 bar, respectively. The remaining process parameters of this part of the study are listed below (tab. 4.5).

Nozzle [µm]	**Temperature**		**Solvent v/v [Acetone/MTBE]**	**Pressure [bar]**	**RDX-Conc. [%-wt]**
	Nozzle [°C]	**Cyclone [°C]**			
60	160	80 and 100	100/0	40/50/60/70	1,0

Tab.: 4.5 – Process parameters: Variation of the nozzle pressure.

4.1.3 Variation of the solvent

The influence of the solvent on the flash-crystallization process was earlier discussed in chapter 3. The term solvent may not be the adequate choice in this context, as the thermodynamic properties of the liquid are as important as its dissolving power.

In table 3.2, seven different solvents with promising thermodynamic properties examined for the flash-crystallization process. As the relevant thermodynamic properties of the different solvents strongly differ among themselves, the evaporation ratio X_{vap} was used in order to compare the solvents with each other.

Referring to the evaporation ratio, acetone is the thermodynamically least suited solvent for the flash-evaporation process, whereas the two ethers from the list have extraordinary thermodynamic properties. Using the ethers would allow working at considerably lower temperatures. Because of the high risk outgoing from diethyl ether, in particular its high flammability and the formation of explosive peroxides, its use had to be ruled out.

As it turned out, RDX is almost insoluble in pure MTBE, which is why MTBE could only be used in combination with a co-solvent, having a high affinity for RDX and being soluble in MTBE. Furthermore, the boiling point of the searched solvent should be in the same order as the boiling point of MTBE, preventing the enrichment of the lower boiling component in the gaseous phase.

From the solvents listed in table 3.2, only acetone and methyl acetate fulfilled those demands. Because of the more narrow boiling temperature, the higher solubility for RDX and the better availability acetone was chosen as co-solvent for this purpose.

Due to the favourable thermodynamic properties of MTBE, its addition to acetone increases the evaporation ratio but decreases the solubility at the same time. In table 4.6, the solubility of the different acetone/MTBE mixtures is listed, as well as their boiling temperature at 5 mbar absolute.

Acetone/MTBE v/v	T_b (5 mbar) **[°C]**	c_∞ (at 25°C) **[g RDX / 100 mL of solution]**
100/0	-45,34	5,37
90/10	-45,74	4,98
80/20	-46,18	4,08
70/30	-46,66	3,34
60/40	-47,17	2,5

Tab.: 4.6 – Solubility of RDX in the studied acetone/MTBE mixtures.

The remaining process parameters of this study are listed in table 4.7, which remained unchanged during the study.

Nozzle [µm]	**Temperature**		**Solvent v/v [Acetone/MTBE]**	**Pressure [bar]**	**RDX-Conc. [%-wt]**
	Nozzle [°C]	**Cyclone [°C]**			
60	160	80	variable	40	1,0

Tab.: 4.7 – Process parameters: Variation of the solvent.

4.1.4 Variation of the nozzle diameter

In this work only hollow cone nozzles were used for the atomization of the superheated solutions. From the group of pressure nozzles, hollow cone nozzles are capable to create the finest droplets. Besides the generation of fine droplets, this type of nozzle may prevent or reduce the coalescence of particles, as the ejection of the droplets happens in a hollow cone profile. Three hollow cone nozzles, all manufactured by the Austrian Plantfog company [4] but with different nozzle diameters were tested in this work. Nozzles with diameters of: 60, 80 and 100 µm were available. According to Lefebvre [5], the lamella thickness, and with it the droplet size, decreases with decreasing nozzle diameter. Moreover, the smallest nozzles create the lowest flow rate what is advantageous in view of the crystallization conditions

On the other side, small nozzles are prone for clogging and require higher pressures to operate flawlessly. As the standard experiment was already performed with the 60 µm nozzle, it is assumed that the particle size increases and the product might get moister with the larger nozzles.

Except for the nozzle diameter, the remaining process parameters were kept constant during this parametric study (tab. 4.8). It must be emphasised that in this part of the parametric study the RDX concentration was lowered to 0,7 %-wt. This change was made to avoid clogging of the cyclones because of the increasing RDX mass flow, accompanying the larger nozzles.

Nozzle [µm]	**Temperature**		**Solvent v/v [Acetone/MTBE]**	**Pressure [bar]**	**RDX-Conc. [%-wt]**
	Nozzle [°C]	**Cyclone [°C]**			
60/80/100	160	80	100/0	40	0,7

Tab.: 4.8 –Process parameters: Variation of the nozzle size.

4.1.5 Variation of the RDX concentration

The RDX concentration in the solvent plays a major role in view of the particle size and on the economy of the process. Because the flash-crystallization process bases on the technique of classic spray drying, it is assumed that the particle size decreases with decreasing concentration. As the standard experiment was already performed with a solution containing just 1 %-wt RDX, only little room downwards was left.

Because of the generally low solubility of RDX in acetone, only solutions containing 0,5; 0,7; 1,0; 1,5 and 2,0 %-RDX were tested. The remaining process parameters are listed below (tab. 4.9)

Nozzle [µm]	**Temperature**		**Solvent v/v [Acetone/MTBE]**	**Pressure [bar]**	**RDX-Conc. [%-wt]**
	Nozzle [°C]	**Cyclone [°C]**			
60	160	80	100/0	40	0,5/0,7/1,0/1,5/2,0

Tab.: 4.9 – Process parameters: Variation of the RDX concentration.

4.2 Results of the parametric study

In the evaluation of this parameter study, the focus was primary placed on the particle size and the PSD. Furthermore, process relevant aspects such as: production rate, product yield, process stability and product quality were additionally taken into consideration.

4.2.1 The influence of the nozzle temperature

According to Owen and Jalil [6], the flashing behaviour gets more intense with increasing overheating temperature. Higher temperatures are insomuch advantageous as the evaporation ratio increases while, at the same time, the density, the surface tension and the dynamic viscosity of the solvent decrease (tab. 4.10).

T_0 **[°C]**	X_{vap}	ρ **[kg m^{-3}]**	σ **[dyn cm^{-1}]**	η **[10^{-3} Pa s]**	c_∞ *(extrapolated)* **[g RDX / 100g solution]**
150	0,755	632,6	8,339	0,135	117,6
160	0,803	616,1	7,246	0,129	146,7
170	0,851	598,8	6,170	0,123	183,0
180	0,903	580,5	5,114	0,118	228,2

Tab.: 4.10 – Physical properties in dependence of the superheating temperature.

The solubility parameters of RDX in table 4.11 were extrapolated, by using the available solubility data [7] between 0 and 58 °C to develop an empiric relation. With the empiric relation $y = 4{,}3025\ e^{0{,}0217x}$, the solubility of RDX was calculated from -40 °C to 180 °C (fig. 4.4). According to Mullin [8], the extrapolation of the solubility curve is inadvisable. However, as the practical measurement of the RDX solubility at 180 °C appears to be quite difficult and risky, the same applies to -40 °C, it seems more reasonable working with extrapolated values.

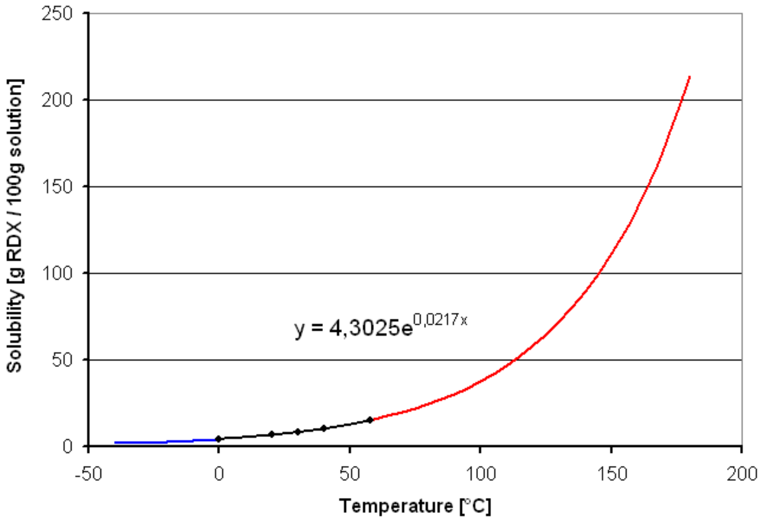

Fig.: 4.4 – Solubility of RDX in acetone extrapolated to temperatures from –40 to 180 °C.

At this point of the parametric study, the increasing solubility is not of great importance, but it points out a way to obtain high concentrated solutions in order to increase the production capacity.

From the collected product the BET surface was measured. The individual measuring points were plotted against the overheating temperature (fig. 4.5). The black curve represents the course of the median BET surface and, referring to a secondary Y-axis, the blue curve shows the course of the mass flow rate.

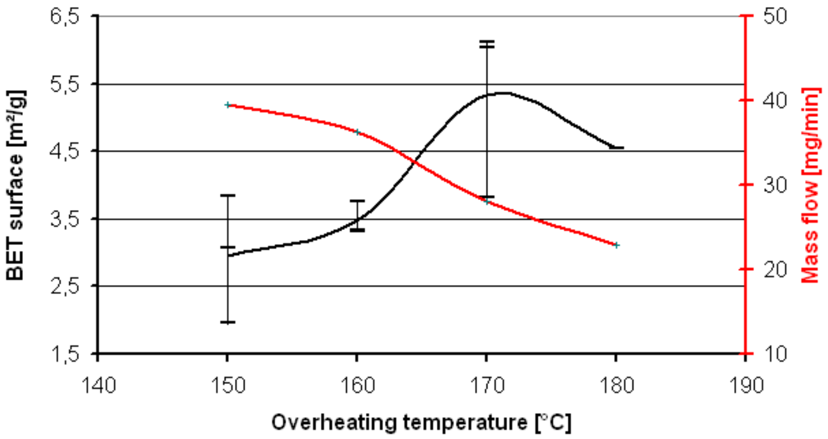

Fig.: 4.5 – BET surface (black) and mass flow rate (blue) in dependence of the overheating temperature.

With increasing temperature the evaporation ratio, an indicator of the evaporation intensity, increased. As shown in table 4.10, even at 180 °C an entirely flash-evaporation was not attained with pure acetone, however the course of the BET curve clearly indicates a trend towards higher BET values with increasing evaporation ratio. Only one run was performed at 180 °C, as the mass flow rate noticeably dropped and the heating jacket tended to overheat the nozzle.

The formation of small particles is also promoted by the decreasing surface tension and viscosity of the solvent, both important factors in the formation of small droplets. The lower surface tension is also advantageous for the initiation of the flash-evaporation process, as the critical diameter of the bubble nucleus decreases.

In figure 4.5, an important dispersion of the individual measured BET values could be observed. During this study it was found that the BET surface of nanocrystallized RDX decreased after several days. Therefore it was inevitable measuring the BET surface directly after the preparation, in order to prevent measurement errors.

An unwanted side effect was observed with regard to the mass flow rate. As already mentioned earlier, a noticeably part of the crystallized material deposits in the atomization chamber as a consequence of the spray cone broadening (fig. 4.6).

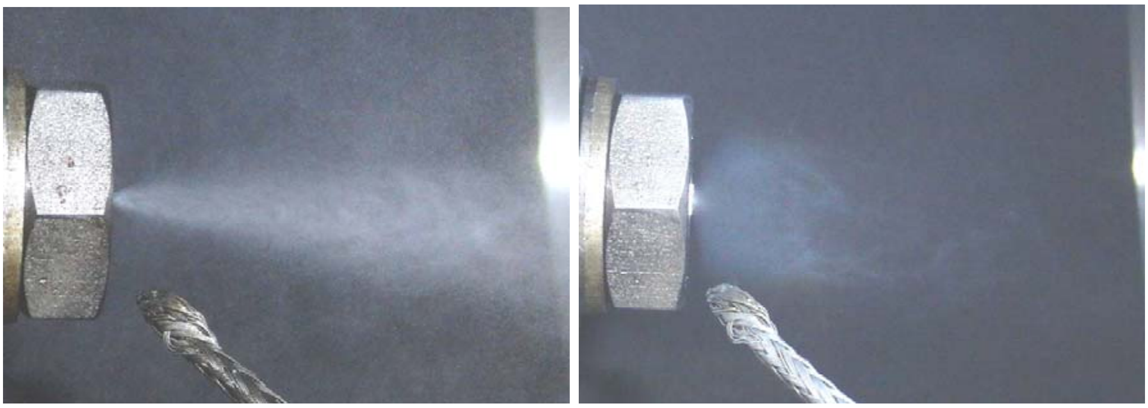

Fig.: 4.6 – Spray cone profiles: (left) normal spray cone with acetone at room temperature, (right) broadened spray cone during flash-evaporation.

A soon as the spray temperature exceeds the boiling temperature of the solvent, the spray cone widens noticeably. It is assumed that, by atomizing a superheated liquid with a hollow cone nozzle, the classic droplet formation mechanism is no longer valid. Instead, it is more likely that gas bubbles, formed within the liquid, tear apart the surrounding liquid. As the evaporating solvent occupies a lot of space, the surrounding droplets get deflected in their trajectory, causing the broadening of the spray cone. As the evaporation sets in earlier with higher temperatures, the spray cone gets blunter and more product deposits in the atomization chamber.

In figure 4.7, the melting points and crystallite sizes of the individual RDX samples were plotted against the corresponding overheating temperatures. It appears that with increasing overheating temperature, the melting point of the nanocrystallized RDX slowly decreased.

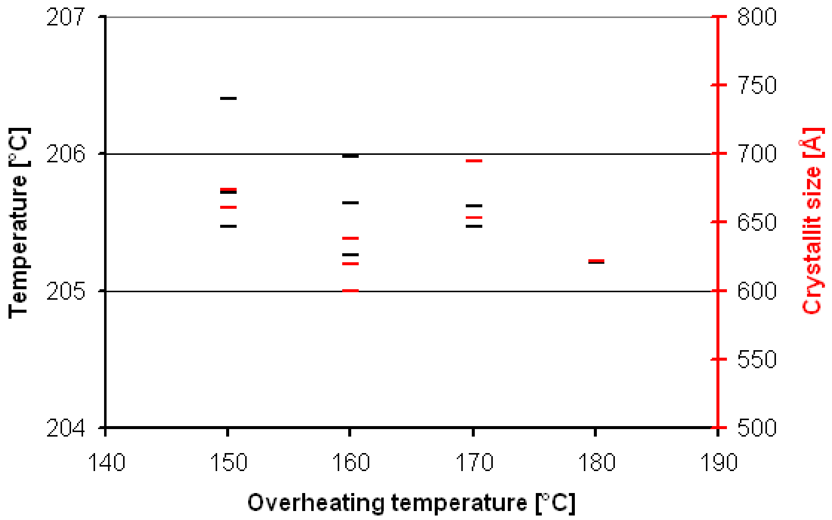

Fig.: 4.7 – Melting point (black) and crystallite size (blue) of RDX prepared at different overheating temperatures.

In contrast to the decreasing particle size, the crystallite size, measured by XRD, remained relatively constant in the order of about 600 to 700 Å. As the prevailing structure of the particles is spherical, equation 2.3 could be used to calculate the median particle diameter from the BET surface (tab. 4.11).

Nozzle temperature [°C]	Run	S_{BET} [$m^2\ g^{-1}$]	Median diameter [µm]
150	# 1	3,069	1,074
	# 2	1,964	1,678
	# 3	3,830	0,86
160	# 1	3,329	0,99
	# 2	3,760	0,876
	# 3	3,320	0,992
170	# 1	3,825	0,861
	# 2	6,032	0,546
	# 3	6,120	0,538
180	# 1	4,538	0,726

Tab.: 4.11 – Median particle diameter calculated from the BET surface.

SEM images of the crystallized product, prepared at 160 °C and 170 °C, are figured below (fig. 4.8 and 4.9). As can be seen from figure 4.8, the particles are subject to a relatively wide particle size distribution, ranging from about 300 nm to 1,35 µm, whereby the majority of the particles is lying in-between 400 and 750 nm.

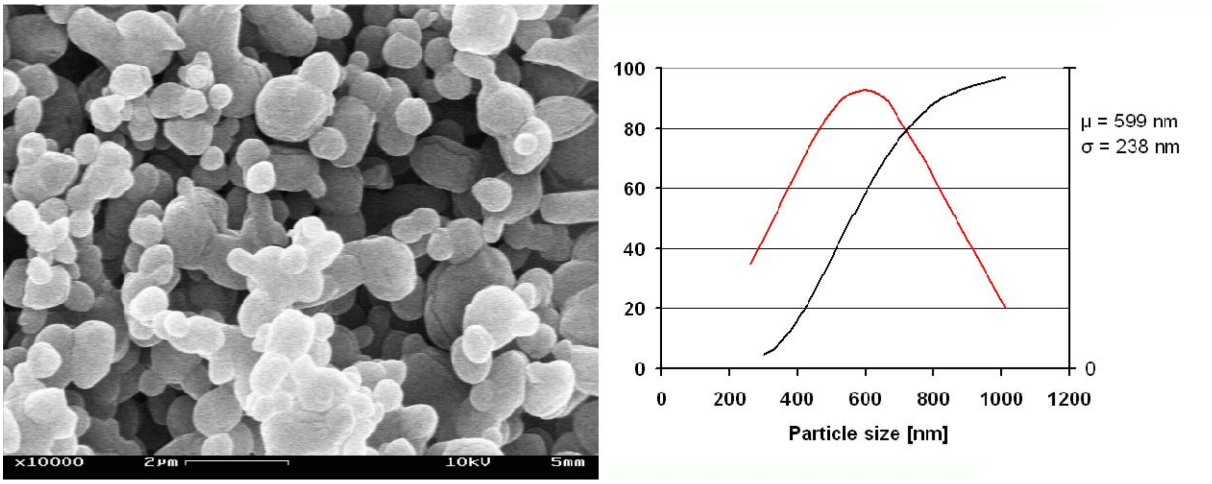

Fig.: 4.8 – SEM image and PSD of RDX prepared at 160 °C.

As submicron RDX is already highly sensitive to the electron beam of the SEM, its sensitivity seemed to increase with decreasing particle diameter. The particles in figure 4.9 were prepared at 170 °C. Due to the high sensitivity towards the electron beam, the image was recorded with a lower magnification.

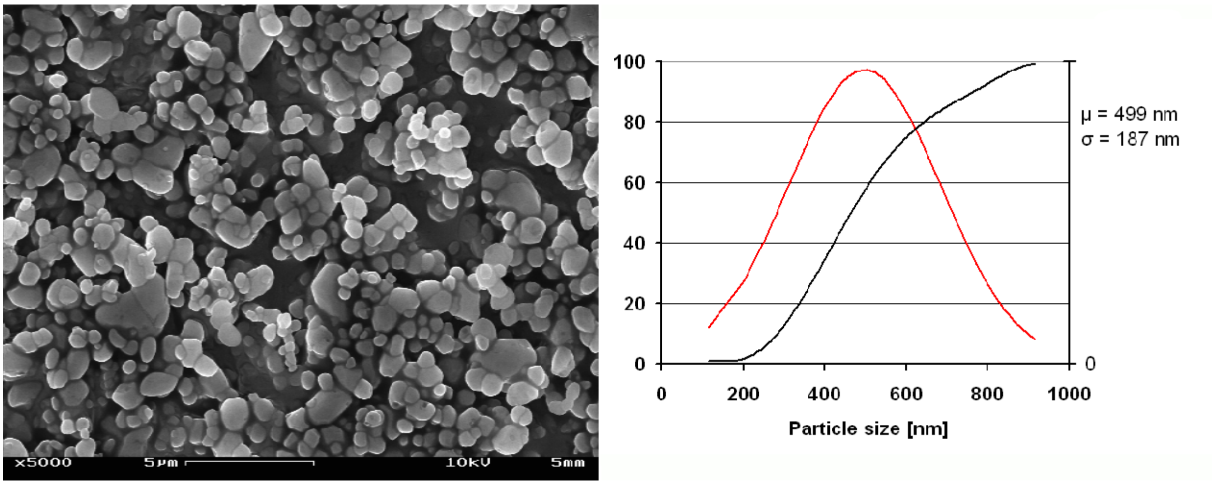

Fig.: 4.9 – SEM image and PSD of RDX prepared at 170 °C.

At 170 °C a noticeable decrease of the median particles size and a narrower PSD were obtained. In the following figure (fig. 4.10), the RDX from figure 4.9 is depicted with a higher magnification. Both images were taken from the same area. The second image, immediately recorded after the first, shows a high degree of degradation. It can not be excluded that degradation of the material already happened at lower magnification.

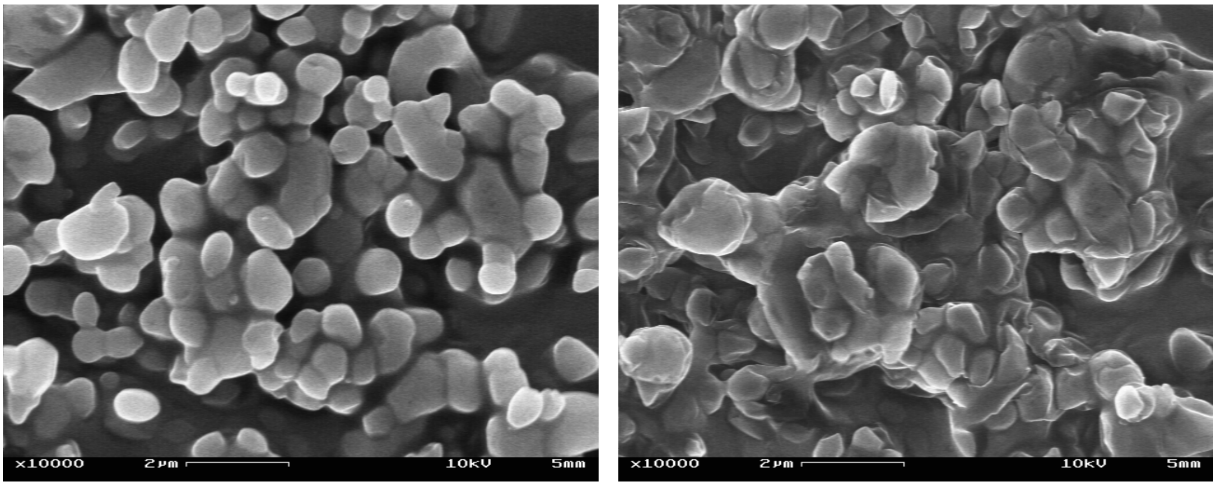

Fig.: 4.10 – SEM image of RDX after the electron beam had scanned the surface.

From the processing point of view, working at higher temperatures is advantageous as it promotes the formation of smaller particles and a narrower PSD. Unfortunately the spray cone broadening caused a noticeable loss of product, what, however, could be solved by optimizing the atomization chamber (e.g. larger diameter).

4.2.2 The influence of the nozzle pressure

The influence of the nozzle pressure was examined over a pressure range from 40 to 70 bar. From the course of the BET curve, a trend towards larger particle surfaces could be observed, appearing to approach a limiting value (fig. 4.11). This behaviour corresponds well with the statement by Richter [3], that from a certain threshold pressure, the droplet size from a hollow cone nozzle only marginally rises.

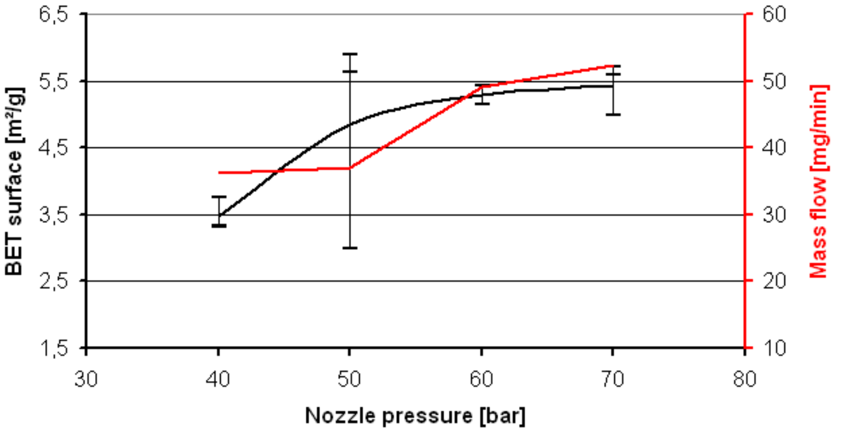

Fig.: 4.11 – Pressure dependence of the BET surface (black) and mass flow rate (blue).

Due to the higher nozzle pressure the volume flow rate increased, causing a slight pressure rise in the atomization chamber (tab. 4.12). It was feared that the higher pressure in the atomization chamber could have impaired the evaporation ratio, but the decrease was so small that its influence appears to be negligible.

Nozzle pressure [bar]	$p_{atomization\ chamber}$ **[mbar]**	X_{vap}
40	5,2 – 5,6	0,800
50	6,0 – 6,4	0,796
60	6,8 – 7,2	0,791
70	8,4 – 8,8	0,785

Tab.: 4.12 – Evaporation ratio in dependence of the nozzle pressure.

Because of the higher volume flow, it was assumed that the collected product contains a higher amount of residual moisture. For this reason, the cyclone temperature in the experiments performed at 60 and 70 bar was raised to 100 °C. In comparative measurements, no change in the content of residual moisture could be observed. In figure 4.12, the melting temperature and the crystallite size of the individual samples is depicted. Neither the melting temperature, nor the crystallite size showed a noticeable change.

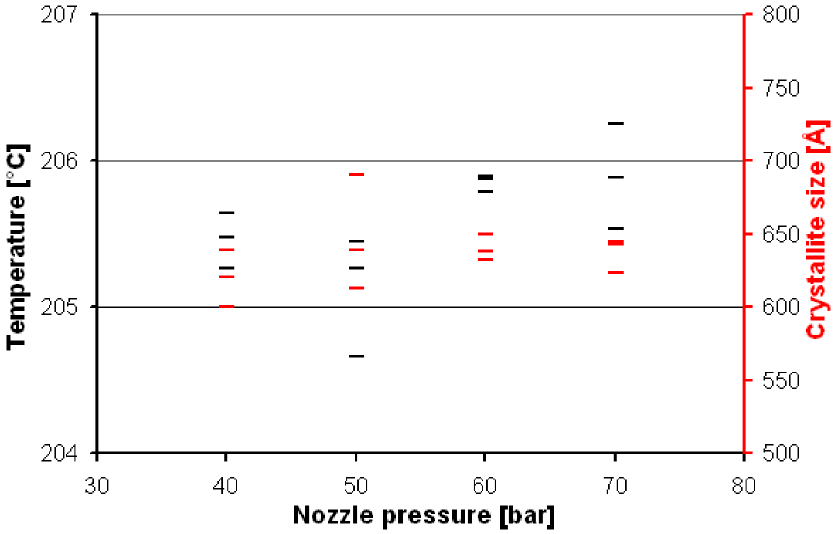

Fig.: 4.12 – Melting temperature (black) and crystallite size (blue) of RDX in dependence of the nozzle pressure.

The median particle diameter, calculated from the BET surface, is listed in table 4.13. In run # 3 at 60 bar, no measurement of the BET surface was made as the collected product in this experiment amounted only 0,255 g, before the installation run out of feed solution.

Nozzle pressure [bar]	**Run**	**S_{BET} [m^2 g^{-1}]**	**Median diameter [µm]**
40	# 1	3,329	0,99
	# 2	3,760	0,876
	# 3	3,320	0,992
50	# 1	5,896	0,559
	# 2	5,632	0,585
	# 3	2,998	1,099
60	# 1	5,141	0,641
	# 2	5,422	0,608
	# 3	No measurement	
70	# 1	5,705	0,577
	# 2	5,587	0,590
	# 3	4,982	0,661

Tab.: 4.13 – Median particle diameter calculated from the BET surface.

The results presented in table 4.13 clearly show that at 40 bar, the 60 µm nozzle was operated below its optimal conditions. SEM images from the RDX particles prepared at 40, 50 and 70 bar confirm the observations that were made so far. SEM images from the experiments performed at 50 and 70 bar are depicted below (fig. 4.13 to 4.15). RDX prepared at 40 bar was already shown in figure 4.8.

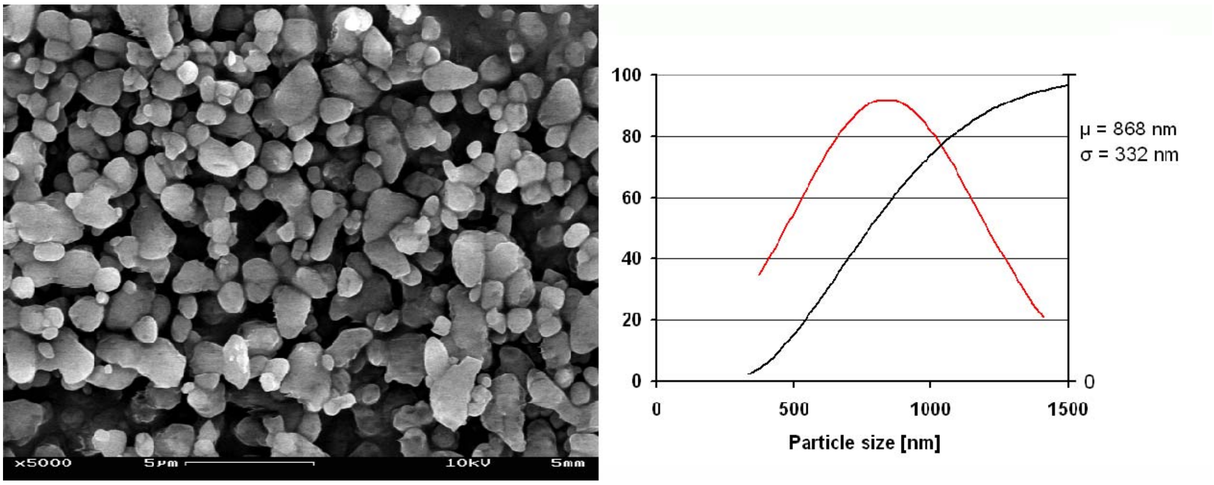

Fig.: 4.13 – SEM image and PSD of RDX particles prepared at 50 bar.

The particles prepared at 50 bar are subject to a broad PSD. It appears that two dominating particle sizes were formed, one in the order of about 500 nm with a spherical structure and the other, ranging from 1,0 to 2,0 µm, having a faceted form. In figure 4.14, showing RDX prepared at 70 bar, a significant decrease of the particle size and a narrower PSD could be observed. The particles prepared at 70 bar have an edged structure, slightly differing from the previous samples. In figure 4.15 a detailed picture of those particles without any signs of degradation is shown.

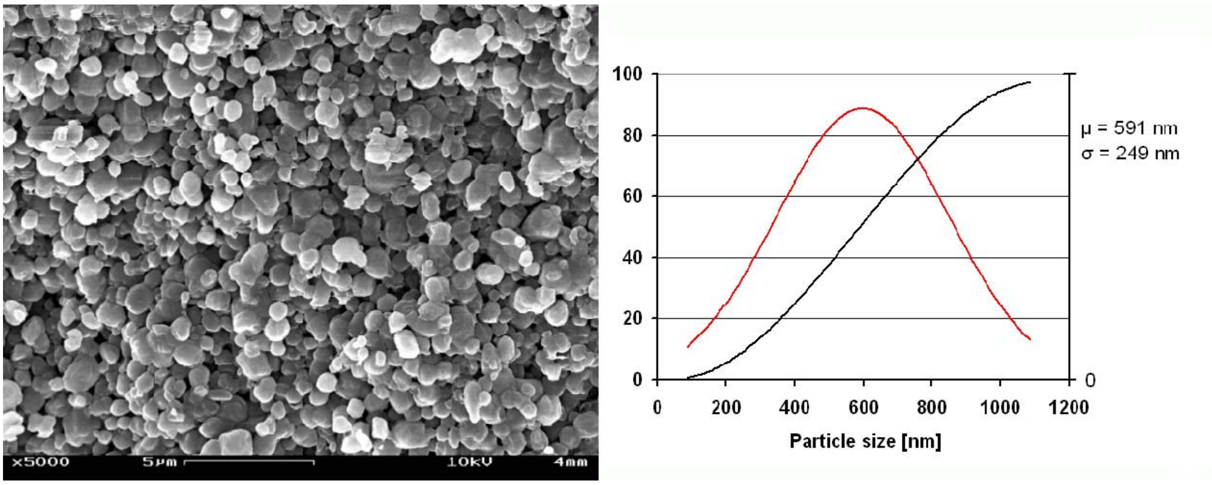

Fig.: 4.14 – SEM image and PSD of RDX particles prepared at 70 bar.

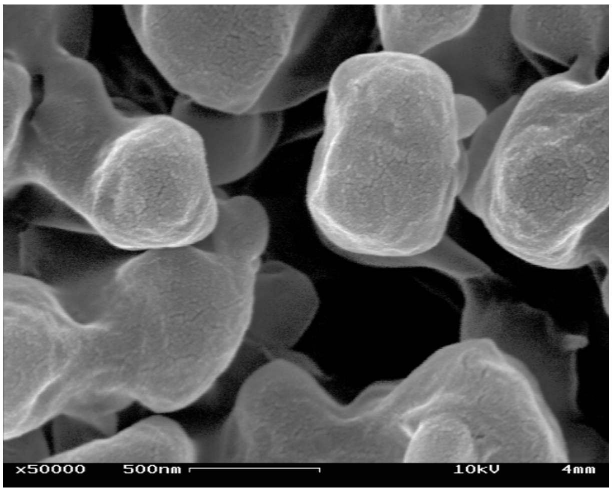

Fig.: 4.15 – Close-up of RDX particles prepared at 70 bar.

It appears that at 70 bar a more homogeneous spray was formed, inhibiting the formation of micrometric particles. It is supposed that, because of the large number of particles, coalescence between adjacent particles occurred in an early state, causing the cross-linked structure that can be seen in figure 4.15

As the manufacturer of the nozzle recommends a noticeably higher working pressure, it is supposed that the relatively large particles, obtained at 40 and 50 bar, were caused by an imperfect atomization.

4.2.3 The influence of the solvent

By using MTBE as a co-solvent with acetone, an improvement of the crystallization conditions was attained. Under equal conditions, a composition of acetone/MTBE 70/30 (v/v) at 160 °C has almost the same evaporation ratio as pure acetone at 180 °C. The evaporation ratio of the various acetone/MTBE compositions under the studied process conditions is depicted in figure 4.16.

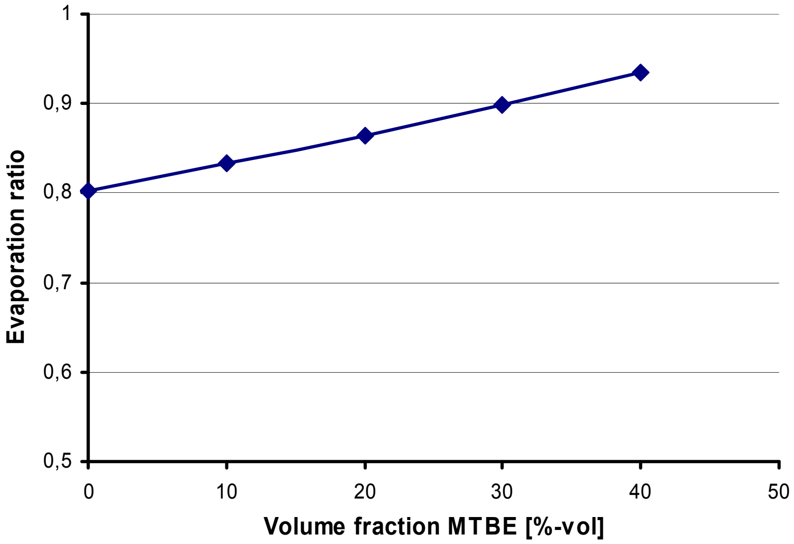

Fig.: 4.16 – Evaporation ratio in dependence of the MTBE content.

It was supposed that MTBE, used as a co-solvent, merely served as energy storage which transferred its *excess energy* to the acetone causing the decrease of the working temperature. But, plotting the measured values into a chart (fig. 4.17), it appears that a plateau was formed. The addition of only 10 % MTBE noticeably increased the specific surface; however, adding further MTBE led to a stagnation of the BET curve at about 5 m²/g.

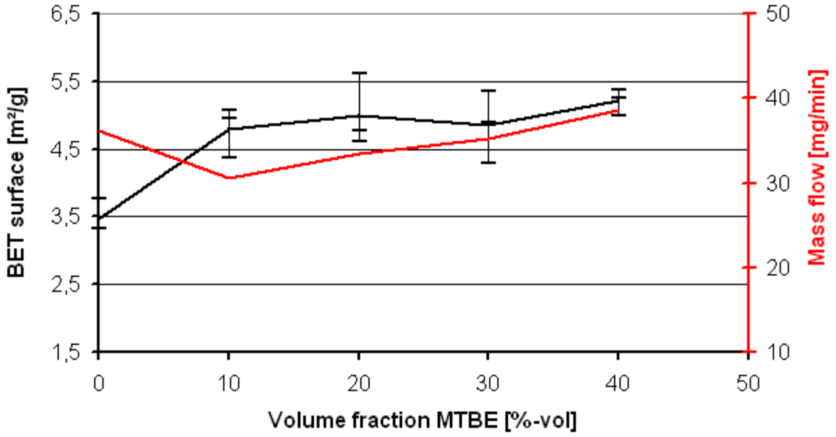

Fig.: 4.17 – Median BET surface (black) and mass flow rate (blue) in dependence of the MTBE content in the solvent.

During this part of the parametric study, the median mass flow rate remained relatively stable in-between 30,6 and 38,6 mg/min. This behaviour was unexpected, as in the first part of the parameter study the mass flow rate continuously decreased with increasing evaporation ratio. The melting point of the RDX, determined by DSC, seems to decrease with increasing MTBE content, reaching its minimum at 30 %-vol MTBE and increases afterwards again (fig. 4.18). The crystallite size remained constant between 600 and 700 Å.

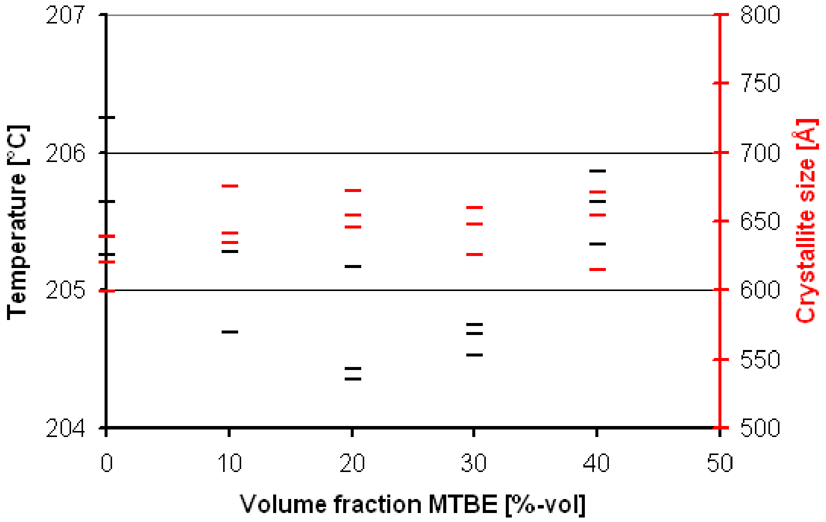

Fig.: 4.18 – Melting point (black) and crystallite size (blue) of nanocrystallized RDX in dependence of the MTBE content in the solvent.

In the following two pictures (fig. 4.19 and 4.20), SEM images of the nanocrystallized product as loose powder are shown. In the first image, showing the product obtained from pure acetone, a relatively large PSD could be observed. The particle diameter ranged from about 300 nm to almost 2 µm.

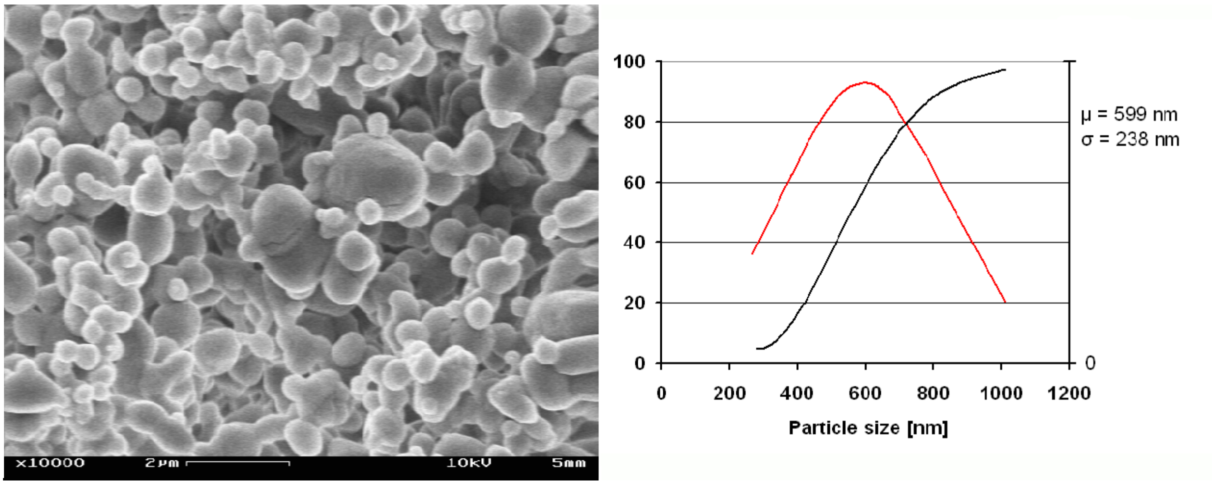

Fig.: 4.19 – SEM image and PSD of nanocrystallized RDX from pure acetone.

Figure 4.20 shows the RDX particles prepared from the acetone/MTBE 60/40 solution. Most striking is the considerably narrower PSD and the decrease of the median particle size.

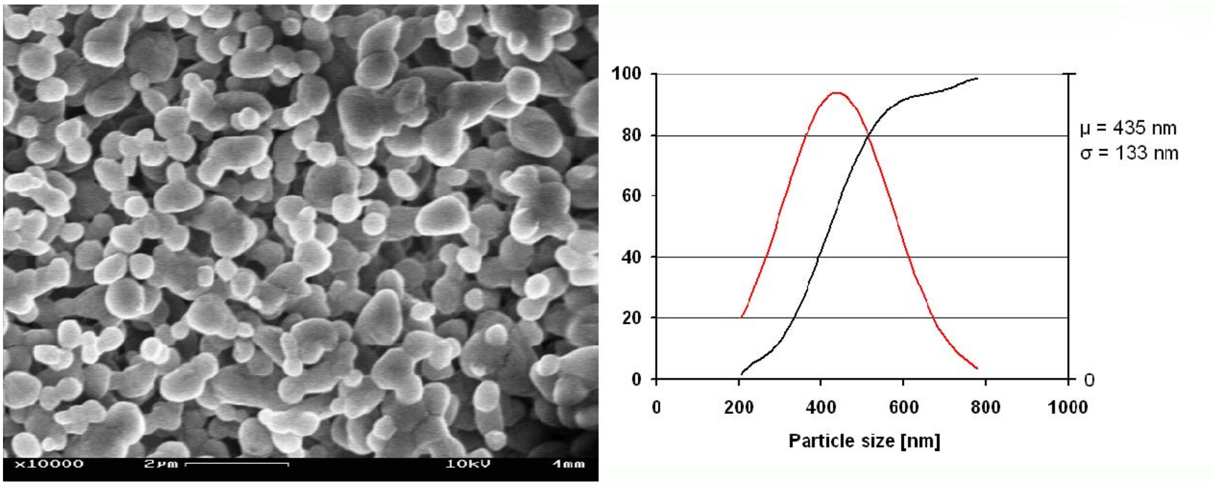

Fig.: 4.20 – SEM image and PSD of nanocrystallized RDX prepared from acetone/MTBE 60/40.

The increasing evaporation ratio is probably not the only mechanism, leading to a decrease of the particle size. As described in chapter 3, the degree of supersaturation plays an important role in view of the number of nuclei and the final crystal size.

As the supersaturation also plays an important role in view of the formation of crystal germs, the lower solubility of RDX in the binary solvents may have increased the supersaturation ratio during the flash-crystallization.

4.2.4 The influence of the nozzle diameter

As the smallest nozzle was already used in the standard experiment, neither an improvement of the process nor a decrease of the particle size had been expected in this part of the parametric study. In the figure below (fig. 4.21) the course of the BET surface and the mass flow rate are shown.

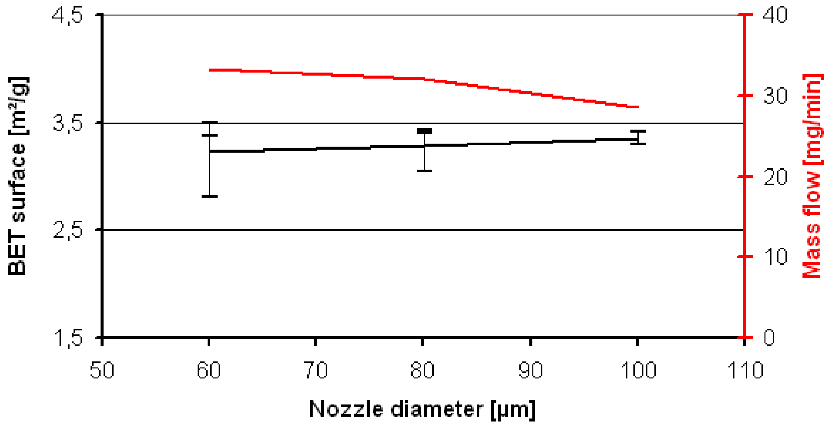

Fig.: 4.21 – Median BET surface (black) and mass flow rate (blue) in dependence of the nozzle diameter.

According to the BET measurements, the use of a larger nozzle diameter did not significantly changed the BET surface, whereas a decrease of the mass flow rate emerged.

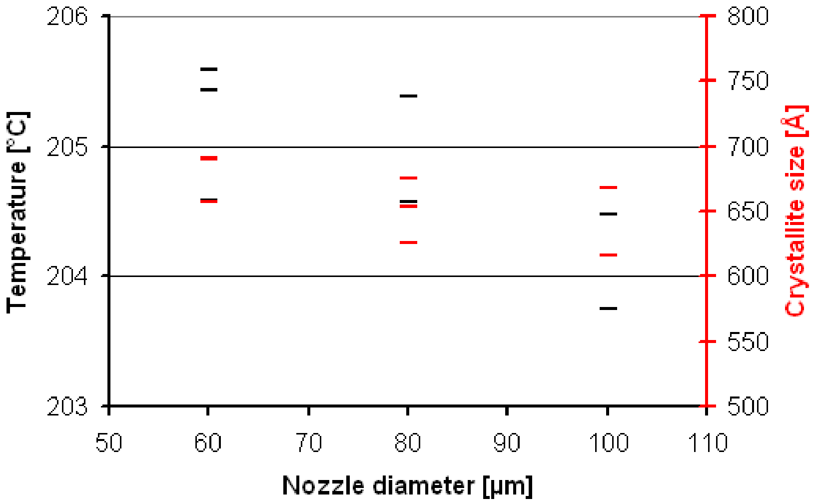

Fig.: 4.22 – RDX melting point (black) and crystallite size (blue) as a function of the nozzle diameter.

Surprisingly, a constant drop of the melting temperature and crystallite size could be observed. However, as only three nozzles were available for this study, further measurements with larger nozzles are needed to confirm this trend.

SEM images (fig. 4.23 and 4.24) were recorded from the RDX, prepared with the 60 and 80 µm nozzle, respectively. In figure 4.23, the product from the 60 µm nozzle is depicted, showing spherical and oval particles that are subject to a wide particle size distribution. The smallest particles in this sample were about 400 nm in diameter, whereas the largest spherical particles even reached diameters of about 1,5 µm.

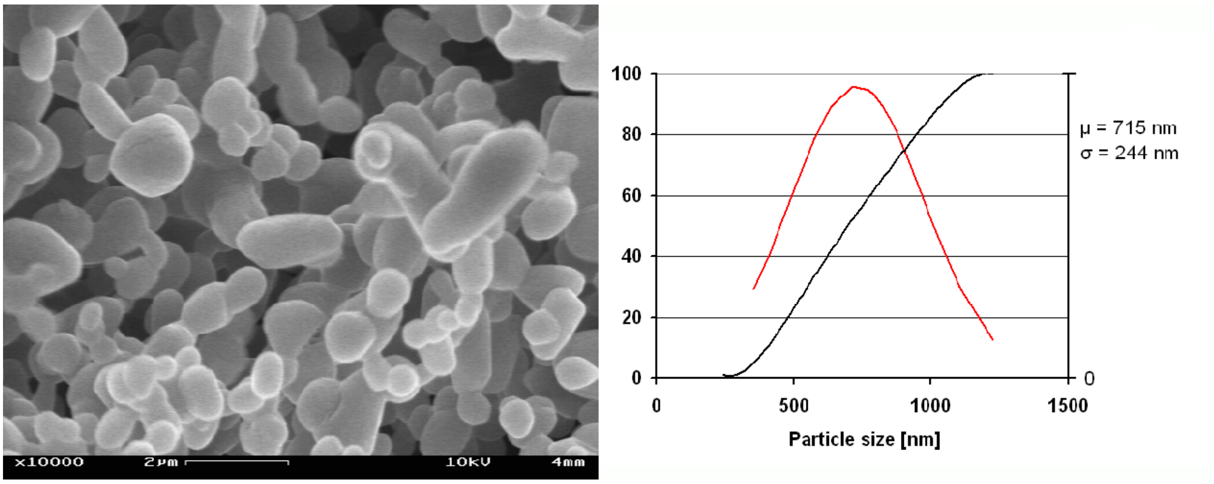

Fig.: 4.23 – RDX particles prepared from a 0,7 %-wt solution using a 60 μm nozzle.

In the following figure, showing RDX prepared with a 80 μm nozzle, a noticeably wider PSD and a larger median diameter was observed.

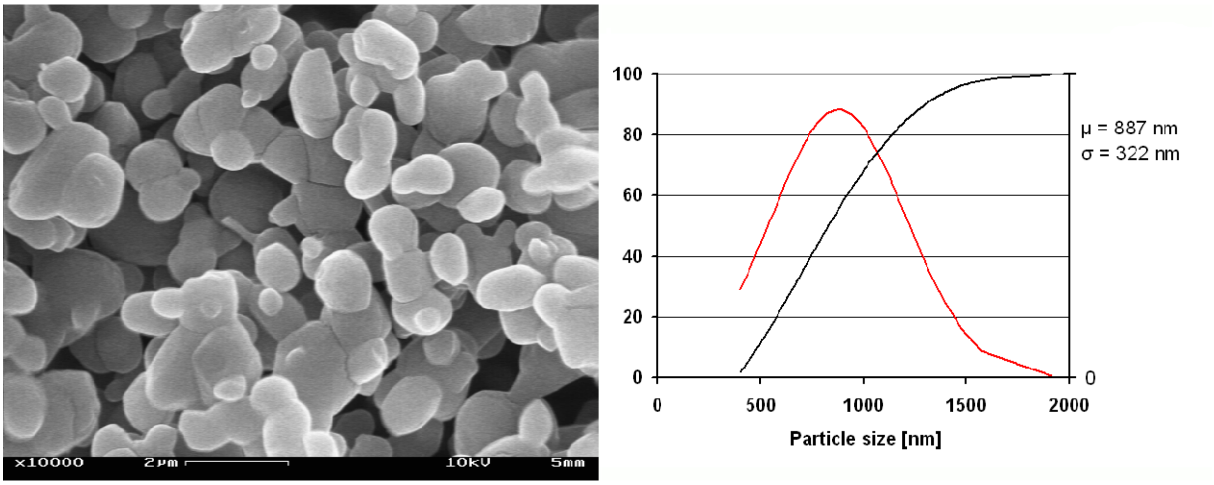

Fig.: 4.24 – RDX particles prepared from a 0,7 %-wt solution using a 80 μm nozzle.

The particles in figure 4.24 are in close contact with each other, and spherical particles were only sporadically found.

The slightly dropping mass flow rate may not appear important at first; however, as the larger nozzles enable a higher volume flow rate, an increasing mass flow rate was expected. The production yield γ describes the ratio of RDX deposited in the cyclone to the initial amount of RDX. The production yield obtained in the individual experiments is shown in table 4.14.

Nozzle [µm]	$\dot{V}_{nozzle}$ **[mL/min]**	$\dot{m}_{RDX,System}$ **[mg/min]**	$\dot{m}_{RDX,Cyclone}$ **[mg/min]**	$\gamma = \frac{\dot{m}_{RDX,Cyclone}}{\dot{m}_{RDX,System}}$
60	10	55,3	33,3	0,60
80	12	66,36	32,1	0,48
100	27	149,3	28,5	0,19

Tab.: 4.14 – RDX production yield in dependence of the nozzle diameter.

From the numerous experiments that have been performed so far, it was known that the production yield usually varies in-between 40 to 50 %, mainly caused by spray cone broadening and the deposition of RDX in the atomization chamber, but also by the loss of 1 - 5 % of the product by passing through the cyclone.

In this case, the low product yield was neither caused by strong spray cone broadening, nor by product loss, which was below 5 % as quantitative measurements with a 100 µm nozzle have shown. The product loss was caused by the high volume flow of the RDX-acetone solution, resulting in larger moisture content and the presence of droplets in the atomization chamber. In experiments performed with the 100 µm nozzle, condensation of acetone on the thermocouples could be observed. During these experiments, a large deposit of RDX was formed at the bottom of the atomization chamber. Due to the bad results that were obtained with the 100 µm nozzle, especially in terms of production rate, only two runs were performed with this experimental configuration.

In its current state, nozzles larger than 100 µm can not be tested in the installation, as the maximum power of the heating jacket is only 150 W. Using SimSci Pro/II, the energy demand for heating up the acetone from 20 to 160 °C at 40 bar was calculated for different flow rates (tab. 4.15). The simulation with its parameters is given in the annex. The load factor, abbreviated with $load$, is the ratio of required energy to the maximum electrical power of the heating jacket.

Nozzle [µm]	$\dot{V}_{nozzle}$ **[mL/min]**	$\dot{Q}_{demand}$ **[J/s]**	$load = \frac{\dot{Q}_{demand}}{P_{heat}}$
60	10	44,09	0,293
80	12	52,91	0,352
100	27	119,04	0,793

Tab.: 4.15 – Heat demand and electric load at different volume flow rates.

The load factor, when using a 60 or 80 µm nozzle, is relatively moderate and enables a good process control, whereas the load factor almost reaches 80 %, when a

100 µm nozzle is used. Nevertheless, in a closed loop where one component is already operated at its maximum capacity, the system becomes very sensitive to external interferences. Such a behaviour was observed in the experiments with the 100 µm nozzle. The equilibration time to regain its target temperature was about three times longer than with a 60 µm nozzle.

4.2.5 The influence of the RDX-concentration

Because the flash-crystallization process has a lot in common with classic spray drying, it was assumed that decreasing the concentration also decreases the particle size. However, the contrary effect was observed. In figure 4.25 the BET measurements and the mass flow rate are depicted, showing both a constant rose with increasing concentration.

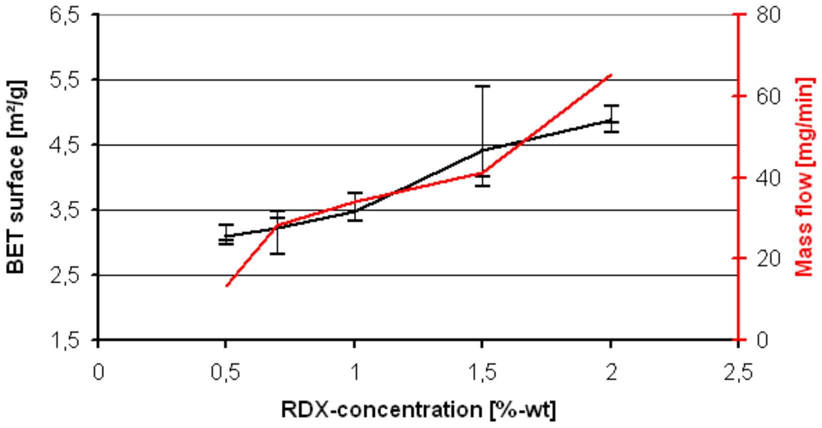

Fig.: 4.25 – BET surface (black) and mass flow rate (blue) in dependence of the RDX-concentration.

Despite the decreasing particle size, the crystallite size and the melting temperature of the RDX remained relatively constant (fig. 4.26).

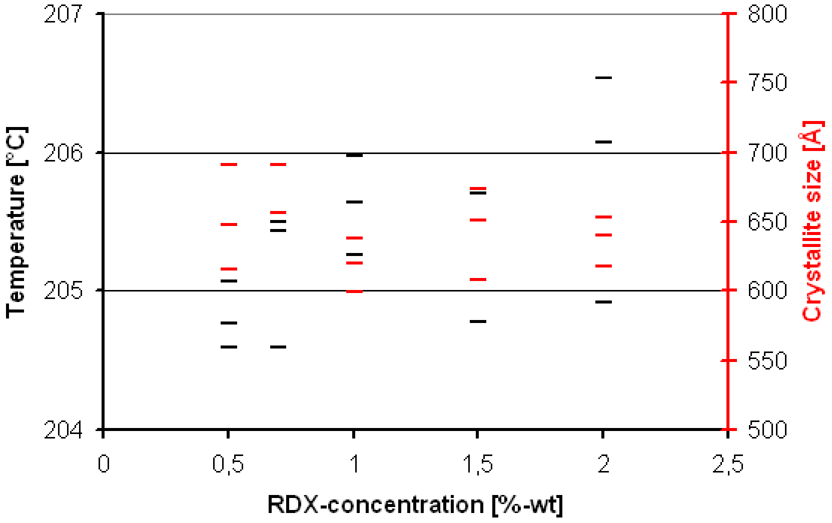

Fig.: 4.26 – Melting temperature (black) and crystallite size (blue) of nanocrystallized RDX prepared from solutions with different concentrations.

The SEM images in figure 4.27 and 4.28, taken from the RDX prepared with the 0,7 and the 2,0 % solution, clearly show the change of the particle size and the PSD.

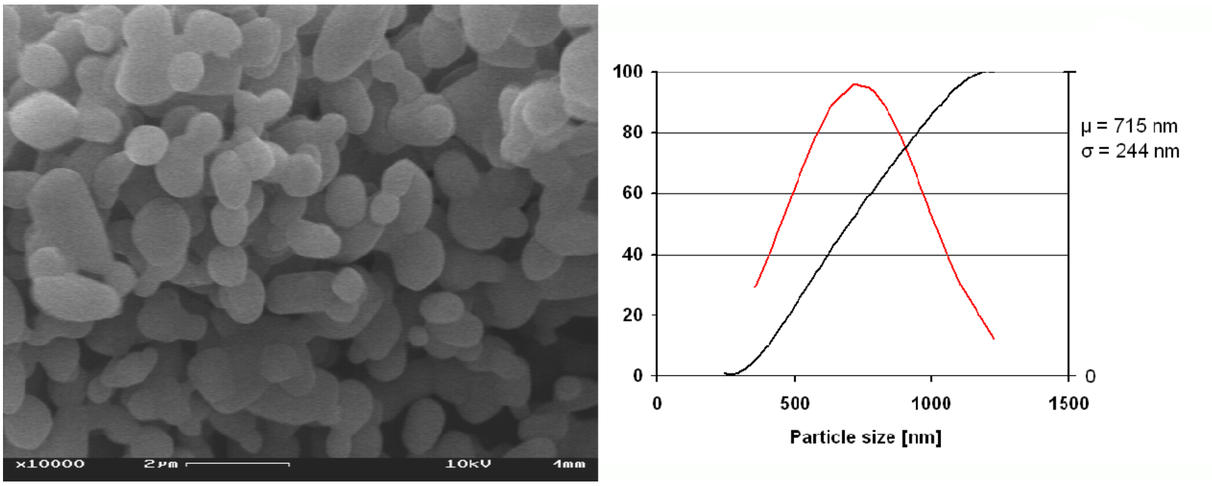

Fig.: 4.27– Nanocrystallized RDX prepared from a 0,7 %-wt solution.

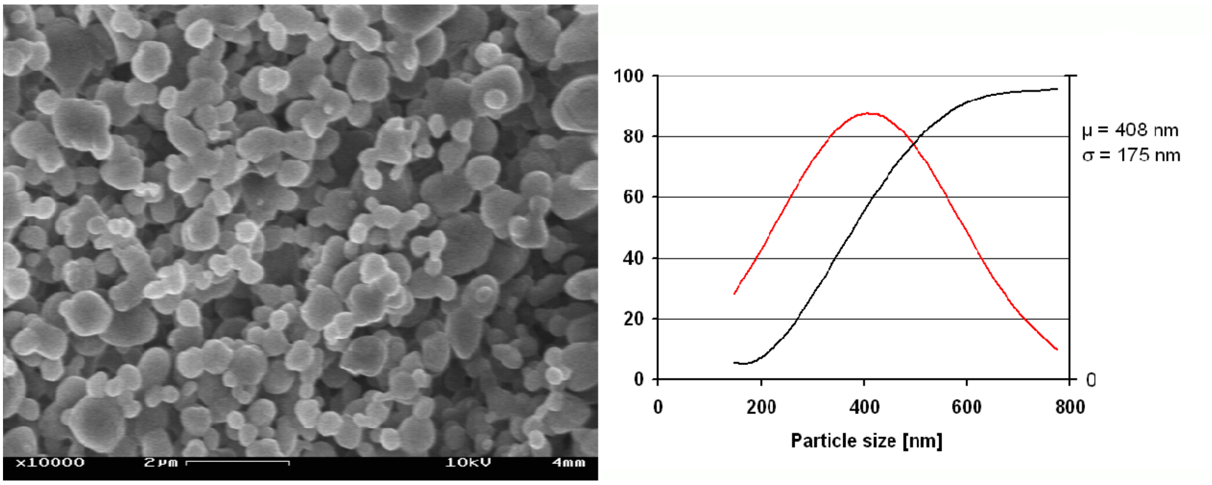

Fig.: 4.28 – Nanocrystallized RDX prepared from a 2,0 %-wt solution.

From the constant crystallite size over the whole study, it can be concluded that the crystal growth mechanism, composed of *nucleation* and *growth*, is unchanged. Under these circumstances, some kind of agglomeration mechanism must exist, defining the final particle size.

Assuming that agglomeration of the individual crystals only happens in the liquid phase, the higher RDX concentration must have earlier triggered the evaporation process. As the liquid, leaving the nozzle, is in a metastable state, its evaporation can be *triggered* by the presence of impurities, dissolved gases or rough surfaces [6, 9]. With increasing RDX concentration, and consequently the degree of supersaturation S, the formation of crystal nuclei sets in earlier and in larger quantities. It is supposed that these crystals, or small agglomerates of them, served as germs for the formation of bubble nuclei.

4.3 Optimized operating conditions

With the knowledge from the parametric study, the operating conditions were optimized in order to decrease the particle size and maximize the production rate.

As the exact mechanisms of certain parameters, such as the content of MTBE or the RDX concentration are still not completely understood, the variation of said parameters was only performed in the already studied range. The optimized operating conditions are listed in table 4.16.

Nozzle [µm]	**Temperature**		**Solvent v/v [Acetone/MTBE]**	**Pressure [bar]**	**RDX-Conc. [%-wt]**
	Nozzle [°C]	**Cyclone [°C]**			
60	170	100	75/25	50	1,5

Tab.: 4.16 – Optimized process parameters.

The experiment was executed with 500 mL of this particular solution. The course of the experiment was performed in the same manner as the standard experiment described earlier.

Shortly after the beginning of the experiment, growing deposits around the nozzle orifice could be observed. Those deposits grew, until they reached a size of 2 or 3 mm, and then they fall away. Fragments of the deposits were later found in the atomization chamber. About 20 min later, the first sight glass was completely covered with RDX. Altogether, the experiment took 45 min until the whole solution was consumed. In total 2,25 g of RDX was collected by the cyclones, corresponding to a mass flow rate of 51 mg/min and a production yield of 0,38. The BET measurement revealed a specific surface of 5,38 m²/g, corresponding to a median diameter of 0,612 µm. A melting point of 205,7 °C was measured by DSC and the crystallite size, according to Scherrer's equation from XRD the diffractogram amounted 591,2 Å.

A SEM image of the product is shown below (fig. 4.29). Instead of applying a platinum layer onto the sample, a gold layer was applied. As gold has a higher thermal conductivity as platinum, more detailed images could be recorded (fig. 4.30).

The additional electrode, required for gold sputtering, was acquired only a few weeks before. This is why the majority of samples were metallized with platinum.

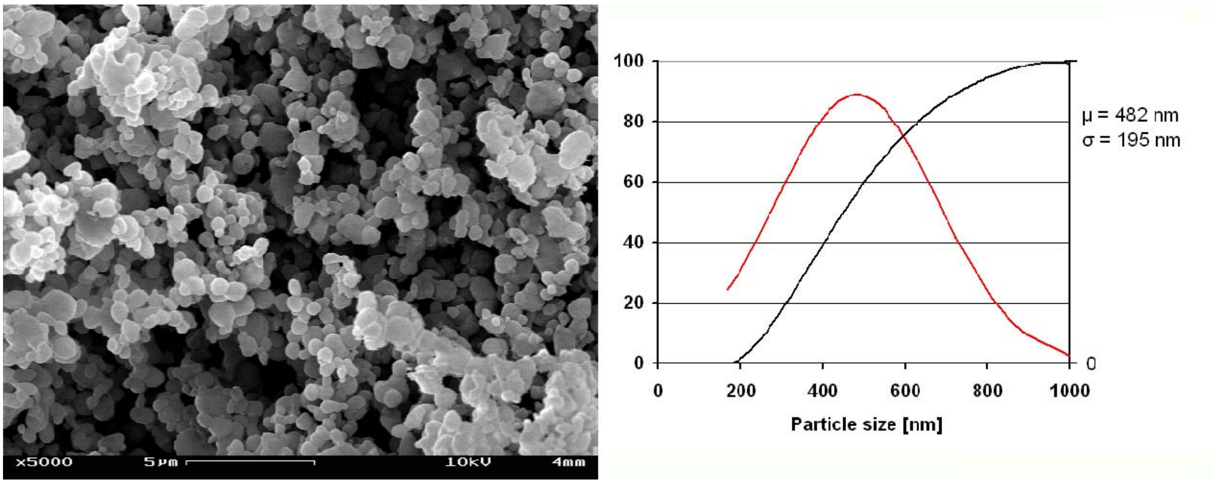

Fig. 4.29 – SEM image and PSD of RDX prepared under optimized conditions.

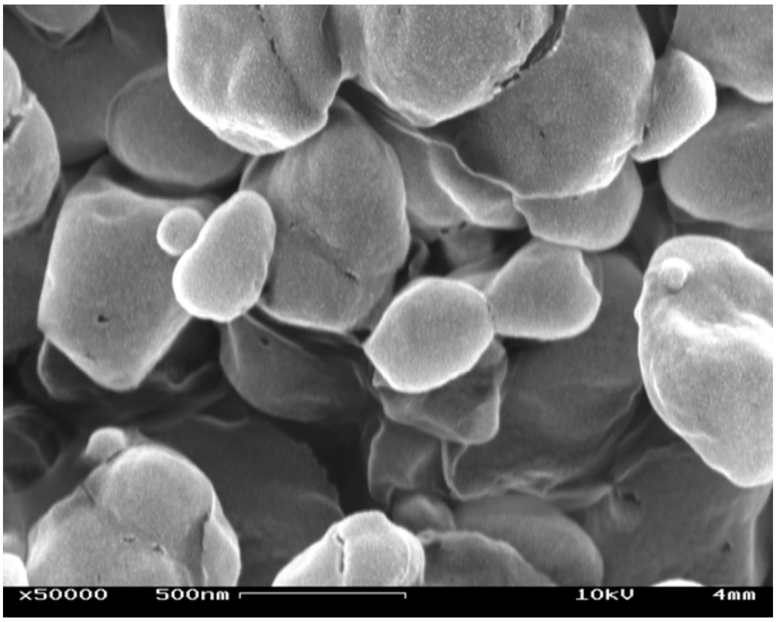

Fig. 4.30 – Close-up from RDX with gold sputtered surface.

From this product the sensitivity towards impact, friction and electrostatic discharge was measured and compared with the measurements from the RDX raw material that has been used in this work (tab. 4.17). A SEM image of the RDX raw material is shown in figure 5.3.

RDX	Impact [J]	Friction [Nm]	ESD [mJ]
M5 (raw material)	>3,52	160 N	119,42
nanostructured	>3,52	>360 N	268,69

Tab.: 4.17 – Sensitivity towards impact, friction and ESD of micron-sized and nanostructured RDX.

As can be seen from the measured values, a noticeable desensitization towards initiation by friction and electrostatic discharge was attained. The noticeably lower sensitivity towards friction bases on the self-lubricating effect, as small particles rather occupy small interstices than to break. The lower sensitivity towards electrostatic discharge can be explained by the smaller hot-spot size, requiring higher temperatures to ignite the explosive. The unchanged sensitivity towards impact is explained by the increasing number of external hot-spots.

With decreasing particle size, the number and size of intercrystalline defects diminish, whereas the relative particle surface increases. In a loose nanopowder, having a considerably lower bulk density [10] than a micron-sized product, the air filled interstices represent an inhomogeneity that may form an external hot-spot.

Summary of the chapter

The objective of this parameter study was the evaluation of the individual process parameters in view of their impact on the particle and process relevant properties. By means of a standard experiment, performed under defined process conditions, the relevant process parameters and their range of variation were determined. The studied process parameters were: the nozzle temperature, the nozzle pressure, the type of solvent, the nozzle diameter and the concentration of the explosive. Because of its high thermal stability and the existence of only a single stable crystal modification, RDX was used in this parameter study. Characterization of the particles happened by means of DSC, XRD and BET. Individual samples were also examined using Raman-spectroscopy and SEM. In detail, the following findings were made in this parameter study:

- With increasing **nozzle temperature** the particle size continuously decreases. Due to the higher degree of superheat the evaporation process happens faster, causing higher degrees of supersaturation.

- The **nozzle pressure** only had a little effect on the particle size and PSD. With increasing pressure the spray becomes finer, but the crystallization conditions got worse at the same time.

- The **addition of MTBE** to the acetone caused a decrease of the particle size. Because of its favourable thermodynamic properties, MTBE can store more energy than acetone. The addition of MTBE to the solvent has an accelerating effect on the evaporation process. Because of its low RDX solubility, MTBE also increases the degree of supersaturation, promoting the formation of even smaller crystallization germs.

- With increasing **nozzle diameter**, the particle size and the PSD increased as well. Because of the higher volume flow rate, the atomization chamber got colder and acetone started to condense on the thermocouples.

- With increasing **explosive concentration**, the particle size decreased and the PSD became narrower. Due to the higher degree of supersaturation, more crystal germs were formed. It is assumed that the higher crystal concentration served as trigger for the evaporation.

The characterization by SEM revealed that submicron RDX exposed to the electron beam already decomposes after a few seconds. The median particle size of the standard experiment was 599 nm. In the course of the parametric study, a decrease of the median particle size to about 400 nm was attained. However, the crystallite size remained almost constant in all experiments, varying only in-between 600 and 700 Å.

The unchanged crystallite size suggests a constant crystallization speed. The formation of larger particles is therefore ought to happen in the liquid state by agglomeration of crystallites. In view of further decreasing the particle size, the nucleation mechanism as well as the agglomeration mechanism has to be taken into consideration.

References

[1] McCrone, W.; *Anal. Chem.*, 22 (7), **1950**, pp. 954-955.
[2] Karpowicz, R.; Sergio, S.; Brill, T.; *Ind. Eng. Chem. Prod. Res. Dev.,* 22, **1983**, pp. 363-365.
[3] Richter, T.; Zerstäuben von Flüssigkeiten, 2. Auflage, **2008**, Expert Verlag.
[4] http://www.plantfog.at/HD_D/Preisliste_HD-Duesen_D.htm , Hollow cone nozzles from the plantfog company, **20.06.2012**.
[5] Lefebvre, A.; *Part. Part. Syst. Charact*., 6, **1989**, pp. 176-186.
[6] Owen, I.; Jalil, J.; *Int. J. Multiphase Flow*, 17 (5), **1991**, pp. 653-660.
[7] Fedoroff, B.; Sheffield, O.; *Encyclopedia of explosives and related items*, **1966**, Vol. 3, Picatinny Arsenal, New Jersey, USA.
[8] Mullin, J.;Crystallization, 4th Ed, **2004,** Elsevier Butterworth- Heinemann.
[9] Sher, E.; Bar-Kohany, T.; Rashkovan, A.; *Prog. Energy Combust. Sci.,* 34, **2008**, pp. 417-439.
[10] Stepanov, V.; Dissertation: Production of nanocrystalline RDX by RESS: Process development and material characterization, **2008,** New Jersey Institute of Technology, USA.

5 Further nanocrystallized materials

During the conception and the development of the flash-crystallization process, numerous energetic and inert substances, and compositions of them, were successfully nanocrystallized by this process. Strongly depending on the current stage of development of the installation, the production rate varied as well. While at the beginning of this work the largest samples amounted only 100 - 200 mg per experiment, the production rate rapidly increased with every further plant component that was finished and added to the process. Now, in its current state, the fabrication of 100 mg only takes about 2 min. From the numerous substances and composites that were successfully nanocrystallized with this process, two further products, due to their special fundamental and pyrotechnical interest, will be presented here, giving a view over the wide application scope of this process. In addition, further nanocrystallized materials are listed in the annex of chapter 5.

5.1 Nanostructured RDX/TNT compositions

RDX/TNT composites, better known as Hexolite, are of great interest, as their performance is higher than that of pure TNT, but can be processed, just like TNT, by simple casting. As pure RDX can not be melted without decomposition, it has to be mixed with a low melting substance, such as wax or TNT. One of the most common RDX/TNT composites is known as *Composition B* and is composed of 60%-wt RDX and 40%-wt TNT. Those mixtures are prepared by melting the TNT and adding a water-RDX slurry while stirring [1]. Because RDX has a higher density as molten TNT, a homogeneous distribution of both components in the solid material is difficult to obtain.

As the flash-crystallization process works with low concentrated solutions, a nanostructured RDX/TNT composite can easily be prepared by using prefabricated solutions with RDX and TNT in the proper ratio [2]. The process conditions for the fabrication of a nanostructured RDX/TNT composite are listed below (tab. 5.1). In total, these experimental conditions were used in the fabrication of more than 150 g of nanostructured Hexolite for different studies and detonation tests. *Among other things, two nanostructured Hexolite charges of 28 and 65 g were tested, being to our knowledge the first of its kind, worldwide*.

Nozzle [µm]	**Temperature**		**Explosive concentration [%-wt]**	**Pressure [bar]**	**Solvent**	**Ratio RDX/TNT [w/w]**
	Nozzle [°C]	**Cyclone [°C]**				
60	160	50	1,0	40	Acetone	60/40

Tab.: 5.1 – Experimental conditions for the fabrication of a nanostructured RDX/TNT composite.

Because of the low melting point of TNT, the cyclone temperature had to be lowered to 50 °C. As the set-up time and cleaning of the installation are taking together in-between 45 - 60 min, long term experiments should be envisaged. If sufficient solution is available, the installation can run for multiple hours. The installation was taken into operation in the same manner as described in the standard experiment in chapter 4. In order to avoid clogging, the cyclones had to be emptied every 5 or 6 minutes. The collected product had a slight pink coloration. Characterization of the collected product happened by means of DSC, BET, XRD, nanocalorimetry, SEM, Raman spectroscopy and Nuclear Magnetic Resonance spectroscopy (NMR). Furthermore, the sensitivity of the nanostructured Hexolite to impact, friction and ESD was measured and compared with those from a classic Hexolite charge prepared from micrometric compounds.

In figure 5.1 the DSC curves of a nano- and microstructured Hexolite, as well as from the RDX and TNT raw materials are shown. The melting temperature of TNT in the nanocrystallized Hexolite amounted only 78,8 °C, in the microstructured Hexolite 83,5 °C and in the pure TNT 81,2 °C. However, the thermogram of both composites did not show a RDX melting signal.

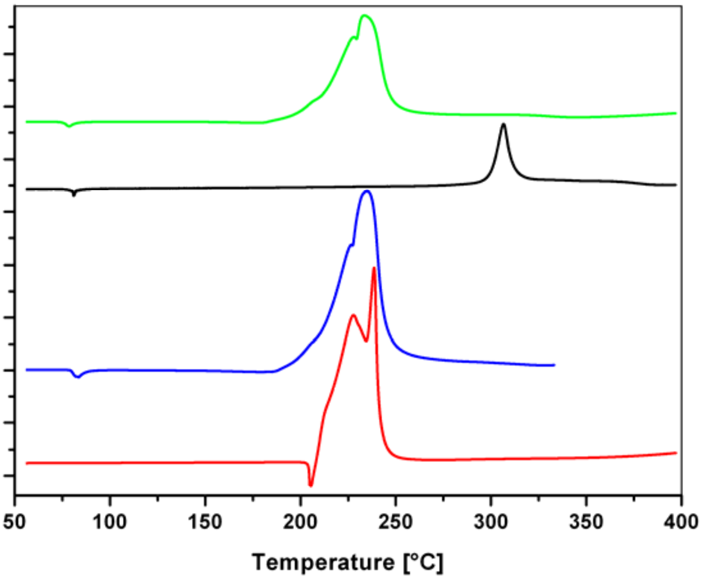

Fig.: 5.1 – DSC curves of nanocrystallized Hexolite (green), TNT (black), microstructured Hexolite (blue) and RDX (red).

Using the nanocalorimetry [3], the thermal behaviour of individual particles in the micrometer range can be measured with high accuracy. Figure 5.2 shows the chip of the nanocalorimeter, measuring only 100 x 100 µm, with a particle placed in its centre. Heating elements are printed on the surface of the chip, making heating rates in-between 10^3 and 10^6 °C/s possible. Thermocouples that are also printed on the chip surface are measuring the temperature of the sample and the environment. The particle in figure 5.2 was heated with a heating rate of 2815 °C/s up to 350 °C, afterwards residues could be found around the chip. The recorded thermogram shows two melting points, corresponding to TNT at 70 °C and RDX at 135 °C.

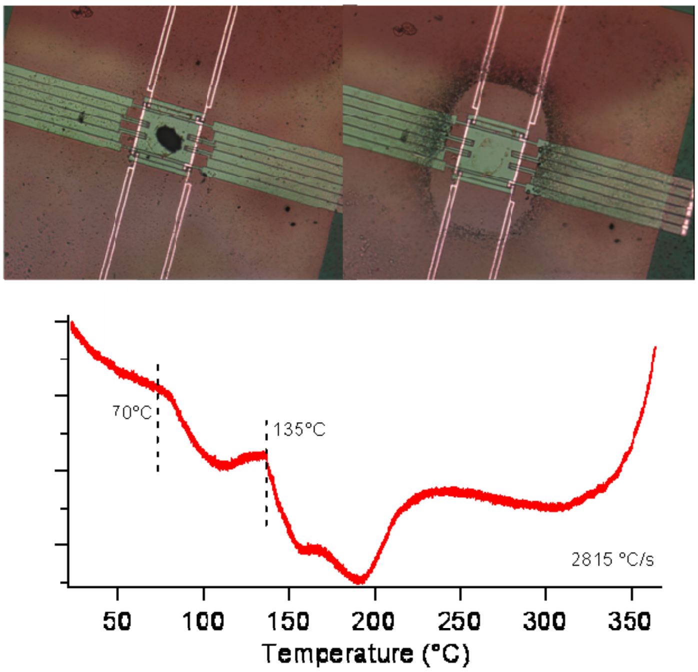

Fig.: 5.2 – Thermogram of the RDX/TNT 60/40 composite recorded with the nanocalorimeter.

For comparison, a Hexolite from micron-sized raw material was prepared by intensive dry physical mixing of both components in a TURBULA® blender. Both, the micron- and the nano-sized Hexolite were prepared from the same lots of RDX and TNT. SEM images of the raw materials are shown below (fig. 5.3). From the nanocrystallized Hexolite, cylindrical pellets of 15,8 mm x 15,8 mm (diameter x height) were prepared by pressing the material for 10 min with a pressure of 2200 bar. After the compression some of the pellets showed small cracks. From the site of fracture of one pellet, SEM images were recorded and subsequently compared with a Hexolite prepared from micron sized raw materials (fig. 5.4 and 5.5).

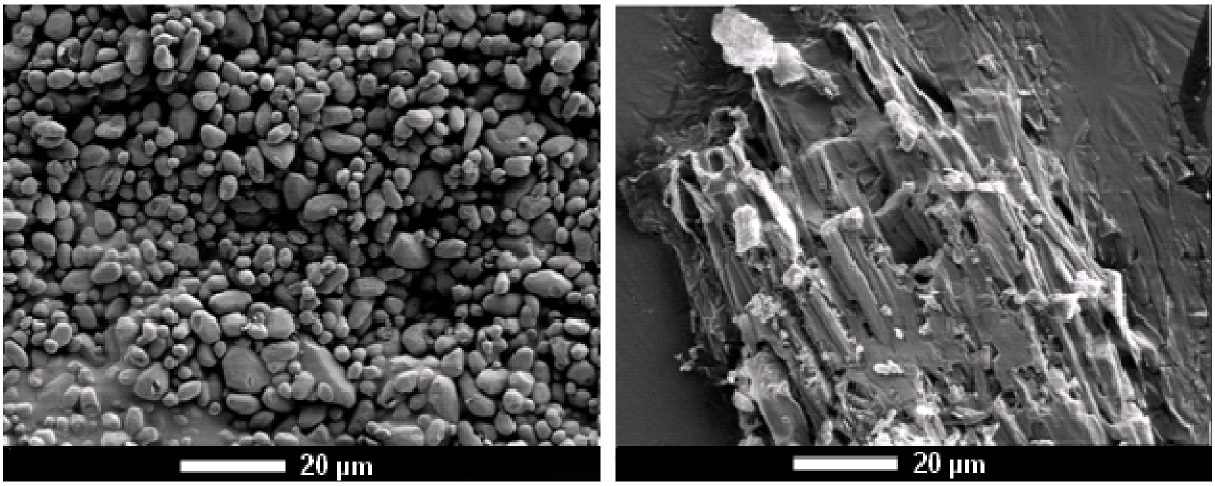

Fig.: 5.3 – Raw materials: RDX (left) and TNT (right).

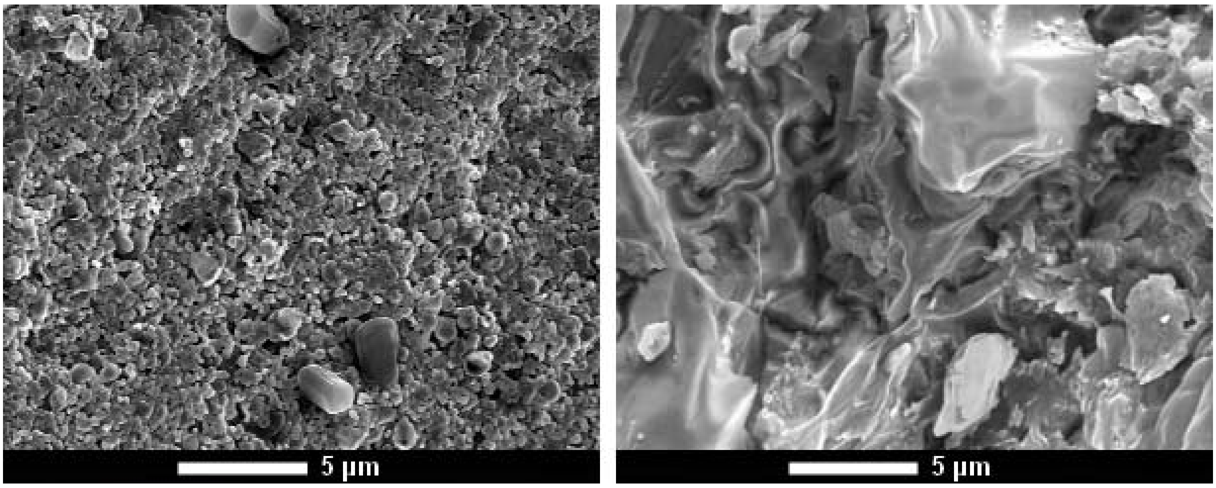

Fig.: 5.4 – Hexolite RDX/TNT 60/40 SEM images recorded with a magnification 5.000x, nanocrystallized Hexolite (left) and microstructured Hexolite (right).

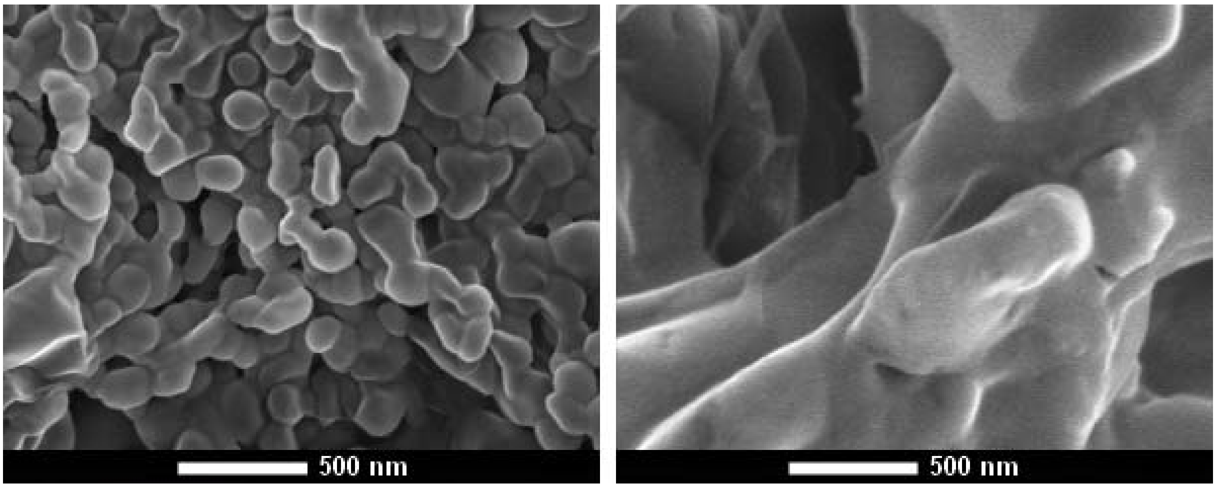

Fig.: 5.5 – Hexolite RDX/TNT 60/40 SEM images recorded with a magnification 50.000x, nanocrystallized Hexolite (left) and microstructured Hexolite (right).

Prior SEM analysis, an approximately 5 nm platinum layer was sputtered onto the fragment surface. Despite the extraordinary small particle size, relatively high-contrast images could be taken. The reasons for this are the better heat dissipation within the sample due to the close contact of the particles, and the lower energy supply caused by an old field emission gun (FEG) tip of the microscope.

Figure 5.5 clearly shows that the sample basically consists of individual spheres with diameters in-between 100 – 300 nm. Scanning a larger area with lower magnification (fig. 5.4), isolated micron sized particles with lengths of about 2 – 3 µm were also found. Due to their regular needle-like structure it is assumed that those particles are TNT, that recrystallized during the compression. In figure 5.6 a more detailed figure of such a micron sized particle is depicted.

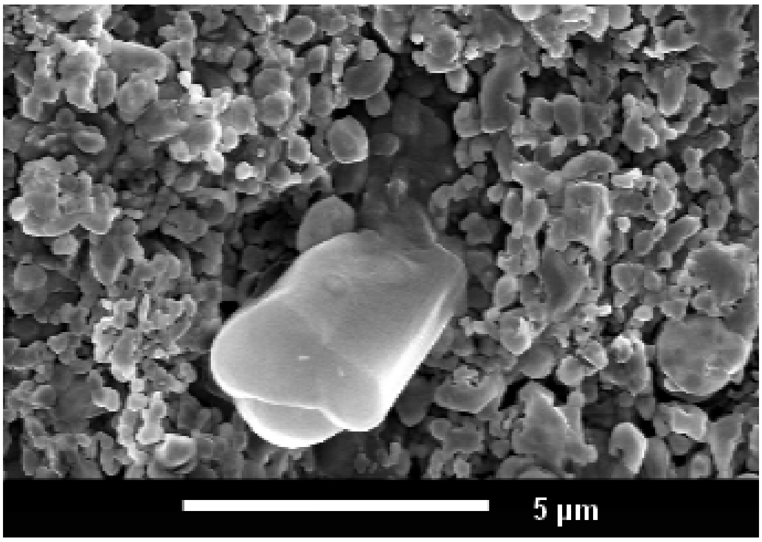

Fig.: 5.6 – Close-up of micron sized particle within the nanocrystallized Hexolite.

This figure clearly shows the empty space around the particle, supporting the assumption that the growth of those needles was *nourished* by the surrounding particles. It also appears that the concealed end of the needle was growing out of the depth. During the preparation of the pellets, it is likely that adiabatic compression of enclosed gases led to a temperature increase that resulted in melting and recrystallization of the TNT. After the compression, the recrystallized TNT must have set the pellet into such an inner stress, causing its breaking.

The BET surface of the nanocrystallized product was measured shortly after its synthesis. Because of the TNT, the sample had to be degassed for 1 h in vacuum at only 40 °C. Despite the actual small particle size, a specific surface of only 2,366 m²/g was measured. This behaviour in conjunction with nanocrystallized TNT is well known, which is why BET measurements with samples containing TNT are not reliable. It is believed that, due to the extremely low melting point, nanocrystallized TNT resembles a liquid, disturbing the N_2 adsorption.

In order to determine the exact distribution of the components in the nanostructured Hexolite, the sample was treated with osmium tetroxide (OsO_4) vapour. As the osmium tetroxide only reacts with the C=C double bond of the TNT, a selective addition of the heavy metal to the TNT is attained.

Using energy-dispersive X-ray spectroscopy (EDS), the position of the metal atoms on the Hexolite surface was located. In an approximately 2,5 x 2 μm^2 area the distribution of the osmium was examined. The red colour indicates the location of the osmium atoms (fig. 5.7). For comparison, the corresponding SEM image of the examined area is also depicted.

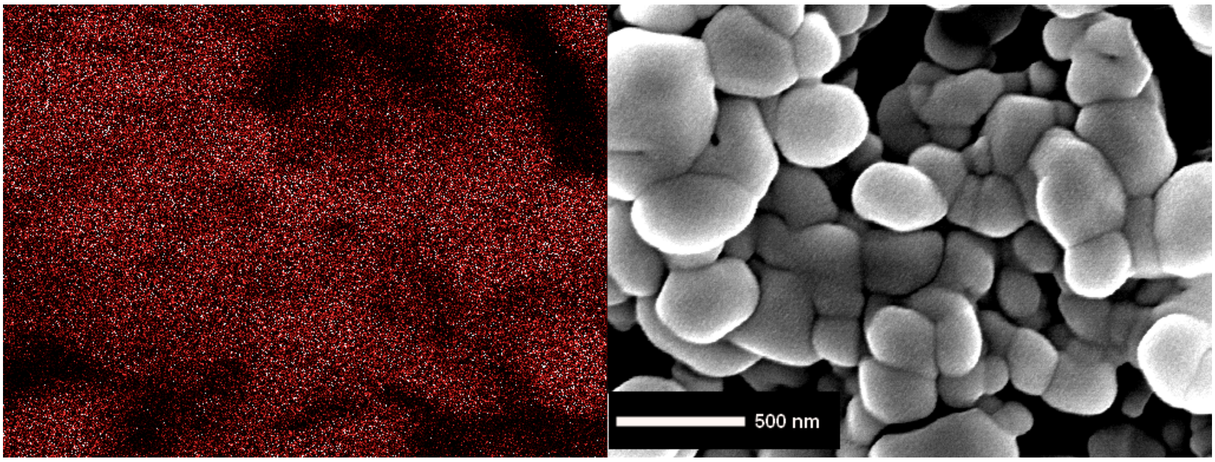

Fig.: 5.7 – EDS (left) and SEM (right) image of OsO_4 marked Hexolite.

According to the even distribution of the osmium, it is assumed that during the crystallization process TNT may have formed a layer around the RDX. As RDX has a noticeably lower solubility in acetone, it is most likely that the crystallization of RDX started earlier. The TNT may have crystallized around the RDX, that serves as crystal germ. Another approach to determine the distribution of RDX and TNT in the micron- and nanosized Hexolite was achieved by pressing small pellets with 4 mm in diameter and about 1,5 mm height. Afterwards, using a microtome, the surface of the pellets was scraped of about 0,2 mm in steps of 10 µm in order to obtain an even surface. The Raman spectrum of Hexolite is shown in figure 5.8, being only a superposition of the Raman spectra of pure RDX and pure TNT. A significant difference between the spectra from the microstructured and nanocrystallized product was not observed.

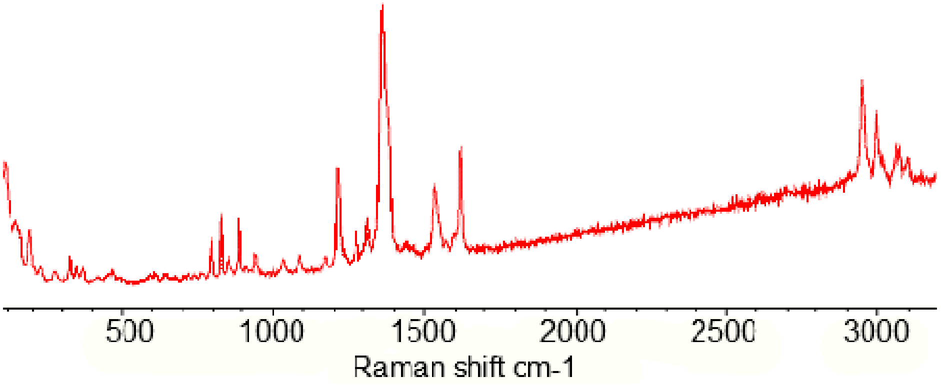

Fig.: 5.8 – Raman spectrum of nanocrystallized Hexolite.

From both pellets, a random 50 x 50 μm^2 area was marked within which every 1,5 µm the corresponding Raman spectrum was measured, resulting in overall 1156 measurements. By defining characteristic peaks as RDX and TNT, their distribution within the pellet could be pointed out. In figure 5.9, the distribution of RDX and TNT in the microstructured and nanocrystallized Hexolite is shown.

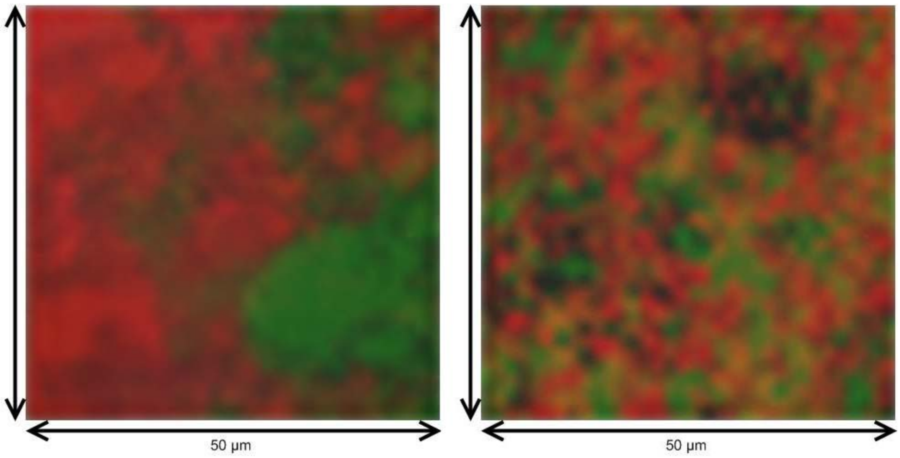

Fig.: 5.9 – Distribution of RDX and TNT in micron-sized (left) and nanocrystallized Hexolite (right).

The characteristic peaks, chosen for the identification of RDX and TNT, are:

Green:	TNT – Peak at 1620 cm^{-1}, measured in-between 1610 - 1630 cm^{-1}
Red :	RDX – Peak at 1272 cm^{-1}, measured in-between 1260 - 1280 cm^{-1}.

By means of the flash-crystallization process, an extraordinary high homogeneity in the composite was obtained. Those results correspond well with the EDS-SEM observations, indicating a distribution below the submicron scale.

The formation of co-crystals can be excluded, as the diffraction pattern of the Hexolite is a superposition of the TNT and RDX diffraction patterns, without any additional or missing peaks (fig. 5.10).

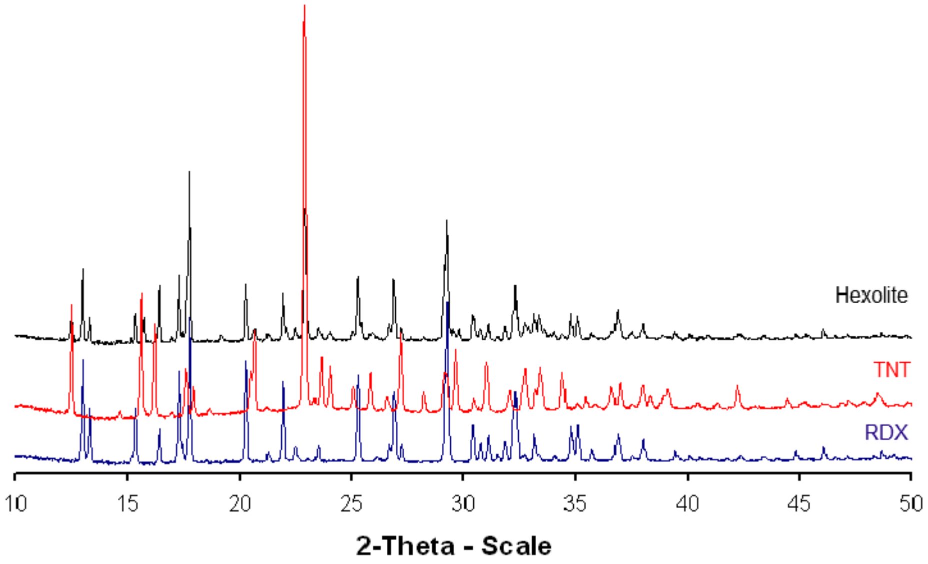

Fig.: 5.10 – X-ray diffraction pattern of nanocrystallized Hexolite (black), TNT (red) and RDX (blue)

The crystallite sizes of RDX and TNT in the nanocrystallized Hexolite are 585 and 415 Å, respectively. From the micron- and nanosized Hexolite, the sensitivity towards initiation by impact, friction and electrostatic discharge were measured, using the procedures described in chapter 1. The results of these measurements are listed in table 5.2.

Hexolite	Impact [J]	Friction [Nm]	ESD [mJ]
micro	6	54	353,6
nano	25,06	72	436,6

Tab.: 5.2 – Comparison of the sensitivity levels of micro Hexolite with those of a nano-sized Hexolite.

By means of the nanostructuration, a distinct desensitization of the Hexolite towards initiation by impact, friction and electrostatic discharge could be obtained.

In total, more than 150 g of this particular nanostructured Hexolite were produced so far for the synthesis of nanodiamonds [4] and detonation tests. In order to increase stability of the compressed material, isothermal compression tests are going to be performed.

5.2 Phase selective CL-20 crystallization

Since its development in 1987 [5], CL-20 represents the most powerful non-nuclear explosive. Due to its favourable explosive properties, CL-20 became one of the most promising energetic materials in recent years.

At room temperature, CL-20 may exist in four different allotropic forms, designated as α, β, ε and γ, that differ in their thermodynamic stability. According to Foltz *et al.*[6], the thermodynamic stability decreases in the order : $\varepsilon > \gamma > \alpha$-hydrat > β.

ε-CL-20 represents the most interesting allotropic form, as it has the highest density, the highest detonation velocity and is the most stable form. Even though ε-CL-20 represents the most stable form of CL-20, it is still highly sensitive against impact and friction. For ε-CL-20 with a grain size of 85 µm the impact and friction sensitivities are 1,7 – 2,2 J and 95 – 125 N [7], respectively. In order to enable its use in military systems, different research groups tried to desensitize CL-20.

Using a sonocrystallization process, Bayat and Zeynali [8] succeeded in the preparation of nano-Cl-20. The nano-CL-20 was less sensitive towards friction, impact and electrostatic discharge as the following table (tab. 5.3) shows.

Average particle size [µm]	Impact [cm]	Friction [kg]	Electrostatic discharge [J]
15	25	6,4	45
0,095	55	No reaction	60

Tab.: 5.3 – Sensitivity of micro- and nano-CL-20 [8].

Even though XRD measurements were made and the allotropic form of the starting material was confirmed to be the ε-form, the allotropic form of the nano-CL-20 was not mentioned in this publication, as well as further information about the sensitivity measuring methods. From own experiences in recrystallizing CL-20, it is very likely that β-CL-20 was formed in this process.

Similar observations were made by Kim *et al.*[9]. They observed that dissolved CL-20 in an evapourative crystallization process preferably forms the β-allotrope when the evaporation rate exceeds a certain value (0,125 mL/h). Using evaporation rates below said value, the formation of ε-CL-20 occurred. The crystallization experiments they had performed took in-between 1 day and 2 weeks. In crystallization experiments that lasted up to 40 h, the β-allotrope was formed, in experiments taking from 40 h up to 2 weeks, the ε-allotrope was obtained.

Brill and Tappan [10] described in their work the synthesis of nanocrystalline α-CL-20 coated with nitrocellulose, using a Sol-Gel process. Due to the presence of water in their process, the formation of the α-form was promoted [6]. The size of the α-CL-20 they have obtained, varied between 20 – 200 nm. They observed a slight desensitization of the impact sensitivity with increasing nitrocellulose content.

In compliance with Ostwald's rule of stage [11], also described by Mullin [12], if a substance may exist in more than one allotropic form, the formation of the kinetically favoured form is more likely to appear than the thermodynamic most stable. Therefore it is assumed that, depending on the evaporation speed, the different allotropic forms will occur in the order: β → α-hydrat → γ → ε.

In practice, the synthesis of β-CL-20 by flash-crystallization did not showed any problems and was possible with various solvents under different conditions. The process conditions for the preparation of β-CL-20 which was used for the later analyses are listed in table 5.4.

Nozzle [µm]	Temperature		CL-20 concentration [%-wt]	Pressure [bar]	Acetone/Cyclohexanon [v/v]
	Nozzle [°C]	Cyclone [°C]			
80	160	120	0,32	20	50/50

Tab.: 5.4 – β-CL-20 process conditions.

As starting material 250 mg of ε-CL-20 were dissolved in 50 mL acetone, then the same volume of cyclohexanone was added to the solution. The execution of the process was performed in the same manner as described in chapter 4, except that, because of the small amount of solution, only one cyclone was used for the collection of the particles. After the experiment, 170 mg of CL-20 were recovered in the cyclone. The product yield amounted 0,68.

Using Raman spectroscopy, the allotropic form can be determined [13]. Within the wavenumber band ranging from 780 – 880 cm^{-1} (fig. 5.11), each of the four allotropic forms possesses a characteristic *fingerprint*, by which each pure form of CL-20 can be identified.

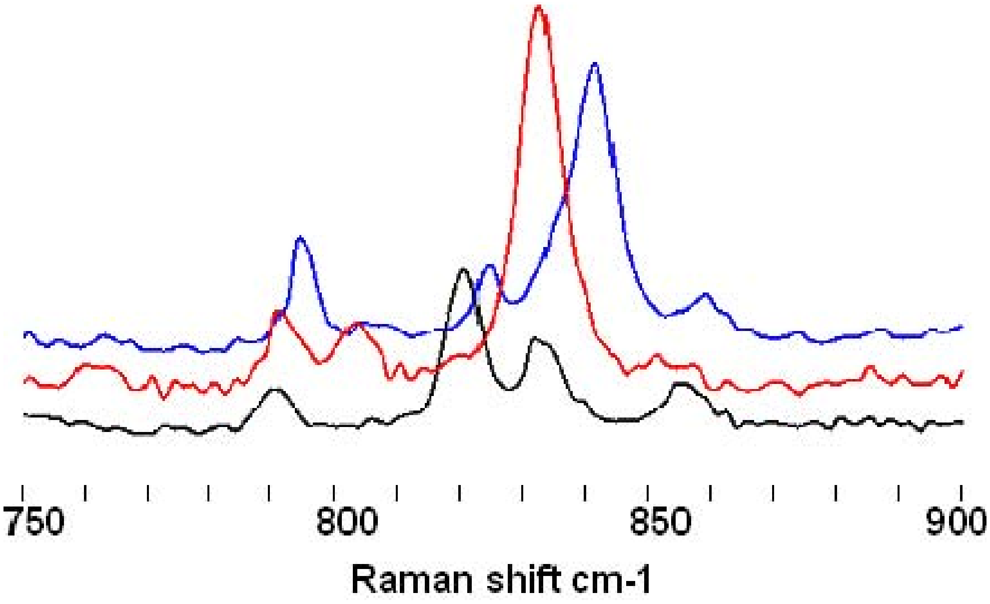

Fig.: 5.11 – Characteristic peak sequences for the identification of α- (blue), β- (red) and ε-CL-20 (black).

The Raman spectrum from the recovered product of the described experiment was recorded, which is depicted in figure 5.12 with the enlarged fingerprint area in figure 5.13.

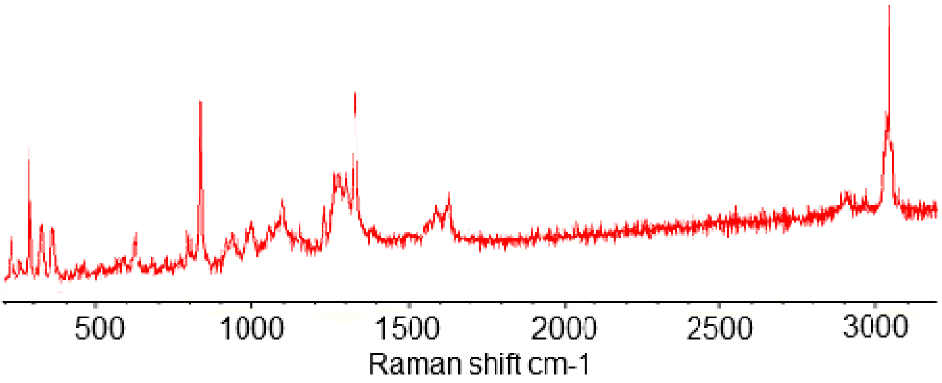

Fig.: 5.12 – Raman spectrum of nanocrystallized β-CL-20.

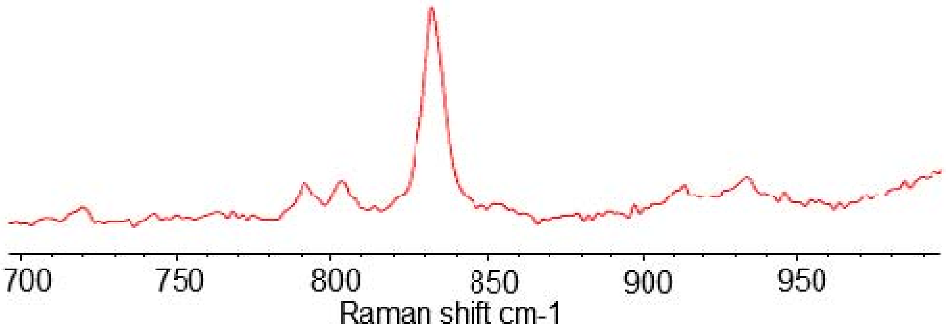

Fig.: 5.13 – Characteristic peak sequence of β-CL-20.

The specific particle surface amounted 8,1 m²/g. Using the density of β-CL-20, the median particle diameter was calculated to be 373 nm. This result corresponds well with the SEM image (fig. 5.14) that was taken from the sample, showing a median particle size of 293 nm with a variance of 80 nm.

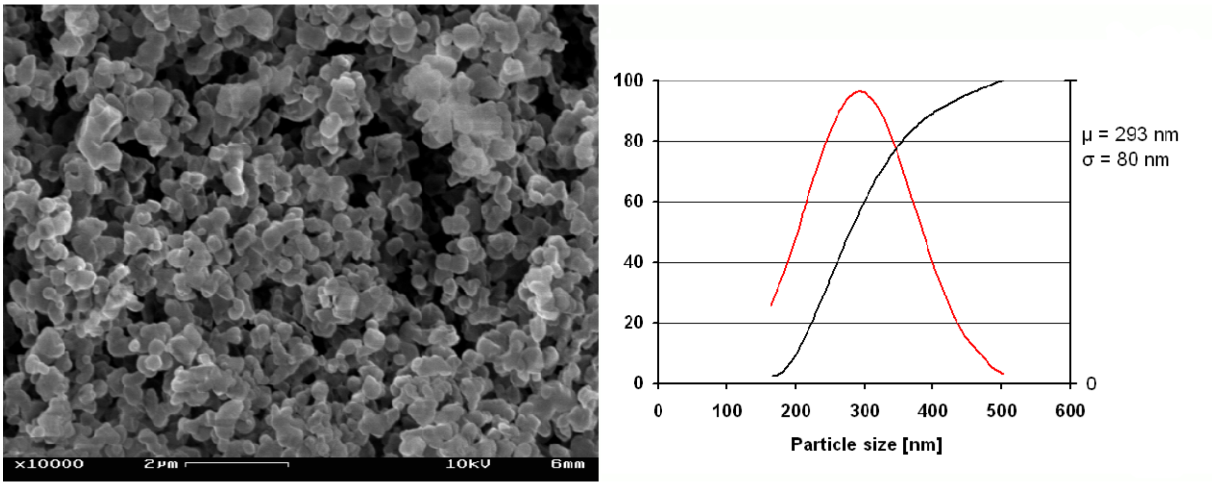

Fig.: 5.14 – SEM image and PSD of nanocrystallized β-CL-20.

In order to obtain the α-allotrope of CL-20, the flash-crystallization process had to be slowed down, to enable the formation of the more stable allotropes. As the formation of α-CL-20 is promoted by the presence of water, an acetone/water solvent was used for the preparation (tab. 5.5)

Nozzle [µm]	Temperature		CL-20 concentration [%-wt]	Pressure		Acetone/Water [v/v]
	Nozzle [°C]	Cyclone [°C]		Nozzle [bar]	Vacuum [mbar]	
80	160	100	0,30	20	13	90/10

Tab.: 5.5 – α-CL-20 process conditions.

The addition of water served in various ways. At first the thermodynamic properties of water helped to decrease the evaporation speed, then water is ought to have a stabilizing effect on the α-modification [6]. Then, the pressure in the atomization chamber was slightly increased by the injection of nitrogen during the experiment, increasing the pressure in the atomization chamber to 13 mbar.

In total, only 100 mL of the acetone/water solution was prepared. 250 mg ε-CL-20 were dissolved in 90 mL acetone, then 10 mL distilled water were added to the solution. The process was taken into operation in the standard manner, except that continuously a small amount of nitrogen was blown into the atomization chamber. With a needle valve, the nitrogen flow was set to a pressure of approximately 13 mbar in the atomization chamber. Because of the small amount of explosive, only one cyclone was used for product collection. In total 115 mg of CL-20 were collected, resulting in a product yield of 0,46.

The Raman spectrum of the collected CL-20 is depicted in figure 5.15. The characteristic peak sequence of α-CL-20, in-between 750 – 900 cm^{-1}, is shown in figure 5.16.

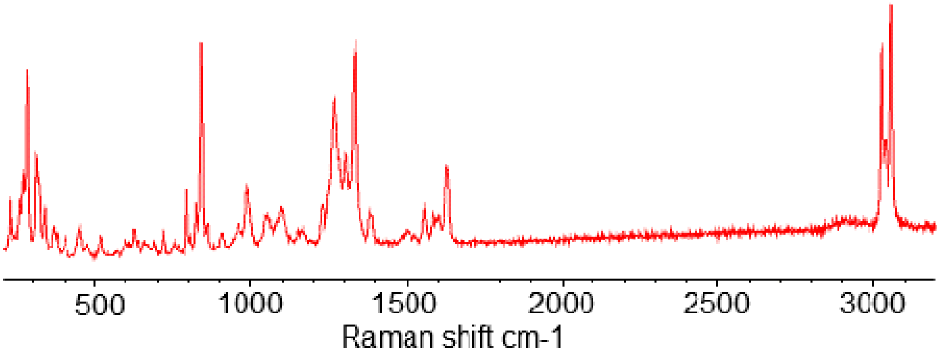

Fig.: 5.15 – Raman spectrum of nanocrystallized α-CL-20.

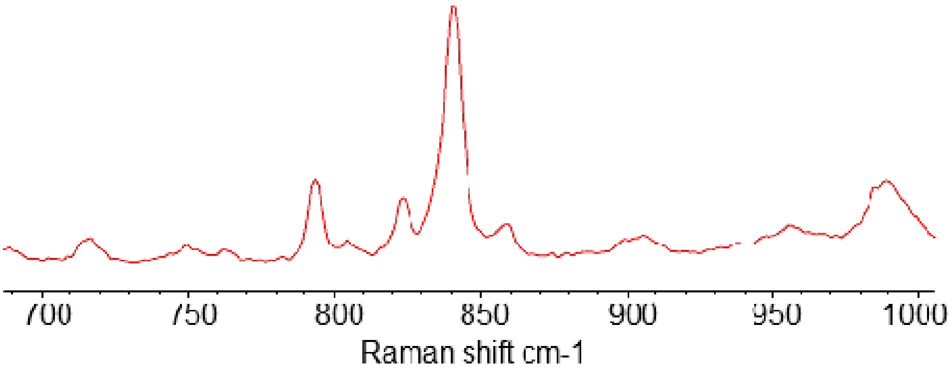

Fig.: 5.16 – Characteristic peak sequence of α-CL-20.

As the crystallization process had to be *slowed down,* an increase of the particle size was expected. The SEM analyses of the nanocrystallized material amounted a median particle size of 401 nm with a variance of 105 nm (fig. 5.17). Because of the low contrast, the particle size of only about 40 particles could be measured.

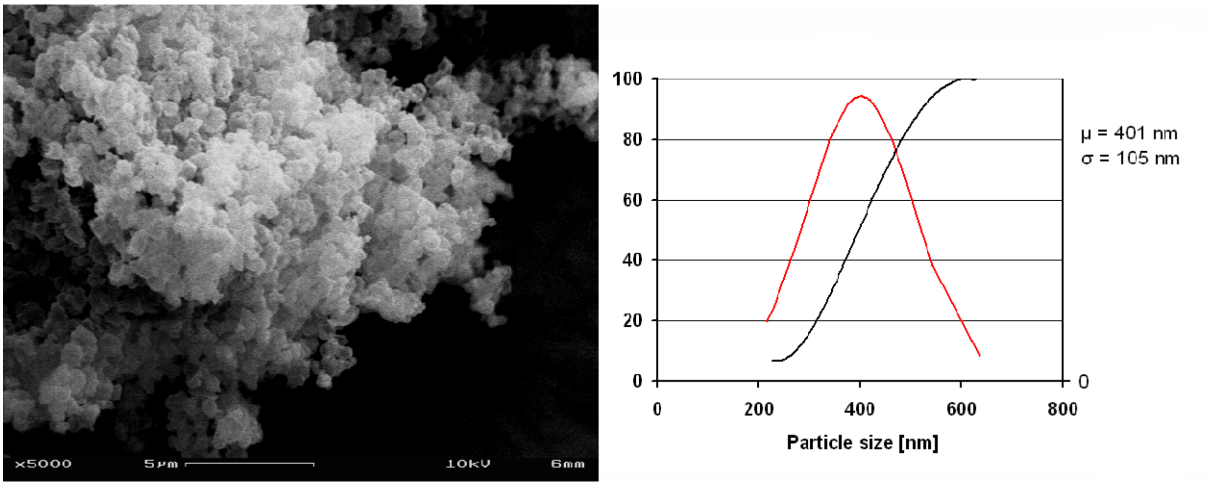

Fig.: 5.17 – SEM image and PSD of α-CL-20.

The BET surface of the α-CL-20 amounted 7,12 m²/g, resulting in a slightly larger median particle diameter of 427 nm.

DSC measurements of the ε-CL-20 starting material and the nanocrystallized α- and β-CL-20 (fig. 5.18), clearly show the higher thermal stability depending on the allotropic form.

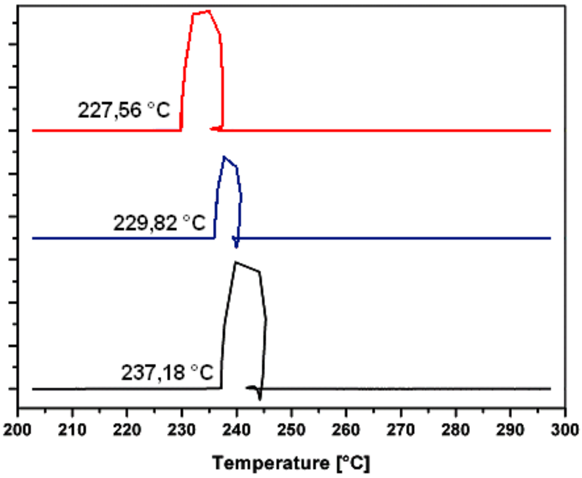

Fig.: 5.18 – Decomposition signal of (red) β-, (blue) α- and (black) ε-CL-20.

At the moment, attempts are made in order to obtain a submicron ε-CL-20 by co-crystallization with other energetic materials.

Summary of the chapter

In this chapter, the successful nanocrystallization of two products was described, showing the wide application scope and the possibilities of the process, elaborated during the present thesis.

Compositions consisting of RDX and TNT are widely known as Hexolite. Over TNT, Hexolite has the advantage of being more powerful, but can be processed with the same ease as TNT. A homogeneous distribution of both components is of highest importance, but can only hardly be realized with common techniques. Especially for the detonation-synthesis of nanodiamonds a homogenous structure is required.

In an unmatched quality, nanostructured Hexolites can be prepared in a single process step by the flash-crystallization of RDX/TNT 60/40 solutions. A change of the RDX/TNT ratio in the final product did not happen. SEM and Raman analyses of pressed Hexolite pellets have shown that a mixing of both components below the submicron scale was achieved. The median particle size of RDX and TNT in the nanostructured Hexolite varied in-between 100 and 300 nm, whereby the structure was roughly spherical. Using SEM, in the sites of fracture of open pellets, isolated 2 - 3 µm long particles could be found. By their structure and their closer environment it is assumed that those particles are TNT which has melted as a consequence of adiabatic compression of enclosed gases and recrystallized afterwards. Due to the recrystallization process, internal stress within the pellet may have caused their breaking. A co-crystallization between both explosives could be excluded by Raman and XRD measurements. For comparison purposes, a micron sized reference-Hexolite was prepared from the same RDX and TNT raw materials. Both finely grounded components were intensely dry mixed using a TURBULA® blender. Despite the homogenous appearance of the readily mixed product, SEM and Raman analyses revealed an exceedingly heterogeneous distribution of both components. Sensitivity measurements have shown that the nanostructured Hexolite was less sensitive towards initiation by impact or friction than the micron sized Hexolite. More than 150 g of Hexolite were prepared by the flash-crystallization process so far, used, among other things, for the preparation of the worldwide first nanostructured Hexolite charges.

The phase selective nanostructuration of the highly powerful CL-20 reveals another strength of the flash-crystallization process. At room temperature and atmospheric pressure, CL-20 may exist in four different allotropic structures. The thermodynamic stability of each phase decreases in the order $\varepsilon > \gamma > \alpha$-hydrat $> \beta$, resulting, at the same time, in an increase of the sensitivity towards initiation. Due to its thermodynamic and physical properties, ε-CL-20 represents the most favoured structure, which, however is only hard to prepare by recrystallization because of its unfavourable kinetic. In fast crystallization processes the preferred formation of β-CL-20 could be observed. In contrast to the thermodynamic stability, it is assumed that in dependence of the crystallization speed, the different allotropic structures appear in the order $\beta > \alpha$-hydrat $> \gamma > \varepsilon$.

By means of the flash-crystallization process, the selective nanostructuration of β- and α-CL-20 succeeded. Because of its kinetic, the formation of the β-structure succeeded with various solvents under different conditions. By decelerating the crystallization process, especially by using an acetone/water solvent, but also by increasing the working pressure in the atomization chamber, the formation of α-CL-20 was attained. By using Raman spectroscopy, the corresponding structure could be validated. As expected, the deceleration of the crystallization process caused the formation of larger particles. The median particle size of the β-CL-20 amounted 293 nm and those of α-CL-20 almost 400 nm.

References

[1] Lea, J.; Adesina, A.; *Fluent News,* Fall, **2006**, pp. 26-27.

[2] Risse, B.; Spitzer, D.; Hassler, D.; Schnell, F.; Comet, M.; Pichot, V.; Muhr, H.; *Chem. Eng. J.*, 203, **2012**, pp. 158-165.

[3] Piazzon, N.; Rosenthal, M.; Bondar, A.; Spitzer, D.; Ivanov, D.; *J. Phys. Chem. Solids*, 71 (2), **2010,** pp.114-118.

[4] Pichot, V.; Comet, M.; Fousson, E.; Baras, C.; Senger, A.; Le Normand, F.; Spitzer, D.; *Diamond Relat. Mater.,* 17, **2008,** pp. 13-22.

[5] Nielsen, A.; US Patent 5,693,794; Dec. 2, **1997**.

[6] Foltz, M.; Coon, C.; Garcia, F.; Nichols III, A.; *Prop. Expl. Pyr.*, 19, **1994**, pp. 19-25.

[7] Dumas, S,; These, Dosage du polymorphisme : spectrométrie IRTF et chimiométrie, Application aux formes polymorphes du CL-20.Université Claude-Bernard, Lyon, **2003.**

[8] Baynat, Y.; Zeynali, V.; *J. Energ. Mater*., 29, **2011**, pp. 281-291.

[9] Kim, W.; Lee, M.; Kim, J.; Park, Y.; Hwang, *J., Ind. Eng. Chem. Res.,* 46, **2007**, pp. 1500-1504.

[10] Brill, T.; Tappan, B.; *Prop. Expl. Pyr.,* 28 (5), **2003**, pp. 223-230.

[11] Ostwald, W.; *Z. Phys. Chem.,* 22, **1897**, pp. 289-330.

[12] Mullin, J.;Crystallization, 4th Ed, **2004,** Elsevier Butterworth- Heinemann.

[13] Goede, P.; Latypov, N.; Östmark, H.; *Prop. Expl. Pyr.*, 29 (4), **2004**, pp. 205-208.

6 Conclusions and perspectives

The flash-crystallization process, submitted for a patent, which has been developed and described in this work, is a promising process which could be the next step towards an industrial production of submicron and nanosized particles or more generally a very large spectrum of energetic or inert or hybrid nano-composite materials. By means of different explosives, the numerous fields of application of this process were demonstrated. Because of using mainly classic solvents, the flash-crystallization process can be adapted to a large number of different substances.

Beside the process development and the plant construction, both consuming most of the time, a parametric study was performed in order to evaluate the influence of the different process parameters on the particle properties. The significant process parameters are:

- Nozzle temperature
- Nozzle pressure
- Type of solvent
- Nozzle diameter
- Explosive concentration

The primary objective of the parametric study was to decrease the particle size and the particle size distribution, in consideration with economic and safety relevant aspects.

Because of the high reactivity of nanostructured particles, the determination of the particle size and the particle size distribution was only possible by analyses of SEM images. Measuring techniques basing on dynamic-light-scattering or Mie-scattering are not suited as the sample has to be dispersed in a liquid, causing its immediate recrystallization.

In summary, measures to enhance the evaporation rate, especially by increasing the nozzle temperature or by using a thermodynamic more suited solvent, lead to a decrease of the particle size. In view of the production rate, the nozzle pressure above a certain value plays an important role, as the volume flow rate increases without altering the particle size.

With regard to the nozzle diameter, if the purpose admits it, it should always be chosen as small as possible, as the smaller nozzles provide a finer droplet size. In anticipation with possible fields of application, it can be quite necessary to use larger nozzles for solutions containing dispersed solids. The importance of the solute concentration was only discovered in the parametric study. With increasing concentration, the particle size decreased while the production rate increased at the same time. Due to this favourable fact, relatively large amounts of nanomaterials can be prepared with little equipment. In order to obtain an even smaller product, further attempts should be made in optimizing the nucleation- and the agglomeration mechanism.

Besides the parametric study, two nanostructured products were prepared, showing the wide application scope of the flash-crystallization process. Other explosives were also nanocrystallized during the thesis but they are not mentioned here for confidential reasons. The synthesis of a nanostructured Hexolite by flash-crystallization represents a novelty. The product quality and quantity of this Hexolite is unrivalled and can not be reproduced by other techniques such as RESS or wet-milling. The most important field of application for this nanostructured Hexolite is the synthesis of nanodiamonds; another process which has been submitted for a patent. The allotrope selective flash-crystallization of CL-20, shows the precision and the versatility with which the process can be operated.

In view of future applications, the possibilities of the flash-crystallization process are sheer endless. By choosing a suited solvent or solvent mixture, the process can be applied to a large number of organic and inorganic substances which, otherwise, can not be treated by plasma processes or other high-temperature techniques.

Another promising field will be the preparation of nano-composites. Composites, consisting of 2, 3 or more dissolved components, can be prepared in a single production step. In addition, by dispersing insoluble nano- or microparticles in those solutions, nano-coatings can be made by this technique. Using two or more individual controlled nozzles, products with multiple and well defined particle size distributions can be prepared. As soon as the cyclone emptying becomes automated, the process could be directly connected with other processing units, reducing the risk of an exposition to nanoparticles.

A scanning mobility particle sizer would represent a useful supplement to the flash-crystallization process, as it enables the in-situ measurement of the particle size distribution from the gas phase with a possible feed-back for the parameter on-line regulation of the process.

7 Summary

In the worldwide course to insensitive explosives and energetic materials, the research is focused on the development of nano-explosives. Despite considerable research in this domain, the successful large-scale production of nano-explosives was not possible so far.

The unintentional initiation of an explosive, be it through the influence of heat, electricity or a mechanical impulse, describes an unwanted mechanism, causing a reaction of the explosive.
A significant role in this mechanism plays the formation of so called *hot-spots*. As hot-spot, all sorts of inhomogeneities, such as entrained gases, pores, impurities or crystal defects, within the explosive structure are designated which are able to convert externally applied energy into heat [1, 2]. Furthermore, it is distinguished between internal, within the explosive particle, and external, at the surface of the explosive particle, hot-spots [3]. Best-known example of such a heat generating process is the adiabatic compression of entrained gas bubbles in consequence of a mechanical impulse, acting on the explosive. The heat that is emitted from the hot-spot, depending on its size, have to be superior a critical temperature and must persist in-between 10^{-5} - 10^{-3} s [4] to initiate a reaction of the explosive. The detonation sequence usually happens as follows:

Initiation → Hot-Spot → Deflagration → Detonation.

Initiation: Describes the primary unintentional event acting on the explosive, like the impact of a projectile or great heat caused by a fire.

Hot-Spot: Area within the explosive where the primary supplied energy is converted into heat.

Deflagration: A decomposition mechanism where propagation of the reaction front happens with a speed lower than the speed of sound within the explosive. The propagation velocity is significantly affected by the heat dissipation in the explosive material and can pass over into a detonation.

Detonation: A decomposition mechanism, initiated by strong shock wave, that traverses the material with a speed higher than the speed of sound in the explosive.

In military applications, a corresponding powerful initiation, consisting of an initiating explosive and a booster charge, is used, so that the initiation directly transfers into a detonation:

Initiation → Detonation

Therefore, the hot-spot sequence represents the lowest-energy initiation mechanism, being able to cause a decomposition reaction of the explosive. As hot-spots have a key function in the initiation of explosives, their elimination should desensitize explosives toward external events. Tarver [4] found out, that the size of a hot-spot must be in-between 0,1 – 10 µm and must attain a critical temperature of at least 700 K, in order to start a reaction. Furthermore, a relation between the size of a hot-spot and its critical temperature exists. With decreasing hot-spot size, the critical temperature increases [4]. So, by decreasing the particle size, the size of the intercrystalline hot-spots decreases as well, resulting in a desensitization of the explosive [5].

Besides the desensitization of the explosives, nano-explosives are ought to have a smaller run-to detonation distance [4], as potential hot-spots are more evenly distributed in the explosive. Because of the smaller particle size and the smaller hot-spots, that require higher temperatures, the liberated energy may diffuse more rapidly to adjacent particles to create further hot-spots.

In the past fifteen years, the following processes for the preparation of nano-explosives were developed:

- Wet-milling
- Sol-Gel processes
- Vacuum-Condensation
- Electrospray
- Ultrasound assisted nanocrystallization
- Rapid expansion of supercritical solutions

In the **wet-milling process** [6], RDX is dispersed in water with a couple of additives and is then milled for about 1h in a mill. Then the grinded RDX is filtered out by a 100 nm filter and is allowed to dry in vacuum. By this technique, the only *top-down* process, up to 16 g of nanostructured RDX could be prepared per batch. Due to the presence of large amounts of liquid, the grinded but still wet product was prone for Ostwald-ripening and had to be dried immediately.

For the **Sol-Gel process** [7, 8] RDX with tetramethoxysilane and a catalyst, initially dissolved in a solvent, were allowed to solidify. After the gelification, the solvent was extracted from the silica matrix. Water was used as extracting agent, in which RDX is nearly insoluble, inducing the crystallization of dissolved RDX. The water that remained in the pores was subsequently extracted using supercritical CO_2. The "contamination" of the product with SiO_2, is one of the major drawbacks of this process.

In the **vacuum-condensation process** [9, 10], RDX initially is evaporated in the vacuum at temperatures between 145 – 202 °C and then gets caught on cooled quarts glass sample carriers. The smallest particles that were made by this technique had a size of 50 nm. The biggest drawback of this process is the extremely low production capacity and the high temperatures that are dangerously close to the decomposition temperature.

The **electrospray process** [11] is a spray drying technique, where a RDX-acetone solution is slowly pumped (2,8 mL/h) through an open metal capillary. The opening of the capillary is pointed towards a metal plate which is positioned a few centimetres away. By applying a high voltage between the capillary and the metal plate, a Taylor-cone arises from the capillary opening. The Taylor-cone disrupts into finest droplets, which are attracted by the opposite charged metal plate. During the flight, the solvent evaporates and the explosive crystallizes. Because of the extraordinary small volume flow, only smallest amounts of RDX can be prepared within a short period. Furthermore, the use of high tension in combination with evaporating acetone holds an enormous hazard.

The **ultrasound assisted nanocrystallization** [12, 13] also belongs to the spray drying processes. By using ultrasonic transducers, a RDX-acetone solution is atomized into a fine mist. With an inert gas flow, the mist is directed into an electric heated furnace where the solvent evaporates. The crystallized explosive is separated from the gaseous solvent in an electrostatic precipitator. The depleted gas flow passes the electrostatic precipitator and condenses in two downstream coolers. In previous studies on this process, an increase of the RDX concentration could be observed, making a constant process control nearly impossible. In order to optimize this process, the ultrasonic transducers were replaced by a nozzle, which was at ISL the first step towards the flash-crystallization process.

The preparation of nanoparticles by the expansion of a supercritical fluid [14, 15], is widely known as the RESS process (**Rapid Expansion of Supercritical Solutions**). The RESS process uses supercritical CO_2 at temperatures at 70 – 75 °C and pressures in-between 150 – 295 bar, in order to dissolve RDX. Subsequently, by means of a nozzle, the supercritical solution is depressurized to a pressure below the critical conditions. Because of the strong pressure and temperature drop, the solubility of the RDX suddenly drops, causing its crystallization. In addition, due to the strong temperature drop, the sub-cooled CO_2 condenses at the surface of the RDX particles, which is essential for its separation. The low solubility of RDX in supercritical CO_2 (0,25 mg RDX / 1 g CO_2 at 480 bar and 80 °C) makes this process not suitable for a large-scale production.

As a consequence of the insufficient production capacity of the individual processes, the information content about nano-explosives is sparse. All publications of the recent years refer to results that could be obtained with small amounts of material (< 1 g). In view of an industrial application, the here presented flash-crystallization process was developed.

The **flash-crystallization** process bases on the principle of flash-evaporation, where a pressurized and heated solution is subject to a sudden pressure drop. By decreasing the surrounding pressure, the boiling temperature of the solvent decreases as well. The liquid is now in a superheated and metastable state, which is characterised by the fact, that the actual temperature of the liquid is higher than its boiling temperature. Due to the thermodynamic imbalance of the liquid, the excess thermal heat is converted into latent heat by an adiabatic evaporation process. The speed with which the evaporation process happens, significantly depends on the degree of superheating. The higher the liquid is superheated, the more thermal energy is stored within, and the higher will be the evaporating proportion of the liquid. The ratio of evaporated solvent to initial solvent is designated as the evaporation ratio X_{vap}:

$$X_{vap} = \frac{\Delta m_{flash}}{m_0}$$

The amount of solvent Δm_{flash}, evaporating in consequence of the pressure drop, can be calculated over the heat balance:

$$\Delta m_{flash} = m_0 \cdot (T_0 - T_S) \frac{c_{p,l}(T_0)}{\Delta_{vap} H(T_S, P_S)}$$

with $c_{p,l}(T_0)$, the molar heat capacity of the solvent at the temperature T_0 and $\Delta_{vap} H(T_S, P_S)$ the molar evaporation enthalpy at the reduced pressure P_S and corresponding boiling temperature T_S. A decisive role in the choice of a certain solvent is, besides its solubility, the ratio of the heat capacity to the evaporation enthalpy, which should be as large as possible. For the preparation of small and dry particles by the flash-crystallization process, the evaporation ratio should be as high as possible, preferably $X_{vap} = 1$. However, in practice satisfying results were already attained with $X_{vap} = 0{,}7$.

Because the energy required for the evaporation is solely withdrawn from the superheated solvent, the solvent has to fulfil certain demands. For a better handling, the normal boiling point should be in-between 30 – 70 °C. The molar heat capacity should be as high as possible, whereas the evaporation enthalpy should be as low as possible. Furthermore, the solvent must be thermally stable to about 300 °C.

From a number of solvents, acetone and methyl tert-butyl ether (MTBE) were chosen for this work. From the studied solvents, acetone possesses the worst thermodynamic properties but still represents an excellent solvent. MTBE was chosen for its extraordinary thermodynamic properties, allowing working at significant lower temperatures. As acetone and MTBE are miscible in any proportion and their boiling temperature only differ by 1 °C, they also can be used for the preparation of binary solvents.

The installation, developed in this doctoral thesis, is divided into a high-pressure and a low-pressure section (fig. 7.1). The high-pressure section comprises both storage tanks B1, B2 and the nozzle D1. By means of compressed nitrogen, the overpressure in the storage tanks is generated. The low-pressure section comprises the atomization chamber R1, the cyclones C1, C2 and the vacuum pump P1. The transition from the high-pressure to the low-pressure section represents the hollow cone nozzle D1. Usually, the pressure in front of the nozzle amounts at least 40 bar and behind the nozzle 5 mbar absolute pressure. The nozzle is heated by a 150 W heating jacket. Furthermore, 150 W electric heat tracings are installed in front of the cyclones. All heating circuits are controlled by Proportional-Integral-Derivative (PID) controllers.

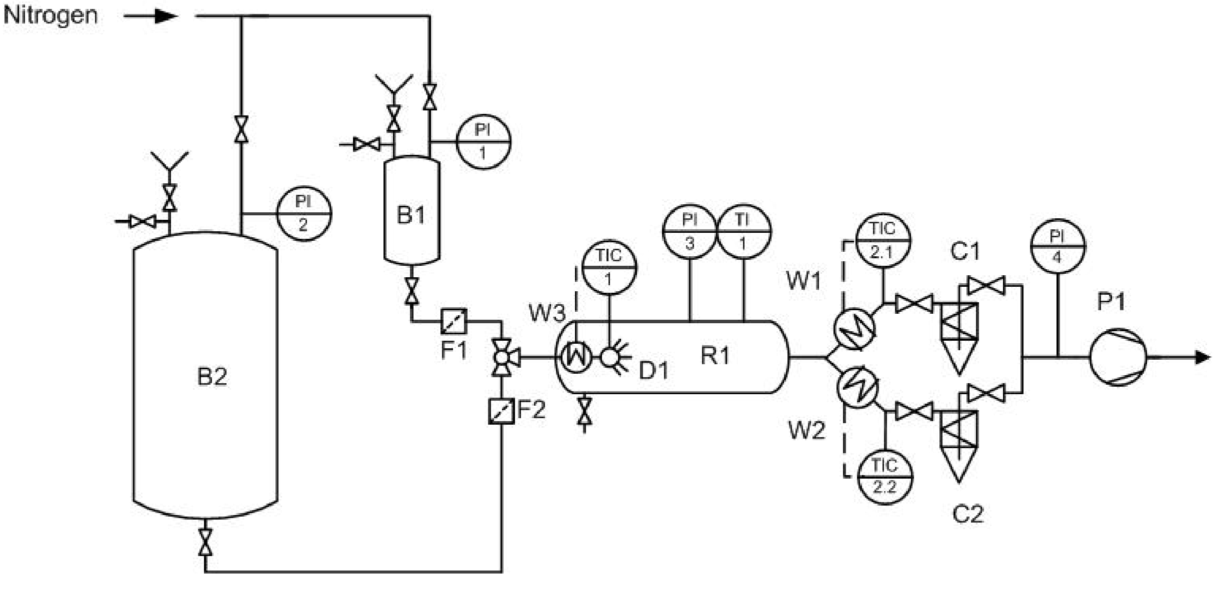

Fig.: 7.1 – Flowchart of the flash-crystallization process.

During operation, one of the storage tanks is only filled with solvent, whereas the second tank is filled with the prepared explosive-solution. Only one cyclone is in operation, while the second cyclone is kept in the stand-by mode.

In order to reduce the particle size and the particle size distribution of nanocrystallized RDX, a parametric study of the process conditions was performed, in consideration of economic and safety relevant aspects. The study was performed on RDX, as it forms only two allotrope structures from which one is instable and transposes into the more stable within a short period [16, 17].

Before the parametric study began a standard experiment was performed in order to identify the individual parameters and serving as reference for the different experiments of the study.
In total, the following five process parameters were investigated within the framework of this study:

- Nozzle temperature
- Nozzle pressure
- Type of solvent
- Nozzle diameter
- RDX-concentration

The conditions of the standard experiment are listed in the table below (tab. 7.1):

Nozzle [µm]	Temperature		Solvent v/v [Acetone/MTBE]	Pressure [bar]	RDX-conc. [%-wt]
	Nozzle [°C]	Cyclone [°C]			
60	160	80	100/0	40	1,0

Tab.: 7.1 – Process parameters of the standard experiment.

In the parametric study, always one parameter was changed, while the remaining parameters were kept identical with the standard experiment. Every experiment of the parameter study was, for reasons of reproducibility, performed several times. Per run, about 1 g of product was prepared, which was subsequently examined using DSC, BET and XRD. Furthermore, selected samples were also examined using nanocalorimetry, Raman spectroscopy and SEM.

The **nozzle temperature** in the parametric study corresponds the overheating temperature T_0. The higher the nozzle temperature, the more violently the evaporation process occurs and the more solvent evaporates. The standard experiment was performed at 160 °C, further experiments at 150, 170 and 180 °C were performed in the parametric study. Because of the high thermal load and the low product yield, only one experiment was performed at 180 °C.
The evaluation of the results revealed, that with increasing nozzle temperature, the particle size and the particle size distribution decreased. The graphic evaluation of SEM images showed, that the median particle diameter in the standard experiment amounted 599 nm with a variance of 238 nm. Heating the nozzle to 170 °C, the

median particle diameter and the variance decreased to 499 nm and 186 nm, respectively. This trend was confirmed by the BET surface that increased with increasing temperature.

According to Richter [18], the increase of the **pre-pressure** causes a decrease of the droplet size. The nozzle that was used, was a hollow cone nozzle with 60 µm orifice from the company Plantfog [19]. From the manufacturer, a pre-pressure of 100 bar was recommended for this nozzle. However, the standard experiment was performed at 40 bar. In the parametric study further experiments were performed at 50, 60 and 70 bar. Experiments at pressures < 40 bar were not performed, because at such low pressures, the formation of the hollow cone structure is incomplete. The evaluation of the BET measurements suggests that with increasing pressure a decrease of the particle size happened. Nevertheless, RDX which was prepared at 50 and 70 bar was additionally examined using SEM. The analysis of the SEM images showed that at 70 bar only a marginal reduction of the median particle size was obtained, however the particle size distribution became larger.

Because of the use of RDX, the number of potential **solvents** was very limited. From the group of low-boiling solvents [20], acetone has the highest solubility for RDX. As RDX is almost insoluble in MTBE, binary mixtures of acetone/MTBE had to be used in this part of the parametric study. The standard experiment was performed using pure acetone. In the parametric study acetone/MTBE v/v mixtures of 90/10, 80/20, 70/30 and 60/40 were used. Because of the favourable thermodynamic properties of MTBE, the evaporation ratio rose with increasing MTBE content. At the same time, the solubility for RDX decreased. The evaluation of the results revealed that, similar to the increase of the temperature, the use of MTBE may accelerate the evaporation process. Furthermore, because of the lower solubility a higher degree of supersaturation was attained, leading to the formation of more nucleation germs. This is well shown in the particle size distribution of the RDX which was crystallized from the acetone/MTBE 60/40 solvent. The median particle size amounted only 434 nm with a variance of 132 nm.

According to Richter [18], the use of a smaller **nozzle diameter** is ought to lead to a finer spray pattern. The available nozzle diameter for this test were 60, 80 and 100 µm. Exceptionally a 0,7 % RDX-solution was used in order to avoid clogging of the cyclones. In the direct comparison of the 60 and 80 µm nozzle a distinct increase of the particle size, accompanied by an enlargement of the particle size distribution was observed. The evaluation of the SEM images revealed a median particle size of 650 nm with a variance of 252 nm for the 60 µm nozzle. Prepared under the same conditions but with a 80 µm nozzle, the median particle size rose to 887 nm with a variance of 322 nm. This study also showed that, by using the 100 µm nozzle the volume flow rate rose so much, that the formation of droplets could be observed in the atomization chamber. Due to the condensing acetone an increasing amount of RDX was dissolved again. For this reason, the product yield of the 100 µm nozzle was more than 3 times lower than the product yield obtained by the 60 µm nozzle.

The **explosive concentration** in the superheated solvent has a significant influence in terms of particle size and production capacity. Besides the standard experiment, performed with a 1 % RDX-solution, solutions with 0,5; 0,7; 1,5; and 2,0 % RDX-content were used in this parametric study. As the course of the BET curve and the evaluation of the SEM images clearly indicate, the particle size and the particle size distribution decrease with increasing RDX-concentration. While the median particle size from the 0,5 % RDX-solution was still at 673 nm, it continuously declined with growing concentration. At the highest concentration in this parametric study, the median particle diameter amounted only 408 nm with a variance of 174 nm. The reason for this behaviour is the higher and earlier appearing supersaturation. With increasing supersaturation, the number of crystal germs increases, while the nuclei size decreases. A further effect which appears to play a role as well, is the initiation of the evaporation process by the crystal germs.

Because in the moment of the pressure drop the superheated liquid is in a highly metastable state, the presence of crystal germs may act as boiling germs, inducing an earlier and faster evaporation. Also remarkable is the fact, that with increasing concentration, the production rate rose as well. The highest production rate, obtained with the 2 % RDX-solution amounted 4,2 g/h.

After the parametric study, an experiment under optimized conditions was performed (tab. 7.2).

Nozzle [µm]	**Temperature**		**Solvent v/v [Acetone/MTBE]**	**Pressure [bar]**	**RDX-Conc. [%-wt]**
	Nozzle [°C]	**Cyclone [°C]**			
60	170	100	75/25	50	1,5

Tab.: 7.2 – Optimized process parameters.

Compared with the standard experiment, the nozzle temperature, the nozzle pressure and the RDX-concentration were increased. An acetone/MTBE 75/25 mixture was used as solvent.

The evaluation of this experiment revealed that, compared with the standard experiment, a decrease of the particle size was obtained, which, however, was not as high as expected. SEM images showed a median particle size of 482 nm with a variance of 195 nm. It was striking that the RDX crystallite size remained in-between 600 – 700 Å over the whole parametric study. This suggests that the mechanism of nuclei formation and crystal growth happened largely under constant conditions. Consequently, further agglomeration mechanisms must exist, defining the final particle size.

In addition to the parametric study on RDX, the nanocrystallization of two further products was demonstrated, showing the versatility of the flash-crystallization process.

Nanostructured compositions of RDX and TNT with a mass ratio of 60/40 were prepared by flash-crystallization in a single step. The ratio of both explosives in the final product matched exactly the ratio from the starting solution. The particle size in the final composition amounted in-between 100 and 300 nm. Basing on SEM and Raman analyses, a highly homogeneous distribution of both explosives below the submicron scale was obtained. The formation of a core-shell structure has still to be verified. A such homogeneous distribution of nanostructured RDX and TNT is particularly important for the synthesis of nanodiamonds. With the preparation of more than 150 g of this energetic material, the worldwide first nanostructured charges were prepared.

Another field of application of the flash-crystallization process is the allotrope-selective crystallization of CL-20. At room temperature CL-20 can exist in the four different allotropic structures α, β, ε and γ, in which the ε-structure if the most favored due to its thermodynamic and energetic properties. The thermodynamic stability of the individual phases declines in the order $\varepsilon > \gamma > \alpha$-hydrat > β [21], corresponding to an increase of the sensitivity towards initiation. However, in fast crystallization processes the formation of the less stable β-structure is favored. By optimizing the parameters of the flash-crystallization process, the selective preparation of β-CL-20 and the more stable α-CL-20 succeeded. The median particle size of the β-CL-20 amounted 293 nm with a variance of 80 nm. As the α-allotrope is stabilized by the presence of water, a few percent of water were added to the solvent. Because of the incomplete evaporation process in the atomization chamber, the atmosphere is slightly enriched with water for a short time. The prepared α-CL-20 had a median particle size of 401 nm with a variance of 106 nm.

References

[1] Field, J.; *Acc. Chem. Res.*, **1992**, 25, pp. 489-496.

[2] Czerski, H.; Thesis, Ignition of HMX and RDX. Cambridge, England, **2006**.

[3] Zygmunt, B.; *Prop. Expl. Pyr.*, 7, **1982**, pp. 107-109.

[4] Tarver, C.; Chidester, S.; Nichols, A.; *J. Phys. Chem.,* 100, **1996**, pp. 5794-5799.

[5] Stepanov, V.; Anglade, V.; Bezmelnitsyn, A.; Krasnoperov, L.; *AIChE Annual Meeting*, **2006**, San Francisco.

[6] Redner, P.; Kapoor, D.; Patel, R.; Chung, M.; Martin, D.; Production and characterization of nano-RDX, Report, U.S. Army, RDECOM-ARDEC Picatinny, NJ 07806-5000, **2006**.

[7] Tillotson, T.; Hrubesh, L.; Fox, G.; Simpson, R.; Lee, R.; Swansiger, R.; Simpson, L.; Sol-Gel processing of energetic materials, 5th international symposium on aerogels, France, **1997**.

[8] Simpson, R.; Lee, R.; Tillotson, T.; Hrubesh, L.; Swansiger,R.; Fox, G.; US 2005/0092405.

[9] Frolov, Y.; Pivkina, A.; Ul'yanova, P.; Zav'yalov, S.; *Comb. Expl. and Shock Waves*, 38 (6), **2002**, pp. 709-713.

[10] Pivkina, A.; Ul'yanova, P.; Frolov, Y.; Zav'yalov, S.; Schoonman, J.; *Prop. Expl. Pyr.*, 29 (1), **2004**, pp. 39-48.

[11] Radacsi, N.; Stankiewicz, A.; Creyghton, Y.; van der Heijden, A.; ter Horst, J.; *Chem. Eng. Technol*. **2011,** 34 (4), pp. 624-630.

[12] Spitzer, D.; Baras, C.; DE 10 2007 003 396 A1, 23.01.2007.

[13] Spitzer, D.; Baras, C.; Schäfer, M.; Ciszek, F.; Siegert, B.; *Prop. Expl. Pyr.*, 36, **2011**, pp. 65-74.

[14] Krasnoperov, L.; Elkina, I.; Zhang, X.; *Prop. Expl. Pyr.*, 30 (3), **2005**, pp. 178-183.

[15] Stepanov, V.; Dissertation: Production of nanocrystalline RDX by RESS: Process development and material characterization, **2008,** New Jersey Institute of Technology, USA.

[16] McCrone, Walter; *Anal. Chem.*, 22 (7), **1950**, pp. 954-955.

[17] Karpowicz, R.; Sergio, S.; Brill, T.; *Ind. Eng. Chem. Prod. Res. Dev.,* 22, **1983**, pp. 363-365.

[18] Richter, T.; Zerstäuben von Flüssigkeiten, 2. Auflage, **2008**, Expert Verlag.

[19] http://www.plantfog.at/HD_D/Preisliste_HD-Duesen_D.htm , Hollow cone nozzles from the Plantfog company, 20.06.2012.

[20] Fedoroff, B.; Sheffield, O.; *Encyclopedia of explosives and related items*, **1966**, Vol. 3, Picatinny Arsenal, New Jersey, USA.

[21] Foltz, M.; Coon, C.; Garcia, F.; Nichols III, A.; *Prop. Expl. Pyr.*, 19, **1994**, pp. 19-25.

Nomenclature

A,B,C	Antoine-parameters	[-]
A	Cross-sectional area	[m^2]
B	Pitch of vanes	[m]
$c_{p,l}$	Molar heat capacity of liquid	[J $mol^{-1}K^{-1}$]
$c_{p,\ gas}$	Molar heat capacity of gas	[J $mol^{-1}K^{-1}$]
c	Concentration	[g / 100 g solution]
$c_{(r)}$	Solubility as a function of the radius	[g / 100 g solution]
$c\,\infty$	Solubility of the bulk material	[g / 100 g solution]
Cu	Cunningham correction factor	[-]
d	Diameter	[m]
d_c	Critical diameter	[m]
d_h	Hydraulic diameter	[m]
d_{pa50}	Aerodynamic cut-off diameter	[m]
$d_{pa50,diff}$	Diffusion dominated cut-off diameter	[m]
D	Nozzle diameter	[m]
D	Velocity of detonation	[m s^{-1}]
F_c	Centrifugal force	[N]
F_{drag}	Drag force	[N]
h	Height	[m]
h_{FG}	Heat of vaporization	[J kg^{-1}]
$\Delta_{vap}H$	Vaporization enthalpy	[J mol^{-1}]
k	Scherrer shape factor	0,89
k	Boltzmann constant	1,38064 10^{-23} J K^{-1}
Kn	Knudsen number	[-]
l	Length	[m]
l_c	Characteristic length	[m]
L	Channel length	[m]
L_{Rl}	Pipe flow coefficient	[m^3 s^{-1}]
LC	Crystallite size	[Å]
m	Mass	[kg]
m_0	Initial mass	[kg]
Δm_{flash}	Vapourized mass	[kg]
$\dot{m}_{gas}$	Gas mass flow rate	[kg s^{-1}]
M	Molar weight	[kg mol^{-1}]
n	Mole number	[mol]
N	Number of vanes	[-]
p	Pressure	[Pa]
Δp	Differential pressure	[Pa]
p_{crit}	Critical pressure	[Pa]
p_S	Saturation pressure	[Pa]
P_{cyc}	Average cyclone pressure	[Torr]
P_{760}	Pressure equal 760 torr	[Torr]

Q_0	Standard volume flow	$[m^3\ s^{-1}]$
$\dot{Q}_{ext}$	External heat supply	$[J\ s^{-1}]$
$\dot{Q}_{in}$	Heat entering system	$[J\ s^{-1}]$
$\dot{Q}_{out}$	Heat leaving system	$[J\ s^{-1}]$
r	Radius	[m]
r_{in}	Spindle inner diameter	[m]
r_{max}	Inner radius cyclone	[m]
r_{min}	Spindle radius	[m]
R	Gas constant	$8{,}314\ J\ mol^{-1}\ K^{-1}$
Re	Reynolds number	[-]
s	Correction factor	[-]
S_{BET}	BET-surface	$[m^2\ g^{-1}]$
t_D	Delay time	[s]
t_m	Median retention time	[s]
T	Temperature	[°C] or [°K]
T_0	Overheating temperature	[°C] or [°K]
T_b	Boiling temperature	[°C] or [°K]
T_{crit}	Critical temperature	[°C] or [°K]
T_m	Melting temperature	[°C] or [°K]
T_S	Saturation temperature	[°C] or [°K]
ΔT_S	Degree of superheating	[°C] or [°K]
U_b	Wetted perimeter	[m]
v	Velocity	$[m\ s^{-1}]$
v_{rel}	Relative velocity	$[m\ s^{-1}]$
V	Volume	$[m^3]$
V_g	Gas volume	$[m^3]$
V_l	Liquid volume	$[m^3]$
V_m	Molar volume	$[L\ mol^{-1}]$
ΔV_m	Molar volume change	$[m^3]$
$\dot{V}$	Volume flow rate	$[m^3\ s^{-1}]$
$\dot{V}_{\max}$	Maximum volume flow	$[m^3\ s^{-1}]$
$\dot{V}_{real}$	Measured volume flow	$[m^3\ s^{-1}]$
$\dot{V}_{theo}$	Theoretical volume flow	$[m^3\ s^{-1}]$
We	Weber number	[-]
X_{vap}	Evaporation ratio	[-]

Greek letters

γ	Surface tension	[N m^{-1}]
γ	Product yield	[-]
η	Dynamic viscosity	[Pa s]
η_L	Dynamic viscosity surrounding liquid	[Pa s]
λ	Wavelength	[m]
λ	Mean free path	[m]
λ_0	Mean free path under standard conditions	[m]
λ_L	Thermal conductivity	[W m^{-1} K^{-1}]
μ	Flow index	[-]
μ	Fluid dynamic viscosity	[N s m^{-2}]
μ	Expected value	
ν	Molecular volume	[m^3]
θ	Diffraction angle	[°]
ρ	Density	[kg m^{-3}]
ρ_l	Liquid density	[kg m^{-3}]
ρ_{po}	Density unit	[1000 kg m^{-3}]
σ	Surface energy	[N m^{-1}]
σ	Variance	
υ_G	Specific volume	[m^3 kg^{-1}]
υ	Kinetic viscosity	[m^2 s^{-1}]
ω	Angular velocity	[rad s^{-1}]
ω	Vane thickness	[m]
$n\xi$	Number of turns	[-]
ξ	Correction factor	[-]

Abbreviations

BET	Particle surface measurement according to Brunauer-Emmett-Teller
CL-20	2,4,6,8,10,12-hexanitro-2,4,6,8,10,12-hexaazaisowurtzitane
DRX	Diffractomètre à Rayons X
DSC	Differential Scanning Calorimetry
EDS	Energy Dispersive X-ray Spectroscopy
ESD	ElectroStatic Discharge
FESEM	Field Emission Scanning Electron Microscope
FWHM	Full Width at Half Maximum
HMX	Octahydro-1,3,5,7-tetranitro-1,3,5,7-tetrazocine
MEB	Microscope Electronique à Balayage
MTBE	Methyl T-Butyl Ether
ODTX	One Dimensional Time to eXplosion
PETN	PentaErythritol TetraNitrate
PID	Proportional-Integral-Derivative
PSD	Particle Size Distribution
RDX	1,3,5-Trinitrohexahydro-s-triazine
RESS	Rapid Expansion of Supercritical Solutions
SEM	Scanning Electron Microscopy
TEM	Transmission Electron Microscope
TNT	2,4,6-TriNitroToluene
XRD	X-Ray Diffraction

Annex - Chapter 3

Acetone				
Temperature **[°C]**	σ **[N m^{-1}]**	η **[10^{-3} Pa s]**	$c_{p,l}$ **[J kg^{-1} K^{-1}]**	$\Delta_{vap}H$ **[kJ kg^{-1}]**
-50	0,0325	0,818	1839,4	596,4
-45	0,0318	0,750	1848,3	592,8
-40	0,0312	0,690	1858,1	589,2
-35	0,0306	0,637	1868,7	585,6
-30	0,0299	0,591	1880,1	581,9
-25	0,0293	0,549	1892,2	578,1
-20	0,0287	0,512	1904,9	574,3
-15	0,0280	0,479	1918,4	570,5
-10	0,0274	0,450	1932,5	566,6
-5	0,0268	0,423	1947,2	562,6
0	0,0261	0,399	1962,5	558,6
5	0,0255	0,377	1978,4	554,5
10	0,0249	0,357	1994,8	550,4
15	0,0243	0,339	2011,8	546,2
20	0,0237	0,322	2029,3	542,0
25	0,0230	0,307	2047,4	537,7
30	0,0224	0,293	2065,9	533,3
35	0,0218	0,280	2084,9	528,9
40	0,0212	0,268	2104,4	524,3
45	0,0206	0,257	2124,5	519,7
50	0,0200	0,247	2145,0	515,0
55	0,0194	0,237	2166,0	510,3
60	0,0188	0,229	2187,6	505,4
65	0,0182	0,220	2209,7	500,5
70	0,0176	0,213	2232,4	495,4
75	0,0170	0,205	2255,6	490,3
80	0,0164	0,199	2279,5	485,0
85	0,0158	0,192	2304,0	479,7
90	0,0152	0,186	2329,2	474,2
95	0,0146	0,181	2355,2	468,6
100	0,0140	0,175	2382,0	462,8
105	0,0134	0,170	2409,7	456,9
110	0,0129	0,165	2438,4	450,9
115	0,0123	0,161	2468,1	444,7
120	0,0117	0,157	2499,1	438,3
125	0,0111	0,152	2531,3	431,8
130	0,0106	0,149	2565,0	425,0
135	0,0100	0,145	2600,4	418,0
140	0,0094	0,141	2637,7	410,8
145	0,0089	0,138	2677,1	403,4
150	0,0083	0,135	2719,0	395,6
155	0,0078	0,132	2763,7	387,6
160	0,0072	0,129	2811,8	379,2
165	0,0067	0,126	2863,8	370,5
170	0,0062	0,123	2920,5	361,3
175	0,0056	0,121	2982,8	351,6
180	0,0051	0,118	3052,1	341,4
185	0,0046	0,116	3129,9	330,6
190	0,0041	0,114	3218,7	319,0
195	0,0036	0,112	3321,5	306,5
200	0,0031	0,110	3443,2	293,0

Methyl t-butyl ether

Temperature **[°C]**	σ **[N m^{-1}]**	η **[10^{-3} Pa s]**	$c_{p,l}$ **[J kg^{-1} K^{-1}]**	$\Delta_{vap}H$ **[kJ kg^{-1}]**
-50	0,0287	0,993	1676,2	380,6
-45	0,0280	0,904	1686,8	378,0
-40	0,0274	0,826	1698,3	375,3
-35	0,0267	0,758	1710,7	372,6
-30	0,0261	0,698	1723,9	369,9
-25	0,0255	0,644	1737,9	367,1
-20	0,0248	0,596	1752,6	364,3
-15	0,0242	0,554	1768,1	361,4
-10	0,0236	0,516	1784,3	358,6
-5	0,0230	0,481	1801,2	355,7
0	0,0223	0,450	1818,7	352,7
5	0,0217	0,422	1836,9	349,7
10	0,0211	0,397	1855,7	346,7
15	0,0205	0,374	1875,0	343,6
20	0,0199	0,353	1894,9	340,4
25	0,0193	0,333	1915,3	337,3
30	0,0187	0,316	1936,2	334,0
35	0,0181	0,299	1957,6	330,8
40	0,0175	0,284	1979,5	327,4
45	0,0169	0,271	2001,8	324,0
50	0,0163	0,258	2024,5	320,6
55	0,0158	0,246	2047,7	317,1
60	0,0152	0,235	2071,3	313,5
65	0,0146	0,225	2095,3	309,8
70	0,0141	0,215	2119,7	306,1
75	0,0135	0,206	2144,5	302,3
80	0,0129	0,198	2169,8	298,4
85	0,0124	0,190	2195,4	294,5
90	0,0118	0,183	2221,6	290,4
95	0,0113	0,176	2248,2	286,3
100	0,0108	0,170	2275,3	282,0
105	0,0102	0,164	2302,9	277,7
110	0,0097	0,158	2331,1	273,2
115	0,0092	0,153	2359,9	268,6
120	0,0087	0,148	2389,4	263,9
125	0,0081	0,143	2419,6	259,0
130	0,0076	0,138	2450,6	254,0
135	0,0071	0,134	2482,6	248,8
140	0,0066	0,130	2515,5	243,4
145	0,0062	0,126	2549,7	237,9
150	0,0057	0,123	2585,1	232,1
155	0,0052	0,119	2622,0	226,0
160	0,0048	0,116	2660,7	219,7
165	0,0043	0,113	2701,4	213,0
170	0,0039	0,110	2744,5	206,0
175	0,0034	0,107	2790,3	198,6
180	0,0030	0,104	2839,4	190,7
185	0,0026	0,101	2892,5	182,2
190	0,0022	0,099	2950,4	173,0
195	0,0018	0,097	3014,1	162,9
200	0,0014	0,094	3085,3	151,7

Ethyl acetate

Temperature **[°C]**	σ **[N m^{-1}]**	η **[10^{-3} Pa s]**	$c_{p,l}$ **[J kg^{-1} K^{-1}]**	$\Delta_{vap}H$ **[kJ kg^{-1}]**
-50	0,0321	1,084	1730,2	452,2
-45	0,0315	1,012	1733,4	449,3
-40	0,0309	0,945	1737,3	446,3
-35	0,0303	0,885	1741,9	443,4
-30	0,0297	0,829	1747,2	440,4
-25	0,0291	0,777	1753,1	437,3
-20	0,0285	0,729	1759,7	434,2
-15	0,0279	0,685	1767,0	431,1
-10	0,0273	0,645	1774,9	428,0
-5	0,0267	0,607	1783,5	424,8
0	0,0262	0,572	1792,7	421,6
5	0,0256	0,539	1802,6	418,3
10	0,0250	0,509	1813,1	415,0
15	0,0244	0,481	1824,1	411,7
20	0,0238	0,455	1835,8	408,3
25	0,0232	0,430	1848,1	404,9
30	0,0227	0,408	1860,9	401,4
35	0,0221	0,386	1874,3	397,9
40	0,0215	0,366	1888,2	394,3
45	0,0209	0,348	1902,7	390,6
50	0,0204	0,330	1917,7	387,0
55	0,0198	0,314	1933,3	383,2
60	0,0192	0,298	1949,3	379,4
65	0,0187	0,284	1965,9	375,5
70	0,0181	0,270	1982,9	371,6
75	0,0175	0,258	2000,5	367,6
80	0,0170	0,246	2018,6	363,5
85	0,0164	0,234	2037,2	359,4
90	0,0159	0,224	2056,3	355,2
95	0,0153	0,214	2076,0	350,9
100	0,0148	0,204	2096,2	346,5
105	0,0142	0,195	2116,9	342,0
110	0,0137	0,187	2138,2	337,4
115	0,0131	0,179	2160,2	332,7
120	0,0126	0,171	2182,7	328,0
125	0,0120	0,164	2206,0	323,1
130	0,0115	0,157	2230,0	318,0
135	0,0110	0,151	2254,7	312,9
140	0,0104	0,144	2280,3	307,6
145	0,0099	0,139	2306,8	302,2
150	0,0094	0,133	2334,4	296,6
155	0,0088	0,128	2363,1	290,8
160	0,0083	0,123	2393,0	284,8
165	0,0078	0,118	2424,4	278,6
170	0,0073	0,114	2457,3	272,2
175	0,0068	0,109	2492,1	265,6
180	0,0063	0,105	2529,1	258,7
185	0,0058	0,101	2568,4	251,4
190	0,0053	0,098	2610,7	243,8
195	0,0048	0,094	2656,4	235,8
200	0,0043	0,091	2706,1	227,4

Methyl acetate				
Temperature **[°C]**	σ **[N m^{-1}]**	η **[10^{-3} Pa s]**	$c_{p,l}$ **[J kg^{-1} K^{-1}]**	$\Delta_{vap}H$ **[kJ kg^{-1}]**
-50	0,0338	0,871	1768,9	489,6
-45	0,0332	0,811	1767,4	486,4
-40	0,0326	0,757	1766,2	483,2
-35	0,0320	0,709	1765,2	479,9
-30	0,0313	0,666	1764,6	476,6
-25	0,0307	0,627	1764,2	473,3
-20	0,0301	0,592	1764,1	469,9
-15	0,0295	0,559	1764,2	466,4
-10	0,0289	0,528	1764,7	463,0
-5	0,0282	0,499	1765,4	459,4
0	0,0276	0,473	1766,4	455,9
5	0,0270	0,448	1767,7	452,2
10	0,0264	0,425	1769,2	448,6
15	0,0258	0,403	1771,1	444,8
20	0,0251	0,383	1773,3	441,1
25	0,0245	0,363	1776,2	437,2
30	0,0239	0,346	1792,6	433,3
35	0,0233	0,329	1809,3	429,4
40	0,0227	0,313	1826,3	425,4
45	0,0221	0,298	1843,7	421,3
50	0,0215	0,284	1861,3	417,1
55	0,0208	0,271	1879,3	412,9
60	0,0202	0,259	1897,6	408,6
65	0,0196	0,247	1916,3	404,2
70	0,0190	0,236	1935,5	399,8
75	0,0184	0,226	1955,0	395,2
80	0,0178	0,216	1975,1	390,6
85	0,0172	0,206	1995,7	385,9
90	0,0166	0,198	2016,8	381,0
95	0,0160	0,189	2038,6	376,1
100	0,0154	0,181	2061,1	371,0
105	0,0148	0,174	2084,3	365,8
110	0,0142	0,167	2108,3	360,5
115	0,0136	0,160	2133,2	355,1
120	0,0130	0,154	2159,1	349,5
125	0,0124	0,148	2186,2	343,7
130	0,0118	0,142	2214,5	337,8
135	0,0112	0,136	2244,3	331,7
140	0,0106	0,131	2275,7	325,4
145	0,0100	0,126	2308,9	318,9
150	0,0094	0,122	2344,3	312,1
155	0,0088	0,117	2382,1	305,1
160	0,0082	0,113	2422,8	297,8
165	0,0076	0,109	2467,0	290,2
170	0,0071	0,105	2515,2	282,2
175	0,0065	0,101	2568,4	273,8
180	0,0059	0,098	2627,7	264,9
185	0,0053	0,095	2694,5	255,5
190	0,0047	0,092	2771,2	245,5
195	0,0042	0,089	2860,7	234,7
200	0,0036	0,086	2967,5	223,0

Diethyl ether

Temperature **[°C]**	σ **[N m^{-1}]**	η **[10^{-3} Pa s]**	$c_{p,l}$ **[J kg^{-1} K^{-1}]**	$\Delta_{vap}H$ **[kJ kg^{-1}]**
-50	0,0259	0,534	1872,9	426,0
-45	0,0252	0,501	1887,3	422,6
-40	0,0246	0,470	1902,6	419,2
-35	0,0239	0,441	1918,7	415,7
-30	0,0233	0,415	1935,5	412,1
-25	0,0227	0,390	1953,0	408,5
-20	0,0220	0,368	1971,1	404,9
-15	0,0214	0,347	1989,8	401,2
-10	0,0207	0,328	2009,2	397,5
-5	0,0201	0,310	2029,1	393,7
0	0,0195	0,293	2049,5	389,8
5	0,0189	0,278	2070,4	385,9
10	0,0183	0,263	2091,9	381,9
15	0,0176	0,250	2113,8	377,8
20	0,0170	0,237	2136,2	373,7
25	0,0164	0,225	2159,0	369,5
30	0,0158	0,214	2182,3	365,2
35	0,0152	0,204	2206,1	360,9
40	0,0146	0,194	2230,3	356,4
45	0,0140	0,185	2255,0	351,9
50	0,0135	0,177	2280,1	347,3
55	0,0129	0,169	2305,8	342,6
60	0,0123	0,161	2332,0	337,7
65	0,0117	0,154	2358,8	332,8
70	0,0112	0,147	2386,2	327,7
75	0,0106	0,141	2414,2	322,5
80	0,0101	0,135	2443,0	317,2
85	0,0095	0,129	2472,5	311,7
90	0,0090	0,124	2502,9	306,1
95	0,0085	0,119	2534,3	300,3
100	0,0079	0,114	2566,8	294,3
105	0,0074	0,110	2600,4	288,2
110	0,0069	0,105	2635,5	281,8
115	0,0064	0,101	2672,1	275,1
120	0,0059	0,094	2710,6	268,2
125	0,0054	0,091	2751,1	261,1
130	0,0049	0,088	2794,0	253,5
135	0,0044	0,085	2839,8	245,6
140	0,0040	0,082	2888,9	237,3
145	0,0035	0,080	2942,0	228,5
150	0,0031	0,077	3000,0	219,1
155	0,0026	0,075	3063,9	209,1
160	0,0022	0,073	3135,2	198,2
165	0,0018	0,070	3215,8	186,3
170	0,0014	0,068	3308,4	173,0
175	0,0011	0,067	3416,9	157,8
180	0,0007	0,065	3546,8	139,9
185	0,0004	0,063	3706,6	117,4
190	0,0001	0,061	3909,6	84,3
195	Supercritical fluid			
200				

Methyl formate

Temperature [°C]	σ [N m^{-1}]	η [10^{-3} Pa s]	$c_{p,l}$ [J kg^{-1} K^{-1}]	$\Delta_{vap}H$ [kJ kg^{-1}]
-50	0,0371	1,005	1634,0	540,6
-45	0,0362	0,908	1633,6	536,7
-40	0,0353	0,823	1633,6	532,7
-35	0,0344	0,750	1633,8	528,7
-30	0,0336	0,686	1634,4	524,6
-25	0,0327	0,629	1635,4	520,5
-20	0,0318	0,580	1643,5	516,3
-15	0,0310	0,537	1656,3	512,0
-10	0,0301	0,499	1669,8	507,7
-5	0,0292	0,466	1683,9	503,4
0	0,0284	0,437	1698,5	499,0
5	0,0276	0,411	1713,8	494,5
10	0,0267	0,388	1729,6	489,9
15	0,0259	0,368	1745,9	485,3
20	0,0251	0,349	1762,8	480,6
25	0,0242	0,333	1780,3	475,8
30	0,0234	0,318	1798,3	471,0
35	0,0226	0,305	1816,8	466,0
40	0,0218	0,292	1836,0	461,0
45	0,0210	0,281	1855,7	455,9
50	0,0202	0,270	1876,0	450,7
55	0,0195	0,260	1896,9	445,4
60	0,0187	0,251	1918,5	440,0
65	0,0179	0,242	1940,7	434,5
70	0,0171	0,234	1963,7	428,9
75	0,0164	0,226	1987,5	423,1
80	0,0156	0,219	2012,2	417,2
85	0,0149	0,212	2037,8	411,2
90	0,0142	0,206	2064,4	405,1
95	0,0135	0,200	2092,1	398,7
100	0,0127	0,194	2121,1	392,3
105	0,0120	0,189	2151,6	385,6
110	0,0113	0,183	2183,7	378,8
115	0,0106	0,179	2217,6	371,7
120	0,0100	0,174	2253,6	364,4
125	0,0093	0,170	2292,1	356,9
130	0,0086	0,165	2333,4	349,1
135	0,0080	0,161	2378,2	341,0
140	0,0073	0,158	2427,0	332,6
145	0,0067	0,154	2480,7	323,9
150	0,0061	0,151	2540,5	314,7
155	0,0055	0,147	2608,0	305,1
160	0,0049	0,144	2685,1	295,0
165	0,0043	0,141	2775,0	284,2
170	0,0038	0,138	2882,3	272,8
175	0,0033	0,135	3014,0	260,6
180	0,0027	0,133	3182,3	247,3
185	0,0022	0,130	3409,4	232,8
190	0,0018	0,128	3742,1	216,7
195	0,0013	0,126	4303,8	198,3
200	0,0009	0,123	5593,9	176,7

Propanal

Temperature [°C]	σ [N m^{-1}]	η [10^{-3} Pa s]	$c_{p,l}$ [J kg^{-1} K^{-1}]	$\Delta_{vap}H$ [kJ kg^{-1}]
-50	0,0325	0,858	1945,0	576,5
-45	0,0318	0,787	1949,0	572,7
-40	0,0311	0,725	1953,7	568,9
-35	0,0303	0,670	1959,2	565,0
-30	0,0296	0,621	1965,5	561,1
-25	0,0289	0,577	1972,5	557,1
-20	0,0282	0,538	1980,2	553,1
-15	0,0275	0,503	1988,7	549,0
-10	0,0268	0,471	1998,0	544,9
-5	0,0261	0,443	2008,0	540,7
0	0,0254	0,417	2018,7	536,5
5	0,0247	0,393	2030,2	532,2
10	0,0240	0,372	2042,4	527,9
15	0,0233	0,352	2055,3	523,4
20	0,0226	0,334	2068,9	519,0
25	0,0220	0,317	2083,3	514,4
30	0,0213	0,302	2098,3	509,8
35	0,0206	0,288	2114,1	505,1
40	0,0200	0,275	2130,6	500,4
45	0,0193	0,263	2147,8	495,5
50	0,0186	0,252	2165,8	490,6
55	0,0180	0,241	2184,4	485,6
60	0,0174	0,232	2203,9	480,5
65	0,0167	0,223	2224,1	475,3
70	0,0161	0,214	2245,0	470,0
75	0,0155	0,207	2266,8	464,6
80	0,0148	0,199	2289,4	459,0
85	0,0142	0,192	2312,9	453,4
90	0,0136	0,186	2337,2	447,7
95	0,0130	0,180	2362,6	441,8
100	0,0124	0,174	2388,9	435,8
105	0,0118	0,168	2416,4	429,6
110	0,0112	0,163	2445,0	423,3
115	0,0106	0,159	2475,0	416,8
120	0,0101	0,154	2506,3	410,1
125	0,0095	0,150	2539,2	403,2
130	0,0089	0,146	2573,7	396,2
135	0,0084	0,142	2610,2	388,9
140	0,0078	0,138	2648,9	381,3
145	0,0073	0,134	2690,0	373,5
150	0,0068	0,131	2734,0	365,4
155	0,0062	0,128	2781,3	357,0
160	0,0057	0,125	2832,4	348,3
165	0,0052	0,122	2888,2	339,1
170	0,0047	0,119	2949,5	329,5
175	0,0042	0,116	3017,5	319,3
180	0,0038	0,114	3094,0	308,6
185	0,0033	0,112	3181,3	297,2
190	0,0029	0,109	3282,5	285,0
195	0,0024	0,107	3402,7	271,9
200	0,0020	0,105	3549,1	257,5

Annex – Chapter 5

The preparation of nanostructured nitrocellulose

Nitrocellulose (NC), is obtained by the direct nitration of a biopolymer, the cellulose. NC is the main ingredient of most modern gun and artillery propellants. As NC may decompose after prolonged storage, stabilizing additives **must** be added to this material. Besides stabilizing agents, NC can also be mixed with different explosives to enhance its performances.

Because of its heavily cross-linked structure, NC compositions require intensive kneading in order to obtain a homogeneous distribution of the additives. In preliminary tests, the nanostructuration of pure NC and the preparation of a NC-composite were investigated. As NC already decomposes at 180 °C, the experiments were performed at 140 °C.

Due to its polymer structure, dissolving NC in pure acetone is quite difficult. Nitrocellulose given into acetone immediately forms a thick, honey-like gel that sticks to most surfaces with which it is in contact. In pure MTBE nitrocellulose does not dissolve, it is rather dispersed. We found out that in a mixture of acetone/MTBE 50/50, NC is rapidly dissolved without the formation of a gel. This binary solvent is also advantageous as the flash-crystallization process can be performed at lower temperatures. In a first experiment, the mentioned NC-acetone/MTBE solution was used in the flash-crystallization process. The process parameters of this experiment are shown below (tab. 1)

Nozzle [µm]	Temperature		Solvent v/v [Acetone/MTBE]	Pressure [bar]	NC-Conc. [%-wt]
	Nozzle [°C]	Cyclone [°C]			
60	140	80	50/50	40	0,5

Tab.: 1 – Operating conditions for the nanostructuration of nitrocellulose.

The process was taken into operation in the usual manner. Even though NC is a long-chain polymer, almost perfect NC spheres were obtained in this experiment.

Fortunately, the SEM analyses was performed in a period where the field emission gun tip of the microscope was already depleted, resulting in a less concentrated electron beam. The SEM image clearly shows isolated NC spheres in the range of 50 to 500 nm.

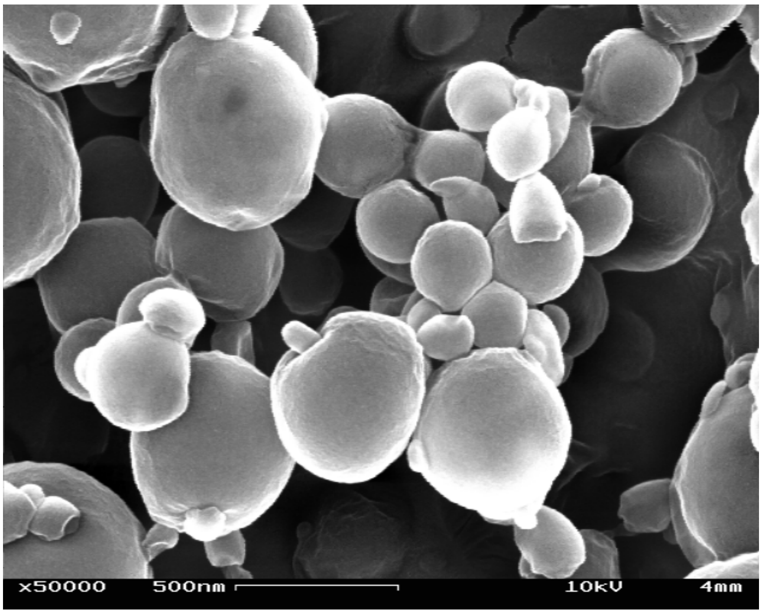

Fig.: 1 – SEM image of nanostructured nitrocellulose

As this experiment served as a feasibility study, only a few hundred milligram of this product were prepared. Due to the promising results, further studies on nanostructured NC propellants will be launched in the next time. The preparation of nanostructured NC and NC-composites is unique so far. The production capacity of the flash-crystallization process is already sufficient for the production of enough material for detailed ballistic investigations.

UNIVERSITÉ
DE LORRAINE

AUTORISATION DE SOUTENANCE
DU DOCTORAT DE L'UNIVERSITE DE LORRAINE

o0o

VU LES RAPPORTS ETABLIS PAR :

Monsieur KLAPOETKE Thomas, Professeur, Ludwig-Maximilians University, Munich (Allemagne),

Monsieur TRAEGNER Ulrich, Professeur, Hochschule Mannheim (Allemagne).

Le Président de l'Université de Lorraine, autorise :

Monsieur RISSE Benedikt Christoph

à soutenir devant un jury de l'UNIVERSITE DE LORRAINE, une thèse intitulée :

"Continuous crystallization of ultra-fine energetic particles by the Flash-Evaporation Process"

en vue de l'obtention du titre de :

DOCTEUR DE l'UNIVERSITE DE LORRAINE

Intitulé du doctorat : **"Génie des Procédés et des Produits"**

Fait à Vandoeuvre, le **17 Septembre 2012**
Le Président de l'Université de Lorraine,

Pierre MUTZENHARDT

UNIVERSITÉ DE LORRAINE
34 COURS LÉOPOLD - CS 25233
54052 NANCY CEDEX
TÉL : 03 54 50 54 00
CONTACT@UNIV-LORRAINE.FR
WWW.UNIV-LORRAINE.FR

Cristallisation continue des particules énergétiques ultra-fines par Evaporation-Flash

Résumé

Sous l'effet d'une forte impulsion mécanique, d'une chaleur très forte ou d'une décharge électrostatique, un explosif comme le TNT ou le RDX peut accidentellement être initié. L'énergie apportée à l'explosif est convertie en chaleur, appelée point-chaud, dans des endroits spécifiques, contenant des impuretés, bulles de gaz, pores ouverts ou autres hétérogénéités. La taille d'un point-chaud de quelques micromètres peut être déjà suffisante pour initier une déflagration ou même une détonation. En réduisant la taille des particules de l'explosif, la formation des points-chauds est empêchée conduisant à un matériau moins sensible.

Au sein de ce travail, un procédé continu est développé, fondé sur le principe de la cristallisation-flash, et permettant la préparation de particules énergétiques submicroniques en quantité de plusieurs grammes. Le procédé repose sur une opération de séchage par atomisation, au cours de laquelle une solution surchauffée est atomisée d'une manière continue. Afin de diminuer la taille moyenne des particules et d'obtenir une distribution de taille des particules très étroite, une étude paramétrique est réalisée. Au moyen de la cristallisation-flash, la préparation de composites énergétiques de haute qualité en grandes quantités est un succès. La qualité et quantité de ce composite énergétique sont uniques. Grâce au potentiel de ce procédé, la cristallisation-flash peut permettre la préparation de nombreuses substances et compositions énergétiques ou inertes.

Mots clés : Nanocristallisation, RDX, TNT, Cristallisation-flash, Procédé, Matériaux Energétiques.

Continuous crystallization of ultra-fine energetic particles by the Flash-Evaporation process

Abstract

High explosives, such as TNT or RDX, may be accidentally initiated under the influence of a strong mechanical impulse, great heat or an electrostatic discharge. Smallest impurities, open pores, entrapped gases or other inhomogeneities within the explosive matrix may convert the delivered energy into heat, causing the formation of a so called *hot-spot*. A hot-spot size of a few micrometers can already be sufficient to initiate a deflagration or even a detonation of the explosive. By decreasing the particle size of the explosive, the formation of hot-spots is inhibited, resulting in a less sensitive material.

In this work, a continuous operating flash-crystallization process was developed, being able to produce energetic submicron particles in a multigram scale. The process bases on a spray drying process where superheated solutions are continuously atomized. A parametric study was performed on this process in order to decrease the particle size and obtaining a narrower particle size distribution. By means of this flash-crystallization process, highly homogeneous energetic composites were prepared in a large scale. The quality and amount of the energetic composite are unique. The versatility of the flash-crystallization process allows the preparation of a large number of energetic and inert substances and compositions.

Key words: Nanocrystallization, RDX, TNT, Flash-Crystallization, Process, Energetic Materials.